Extracting Root System Architecture from X-ray Micro Computed Tomography Images using Visual Tracking

Stefan Mairhofer, M.Sc.

Thesis submitted to the University of Nottingham
for the degree of Doctor of Philosophy

December 2014

Abstract

X-ray micro computed tomography (μCT) is increasingly applied in plant biology as an imaging system that is valuable for the study of root development in soil, since it allows the three-dimensional and non-destructive visualisation of plant root systems. Variations in the X-ray attenuation values of root material and the overlap in measured intensity values between roots and soil caused by water and organic matter represent major challenges to the extraction of root system architecture. We propose a novel technique to recover root system information from X-ray CT data, using a strategy based on a visual tracking framework embedding a modified level set method that is evolved using the Jensen-Shannon divergence. The model-guided search arising from the visual tracking approach makes the method less sensitive to the natural ambiguity of X-ray attenuation values in the image data and thus allows a better extraction of the root system. The method is extended by mechanisms that account for plagiatropic response in roots as well as collision between root objects originating from different plants that are grown and interact within the same soil environment. Experimental results on monocot and dicot plants, grown in different soil textural types, show the ability of successfully extracting root system information. Various global root system traits are measured from the extracted data and compared to results obtained with alternative methods.

Acknowledgements

I would like to express my deepest gratitude to my supervisors Professor Tony Pridmore, Professor Malcolm Bennett and Professor Sacha Mooney, for all the support and intellectual guidance throughout those years, which has made this academic journey and research possible. Their knowledge and expertise in their different fields has been a unique and invaluable contribution in the realisation of this interdisciplinary project and a constant source of inspiration. I am especially grateful for all the trust and confidence placed in me that has motivated and allowed me to explore my own ideas. I could not imagine having had better mentors for my PhD study. I have been truly privileged to have had the opportunity to be part of such an excellent group.

I am very grateful to Professor Ian Dryden. His lectures and pleasant discussions we had on various aspects of statistics have been very helpful and, although he might not be aware, have played an important role in the presented and final outcome of this work.

Much appreciation goes to Craig Sturrock for his assistance and patience in helping me with operating the X-ray micro computed tomography scanner and for his effort and commitment to provide high quality image data. I am very thankful to Susan Zappala, Saoirse Tracy and Jonathan Helliwell, who helped and taught me how to grow plants the right way and without whom my plants would have never lived up to the stage of scanning.

I am thankful to my colleagues James Johnson, Tuan Nguyen and Haris Khan with whom I had countless stimulating and interesting discussions over the past years on various approaches and ideas in image analysis and visual object tracking.

Special thanks go to my family, Norbert, Renate and Antonia, for the emotional support and encouragement throughout the process and who never stopped believing in me. I am particularly thankful to On for the wonderful and memorable time we shared together, for all the comfort given and for being always by my side during this long and incredible journey. To them I dedicate my thesis.

This research would not have been possible without the financial support I received from the University of Nottingham Interdisciplinary Doctoral Training Centre (IDTC) in Integrative Biology.

Contents

List of Figures

List of Tables

Chapter 1

Introduction

The United Nations have ranked poverty and hunger as number one of the Millennium Development Goals (MDG), with the target to halve, between 1990 and 2015, the proportion of people who suffer from hunger [UN, 2013]. The target is within reach, but most of the progress in this direction was made before 2007-08 and has since then slowed down [FAO, WFP, and IFAD, 2012]. In 'The State of Food Insecurity in the World - 2012', the Food and Agriculture Organization of the United Nations (FAO) reported that about 870 million people, 12.5 percent of the population or one in eight people, are undernourished. Due to the growth in population and associated rising demand for food, it is estimated that by 2050 agricultural productivity has to increase by 60 percent [OECD and FOA, 2013]. The FAO recognises research and development as one of the key drivers for agricultural productivity [FAO, 2013a].

In the 1960s, breeding efforts in cereals, initially for rice and wheat and later for other crops, led to high-yielding dwarf varieties that were more responsive to nutrient availability in soil and less susceptible to lodging (plants falling over) [Borlaug, 1970]. As a result of the 'Green Revolution', cereal yields have rapidly increased. Evenson and Rosegrant [2003] estimated that without the achievements of the 'Green Revolution', today's global crop yields would be 8-12 percent lower while prices would be 35-66 percent higher and agricultural lands expanded by 2.8-4.6 percent, with attendant environmental consequences. Increased yields were reached through the combined use of these new varieties with mechanisation, crop protection chemicals and chemical fertilisers. Whilst developed countries had access to these resources

[Hazell and Ramasamy, 1991] farmers in developing countries still have limited access due to high costs, thereby limiting their agricultural output.

Jonathan Lynch [2007] foresees a 'Second Green Revolution' through redesigning plant root architecture to enhance nutrient acquisition, making plants tolerant to infertile soils while at the same time boosting yield. Root systems that are adapted to the low nutrient availability in soil are more efficient in taking up the sparse resources from the ground. This would make agriculture less dependent on chemical fertilisers and thus help prevent the rapid degradation of soil, while becoming more resilient to the uncertain effects of global climate change.

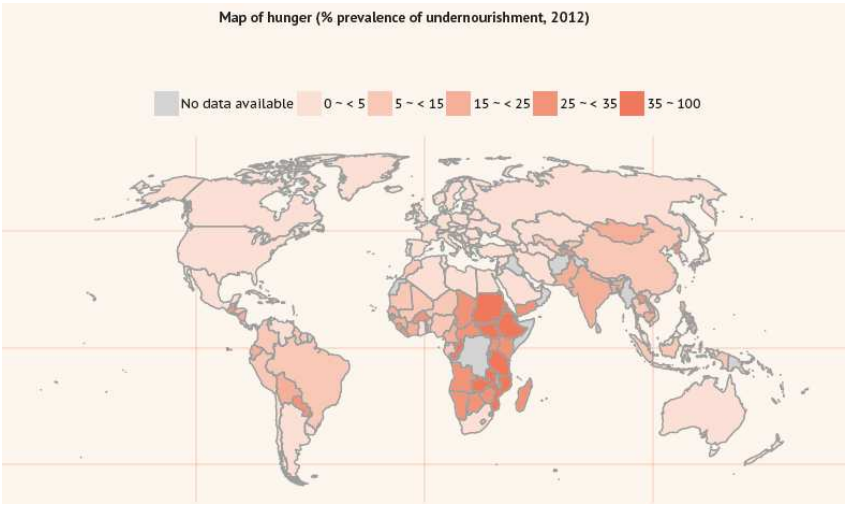

Figure 1.1: Map of hunger - image taken from [FAO, 2013b]

Understanding the development of plant roots and their interaction with the soil environment is vital to efforts toward food security. Roots provide anchorage and facilitate acquisition of water and nutrients from soil. Growing roots explore their local environment to exploit those resources and as such they depend on a wide range of soil properties [Lynch, 1995]. However, the complex relationship between roots and soil is not one sided. Plant roots have a large impact on the surrounding soil's physical and biochemical properties. They stimulate the growth and activity of microorganisms and hence affect the regulation of soil organic matter decomposition [Gregory, 2006a]. Furthermore, roots help develop the stability of soil aggregates and thus prevent soil erosion.

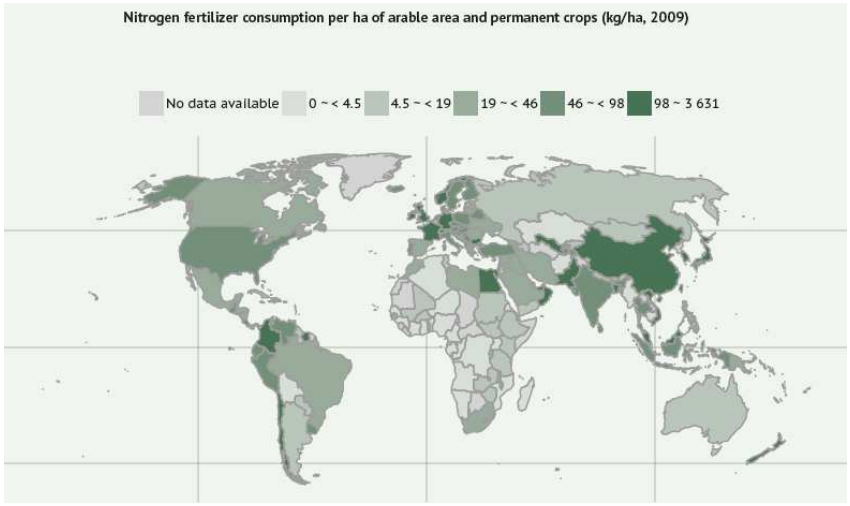

Figure 1.2: Fertiliser consumption - image taken from [FAO, 2013b]

1.1 Motivation

Roots represent the 'hidden half' of plant biology [Waisel et al., 2002] since soil makes them difficult to image non-invasively. Many different methodologies have been used to study the development of roots (see chapter 2, section 2.1). Popular techniques include the use of artificial growth media such as semi-transparent nutrient agar [Clark et al., 1999; French et al., 2009] or gellan gum [Clark et al., 2011]. While this overcomes the major problem of root visibility, it is not representative of a plant's natural environment. The most common method used to study the root system of plants grown in soil is root washing [Smit et al., 2000; Gregory, 2006b]. However, this often leads to the underestimation of fine roots through breakage, while information about the spatial distribution of roots is lost. Rhizotrons and mini-rhizotrons [Vamerali et al., 1999; Johnson et al., 2001], which are flat containers or tubes with a transparent wall, have also been used extensively. They allow roots to be grown in soil, but artificially restrict the direction of root growth to two dimensions. In addition, observations are limited to the boundary surface, showing only a small fraction of the entire root system. An alternative approach is the use of X-ray micro computed tomography (μCT), a non-destructive imaging technique that can visualise the internal structure of opaque objects. An X-ray μCT scanner acquires a series of projections from different angles, measuring the attenuation of ionising ra-

diation passing through the examined object. These projections are used for the reconstruction of the CT data in three-dimensional space. Data values are expressed in Hounsfield units and are usually mapped to greyscale intensity values for visualisation purposes (see chapter 2, section 2.2). X-ray μCT allows observation not only of plant roots, but also of the surrounding soil structure and associated pore volume.

Many researchers have argued that X-ray μCT is an effective tool with which to visualise plant roots growing in soil [Moran et al., 2000; Gregory et al., 2003; Jenneson et al., 2003; Tracy et al., 2010], yet there is still a lack of suitable methods to analyse the resulting data. The limiting factor has been the overlap in X-ray attenuation values of plant roots and the organic matter in soil, along with the variations in attenuation of the X-rays caused by water retained in roots and stored in the soil pores. Together these have made the automatic extraction of roots very difficult (see chapter 3). Previous attempts, reported in the literature, were all based on strategies that operate on a data-driven or bottom-up information processing system, starting with the raw data and moving toward root descriptions through a sequence of operations, each applied to the entire sample (see chapter 2, section 2.3). Local image-based criteria are used to define and successively refine groups of pixels that are likely to belong to the same class. This is often implemented as a fixed pipeline comprising multiple processing steps. This, however, suffers from several drawbacks. For example, errors tend to accumulate as each process introduces some inaccuracy. These are typically addressed by introducing interactive error correction tools. Manual correction, however, is often time consuming, as incorrectly classified objects are frequently small and usually distributed across the data set. Image analysis methods capable of providing high quality root descriptions, either fully automatically or with minimal human input, are badly needed.

1.2 Contribution

We present a novel segmentation technique that follows a model-driven or top-down strategy, in which a representation of an object is built from previously collected information and is used to control detection of further objects of the same class. This is achieved by adapting a visual tracking based framework, in which root objects are followed through a stack of cross-sectional

images derived from the volumetric CT data. Through continuous updates, the tracker adapts to changes in the appearance of the root objects, leading to a more dynamic extraction of the plant root system. In an additional step, the method is extended by a mechanism that goes beyond the separation of roots from the surrounding environment, and allows recovery of root systems of multiple interacting plants, associating each root with its originating plant. Extracted root systems are visualised and their traits characterised to promote better understanding of their complex architecture.

1.3 Overview

The rest of the thesis is organised as follows. In chapter 2, an overview is given of the various methodologies used in plant root studies (section 2.1), the principles of X-ray CT (section 2.2), related image analysis methods applied in the field of medical imaging (section 2.3.1 and 2.3.2) as well as different techniques developed for the purpose of root system extraction from two- and three-dimensional image data (section 2.3.3 and 2.3.4). In chapter 3, a novel extraction technique is presented, with the aim of recovering plant root systems form X-ray μCT image data of plants grown in soil. This technique is extended by mechanisms for the extraction of plagiotropic root systems (chapter 4). In chapter 5 information is provided on the visualisation of extracted data and the measurement of commonly desired root system characteristics. The presented method is evaluated in chapter 6 on artificially generated data (section 6.1), CT image data of real plant roots (section 6.2 and 6.3) and compared to extraction methods previously presented in the literature (section 6.4). The presented method is further extended to allow the extraction of multiple interacting root systems (chapter 7). The thesis is concluded with general discussions and outline of possible future work in chapter 8.

Chapter 2

Methods and techniques used in plant root studies

Agronomists have known for centuries that roots have a significant impact on the growth and productivity of crops. Early in the 19th century, Thomas Knight [1806; 1809; 1811] was keen to learn how roots develop and adapt to their environment. He was convinced that roots have the ability to locate and grow towards areas that best nourish the plant, but was not able to provide supportive evidence [Knight, 1806]. In a later letter [Knight, 1811] he in fact rejected his hypothesis, noting that plants have no such thing as an intellect, but are heavily influenced by their close surroundings. He was also among those who showed that gravitation has an impact on the direction of root growth. Knight [1806] demonstrated that the radical emerging from the seed responds to gravitation, always growing towards the centre of gravity. In order to show this, he bound a number of garden bean (*Phaseolus vulgaris L.*) seeds to a wheel that was rotated with the aid of water to generate a centrifugal force simulating gravity. Everything was enclosed in a box to prevent interference from the outside. Understanding the mechanism of gravitropism has found wide appeal. Wilhelm Pfeffer [1894], for instance, was interested in finding the stimulus for root gravitropism and showed that in uninjured roots, the root tip is solely responsible for sensitivity to gravitation. To demonstrate this, Lupin plants (*Lupinus L.*) were placed so that their roots would grow into glass tubes mounted on a clinostat, which is a rotating platform to simulate microgravity. Several decades later it was

discovered that auxin, a plant hormone responsible for growth and cell elongation regulates, among other things, gravitropism [Bennett et al., 1996] and that in fact the lateral root cap is required to transport the hormone into elongating epidermis cells, making it possible for roots to bend in response to gravitropic stimulus [Swarup et al., 2005]. This has been demonstrated by an experiment in which different mutants of Arabidopsis (*L.*) were grown in MS (Murashige and Skoog) medium plates. The root tissue was examined using confocal microscopy and a marker was used to show the expression of the AUX1 protein, which is known to be an auxin uptake carrier [Bennett et al., 1996]. It has been comprehensively shown that gravity is one external stimulus that can affect roots, but there are many other environmental factors that can change root growth. That water is an important resource for plants is generally known. It therefore seems reasonable that roots would show a different response to the absence or presence of nearby water, as this would improve their chances of survival. To what extent roots respond to water stress was one of the questions that Newman [1966] tried to answer. He used transparent tubes filled with soil in which flax (*Linumusitatissimum L.*) was grown, allowing the observation of roots through the tube wall. The tube was covered with plastic sheets that were only removed when taking measurements. This prevented roots from being exposed to too much daylight. By closely monitoring root growth and the moisture content of the soil, he observed that root growth decreases as the soil gets drier, but also discovered that roots located in dry soil layers are not influenced by the moisture content elsewhere around the root system. He therefore stated that roots differ locally in their responses to water content [Newman, 1966]. As part of the effort to advance understanding of the impact low water potential has on the growth of roots, Sharp and collaborating researchers have conducted numerous experiments [Sharp et al., 1988; Sharp and LeNoble, 2002; Sharp et al., 2004; Yamaguchi and Sharp, 2010], and discovered, among other things, that the elongation rate in the apical meristem (region of undifferentiated and actively dividing cells at the root tip), of a primary maize root is independent of soil water potential, which can be as low as -1.5MPa to -1.6MPa (permanent wilting point). There is, however, a notable difference in elongation rate in the region after the apical section. The further cells are from the apex, the lower the elongation rate as the soil gets drier, until there is no elongation observed in either of the two conditions, wet or dry soil. For this

phenomenon to be observed, Sharp et al. [1988] cultivated maize (*Zea mays L.*) in a Plexiglas box filled with vermiculite, to minimise the mechanical influence during drying. The elongation rate was determined by marking points 1mm apart with a very fine ballpoint pen on roots that were imaged every 15 minutes for a period of 1 hour. He also suggested that abscisic acid (ABA), another plant hormone often associated with inhibition of growth, may play an important role in maintaining root and shoot growth in water stressed plants rather than completely inhibiting their development under low water potential, as commonly assumed [Sharp and LeNoble, 2002].

Gravity and water are not the only factors that have an effect on the growth and development of plant roots. Intrinsic factors also play important roles, such as genetic differences or the large variety of plant species with their different root system topologies. An idea of how complex a root system can become is given in the comprehensive review written by Jonathan Lynch [1995] and will not be further discussed here. The few examples of classical studies on plant roots mentioned above shed some light on the different ways in which researchers have set up their experiments in order to observe the particular root behaviour that they were interested in. Several other methods have been reported. Some have found wide acceptance and have been used in numerous studies while others are still considered relatively novel, but have shown high potential to yield new discoveries. In section 2.1 we will briefly discuss some of these methods. Since we are primarily interested in the use of X-ray micro computed tomography (μCT) for the examination of root systems, we devote a separate section of this chapter to the principles of X-ray CT (section 2.2). The method chosen for a particular experiment dictates, to a certain degree, the environment plants are grown in. This, in turn, often determines the way in which image data is collected and used for further analysis. Depending on the available image data, different tools and algorithms have been reported that allow the semi- or fully-automated extraction of useful information and the measurement of root system traits. An overview of some of these image analysis techniques is given in section 2.3.

2.1 Plant growth systems facilitating root observation

In this section we give a brief overview of the plant growth systems that are frequently used in studies of root growth and development. By giving the reader an idea of the different and numerous experimental set-ups and their limitations, we hope to explain why, for certain experiments, X-ray μCT seems to be the best alternative currently available.

In order to gain a better understanding of the complexity of plant roots, it is indispensable for researchers to be able to observe their growth and development. This might seem trivial at first glance, but since roots grow naturally in soil, which is opaque, the problem of making them observable becomes a major issue. One way of overcoming this hurdle is to grow plants outside of their natural soil environment. This approach is fairly common in root related studies, because it overcomes the obstacle completely. To sustain and keep them healthy, one must, however, ensure that enough water and nutrients, such as nitrogen (N), phosphate (P) or potassium (K), are provided. There are many different ways in which plants can be grown without having to rely on soil, one of which is by using aeroponic systems. With this technique, plant roots are suspended in air and sprayed with a fine mist of nutrient solution [Zobel et al., 1976; Robertson et al., 1985, 1990; Varney and Canny, 1993; Biddinger et al., 1998]. Another technique, similar in many aspects to aeroponics, is the hydroponic system. Instead of growing plants entirely in air, they are grown in containers filled with water and a mix of essential plant nutrients [Price et al., 1997; Förster et al., 1998; Price et al., 2002a; Tuberosa et al., 2002]. Both of these methods allow easy access to the root systems for observation and examination purposes. Also, with both techniques, it is possible to dynamically control the amount, as well as changing the combination of nutrients provided to the plant. Root systems, however, may respond differently depending on the method chosen. For instance, roots maintained in aeroponic cultures show an increased number of root hairs compared to roots grown in hydroponic cultures [Zobel et al., 1976]. While roots that develop naturally have to penetrate through the growing medium, none of the methods above apply any physical resistance on roots as they grow. In addition, there is no solid medium that physically supports the root system at any stage of development. Its three-dimensional

shape may therefore be significantly different from that of a naturally occurring root system.

This is not the case for plants grown in semi-transparent growth media, such as agar or gellan gum, which is used in plant tissue culture [Fujita and Syōno, 1997; Van der Weele et al., 2000; Lucas et al., 2011]. Both agar and gellan gum serve only as a support medium for the root system and need to be supplemented with nutrients to promote plant growth. Growing roots in a supportive medium makes it much easier to study development over time and to determine the growth rate at certain stages for particular roots, since time and position can be exactly recorded. On agar or gel plates, plants grow in a sterile and well-controlled environment, reducing inter-experimental variability. This makes semi-transparent media a popular choice. Despite the benefits, however, the reader will realise that the methods described so far constitute a rather artificial environment, which could make the applicability of certain results to field conditions questionable. It is very well known that the soil biological, chemical and physical properties and conditions have a strong influence on the development and growth of plant root systems [Gregory and Hinsinger, 1999; Gregory, 2006a; Hinsinger et al., 2005], which might be difficult to accurately imitate in an artificial environment due to their complexity. Nonetheless there have been a few attempts to close the gap between commonly used artificial growth media and the natural soil environment. One such example is the use of glass beads [Antonsen et al., 1999; Futsaether and Oxaal, 2002], which have been used, for instance, to simulate porosity between soil particles.

An obvious alternative to trying to create an environment that closely resembles soil, with all its manifold properties, is to actually use soil as a growth medium. Probably the oldest and simplest way to study how plant roots grow and adapt to soil conditions usually found in the field, is by growing plants in the field (as pioneered by Weaver in the 1920's [Weaver, 1926]). The roots, in order to be examined, are then excavated and/or washed free of the soil, making it possible to record and analyse their characteristics. This latter method of studying roots, even though it seems rather old-fashioned, is still a widely accepted and common approach [Trachsel et al., 2011]. There are, however, a number of major drawbacks. Roots, especially fine roots, can easily break off while being removed from the soil, if this is not done with utmost care. Even then it cannot be guaranteed that all the root system

will stay intact. Once the root system has been freed from the soil, the plant cannot be placed back into the soil environment, making it impossible to observe the development of the root system over time. But by far the biggest disadvantage of excavating roots is that the three-dimensional structure of the root system is not preserved. A great deal of information is lost during the process.

In cases where the complex interaction between soil and roots, and the effects they have on the rhizosphere (narrow region of soil adjacent to plant roots), is the subject of study, it becomes indispensable to grow the roots in soil and to preserve the area in which they interact with each other. A well-proven method in soil-root studies is the use of (mini-)rhizotrons [Gregory, 1979; Hodge et al., 1999; Johnson et al., 2001]. Rhizotrons are found in many different variations, the basic principles, however, remain the same. Plant roots are grown in soil against a transparent wall (usually glass or acrylic plastic), through which roots can be observed and measured. The most intricate forms of rhizotrons are underground observation chambers, which are stationary and usually quite expensive, but provide also the widest view of underground soil-root interaction compared to other rhizotron variations [Hilton et al., 1969]. Other commonly found forms of rhizotrons are transparent boxes or sheets that are filled with soil in which plants are grown [Chaudhuri et al., 1986; Price et al., 2002b; Kuchenbuch and Ingram, 2002], or rhizotron tubes [Gregory, 1979; Andrèn et al., 1991], usually referred as mini-rhizotrons. Compared to larger devices, mini-rhizotrons are relatively cost-effective and easy to install. The installation of mini-rhizotrons, however, requires holes to be drilled into which the tubes are inserted. This process usually disrupts the soil environment and can break existing roots. Great care is needed to minimise any external influence to the soil-environment as well as to the root system under observation. If properly installed, mini-rhizotrons provide a minimally disruptive technique for monitoring roots and their interaction with the surrounding soil over a given period of time. A key limitation of this method, however, is the bound and partial view. Only roots that grow along the transparent wall of the rhizotron can be monitored; these might not be the area of interest. It should also be noted that data is always collected from a small sample of the whole root system and therefore care must be taken in drawing any conclusions related to the rest of the root system.

The major drawbacks of the last two methods described, namely the difficulty of preserving the root system and its structure, which is needed for the collection of time series, and the visualisation of the entire root system, can be overcome with current and emerging technology such as neutron radiography [Willatt et al., 1978; Menon et al., 2007; Moradi et al., 2009; Carminati et al., 2010], X-ray radiography [Moran et al., 2000; Pierret et al., 2003] and CT [Gregory et al., 2003; Kaestner et al., 2006; Hargreaves et al., 2009], nuclear magnetic resonance (NMR) [Bottomley et al., 1986; Antonsen et al., 1999] or magnetic resonance imaging (MRI) [MacFall et al., 1991; Jahnke et al., 2009; Nagel et al., 2009]. X-ray μCT and MRI in particular have attracted considerable attention from plant and soil scientists in recent years. Advances in the technology allow imaging of very fine details due to an increase in resolution. High resolution X-ray μCT scanners, for instance, are capable of generating three-dimensional data with a theoretical voxel size of 0.5μm [Mooney et al., 2012]. Most studies, however, have reported a practical voxel size in the range of 10 to 100μm, which is still slightly higher compared to MRI systems that operate with a theoretical voxel size up to 30μm, but have been used at a voxel size of 400μm [Jahnke et al., 2009]. Compared to X-ray CT, MRI suffers in the presence of magnetic compounds such as Cu^{2+}, Fe^{2+}, Fe^{3+} and Mn^{2+}, which are common in natural soil [Mooney et al., 2012], but can be particularly effective in studies related to water content and flow in plants [MacFall et al., 1991; Windt et al., 2006]. Due to the high contrast related to local water content, MRI seems to provide better detectability while X-ray μCT favours descriptiveness and accuracy. That X-ray CT is a potential and suitable instrument for soil-root studies has already been shown by Tollner [1991], who demonstrated that both biotic and abiotic components are identifiable in soil. Scanned cores showed that the seed of a Lima bean (*Phaseoluslunatis L.*) is clearly visible, but also that it is possible to observe the wetting front in dry soil, from which he concluded that X-ray CT can be used to monitor the moisture content change in soil cores. Since then other studies have been reported in which X-ray CT has been used to visualise roots within the soil environment [Heeraman et al., 1997; Gregory et al., 2003; Flavel et al., 2012]. Schmidt et al. [2012] not only showed that X-ray μCT is useful in visualising plant root systems grown in soil, but went a step further and demonstrated the ability of X-ray μCT to look at the level of interaction between roots and the soil

environment. They estimated the soil-root contact area using growth media with different particle sizes. A current limitation of methods such as X-ray CT and MRI is the restricted sample size. Studies with X-ray CT have been made with columns of a maximum reported diameter size of 250mm [Pierret et al., 2003; Mooney et al., 2012]. In order to obtain maximum contrast between plant roots and the surrounding soil environment, the most common choice of growth medium is a sand dominant soil type. Only a few studies have been conducted using soil that is more representative of field conditions [Mooney et al., 2012]. Early systems were slow in operation, but in newer and more technologically advanced systems, scanning time has been reduced considerably compared to systems used almost a decade ago, speeding up the process of imaging from 8 hours [Kaestner et al., 2006] to 20 minutes [Tracy et al., 2012] per sample. Despite the decrease in scan time, root data collection using techniques such as X-ray CT or MRI, is still considered low-throughput compared to semi-transparent screening methods. All this shows that there is no single best method suitable for all plant root studies; they are complementary. For the genetic analysis of plant roots, a high-throughput screening method is crucial, but at the same time it must be considered that plants often behave differently when grown in artificial environments [Hargreaves et al., 2009] and that it is essential to learn how plant roots grow, develop and compete for resources in soil. Here techniques such as X-ray μCT or MRI, offer great potential to increase our understanding and to open new doors that otherwise would remain locked. At the current stage of technology and within the same category of devices, serving the similar purpose of three-dimensional and non-destructive analysis, X-ray μCT seems to be favourable and more beneficial [Zhu et al., 2011], which supports our choice of technical imaging system for the scope of this work.

2.2 Principles of computed tomography

A key element in this study, which deserves its own section, is the imaging system itself - X-ray micro computed tomography (μCT). Having a sound knowledge of the concepts and principles behind the technology allows a better understanding of the capabilities and limitations of the system, and aids comprehension of CT image data. This plays an important role when designing a method aimed at extracting specific information while avoiding

potential pitfalls. To provide an idea of the datasets we work with and their characteristics, we will briefly review some background information on X-ray CT. In the following sections we discuss the fundamental principles of the system, how the volume data is generated and how the quality and noise level of these images can be determined.

2.2.1 X-ray (micro) computed tomography

Sir Godfrey Hounsfield, known as the father of X-ray CT, introduced the first scanner in 1971 [Hounsfield, 1973; Ambrose, 1973; Perry and Bridges, 1973; Kalender, 2006], revolutionising radiographic imaging. The real history of X-ray CT, however, dates back to 1895 when William Conrad Röntgen first presented a new kind of radiation, which he called X-rays ('X' symbolising the unknown), also sometimes referred to as Röntgen rays [Röntgen, 1898, 1896]. Röntgen quickly discovered that X-rays can pass through solid objects and be recorded on photographic film, producing two-dimensional shadow images revealing objects' internal structure. In radiographic imaging systems, X-rays are generated by an X-ray tube. Electrons are emitted by electrically heating a filament (cathode) and accelerated toward a positive target (anode), for which a high atomic weight material such as tungsten (W) or molybdenum (Mo) is usually chosen. When accelerated electrons are suddenly slowed down or stopped, a large portion of their energy is released in two forms; heat and X-rays. This phenomenon is called Bremsstrahlung [Hendee and Ritenour, 2002]. The intensity of radiation is measured by X-ray detectors. The most common detectors found in X-ray CT systems today are gas-filled ionisation chambers and scintillator-photodiode solid state detectors [Hendee and Ritenour, 2002].

With Hounsfield's invention of CT, it became possible to generate cross-sectional and three-dimensional visualisations of an object's internal structure. Unlike conventional X-ray radiography, CT acquires a series of projections from different angles, measuring the attenuation of ionising radiation passing through the examined object. These projections are used for the reconstruction of the CT data [Herman, 2009]. From a mathematical standpoint, the principles of CT and how to reconstruct a function from its projected data, had already been presented in 1917 by Johann Radon [Radon, 1917, 1986; Hendee and Ritenour, 2002]. A contribution to mathematical reconstruction algorithms was also made by Allan Cormack [1963], who shared the Nobel Prize for the invention of CT with Hounsfield in 1979.

However, when Hounsfield built his first CT scanner, he was unaware of the earlier work carried out by Radon and Cormack.

In recent years CT has undergone significant technical improvements, leading to different types of CT systems. First generation CT scanners have a single X-ray source and detector (both collimated) that are translated along and rotated around the specimen, resulting in projections with pencil- or parallel-beam geometry. The second generation CT scanners use the same procedure, but instead of a pencil beam and a single detector, they have a narrow fan beam and a linear detector array. Third generation CT scanners have a single non-collimated X-ray source, wide enough to capture the entire specimen and thus making translation of both X-ray source and detector unnecessary. The resulting data are projections with fan-beam geometry. Another generation of CT scanners are multi-detector CTs, which also have a single non-collimated X-ray source but a two-dimensional detector panel where projections are obtained from a cone-beam. Most common types of μCT scanners found today are either fan- or cone-beam systems [Stock, 2008]. A sketch of a cone-beam system is shown in figure 2.1. The different beam geometries play an important role in the reconstruction process, since the geometric magnification factor needs to be taken into account, which is determined by the distance of the sample to the X-ray source and the detector. Also to be considered for fan- and cone-beam geometries are the two different types of projections, whether they are sampled at equiangular or equispaced intervals [Kak and Slaney, 1988]. For the former, all X-rays are spaced with the same angle between neighbouring rays and if projected on a straight detector plane will result in unequal distances between incident rays, with increased space the further away they are from the centre location. This can be rearranged so that the space between the rays at the detector panel is equidistant, but this requires the angular intervals between rays to be unequal. The data needs to be weighted differently during the reconstruction process, depending on which projection type is used, and thus complicates the overall reconstruction algorithm compared to data acquired with parallel-geometry systems.

When a sample is scanned, photons emitted by the X-ray source can be absorbed or scattered as they pass through the object. This leads to a

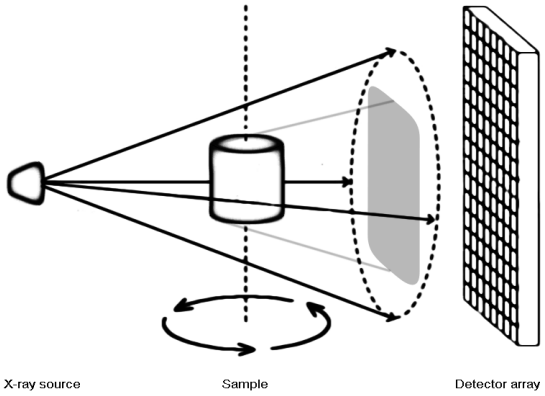

Figure 2.1: Sketch of an X-ray CT scanner with a multi-detector panel, showing a cone-beam directed at the sample and its magnified projection

reduction of intensity which is understood as attenuation and follows the Beer-Lambert law

$$I(t,\theta) = I_0 e^{-\int \mu(x,y)ds} \tag{2.1}$$

I_0 is the emitted intensity of the X-ray beam passing through the sample where the intensity is reduced based on the attenuation coefficient function $\mu(x,y)$. $I(t,\theta)$ is the received intensity transmitted through the sample on the projection line s with distance t from the origin at an angle θ. From this the projection $P(t,\theta)$ can be derived as follows

$$P(t,\theta) = -\ln \frac{I(t,\theta)}{I_0} = \int \mu(x,y)ds \tag{2.2}$$

Other photons that are neither absorbed nor scattered and thus exit the object are referred to as transmitted [Cullity, 1978; Herman, 2009]. Whether a photon is likely to be transmitted or attenuated depends on the density of the imaged object, but also on the energy of the photon itself. In order to penetrate high density material a high energy is needed. Low energy photons would almost be completely absorbed and thus are only capable of penetrating low density material. For convenience, we consider the target object to be composed of many small cubes or volume elements (voxels). When the object is imaged, each voxel will be traversed by numerous X-ray photons, some of which will be absorbed. From the intensity readings, it is possible to assign a value to each voxel that is proportional to its average

linear attenuation. The linear attenuation coefficients are then calibrated to a standard scale using the attenuation values of water (0HU) as a reference point

$$CT_{number} = K \cdot \frac{u_{voxel} - u_{water}}{u_{water}} \tag{2.3}$$

with K usually chosen to be 1,000. These calibrated values are known as CT numbers and are expressed in Hounsfield units (HU), which, for visualisation purposes, are often mapped to greyscale intensity values [Kak and Slaney, 1988]. It should be noted that CT numbers can vary not only between scanners, but also between scans taken with the same imaging device [Levi et al., 1982].

The photons generated by an X-ray tube usually consist of different wavelengths (are polychromatic), since not every electron is decelerated in the same way. This results in a continuous energy spectrum, which is different depending on the target material used [Herman, 2009]. This spectrum is composed of low as well as high energy photons. Low energy photons, especially for thick or high dense materials, are usually completely absorbed by the sample, yet would saturate the detector if they go around the scanned object, reducing the contrast in the volume data. Filters of different thickness and material, whose purpose is to absorb the low energy radiation, are therefore often placed between the target and the sample to harden the beam [Cullity, 1978] and eliminate undesirable energy levels.

Image contrast is an important factor when differentiating and identifying particular components in CT data and is influenced by, among other factors, the number of scattering events which occur when an X-ray photon is deflected from its original path. Scattering events are more likely found at higher energies [Ketcham and Carlson, 2001], which makes the application of lower energies more favourable. Low energy X-rays are also much more sensitive to small differences in material densities [Ketcham and Carlson, 2001], but their energy needs to be high enough to allow transmission through the scanned specimen.

Data acquired with X-ray CT is susceptible to numerous imaging artefacts. A common artefact is caused by beam hardening [Herman, 2009]. As mentioned above, the energy distribution spectrum is polychromatic. As the beam passes through the scanned object, lower energy photons are attenuated at a much higher rate than higher energy photons, causing the spectrum

to change and its mean energy to increase - the beam is hardened. For a cylindrical object, it also means that the beam passing through the centre is hardened more than the beam passing through the edges, and therefore the average linear attenuation in the centre is lower compared to that measured at the edges (figure 2.2a). This phenomenon is referred as cupping [Buzug, 2008]. Another implication of beam hardening is that the energy spectrum at a certain point in the object varies with the direction in which the beam passes through the sample and therefore it becomes difficult to assign a single value, sometimes resulting into bright and dark bands or streaks (figure 2.2b). This effect is known as a streak artefact [Buzug, 2008]. Streaks can also have other origins, including photon scattering [Stock, 2008]. Ring artefacts are also common, which usually arise from defective or insufficiently calibrated detectors, giving constant erroneous readings at the same position as the sample rotates, resulting in circular artefacts [Barrett and Keat, 2004]. An example of a ring artefact is shown in figure 2.2c. Image reconstruction becomes problematic when the sample moves slightly during the imaging process, which leads to variations and inconsistencies in the projection data [Buzug, 2008]. This in turn results in blurred images, which makes the analysis of the CT data difficult and inaccurate. The effect is known as motion artefact (figure 2.2d). When scanning a sample, it is necessary to ensure that enough angular projections are taken. Given too few projections, there is not enough information for the reconstruction of the data and the quality of images degrades, introducing fine stripes. This is referred to as undersampling [Barrett and Keat, 2004]. There are many more X-ray CT scanning artefacts that can arise, of which some are system or application specific, and will not be further discussed in this chapter. More details, however, can be found in [Buzug, 2008; Stock, 2008; Herman, 2009].

2.2.2 CT image reconstruction techniques

In CT, one- (for parallel- or fan-beam geometries) or two-dimensional (for cone-beam geometries) X-ray projections are taken at different angles to the sample, revealing in shadow images the interior of the scanned object. The aim of the reconstruction process is to find a suitable approximation of what object would give the data that is measured at the detector panel. This process is an inverse mathematical problem for which different solutions have been developed over many years. In this section we will discuss some

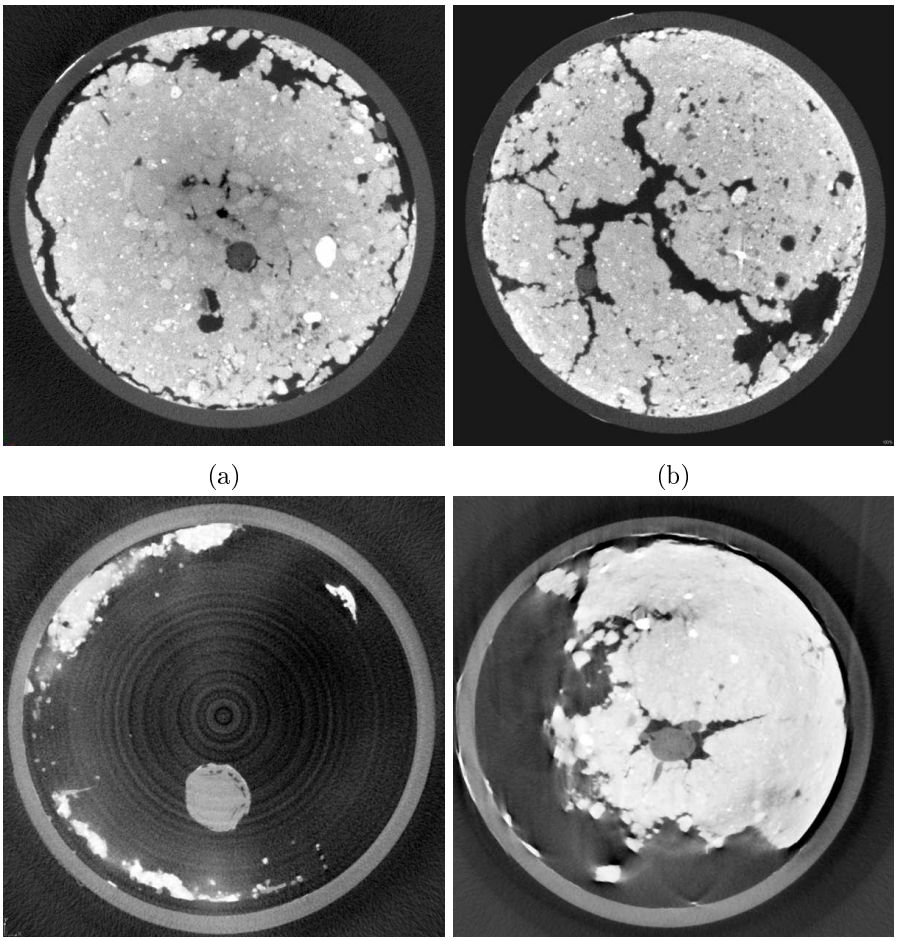

(a) (b)

(c) (d)

Figure 2.2: Various artefacts found in X-ray CT image data (a) cupping, (b) streak artefact, (c) ring artefact and (d) motion artefact

of the principles of CT image reconstruction and give an idea of how cross-sectional and volumetric image data can be obtained from these projections. For simplicity, we consider as an example a two-dimensional phantom (Shepp and Logan [1974], figure 2.3) and assume that X-rays pass through the sample parallel to each other. If the traversal of the X-rays were non-parallel (which is the case for fan- and cone-beam geometries), then the magnification factor must be taken into account in the reconstruction process.

Before we begin with the different reconstruction methods, we will first define the projections mathematically. An X-ray passing through an object follows a straight line whose attenuation is represented by a line integral.

Figure 2.3: Shepp-Logan phantom as defined in [Shepp and Logan, 1974]

The projection line through the phantom $f(x, y)$ at orientation angle θ (as shown in figure 2.4) is expressed as

$$x\cos\theta + y\sin\theta = t \tag{2.4}$$

The line integral $P(t, \theta)$ is defined as

$$P(t,\theta) = \int_{-\infty}^{\infty} f(t\cos\theta - s\sin\theta, t\sin\theta + s\cos\theta)ds \tag{2.5}$$

where t is the distance from the origin to the projection line s as shown in figure 2.4. This can be rewritten as

$$P(t,\theta) = \int_{-\infty}^{\infty}\int_{-\infty}^{\infty} f(x,y)\delta(x\cos\theta + y\sin\theta - t)dx\,dy \tag{2.6}$$

which is known as the Radon transform [Kak and Slaney, 1988]

$$P(t,\theta) = \Re f(x,y) = \check{f}(t,\theta) \tag{2.7}$$

By applying the Radon transform at different angles to the phantom $f(x, y)$, we obtain a series of line projections, known as a sinogram (figure 2.5a).

The aim of the reconstruction process is to recover the phantom from its projections. Hounsfield used an iterative algorithm in his first CT system. This was improved soon after and is today known as the algebraic

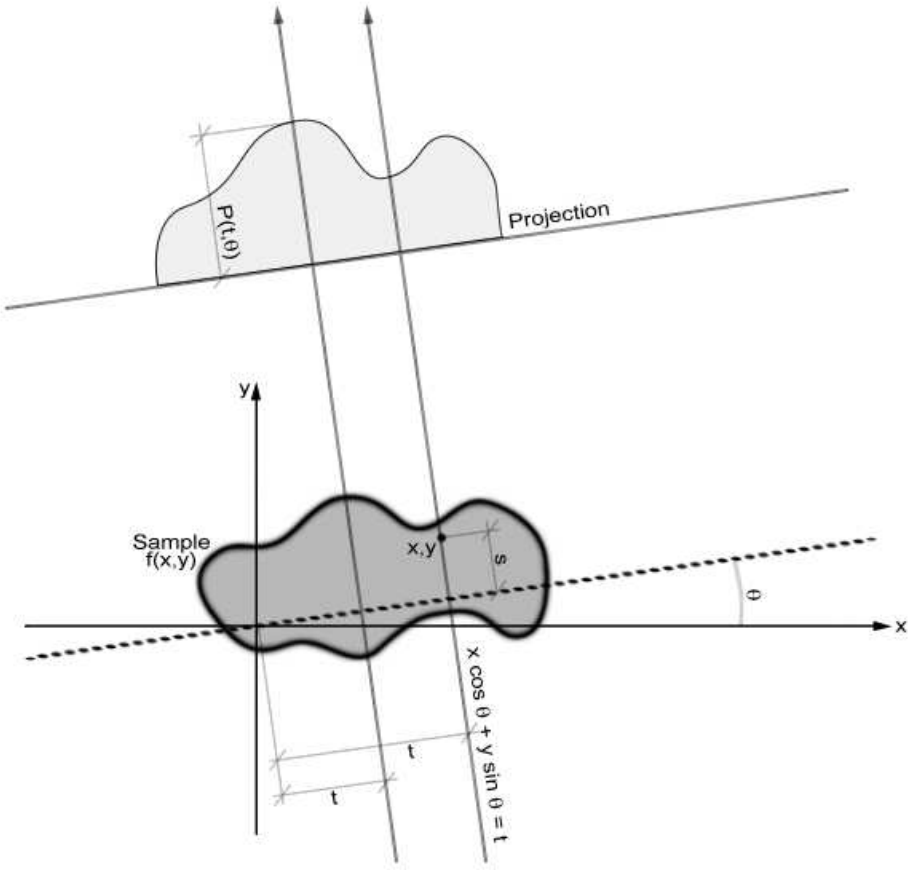

Figure 2.4: Sample function $f(x, y)$ and its projection $P(t, \theta)$

reconstruction technique (ART) [Goldman, 2007]. The method is computationally intensive and often considered not to be accurate enough for medical applications. This has limited its use in practice. Unlike other techniques however, this method works comparatively well given low numbers of projections and does not require them to be equally spaced over 180 or 360 degrees [Kak and Slaney, 1988]. The reconstruction problem can be rewritten in a matrix-vector formulation

$$\begin{array}{ccccc} P_\theta(t) & = & \mathfrak{R}f(x,y) & & \\ \downarrow & & \downarrow & \downarrow & \\ \mathbf{b} & = & \mathbf{A} & \mathbf{x} & \end{array} \tag{2.8}$$

where $\mathbf{b}$ is the sinogram represented in a single vector and $\mathbf{x}$ the image to

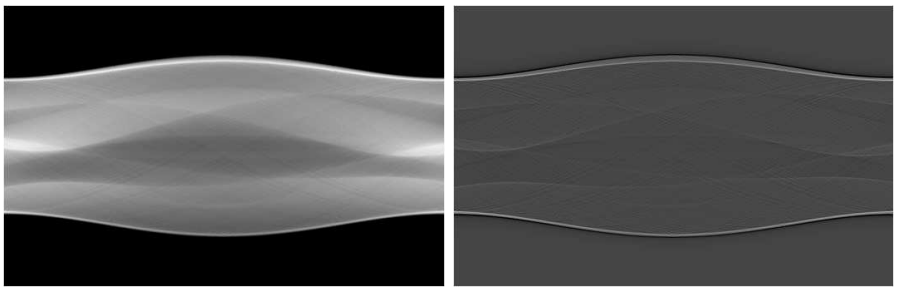

(a) (b)

Figure 2.5: Sinogram from projections over 180 degrees of the Shepp-Logan phantom; original (left) and after filtering (right)

be reconstructed. **A** is the system matrix, representing the relation between sinogram and the pixels in the reconstructed image and can be estimated using the nearest neighbourhood approximation, setting the element a_{ij} to 1 if the line (t, θ) crosses a pixel in the image plane and 0 otherwise. Other methods exist that provide a better estimation of the system matrix **A** and hence give better results. For more detailed information refer to [Toft, 1996]. The solution vector **x** can then be obtained through an iterative process

$$\mathbf{x}^{(k+1)} = \mathbf{x}^{(k)} + \frac{b_i - \mathbf{a}_i^T \mathbf{x}^{(k)}}{\mathbf{a}_i^T \mathbf{a}_i} \mathbf{a}_i \tag{2.9}$$

where i is a row of the system matrix **A** and best randomly chosen from a uniform distribution.

An alternative technique is built on the Fourier Slice Theorem, also known as the Central Slice Theorem, which states that the Fourier transform of a parallel projection $\check{f}(t, \theta)$ equals to the line at the same angle through the two-dimensional Fourier transform of the image $f(x, y)$ [Kak and Slaney, 1988].

$$F(v\cos\theta, v\sin\theta) = \int_{-\infty}^{\infty} \check{f}(t, \theta) e^{-2\pi i t v} dt \tag{2.10}$$

$$f(x, y) = \int_{-\infty}^{\infty} \int_{-\infty}^{\infty} F(k_x, k_y) e^{2\pi i (k_x x + k_y y)} dk_x \, dk_y \tag{2.11}$$

Reconstruction is therefore based on the relationship found in the frequency domain between the projections and the image rather than in the spatial domain.

Probably the most straightforward reconstruction method is the back-projection technique. The concept behind it is to take each projection and 'smear' it back over the reconstruction plane at the same angle the projection was taken from the image. The final pixel value is then obtained by superimposing all back-projected views [Kak and Slaney, 1988; Toft, 1996]. This can be mathematically formulated as

$$f(x,y) = \int_0^{\pi} \check{f}(x\cos\theta + y\sin\theta, \theta)d\theta \tag{2.12}$$

The back-projection method does not correctly solve the inverse problem, as the reconstructed image is severely blurred (figure 2.6c). The problem, however, can be overcome by convolving the sinogram with a filter (figure 2.5b). Many different filters have been presented in the literature. The simplest and probably most used filter is the Ram-Lak filter, also known as a ramp filter.

$$\check{f}_{filtered}(t,\theta) = \mathfrak{F}^{-1}(|v|\mathfrak{F}(\check{f}(t,\theta))) \tag{2.13}$$

$$f(x,y) = \int_0^{\pi} \check{f}_{filtered}(x\cos\theta + y\sin\theta, \theta)d\theta \tag{2.14}$$

where $\mathfrak{F}$ and $\mathfrak{F}^{-1}$ denotes the Fourier transform and inverse Fourier transform respectively and $|v|$ the ramp filter. This extension to the method is known as filtered back-projection reconstruction and is probably one of the most common techniques found in X-ray CT systems today.

2.2.3 Noise characteristics and quality of CT image data

All imaging devices are inevitably prone to sources of noise, which can degrade the quality of the image data and make it harder to identify objects of interest. Understanding the specific nature of noise in image data can have several advantages. It allows targeted filtering of the data to enhance the quality while preserving essential information, can be useful in seeking for an optimal scanning configuration in order to minimise the amount of undesired noise, and/or allow reproduction of the noise in artificially generated data that can be used in various testing scenarios. This section outlines the statistical characteristics of the noise that arises from the scanning process and shows a possible way of evaluating the quality of CT image data.

CT noise originates from the physical nature of the process - the generation of X-ray photons, the interaction of photons with matter and the detection of photons - and can be described by a Poisson distribution (for

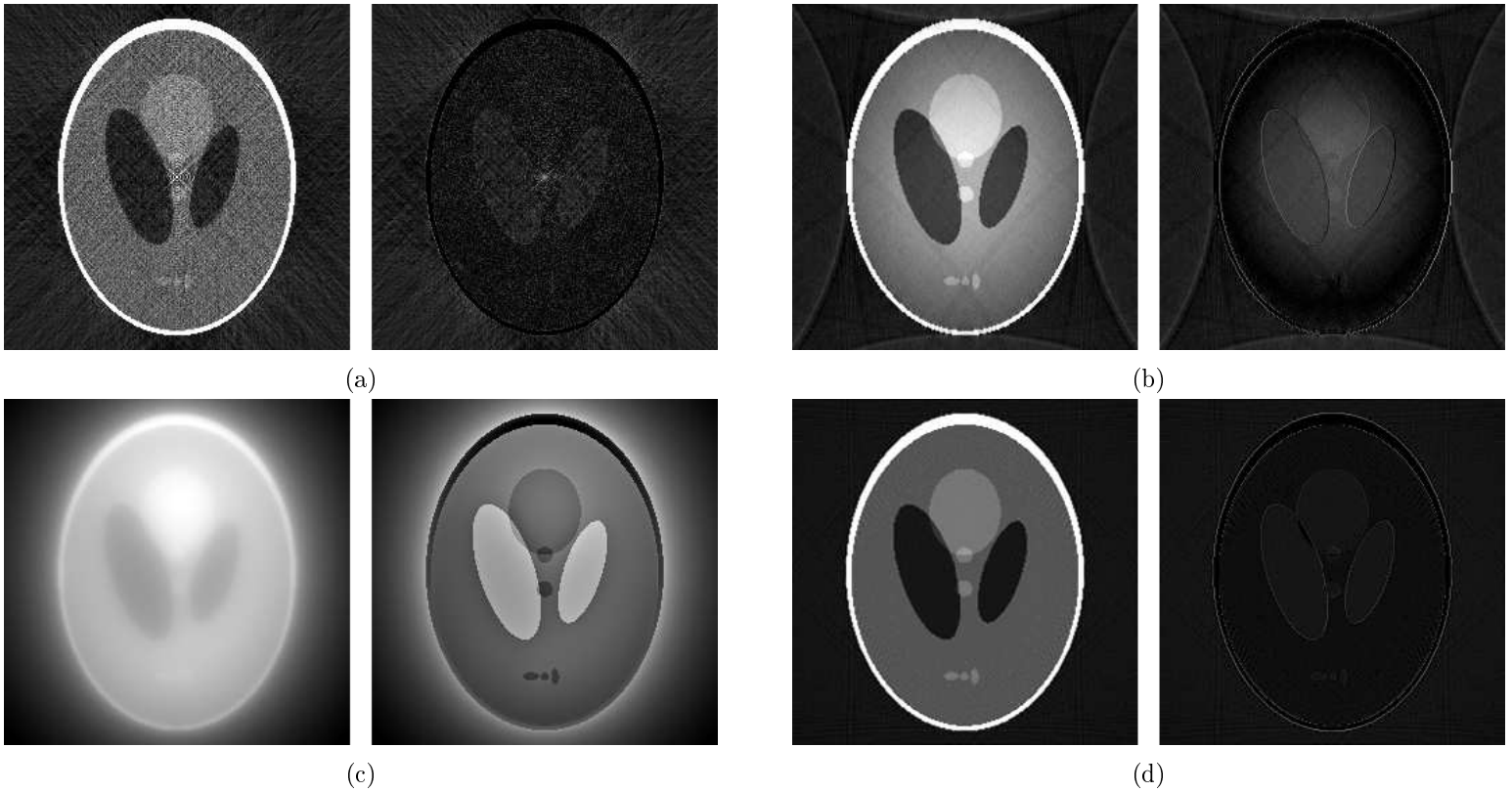

Figure 2.6: Reconstructed images and their difference to the original phantom using different techniques; (a) algebraic reconstruction technique (ART), (b) Fourier Slice Theorem, (c) back-projection reconstruction and (d) filtered back-projection reconstruction - (algorithms have been re-implemented following the steps and definitions presented in [Kak and Slaney, 1988; Toft, 1996])

more details see [Herman, 2009]). In a single projection the random noise at one point in the image is usually independent of the random noise at another point and is therefore uncorrelated, which is shown from its noise power spectrum (described in later paragraphs) that has a white noise characteristic, meaning that the noise is roughly constant over a range of frequencies [Hanson, 1981]. Through the reconstruction process, however, noise can generate peculiar characteristics, which usually differ from the white noise spectrum found in the projection data.

To evaluate the quality of CT image data, the spatial resolution and level of noise is often determined. Statistical properties, such as mean or variance are relatively easy to calculate, but are often not sufficient for a complete analysis [Kijewski and Judy, 1987]. Frequency domain analysis is often more suitable for the evaluation of quality, and has been extensively used in relation to medical imaging systems [Faulkner and Moores, 1984; Abdou and Dusaussoy, 1986; Cunningham and Shaw, 1999]. Metrics such as the modulation transfer function (MTF) or the noise power spectrum (NPS), also called Wiener spectrum, are often employed for the performance evaluation of X-ray detectors and medical imaging devices [Yaffe and Rowlands, 1997; Siewerdsen and Jaffray, 2000; Goertzen et al., 2004], to determine an optimum trade-off between radiation dose and image quality [Haus and Yaffe, 2000; Seibert, 2004], and for the comparison of different CT data reconstruction techniques [De Man and Basu, 2004; Thibault et al., 2007; Marin et al., 2010].

Relevant in this context is the point spread function (PSF), which is a significant characteristic in optical systems. The PSF describes the impulse response of an imaging system to a single point source. A measured point typically does not reflect exactly the original source, but introduces some degree of scatter or spread, which if it is too large will result in images that appear to be out of focus. Since imaging single point sources is difficult with most systems, alternatively a single line source can be used to measure the line spread function (LSF), which corresponds to the PSF defined in one dimension. This, however, only holds if the PSF is isotropic, meaning the spread is equal in all directions. Unfortunately, imaging a single line is often as complicated as imaging a single point. Therefore, the most common approach is to image a sharp edge and measure the edge spread function (ESF), which by differentiation gives the LSF. The MTF is then obtained by

the magnitude of the Fourier transform of the PSF, providing information about the reduction in contrast with increased spatial frequency [Smith, 2003].

$$MTF(u,v) = \|\mathfrak{F}(PSF(x,y))\| \tag{2.15}$$

As previously mentioned, noise can be characterized by the NPS, which gives a representation of the power of noise at various spatial frequencies [Cunningham and Shaw, 1999]. NPS is usually measured over a homogeneous area $d(x,y)$ in the image by taking the Fourier transform of $K_{dd}(x,y)$, the auto-covariance of $d(x,y)$

$$NPS(u,v) = \mathfrak{F}(K_{dd}(x,y)) = \mathfrak{F}(Cov(d(x+h,y+h),d(x,y))) \tag{2.16}$$

or alternatively given as

$$NPS(u,v) = \lim_{X,Y\to\infty} E\left\{\frac{1}{2X}\frac{1}{2Y}\left|\int_{-X}^{X}\int_{-Y}^{Y}\Delta d(x,y)e^{-2\pi i(ux+vy)}dxdy\right|^2\right\} \tag{2.17}$$

with $\Delta d(x,y) = d(x,y) - E\{d(x,y)\}$ and $E\{\}$ being the expectation operator. Given the MTF, the NPS and the average output signal $\overline{d}$ it is possible to determine the frequency dependent signal-to-noise ratio (SNR) [Cunningham and Shaw, 1999], which is defined as

$$SNR(u,v)^2 = \frac{\overline{d}^2 MTF^2(u,v)}{NPS(u,v)} \tag{2.18}$$

2.3 Image analysis as a tool to aid in the extraction of plant roots

Image analysis has become fundamental to the study of plant roots. When Newman [1966] conducted his study on how roots respond to water stress almost half a century ago, he monitored and examined the growth rate of each sample by hand. This was a tremendous amount of work, very time consuming, and one of the reasons why his study was limited by a low number of replicates. He stated that by using cameras and taking images, he would have been able to analyse the data at leisure and therefore use a larger number of samples. Nowadays, collecting data by taking images has

become part of most experimental methodologies. This, however, does not mean that the workload has been reduced. When root characteristics are measured manually, it is only postponed. In order to reduce workload, and thus to save time, a number of different image analysis tools have been developed. Reducing the time spent taking measurements allows researchers to put their efforts into core activities rather than routine tasks. Another great benefit of image analysis tools is that they decrease, to a degree, the subjectivity involved in an experiment. With so many different imaging techniques used in plant root studies, serving a wide range of different purposes, there exist even more image analysis tools for the extraction and quantification of root characteristics. The acquired image data depends on the experimental set-up but also on the imaging device that is used. For instance, when using rhizotrons, the data recorded is usually restricted to two dimensions [Johnson et al., 2001]. Another example are studies for which agar plates are used, where images are often taken either with normal digital cameras [French et al., 2009], in particular when looking at the root system architecture, or microscopy [Schiefelbein and Somerville, 1990], when the focus lies in observing very fine or cellular details. This results in image data that differs in its characteristics, but also in the information that needs to be extracted. All these variations led to the development of a wide range of tools, all optimised for a particular application. In this section we will limit our discussion to image analysis methods for whole or partial root system architectures, but divide it into two- and three-dimensional techniques. Due to its high relevance for this project, we will start the discussion, however, with some related image analysis methods that have been reported in the field of medical imaging.

2.3.1 Extraction techniques for medical X-ray CT

Though it only became interesting as a technology for soil-root studies within the last few years, X-ray CT has a long history. Its remarkable success was mainly achieved due to its wide acceptance in medical circles. X-ray CT is seen as the second major technological breakthrough in radiological diagnostics, after the discovery of X-rays. It is therefore not surprising that most of the image analysis and processing methods intended for CT data have been developed with a focus on medical research. Due to continuing technological advances, images can be produced with better quality and with higher res-

olution, which makes the interpretation of data easier but at the same time also susceptible to misinterpretation. Image analysis and processing algorithms have been introduced and extensively used to aid in the examination of the human body. Generally, the aim is the semi- or fully-automated separation of features, making the semantic analysis of data simpler and more understandable to users. Due to the enormous effort made in this area, this section is devoted, among others, to methods that have been developed for the extraction of information from medical X-ray CT images.

Thresholding is a frequently used method for medical image segmentation. It has been used, for instance, as part of the extraction process for bones and human organs [Ding et al., 1999; Hu et al., 2001; Leader et al., 2003]. Thresholding enjoys widespread popularity, mainly because of its simplicity, which is also the reason for its limited capability. Nonetheless, it is a technique commonly applied in image segmentation. Threshold based segmentation techniques require that features in images are very well distinguished from other objects and that all the greyscale or colour values of an object can be grouped into a single set of intensities. The method is usually performed on a per-pixel basis and thus exploits little or no information about the spatial distribution of grey levels. It is generally considered a crude segmentation step, extended with further operations to refine the separation towards a desired outcome. Segmentation methods that use clustering techniques are a little more sophisticated and have been used, among others, for the analysis of brain tissue [Loncaric et al., 1995; Masulli and Schenone, 1999]. Unlike thresholding, clustering techniques group similar data points together to form separate classes. This is usually done through an iterative process that seeks the optimum partition of the data. Clustering algorithms aim to maximise homogeneity within and heterogeneity between clusters, and thus are more robust against outliers. Another class of segmentation techniques are region-based methods, which have been successfully applied for the extraction of lung lobes and airways [Sonka et al., 1996; Kuhnigk et al., 2003; Ukil and Reinhardt, 2009]. This class of methods operates on regions rather than single pixels, which makes it hence more tolerant to noise. A common problem with region-based methods, however, is over- or under-segmentation, resulting in too many small and similar regions or too few large regions respectively. A somewhat different approach is taken by edge-based segmentation techniques [Gao et al., 1996; Gudmundsson et al.,

1998], which, instead of separating features by their area, operate on the boundaries of objects, that are extracted as contours. These methods are less affected by local variations within objects, and are particularly reliable on clear and sharp edges. In images with blurry objects or low contrast backgrounds, the extraction of boundaries becomes a challenging problem, which in certain situations can result in gaps or disconnected contour fragments. Among the wide variety of techniques and categories of image segmentation methods that have been introduced and applied to medical imaging over the years, it is worthwhile to mention the class of neural networks [Özkan et al., 1993; Koss et al., 1999]. Neural networks are a powerful tool, inspired by biological systems, with the ability to learn and discriminate between particular features. Learning, however, demands high levels of computational resource. Some methods rely on prior, rather than learnt, knowledge to guide the segmentation process. This approach has, for instance, been used in the extraction of kidneys and vertebra [Weese et al., 2001; Joshi et al., 2002]. Using prior knowledge can be beneficial, particularly in the presence of noise or imaging artefacts, but is not always available and varies with the application area. Furthermore, care must be taken not to extract features that are actually not present in the image (false positives).

2.3.2 Extraction of arterial structures

Most of the objects extracted by the methods discussed above have little to nothing in common with the structure of plant root systems. There is, however, a network that might, in a way, resemble the structure and complexity of root systems, namely blood vessels. Methods that have been developed for their segmentation are of relevance, because arterial trees show a certain degree of structural similarity to plant roots and as such present similar issues. Worth mentioning in this context is a medical imaging technique known as angiography. Digital subtraction angiography (DSA) is a method traditionally used for planar imaging by using two-dimensional X-ray projections, but is nowadays more frequently found in combination with either computed tomography (CTA) or magnetic resonance (MRA). The technique is designed in particular for vascular imaging, by using intravenous contrast agents [Piotin et al., 2003; Bash et al., 2005]. Angiography as a method has been known since 1927 when it was introduced by António Egas Moniz for the diagnosis of cerebral tumours [Moniz, 1927; Antunes, 1974].

A large number of segmentation techniques have been developed with two-dimensional DSA images in mind [Stansfield, 1986; Collorec and Coatrieux, 1988; Malladi et al., 1993; Figueiredo and Leitão, 1995]. One reason for this might be that conventional DSA has been used as a routine diagnostic method for a long period of time and is still used in practice today, while three-dimensional imaging techniques are still comparatively young. Stansfield [1986] segmented coronary vessels using a combination of image analysis methods and knowledge-based approaches. For the extraction of vessels, both an edge-detection operator and a region based thresholding method were applied independently, to achieve a crude segmentation of the vascular structure. The information obtained from the edge analysis was then used to refine the results of the region analysis, which was further used to look for elongated shapes. These shapes were finally matched against a set of rules comprising prior knowledge of the anatomical structure, eliminating undesired components that have made it through the previous steps. The approach presented by Collorec and Coatrieux [1988] is applicable, but not limited, to coronary vessels. Their method differs from conventional techniques that are often either based on morphological operators [Figueiredo and Leitão, 1995; Eiho and Qian, 1997; Zana and Klein, 2001] or threshold based segmentations [Kottke and Sun, 1990; Wilkinson et al., 2003], by considering a strategy that traces the centreline stepwise from automatically detected seed points towards the end of vessels, using a method based on vector averaging. With this approach it was possible to successfully identify the centrelines, which, in a secondary processing step, are used to further extract the boundaries of blood vessels. A problem when tracing vessels' centrelines is the possibility of loops being formed due to crossings with other vessels or irregularities in the image data. Trying to suppress these cyclic loops by weighting each vector point has been found to be inadequate. Therefore to reduce the effect of unexpected behaviours, a constraint was imposed based on the general assumption that the outline of vessel sections are symmetric and parallel to the centric base line. Malladi et al. [1993; 1995] presented a method aimed at extracting the shapes of arbitrary objects, which was tested on, among others, angiograms. Their method is based upon the level set method [Sethian, 1999] and uses an expanding speed function that stops at strong image gradients. The starting point of the level set method could be placed anywhere inside the arterial tree structure, the level set then evolves towards and converges on the vessel boundaries.

More challenging, compared to the two-dimensional problem, is the extraction of blood vessels from data that has been acquired with three-dimensional imaging systems, such as MRA or CTA [Wilson and Noble, 1999; Flasque et al., 2001]. Wilson and Noble [1999] used a statistically based approach for the extraction and localisation of cerebral vessels and aneurysms. Vessels and brain tissue within the image data differ from each other in their greyscale intensities. The expectation maximization (EM) algorithm was used to maximise a likelihood function to find the best parameters to cluster these intensities. A basic EM algorithm, however, had difficulties coping with the intensity variations found within the vascular network. Therefore, an adaptive variant of the EM algorithm was presented that recursively divides the volume into smaller sub-volumes on which a localised segmentation was performed. Sub-volumes can arise which contain only one tissue class. These were defined as special cases and were treated individually. Final steps included a smoothing process and a connectivity check to remove undesired segmented fragments and artefacts that could arise during the recombination of the data extracted from each sub-volume. Such statistical classification and clustering approaches are frequently adopted when segmenting three-dimensional data [Wilson and Noble, 1997; Chung and Noble, 1999; Yang et al., 2004]. This might be due to the simplicity of extending two-dimensional concepts to three-dimensional problems. Some other approaches that work well in two dimensions, however, can easily become quite complex when a third dimension is added to the dataset. A centreline based extraction method for cerebral vascular networks that works on three-dimensional MRA image data, was developed by Flasque et al. [2001]. The centreline was traced stepwise, with successive points being estimated by searching within an orientated parallelepiped around previously identified points. Rules, like the definition of a maximum allowed curvature, were imposed for each search area. Such a rule-based concept allowed the specification of a profile that is based on prior knowledge. A common problem for centreline based approaches is the detection of junctions or branches. Flasque et al. solved this problem by analysing the number of entry and exit points along the surface of each parallelepiped. By the definition of a continuous vessel, a parallelepiped must have exactly one entry and exit point. If more than one exit point is detected, then the presence of a junction is assumed, for which a new starting point is created. With this solution it is

further possible to restrict the maximum number of allowed junctions per vessel fragment. In a final step, all traced centreline points are connected using B-spline curves. To the reader's awareness it is worth mentioning that besides the numerous segmentation techniques, various vessel-specific filtering approaches have been presented for the extraction in two-dimensional DSA or three-dimensional MRA and CTA image data [Frangi et al., 1998; Sato et al., 1998].

Intravascular ultrasound (IVUS) is often used, as an alternative to contrast enhanced angiography, for imaging coronary arteries [Potkin et al., 1990]. An ultrasound transducer is placed at the end of a small catheter and inserted into the blood vessel, examining the interior arterial wall. Sonka et al. [1995] presented an automatic segmentation method for the study of lumen and arterial wall morphology using IVUS. Their method is based on an edge-detection operator in which each pixel of the detected edge is considered as a unique node in a graph and associated with a cost that is related to the likelihood of it being part of the desired outline. A heuristic graph search algorithm is then used to extract the boundaries. A priori information about the anatomical structure of vessels is incorporated to determine the plaque, internal and external lamina borders. Guerrero et al. [2007] used ultrasound imaging for the diagnosis of deep venous thrombosis in carotid arteries. Starting from a seed point within the artery, a probabilistic edge detection function is used to find elliptic arterial boundaries. The seed point is then tracked in successive image frames using a Kalman filter, which estimates the trajectory of points along the centreline of a vessel. Segmentation methods that have been developed for vessel extraction in ultrasound images usually do not deal with branching structures, as the main objective lies in identifying vascular abnormalities and not the artery tree structure.

Other complex root-structure-like networks in medical imaging are found, for instance, in neuronal arborescences [Meijering, 2010] and airway trees [Sonka et al., 1996].

2.3.3 Root extraction methods in 2D

Most of the methods presented in the literature with the aim of aiding the extraction of root systems from images have been developed for the analysis of two-dimensional images. There are many reasons for this. One is that the equipment needed to take two-dimensional images, such as a common

digital camera, is much cheaper and more accessible than imaging devices (such as X-ray CT or MRI) that allow direct acquisition of three-dimensional datasets. Cameras allow a higher throughput and have been around much longer and in many more forms than their counterparts. Sometimes, however, the experimental set-up also restricts the acquisition of data in two dimensions; rhizotrons, for example, allow only roots to be viewed on their observation plane. Since there are many different ways to set-up an experiment, the acquired two-dimensional images will differ as well, and with them also the complexity of extracting plant roots. It would therefore not be fair to compare the quality of extraction between the various methods, but we will discuss here the ideas behind them and the difficulties they face.

No matter in which medium plants are grown, the aim of extracting the root system is always the same, namely to separate them from the background. A popular method often used for the extraction of root systems from images, is simple global thresholding. Thresholding, converts a grey level or colour image into a binary image, in which a pixel is either part or not part of the extracted data, depending on whether its value lies in between or outside given limits. Thresholding only works well if the object of interest is clearly distinguishable from anything else in the image and pixel values do not overlap with pixels belonging to the background. This usually requires a well, for imaging purposes, prepared set-up, such as in [Lebowitz, 1988], where roots have been placed into a Petri dish filled with water and illuminated from underneath, so that roots appear dark on a bright background.

Thresholding alone is rarely sufficient enough to reliably extract root systems from images. Artefacts such as external light sources can induce variations in brightness and disrupt data extraction. Heterogeneous backgrounds, as found for example in rhizotron images, where soil is the growing medium, can make identification of suitable thresholds problematic. Image filtering techniques are often applied to reduce noise and increase contrast before thresholding is applied [Kokko et al., 1993; Andrèn et al., 1996]. In some cases, images are first decomposed into separate colour channels or transformed into luminance space, with the object of obtaining better results from the image processing method [Vamerali et al., 1999; Zeng et al., 2006]. While this might appear beneficial, the shortcomings of global thresholding remain. Slightly better results can be obtained via local thresholding

[Iyer-Pascuzzi et al., 2010]. Local thresholding uses different threshold values for different regions in the image. The image is usually split into multiple, fixed sub-regions, to which thresholding is applied independently, making it robust to gradual changes in brightness. To compensate for the limitations of thresholding, it is quite common to apply additional post processing methods to discriminate between root objects and other components that have been extracted erroneously. For instance, in [Zeng et al., 2006], an AdaBoost-based classifier is used for that purpose. How the threshold values are selected differs between methods. In some cases the values are pre-set [Andrèn et al., 1996; Vamerali et al., 1999], in others they can be manually defined by the user [Armengaud et al., 2009] or automatically assigned [Iyer-Pascuzzi et al., 2010].

Nater et al. [1992] pointed out that thresholding is not a suitable technique for the extraction of plant roots in mini-rhizotron images, since greyscale histograms are not bimodal. As an alternative solution, they presented an approach based on artificial neural networks, which have the ability to learn patterns form input signals and deliver an adequate output when the classes to be recognised are linearly separable. In their method, the system is given horizontal and vertical derivatives of the image and returns a single binary output whose value depends on whether a certain pixel belongs to root or background. The system is trained with a number of previously segmented and hand-edited images showing parts of a root system. Another method which operates without the use of threshoding was presented by Heeraman et al. [1993]. Their method is based on an image overlay strategy. Images are taken on different dates after which the first image is superimposed with different combinations of the red, green, and blue channels of later images, so that regions without any change would appear white. Regions that have experienced changes, however, generate a distinctive colour. Accurate registration of the overlaid images is necessary if this technique is to work. Not only does this method show the presence of roots, it also highlights roots that were present at one moment but absent in a second due to roots dying over time. Inspired by the problems and the inventive solutions applied in medical imaging, in particular for the segmentation of retinal blood vessels, Page et al. [2008] presented a method, similar to the approach originally reported by Chaudhuri et al. [1989], which is based on a two-dimensional matched filter technique. Under the assumption that roots are linear and

that their edges run in parallel, a Gaussian based filter is used at different rotations and lengths, and passed over the image. The applied filter will peak as a match is found, with each considered as a root fragment if the correlation value is above a threshold.

Some methods have been developed with the aim of using the computer to aid in the process of root extraction from two-dimensional images, but unlike the techniques mentioned above, the extraction is done manually, by the user operating the tool. One example is DART (Data Analysis of Root Tracings) [Le Bot et al., 2010], in which the user defines points along the roots that are then linked together to form a network describing the root system. The tool also allows a previously defined network to be overlaid on another root image, for instance an image of a root system taken at a later date, so that the user can extend the system by adding missing links. This option allows the analysis of root growth, since nodes can be associated with different time points. DART is not the only tool pursuing a manually tracing strategy for the extraction of roots. Another tool that uses the computer merely as an instrument to assist rather than to contribute in the process of extraction is RMS (Root Measurement System) [Ingram and Leers, 2001]. As in DART, users working with RMS follow and define roots by setting points along its path that are connected with lines, resulting in a complete description of the root system.

Both tools mentioned above emphasise the analysis and measurement of the root system, and leave the task of root extraction completely to the user. A little bit more accommodating to users are tools that actively take part in the extraction process but, since they are not infallible, allow users to interact and correct incomplete or false detections. Such extraction methods are considered semi-automated, since the task cannot be completed without external input or would perform poorly without the user's supervision. An example of a tool falling in this category is EZ-Rhizo [Armengaud et al., 2009], which requires the user to slide the threshold to a value that visually gives the best result, after which the image is cropped and noise or speckles removed by selecting and applying a filter from a list of available options. Once the user is satisfied with the selected settings, the data is forwarded to the next step of quantification and analysis. Another semi-automated tool made available to the community is RootReader2D [Clark et al., 2013]. After thresholding the image, the extracted object is skeletonised and further

separated into individual root segments defined by two endpoints and several connector points linking them together. These paths can then be manually rearranged, to match the network to the underlying and true root system in the image. Recently, Pound et al. [2013] have reported a semi-automatic method for the extraction and quantification of complex root system architectures in a range of different plant species. In RootNav, a pre-processing stage employing the expectation maximisation (EM) algorithm estimates the probability of each pixel in a grey level image arising from root material or background. The user indicates the start and tip of a root segment, aided by an automatic tip detection process, and an optimal path between the two points is computed using the A* algorithm. While not high-throughput, RootNav allows users to produce high quality structural descriptions of root architectures much faster and more easily than via completely manual mark-up methods. An interesting approach is adopted by SmartRoot [Lobet et al., 2011] and RootTrace [French et al., 2009]. Both tools are based on an idea that is different from usual segmentation strategies. Instead of seeing the extraction task as a segmentation problem, where the image is divided into roots and background regions, the root system is traced stepwise from the top of the system towards the end of the root tips, and as such emulate more closely the behaviour of a human solving the problem (for instance by using the manual extraction tools mentioned above). In SmartRoot, the user places a first node defining the starting point from where the search for more roots begins. The tracing is done by exploring the area in front of the current node (the opposite direction of previous nodes) at two times its radius within a 90 degree arc. The best candidate is chosen to create and place the next node, or in case if none is found, the radius is shortened and the arc length increased to 120 degrees. If the second search does not return any potential candidate for new nodes, it is assumed that the end of the root tip has been reached. By continuing the search from one node to the next, the primary root can be traced to its end. Lateral roots are automatically added by scanning along the identified primary root and then traced in a similar way. The user can edit and reposition nodes to make corrections. RootTrace also extracts roots from images by tracing them rather than segmenting them from the background. Tracing is accomplished with the use of a particle filter. At each step through an iterative process, particles are assigned weights according to their likelihood of representing root material

and then sampled from a set of particles to form a new population. Particles with a higher weight are more likely to be selected and advanced according to a simple motion model, which is downward directed predicting the location at which the next root segment can be found. Through this it is possible to trace the primary root down until the end of its tip is reached, where all particles weight will fall below an automatically determined threshold value. In this process, the user determines only the starting point from where the tracing starts as well as a few points from the background, of which a distribution is built and used in the weighting step. The final root description is obtained by identifying the optimal path, from start to tip, through the particles generated during tracing. By minimising the control a user has upon the extraction process, the result becomes more objective. Reducing the interaction between user and application also saves precious time and brings the analysis closer to fully automated.

2.3.4 Root extraction methods in 3D

The extraction of root systems from two-dimensional images has the advantage that high throughput is easier to achieve. Not only does the analysis require less time due to the reduced dimensionality of the data, but the acquisition of the image data is usually also fast. On the other hand, since the data is only given in two dimensions, three-dimensional measurements such as root volume, root surface area and other traits have to be estimated from two-dimensional parameters. Crossing or overlapping roots can cause major issues in two-dimensional analyses and are often the reason why automated procedures fail to accurately extract the data. This type of artefact can also seriously affect any method which attempts to recover three-dimensional from two-dimensional root descriptions. Thus, humans are often required to intervene in the process. In three-dimensional datasets, roots are never hidden behind other roots or occluding objects. Because it is possible to acquire data in three dimensions, plants do not have to be forced to grow along a two-dimensional plane, which is usually done to reduce occlusions making it easier to capture as much of the root system as possible. Since this limitation does not apply, plants can be grown in a more natural way. Depending on the three-dimensional image data, which in turn depends on the imaging device and the environment in which plants are grown, different methods for extracting useful information have been reported. In this sec-

tion we will give a short overview of some of these methods, starting with solutions proposed for X-ray CT images.

Using a high energy X-ray CT scanner, Heeraman et al. [1997] endeavoured to image and quantify the root system of bush bean (*Phaseolus vulgaris L.*) that were grown in sand culture. The water content of the sand was kept at approximately 50 percent field capacity. Their primary aim was to show the suitability of X-ray CT as a novel technology in plant root studies, rather than to develop a new method for the extraction of root systems from the image data. Nonetheless, rather than doing the segmentation manually, they tried to extract the roots based on statistical measures, making the analysis more objective. With this attempt they were among the first who showed that roots can be separated from non-root material on a computational basis and not just by human assumption of the presence of roots. The plants used in their study were grown for 14 days in a controlled growth-room and scanned with 420keV and 3mA at a resolution of $0.16\times0.16\times0.20$mm per voxel, for a total height of 8mm resulting in a volumetric dataset of $412\times412\times40$ voxels. In order to separate roots from the surrounding material, a subset of voxels from different components were selected and defined either as air, roots, sand or part of the column. Each component was then tested for normality using the one sample Kolmogorov-Smirnov Goodness-of-Fit test. From all the four components only the voxel distribution of the column resulted in a non-normal distribution; for the others the mean, variance and confidence interval were calculated and used to classify the remaining voxels into one of the components. Figure 2.7 shows an image of the rendered, extracted roots. This method relies solely on the greyscale values of each voxel, which is then associated to the component that it best fits into. This, however, presumes that none of the initially defined components have overlapping distributions, otherwise tail values might be assigned to an incorrect category. Heeraman et al. concluded from this study that roots as fine as the spatial resolution used for the scan can be detected, but also that the imaging and extraction technique for root studies using X-ray CT required further development.

Seeking to advance imaging and analysis procedures, Lontoc-Roy et al. [2005; 2006] presented methods and results obtained using X-ray CT for soil-root studies. In their experiment they used homogeneous and loamy sand in

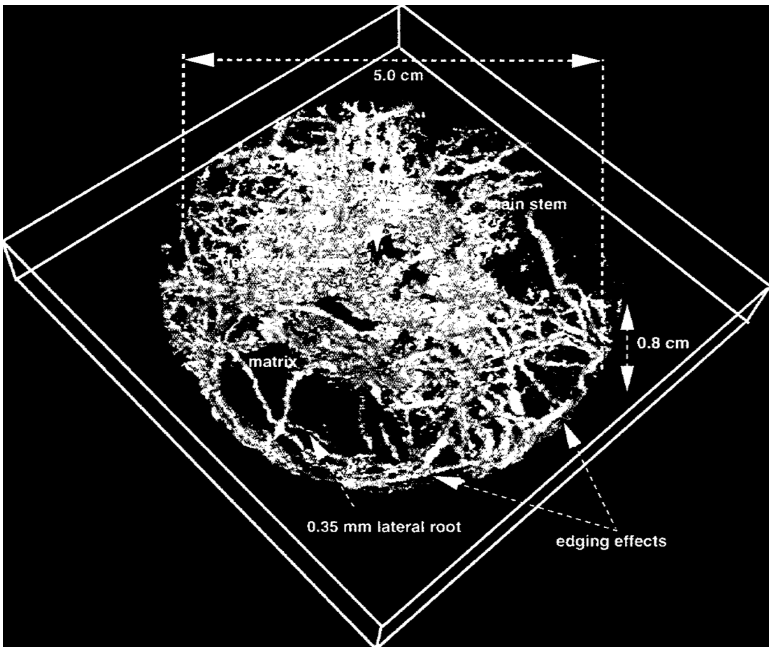

Figure 2.7: Root system extracted using a statistically based approach - image taken from [Heeraman et al., 1997]

which Maize (*Zea mays L.*) was grown for 5 and 3 days after germination. Samples were scanned under dry and water saturated conditions with 130keV and 100mA, generating data with a voxel size of $0.12 \times 0.12 \times 0.1$mm. A total of 500 cross-sections, each of size 512×512, were taken, covering the height of 50mm. After acquisition of the CT data, roots were segmented from the images by choosing visually a lower and upper threshold value. These values were different depending on the growth medium used. The resulting segmentation included primarily larger roots. In a second step, an iterative three-dimensional region growing method was used, appending voxels that are connected to the initial extraction, but also fall within a second threshold boundary, which was chosen to be wider than the boundary in the first step. The result of their extraction of root material from homogenous sand is shown in figure 2.8a, while 2.8b shows roots recovered from loamy sand. Thresholding, be it in two dimensions as discussed in the previous section or in three dimensions, only gives satisfactory results if the greyscale values of different components do not overlap. Even though the three-dimensional region growing process ensures that only voxels that are actually connected to the root system are included in the segmentation, it is still prone to include

non-root material that has the same greyscale intensity and is in contact with previously extracted data. Components consisting of clearly distinguishable greyscale values remain essential for a successful segmentation.

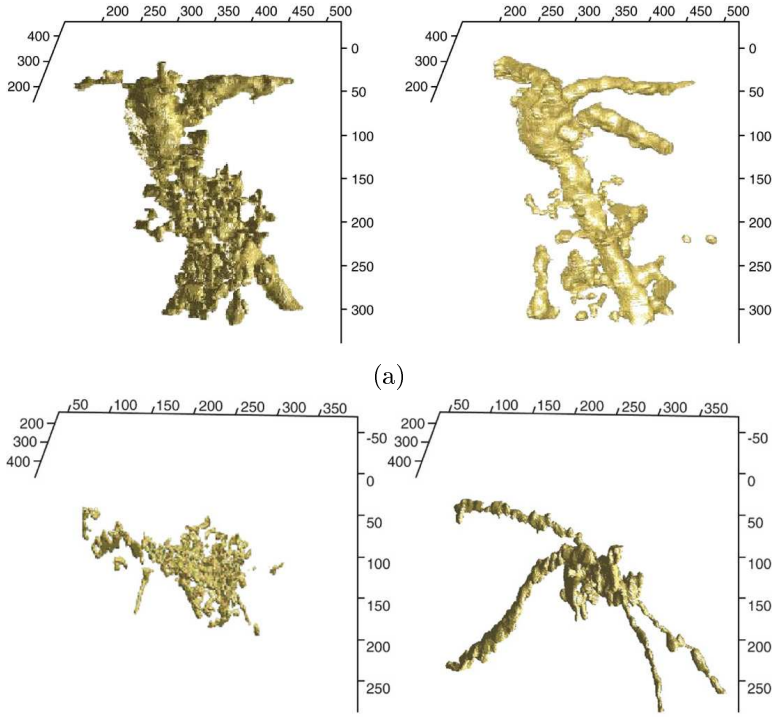

Figure 2.8: Root system extracted using a region growing based approach, showing roots grown in homogeneous sand (top) and loamy sand (bottom), in dry (left) and water-saturated (right) conditions - image taken from [Lontoc-Roy et al., 2006]

Similar to the previously presented method, and suffering from the same limitations, is the approach reported by Perret et al. [2007]. To extract the root system from the growth media, a predefined threshold boundary was applied after which a 26-neighbour connectivity constraint was imposed. This guarantees that only voxels that are in contact with the plant's root system are extracted. The plant selected for the study and grown in sand pots, was Chickpea (*Cicerarietinum L.*), which was scanned with 130keV and 160mA. The three-dimensional generated dataset consisted of 512×512×150 voxels, each of which had the size of 0.275×0.275×1.0mm. The rendered result after segmentation is shown in figure 2.9.

Figure 2.9: Root system extracted using thresholding combined with a 26-neighbour connectivity constraint - image taken from [Perret et al., 2007]

The methods presented by Pierret et al. [1999] and Kaestner et al. [2006] are slightly more sophisticated. Even though both methods make use of thresholding to perform an initial crude segmentation, additional rules are applied to help decide whether an extracted object reflects the characteristics of a root segment. In the experiment of Pierret et al. [1999] the roots of maples (*Acer pseudoplatanus L.*) and chestnut trees (*Aesculushippocastanum L.*) were examined. These were grown in sandy clay and homogeneous sand respectively. The samples were obtained from the field. A field impregnation technique with resin allowed the recovery of soil cores, which were scanned with 140keV and 140mA at a resolution of approximately 0.5×0.5×2.0mm per voxel. Image slices were first segmented using a combination of thresholding and a top-hat filter [Meyer, 1996]. As in the previous methods, extracted objects were tested for continuity. This was done by superimposing two consecutive images, in which objects in the earlier image had been labelled. This was not done because it was assumed that all roots would belong to one root system and therefore had to be connected, but to identify which extracted area in each image slice forms a single object. In addition, traversing the

image slice in search of connected objects allowed a rough definition of the root's skeleton. Since elliptical objects were prone to artefacts, they were ignored in the analysis, which had the disadvantage of missing out horizontally growing roots. The authors were aware of this limitation, but considered it as a reasonable compromise, leaving the methods useful for preliminary investigations. Further quantification was made based on the extracted skeletons, of which an example is shown in figure 2.10.

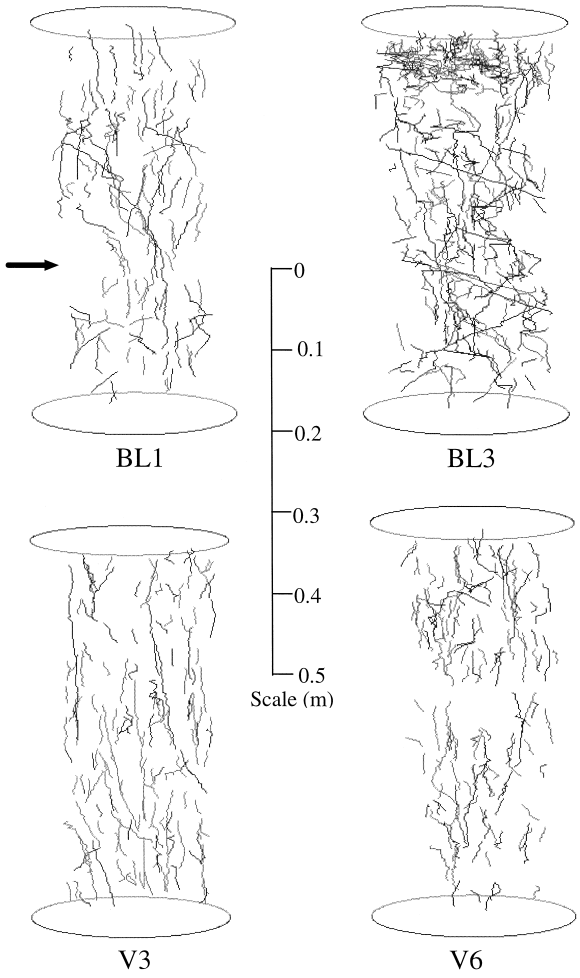

Figure 2.10: Root system extracted using thresholding followed by a selective detection process - image taken from [Pierret et al., 1999]

Another attempt to extract roots from X-ray CT images has been presented by Kaestner et al. [2006]. Their specimens, alder plants (*Alnusincana*

(L.) Moench), were grown in natural moraine soil for four months but, due to the resulting high X-ray attenuation, replanted in columns filled with quartz sand. These were subsequently scanned at 50keV and 114μA. The volumetric dataset had a size of 1,024×1,024×1,643 voxels, measuring a total dimension of 36.9×36.9×59.15mm. The voxel data can be classified into three components; sand matrix, pore space and roots. Since the greyscale distributions of these components are unimodal, thresholding on the raw data would yield poor results. The authors were aware of that and proposed a pre-processing step in which a non-linear diffusion filter was applied multiple times with different parameters to smooth out the texture of the sand matrix, while at the same time preserving the integrity of root objects. The resulting distribution was still unimodal, but the distribution of root material was shifted towards the tail of the main distribution, making Rosin's unimodal thresholding algorithm applicable [Rosin, 2001]. Even though the volume was enhanced to make it suitable for thresholding, the segmented data still included numerous misclassified voxels. This was dealt with by applying a dilation by reconstruction operation [Vincent, 1993], which eliminates speckles but at the same time preserves thin root segments and enforces connectivity of the root system. The result obtained after applying it to the acquired X-ray CT image data is shown in figure 2.11.

Imaging the root system in three dimensions does not mean that X-ray CT has to be used. An alternative technique to X-ray CT, and a method for extracting the root system from the acquired image data, has recently been presented by Clark et al. [2011]. Plants are grown in cylinders filled with semi-transparent gellan gum. Samples are placed on a turntable and imaged with a digital camera from different angles spread over 360 degrees. The software tool that is described along with the imaging technique is named RootReader3D and is responsible for the extraction and quantification of root systems. The projections are first thresholded and then reconstructed into a volumetric dataset using a silhouette-based reconstruction technique, which results in a stack of cross-sectional images that, although not revealing the internal structure of roots, shows them as completely filled objects. Each cross-section is then segmented again to remove artefacts introduced during the reconstruction process. In the reported study, only 40 projections are taken. While an increase in projections would lead to a better volumetric dataset, it would also increase the time of analysis per sample. Examples

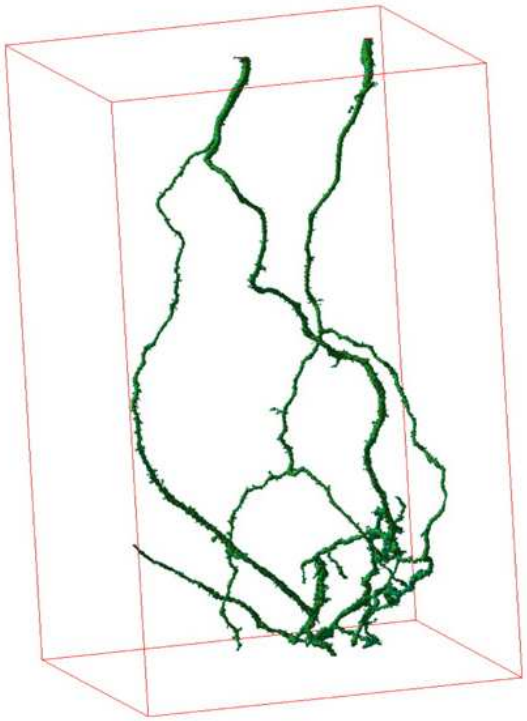

Figure 2.11: Root system extracted using a threshold based segmentation together with various pre-filtering and post-processing steps - image taken from [Kaestner et al., 2006]

of root systems that have been imaged and extracted with their proposed system are shown in figure 2.12.

Though MRI is used for three-dimensional soil-root studies [Jahnke et al., 2009], only a little work has been reported on root extraction methods from its data [Schulz et al., 2012; Stingaciu et al., 2013]. The approach presented by Schulz et al. [2012] uses a filtering technique based on the method presented in [Frangi et al., 1998] that searches for tubular structures within the data and assigns a likelihood value to each voxel using a given dissimilarity measure. The following step involves finding the top of the root system, which is assumed to be at the position with highest water concentration and largest diameter, and is marked as the root node of a tree-graph structure. Every voxel is connected through a path to its root node, which is determined using Dijkstra's shortest path algorithm [Dijkstra, 1959]. In the final step, all voxels with an intensity value below a given threshold are removed

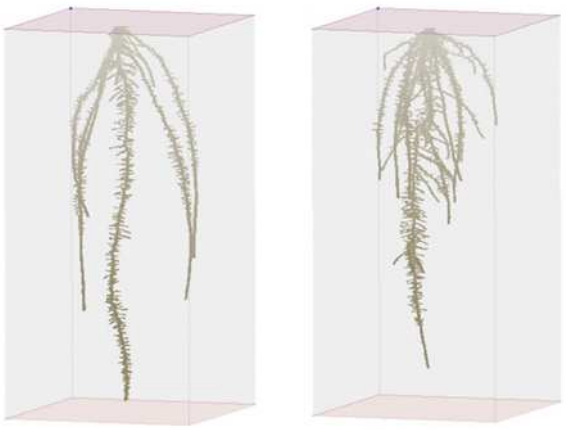

Figure 2.12: Root system extracted using the RootReader3D system and software tool - image taken from [Clark et al., 2011]

from the graph and leaf node candidates identified based on a ratio of neighbourhood values [Schulz et al., 2012]. The outcome is a model of the root system structure.

2.4 Summary

Plant root systems can be studied in many different ways; using a range of equipment and under different environmental settings. These are often determined by the nature of study, such as whether a controlled or natural environment is necessary, whether plants must be preserved for time series analysis or can be examined destructively, or whether three-dimensional information is required. Many of these factors must be carefully considered. For three-dimensional and non-destructive analysis of plant root systems in soil, X-ray μCT, shows several advantages compared to alternatives, such as MRI. X-ray μCT provides a link between controlled but artificial laboratory environments and the natural environment in the field.

Image analysis is a supportive analytical tool essential in many plant root related studies. No matter for which purpose image analysis methods are developed, it is important to understand the characteristics of the data that is generated. This allows serious degradation of image quality arising from incorrect use of the technology to be avoided, and highlights potential difficulties. Noise and the several artefacts common in X-ray CT are well defined by the physical properties of X-rays and their detection, as well as

the reconstruction method used for obtaining the volumetric data. Available techniques allow the specification and quantification of image noise, which is useful for testing and evaluating the developed method, providing background for the generation of a better artificial test data set.

Various image analysis methods have been presented in the literature, most of them developed to meet particular needs. These methods range from global to local and more adaptive segmentation techniques, supported by various pre- and post-processing operations, to tracing or tracking techniques that have been successfully applied in tools for two-dimensional root extraction as well as for the extraction of similar features in medical images.

As apparent from section 2.3.4, the work carried out so far in three-dimensional and non-destructive plant root analysis, is largely centred around X-ray μCT, yet there are still limitations that need to be overcome in methods developed for plant root extraction. These methods have often difficulties distinguishing between root and non-root material, or achieve only a partial extraction of the plant root system. Some methods were also designed for the analysis of samples that were prepared in a particular way to facilitate the extraction, but come with the cost of being less representative of field conditions.

In the following chapter (chapter 3) we present a novel method that allows the extraction of plant root systems grown in soil from X-ray μCT images. The extraction methods is able to deal with the highly heterogeneous environment that the roots are embedded in and with the variations of greyscale intensity values along individual root branches.

Chapter 3

Extraction of plant roots grown in soil

With X-ray CT providing an imaging system that allows the observation of roots in their natural soil environment, researchers have a valuable tool which permits the design of experiments crucial for gaining new insights into plant root growth under natural conditions, as well as for understanding the mutual influence that plants and soil have on each other. However, researchers are still overwhelmed by the workload required to analyse and evaluate the large sets of image data produced. Image analysis is a bottleneck limiting the potential and benefits that can now be obtained from today's advanced CT technology. Manual analysis of CT image data is laborious and potentially subjective; automatic image analysis can make a significant impact and be used to complement experimental studies. Researchers can be assisted in their routine data analysis by computational techniques which minimise their input and hence save significant amounts of time. In order to accommodate researchers and to support them in their studies, we will introduce in this chapter a novel way of extracting root system information of plants cultivated in soil from X-ray μCT images.

In the following sections we first discuss the challenges of and outline our approach to extracting root systems from X-ray μCT images (section 3.1), introduce the basic concepts of the level set method (section 3.2), the Jensen-Shannon divergence (section 3.3) and Fourier shape descriptors (section 3.4) which are each a fundamental part of the extraction method that is presented in detail in section 3.5. In section 3.6 the method is applied to image data of plant roots in soil acquired with X-ray μCT.

3.1 A visual tracking approach

The soil texture, in which plants naturally grow, can be highly heterogeneous, consisting of various sized mineral particles, organic matter and pore spaces that are partially filled with water. All these contribute to a wide range of different densities which causes some of the X-ray attenuation values to overlap with the attenuation coefficients of plant roots, resulting in very similar greyscale intensities in the image data. This makes the extraction of roots from X-ray μCT images a difficult task. Figure 3.1 illustrates the problem. Here, a cross-sectional image slice is taken and, although performing poorly, thresholded to separate root material from the background, in order to highlight that there are various other regions that fall within the same range, yet do not belong to the plant.

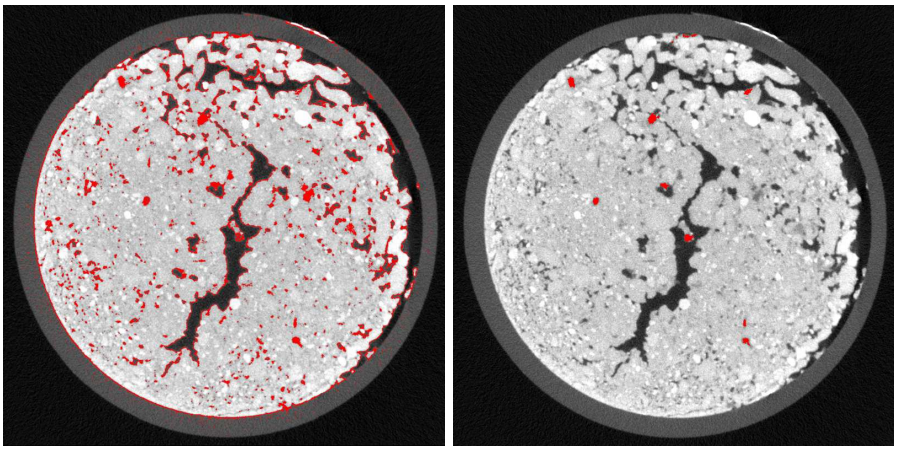

(a) (b)

Figure 3.1: Cross-sectional image slice highlighting root material obtained by (a) manual thresholding and (b) as part of the extraction process using the proposed method

In addition to overlapping greyscale intensity values, another issue is caused by the variation of greyscale distributions along roots, as shown in figure 3.2. This may result from the physical properties of the plant, but is more likely due to the influence of the surrounding environment the roots are embedded in. Artefacts and imaging characteristics of X-ray CT may also contribute to the wide variation of intensity values. Whatever the cause, this further complicates the process of root system extraction from X-ray μCT images. Extraction criteria that are effective at one point on a given root may fail at another point.

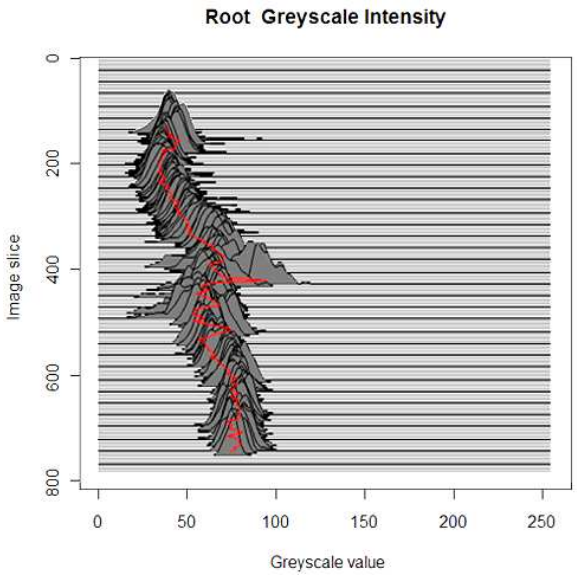

Figure 3.2: Greyscale intensity distribution of a single root in different image slices from 8-bit data (Maize (*Zea mays L*)) - image taken from [Mairhofer et al., 2012]

In this chapter we describe a novel approach to the segmentation of X-ray μCT scans of plant roots growing in soil. The volumetric data is viewed as a sequence of x-y cross-sectional images aligned along the z axis. As the image stack is traversed, root cross sections appear to move around the image, though in reality everything is fixed in place. The sense of movement is created by the fact that roots cut across the soil sample, and are not limited to growing straight down. Hence, a root cross-section will be located at slightly different locations in neighbouring images and will have slightly different shapes, as the root orientation and thickness changes. This appearance makes the problem of extraction eligible for a tracking based solution, tracing roots through a sequence of images. That tracing is a suitable solution for the extraction of data with root-like structure, has previously been shown by methods developed for the segmentation of plant roots in two-dimensional images and presented in [French et al., 2009] and [Lobet et al., 2011], and by the extraction methods designed for medical applications presented in [Collorec and Coatrieux, 1988] and [Flasque et al., 2001], in which target objects are followed stepwise from one location to the next, instead of applying global segmentation techniques. This has the advantage of a highly flexible search that can adapt to various changing circumstances, making the

approach more robust to the highly heterogeneous environment and to the variations occurring across the root system architecture. Therefore, by using a tracking based strategy, the problem of extracting an object of varying greyscale intensity values from a heterogeneous and complex background, is reduced to a local and minimum problem of extracting a root object from a single cross-section. Local information obtained through this process can be used to correct and adapt to intensity changes in the data, and thus are more responsive than global three-dimensional segmentation methods. This is a key characteristic in order to overcome the difficulties observed in the image data.

Visual object tracking is a widely studied problem in the field of computer vision. The general idea is to identify a target object, which is followed through a sequence of images, so that at any point in time it is possible to locate the target's position. Various techniques, developed for a range of applications, have been presented in the literature [Pavlovic et al., 1997; Coifman et al., 1998; Hu et al., 2004; Yang et al., 2011]. Target objects are often represented either by discrete features such as points or lines, region templates or shape descriptors [Cannons, 2008]. Tracking algorithms rely on appearance and motion models. The motion model is used to estimate the trajectory of the object and thus gives an indication of the target's location, while the appearance model describes outstanding features that allow the identification and recognition of target objects in later images. Appearance and motion models are combined in a tracking engine or framework. Most take the form of a predictive filter, in which target location and properties at time t are used to predict target location and properties at time $t + 1$. A localised search is then performed near the target's predicted location. Kalman filters [Kalman and Bucy, 1961], particle filters [Isard and Blake, 1998] and mean shift algorithms [Comaniciu et al., 2000] are among the most widely used predictive tracking frameworks. Active contours or snakes [Kass et al., 1988] provide an alternative approach, mixing segmentation and tracking by using an energy minimisation procedure to fit a model of the target's boundary shape to the input image or image sequence. A broadly similar approach is adopted by level set methods [Sethian, 1999].

The task of visual object tracking is often complicated by partial or full occlusion of the target object [McKenna et al., 2000], variation in appearance [Matthews et al., 2004] or an abrupt change in motion [Li et al., 2008]. Due

to the high resolution achieved when using X-ray μCT scanners, typically $<50\mu$m, we believe that there is no complex motion to be expected from tracking root objects. Although roots can frequently change the direction of growth, the movement that occurs between two consecutive images is quite small, resulting in a partial overlap of the target object. A variation in appearance, however, is frequently encountered, being present in both the shape and greyscale intensities, as described in the previous paragraphs. Because samples are imaged in three-dimensional space, there is no proper occlusion between objects. However, as we show later in chapter 7, root objects from different plants can interact with each other and appear as a single merged target, which constitutes a particular situation that requires additional processing steps. For a comprehensive introduction and overview of various visual tracking approaches, the interested reader is referred to [Yilmaz et al., 2006; Cannons, 2008].

The key feature of the proposed method is the level set segmentation technique [Sethian, 1999], which is adopted to locate the boundary of a target root object. The interface is not defined by a number of control points, but represented implicitly by a level set function, which gives the method the ability to adapt to changing topologies (such as splitting or merging interfaces) that is relevant in detecting emerging lateral roots, but also provides high accuracy and robustness.

3.2 The level set method

The proposed root extraction method is based upon the level set method. This method, which was originally presented as a class of algorithms named PSC (Propagation of Surfaces under Curvature) schemes, was introduced by Osher and Sethian [1988] in the late 1980s. The numerical method was initially developed to describe the motion of a propagating front driven by its curvature, for the purpose of studying the flow and dynamics of physical phenomena such as crystal growth, flame front propagations or vortex sheet roll-ups [Sethian, 1999]. The level set method has since been adopted and further refined in diverse fields, including image processing and computer vision [Tsai and Osher, 2003], in which the front represents the boundary of some object or region of interest and is propagated across the image until it is a sufficiently good fit to the image data.

Malladi et al. [1995; 1995], inspired by the work in [Sethian, 1985; Osher and Sethian, 1988] used the level set method to recover objects of any complex shape from images. The level set method evolves with curvature dependent speed around high gradients at which the front eventually comes to a stop. A different formulation of the level set method, popular in image analysis, is the framework presented by Chan and Vese [2001a; 2001b], whose method is based on the Mumford-Shah model [Mumford and Shah, 1989]. The level set framework aims to partition an image into two regions of approximately equal values, by minimising an energy function that guides the front such that the inside area consists of one value and the outside area of the other. Therefore, the evolving front is not dependent on edges but relies solely on image values. This makes the method suitable for the detection of objects whose boundaries are not defined by gradients. The level set method has been adopted in many applications, such as for image recovery and noise removal [Marquina and Osher, 2000; Whitaker and Xue, 2001; Combettes and Luo, 2002], image registration [Vemuri et al., 2000, 2003; Droske and Ring, 2006], texture [Paragios and Deriche, 2002; Sandberg et al., 2002; Aujol et al., 2003] and prior knowledge based segmentation [Rousson and Paragios, 2002; Cremers and Soatto, 2003; Chan and Zhu, 2005]. A general overview of different level set formulations and their application in image analysis is given in [Tsai and Osher, 2003] and [Cremers et al., 2007].

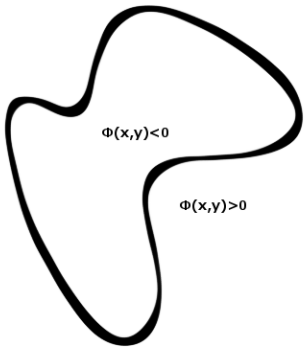

Figure 3.3: Front of a level set function $\Phi(x, y)$, with negative values inside and positive values outside the zero level interface

In this work we refer to the definition of the level set method given in [Sethian, 1999]. The level set method represents the boundary of a given shape as the intersection of some function $\Phi(x, y, t)$ with the plane $t = 0$.

Points on the x-y plane for which the value is negative lie inside the shape, while those with positive values are outside, as illustrated in figure 3.3. The motion of the front is controlled by a defined speed function F. Changes are made to the boundary curve, not by direct manipulation of the points lying on it, but by changing, or evolving, the level set function $\Phi(x, y, t)$, which is found by solving a partial differential equation

$$\frac{\partial \Phi}{\partial t} + F\left|\nabla \Phi\right| = 0 \tag{3.1}$$

The interface of the front C at time t is given by the zero level of the function Φ, which defines the inside and outside areas as sets of negative and positive values respectively.

$$C\left(t\right) = \left\{ \left(x, y\right) \middle| \Phi\left(x, y, t\right) = 0 \right\} \tag{3.2}$$

The equation 3.1 can be approximated by using a finite forward difference scheme in time

$$\frac{\Phi(x, y, t+1) - \Phi(x, y, n)}{\Delta t} + F\left|\nabla_{x,y} \Phi(x, y, t)\right| = 0 \tag{3.3}$$

which allows $\Phi(x, y, t+1)$ to be derived as follows

$$\Phi(x, y, t+1) = \Phi(x, y, t) - \Delta t F\left|\nabla_{x,y} \Phi(x, y, t)\right| \tag{3.4}$$

To solve the spatial derivative $|\nabla_{x,y}\Phi(x, y, t)|$ an appropriate finite difference scheme can be used. The simplest is the first order upwind scheme [Sethian, 1999], which uses values upwind of the direction of information propagation. For this we define the forward and backward difference operator as follows

$$D^{+x}\Phi = \frac{\Phi(x + \Delta x, y, t) - \Phi(x, y, t)}{\Delta x} \tag{3.5}$$

$$D^{-x}\Phi = \frac{\Phi(x, y, t) - \Phi(x - \Delta x, y, t)}{\Delta x} \tag{3.6}$$

In a similar way we define D^{+y} and D^{-y}, which allows us to write

$$\nabla^{+} = \left[max(D^{-x}, 0)^2 + min(D^{+x}, 0)^2 + max(D^{-y}, 0)^2 + min(D^{+y}, 0)^2\right]^{1/2} \tag{3.7}$$

$$\nabla^- = \left[max(D^{+x},0)^2 + min(D^{-x},0)^2 + max(D^{+y},0)^2 + min(D^{-y},0)^2\right]^{1/2} \tag{3.8}$$

Information propagation depends on the direction of movement and hence the speed function F. Combining all the terms defined so far gives the first order level set scheme

$$\Phi(x,y,t+1) = \Phi(x,y,t) - \Delta t \left[max(F(x,y,t),0)\nabla^{t+} + min(F_(x,y,t),0)\nabla^{t-}\right] \tag{3.9}$$

A more accurate approximation can be achieved with higher order schemes. In this work however, we choose to use the first order scheme, since for our purposes it works well and higher order methods incur significantly higher computational cost. Note that the formulation of the level set equation as in equation 3.9 permits an arbitrary speed function F and hence allows the front to revisit a point (x, y) several times.

The level set method is a computationally demanding technique, yet it is a robust and attractive method because it has the advantage of easily handling topological changes, such as splitting or merging interfaces. The level set function is usually initialised as a signed distance function $\Phi = \pm d$ such that $|\nabla\Phi| = 1$ and d is the distance from a point to the front. As the interface evolves, the level set function is likely to drift away from its initial state. This is the result of the discretisation of the level set function and the use of non-uniform velocities during the calculation. It is not necessary for Φ to be a signed distance function, but gradients that are too steep or too flat can lead to numerical inaccuracy and instability near the interface. By maintaining the signed distance function, the calculation of parameters, such as the curvature of the front, becomes more accurate. To avoid the loss of the signed distance property, the speed function can either be designed to preserve it as the front evolves or the level set function can be re-initialised from time to time, to ensure that Φ remains approximately a signed distance function [Li et al., 2005; Min, 2010]. Another reason for re-initialising the level set function is the use of a narrow band approach [Chopp, 1993], which reduces the computation of the level set function to a band around the interface and hence increases performance. An inner and outer boundary is set at predefined distances from the zero level and only values that fall within this band are updated. As the front evolves it will sooner or later hit one of

the boundaries. The boundaries of the narrow band are then moved and the new points residing within the band updated using one of the re-initialisation methods [Sethian, 1999]. Thus, the narrow band evolves together with the zero level of the function $\Phi(x, y)$.

Several solutions have been proposed for re-initialising the level set function to rebuild the signed distance property [Sethian, 1999]. Sussman et al. [1994] re-initialised the level set function by solving $\Phi = sign(\Phi)(1 - |\nabla\Phi|)$ to steady state. An alternative approach is to use the fast marching method [Sethian, 1996, 2001], which keeps the interface values intact and thus preserves the front while rebuilding the level set function [Sethian, 1999]. The fast marching method is a technique for solving boundary value problems, and closely related to the level set method. However, unlike the level set method, it requires F to be strictly positive $F > 0$ for all time and therefore the front moves always in the same direction. This implies that a point (x, y) cannot be revisited twice by the moving interface. For the moment we consider a function $T(x, y)$ in two-dimensional space, which has zero values at an initial interface, similar to the definition of the level set function. Assuming the boundary moves in normal direction with a predefined positive speed $F > 0$, the function $T(x, y)$ gives the time at which the interface reaches the point defined by (x, y). The motion of the front can be characterised by

$$|\nabla T|\, F = 1 \tag{3.10}$$

which is known as the Eikonal equation. An example of a circular front expanding with constant speed $F = 1$ is shown in figure 3.4.

The equation 3.10 can be solved using the fast marching method, which is a robust and accurate method and would be our method of choice for the re-initialisation of the level set function, since the interface is completely preserved and thus guarantees stability. In fact, the method has been used in a previous version of our work presented in [Mairhofer et al., 2012]. However, the fast marching method, as presented in [Sethian, 1999], is also highly sequential. Starting from the grid points at the zero level interface, information is propagated in a single direction away from the boundary in a systematic manner, updating all other grid points one by one. The com-

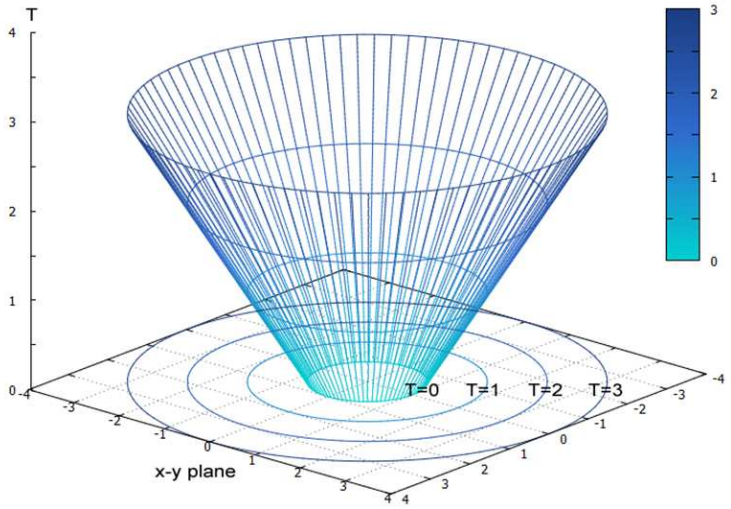

Figure 3.4: Arrival function $T(x, y)$, starting with an initial location of a circular front $T = 0$

putational complexity of the fast marching method is $O(N \log N)$. Another approach for solving equation 3.10 is presented in [Tsai et al., 2003; Zhao, 2005] and referred as the fast sweeping method, which has a computational complexity of $O(N)$. Gremuad and Kuster [2006] have demonstrated that in the absence of obstacles, which are locations in which the front is propagated at infinitely slow speed, the fast sweeping method is more efficient than the fast marching method, since only a single sweep in each direction is required. For the purpose of re-initialisation the grid points are updated at constant speed and therefore there are no obstacles to overcome. Since the fast sweeping method is used in the current version of our application, its basic principles are described in the following paragraph. For a detailed description of the fast marching method, the interested reader is referred to [Sethian, 1996] and [Sethian, 2001].

The fast sweeping method is based on the concept of sequentially scanning and propagating information along a certain direction, which later became known as 'sweeping', and was first introduced by Danielsson [1980] for the computation of the Euclidian distance map. The original method, however, does not satisfy the Eikonal equation in 3.10. The fast sweeping method presented by Tsai et al. [2003] and Zhao [2005] builds on this idea

but at the same time is a valid solution for the Eikonal equation (3.10). The upwind scheme presented in [Rouy and Tourin, 1992] is used for the discretisation of the partial differential equation and is defined as follows

$$max(u_{x,y} - u_{x\wedge}, 0)^2 + max(u_{x,y} - u_{y\wedge}, 0)^2 = F(x,y)^2 \tag{3.11}$$

where $u_{x,y}$ is the value of the grid point (x, y) and $u_{x\wedge}$ defined as

$$u_{x\wedge} = min(u_{x-1,y}, u_{x+1,y}) \tag{3.12}$$

$u_{y\wedge}$ is defined in a similar way to $u_{x\wedge}$. The grid is initialised by fixing the values of the interface and assigning large positive values to all other grid points. The domain is then swept in alternating directions

$$\begin{aligned} x &= 1:X, \quad y = 1:Y \\ x &= X:1, \quad y = 1:Y \\ x &= X:1, \quad y = Y:1 \\ x &= 1:X, \quad y = Y:1 \end{aligned}$$

where the value $\bar{u}$ is computed for the grid point (x, y) using its neighbours $u_{x\pm1,y}$ and $u_{x,y\pm1}$ and updated only if the new value is smaller than its current $u_{x,y} = min(u_{x,y}, \bar{u})$. $\bar{u}$ is obtained from the equation 3.11 which can be solved using

$$\bar{u} = \begin{cases} min(u_{x\wedge}, u_{y\wedge}) + F(x,y), & \text{if } |u_{x\wedge} - u_{y\wedge}| \geq F(x,y) \\ \frac{u_{x\wedge}+u_{y\wedge}+\sqrt{2F(x,y)^2-(u_{x\wedge}-u_{y\wedge})^2}}{2}, & \text{if } |u_{x\wedge} - u_{y\wedge}| < F(x,y) \end{cases} \tag{3.13}$$

In equations 3.9 and 3.13, we now have a complete formulation for evolving and re-initialising the level set function. When using level sets for physical simulations it is common to observe the motion or interaction between multiple interfaces for a fixed period of time. However, in image analysis termination criteria are important to determine the completion of an operation. The evolution process is often halted when the front converges to a stationary solution. Alternatively, the number of sign changes can be used to terminate the computation when it has settled down to a stable configuration. This could be useful in situations where the front might start to oscillate. In order to avoid endless computation of the level set function,

the number of iterations is sometimes also limited to a finite number. This value, however, is usually fairly high and unlikely to ever be reached [Sethian, 1999].

3.3 Jensen-Shannon divergence

The evolution of the level set function used in the proposed root extraction method is based on the distribution of greyscale values; to be precise, on the similarity between two probability density functions derived from their distributions. In order to determine how similar or dissimilar two probability density functions are, we employ statistical measures. Many statistical techniques have been developed for this purpose, among which is the Jensen-Shannon divergence [Lin, 1991]. Alternative methods that are frequently used, in particular in image analysis, are for instance, Kolmogorov-Smirnov [Geman et al., 1990], Chi-square [Puzicha et al., 1997], histogram intersection [Swain and Ballard, 1991], Bhattacharyya [Bhattacharyya, 1943], Sørensen [Sørensen, 1948], Kullback-Leibler [Kullback and Leibler, 1951] and Earth mover's distance [Rubner et al., 2000]. For a more detailed overview of different distance measures, the interested reader is referred to [Rubner et al., 2001] and [Cha, 2007]. The Jensen-Shannon divergence provides a statistical measure of distance between two or more probability density functions. Lin [1991] proved that the Jensen-Shannon divergence is always non-negative, symmetric and bounded, which are important properties for a dissimilarity measure. Endres and Schindelin [2003] and Österreicher and Vajda [2003] showed further that even though the Jensen-Shannon divergence does not fulfil the triangle inequality, its square root does, and thus defines the square of a true metric. The Jensen-Shannon divergence presented in [Lin, 1991], is defined as follows

$$JS(p,q) = H(w_p p + w_q q) - w_p H(p) - w_q H(q) \tag{3.14}$$

where H is called the Shannon entropy function and calculated as shown in equation 3.15, p and q are the two probability density functions that are compared to each other and $w_p, w_q \geq 0$ are two weighting parameters such that $w_p + w_q = 1$, used to balance the contribution of the two statistical probability density functions, which makes the Jensen-Shannon divergence

suitable for conditional probability studies where the weighting parameters represent prior probabilities.

$$H(p) = -\sum_{i=0}^{n} p_i \, log_b \, (p_i) \tag{3.15}$$

The Jensen-Shannon divergence measure is bounded by $[0, log_b 2]$, for which using a logarithm of base 2 results in a distance that is measured within $[0, 1]$, where 0 is considered a complete match between two probability density functions. The higher the value of the Jensen-Shannon divergence the lower is the probability that the data come from the same distribution.

The Jensen-Shannon divergence is a popular method in probability and information theory. In image processing and recognition, the Jensen-Shannon divergence has been used, for instance, for edge detection in noisy images [Gómez-Lopera et al., 2000], in the process of image retrieval [Hörster et al., 2007] and for the representation and recognition of three-dimensional object shapes [Hamza and Krim, 2003]. The Jensen-Shannon divergence was chosen in this context due to its symmetric and bounded properties and because it does not require the data to follow a certain distribution, which is important, since the distribution of greyscale intensity values in the image data is unknown and cannot be assumed to follow the same distribution in all the samples. In figure 3.5, we show an example in which the Jensen-Shannon divergence has been used to measure the similarity between image patches.

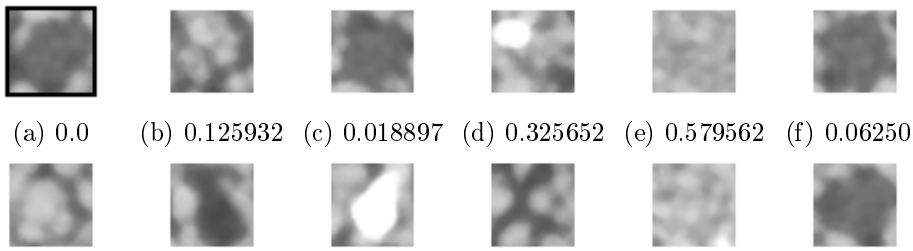

(a) 0.0 (b) 0.125932 (c) 0.018897 (d) 0.325652 (e) 0.579562 (f) 0.062500

(g) 0.273964 (h) 0.169698 (i) 0.458841 (j) 0.129289 (k) 0.602166 (l) 0.019704

Figure 3.5: Jensen-Shannon divergence applied to a set of images where the first image is used as reference and compared against all others. Note that all samples with roots (a,c,f,l) have a distance < 0.1. Also to be considered is that the reference image (a) has a small portion of soil particles and pore spaces included, which are present in all samples and hence reduces the distances for samples without root objects.

3.4 Fourier shape descriptors

The ability to detect changes in shape is a key feature of the proposed method. The way in which this is integrated into the extraction method and the particular role it plays are described in detail in later sections. In order to detect whether a shape has remained constant or not, it is necessary to identify features that are suitable for comparison. Many studies have been concerned with the analysis of shapes, proposing a variety of methods. These can be classified into two major categories, contour-based and region-based techniques [Zhang and Lu, 2004]. The first derives features, as its name suggests, only from the outline while the latter takes the entire object region into consideration. This makes techniques that are part of the former class favourable in our context, since they are not affected by a high variability within the shape, as it might be the case for root objects scanned at a very high resolution where the internal structure of the root, such as the aerenchyma, becomes visible and thus gaps are likely to appear within the extracted data. Techniques using Fourier descriptors, for instance, are members of the class of contour-based methods, of which one specific method is discussed in detail in the following paragraphs. A comprehensive literature review of the large variety of different shape representation and description techniques is given in [Mehtre et al., 1997; Loncaric, 1998; Rui et al., 1999; Veltkamp, 2001; Zhang and Lu, 2004].

Fourier shape descriptors are techniques suitable for detecting changes in shape. In comparison to some other methods they can be computed very efficiently, which makes them a popular tool in shape recognition applications [Zahn and Roskies, 1972; Persoon and Fu, 1986; Cortese and Dyre, 1996]. Fourier shape descriptors have also the advantage that the level of detail they capture is related to the frequencies in the spectrum. Low frequencies capture the global and general characterisation of a shape, while high frequencies can detect very fine details but are also prone to noise [Zhang and Lu, 2001]. By filtering out a band of frequencies, it is possible to extract and use only information that is relevant to a particular task. Among the shape analysis methods using Fourier descriptors, different variations and modifications have been reported [Zhang and Lu, 2001]. In this work we adopt the method presented in [Granlund, 1972; Gonzalez and Woods, 2002], which is known as complex Fourier descriptor.

Starting from an object's boundary, points are distributed along the outline at equally spaced intervals $(x(k), y(k) : k = 0, 1, ..., N-1)$ and ordered in either a clockwise or counterclockwise direction. The coordinates of each point (x, y) can be treated as complex numbers

$$z(k) = x(k) + iy(k) \tag{3.16}$$

This translates two-dimensional coordinates into a one-dimensional function, which can be transformed from its spatial domain into the frequency domain to obtain the coefficients $(c(u) : u = -N/2 + 1, ..., N/2)$, which are called the Fourier descriptors

$$c(u) = \sum_{k=0}^{N-1} z(k) e^{-2\pi iuk/N} \tag{3.17}$$

Using the inverse Fourier transform, $z(k)$ can be restored

$$z(k) = \frac{1}{N} \sum_{u=0}^{N-1} c(u) e^{2\pi iku/N} \tag{3.18}$$

In the context of this work we are only interested in the general appearance of the shape, and not in the details of the outline. Therefore, we restrict our comparison to the lower frequencies of the spectrum, that is the coefficients located around zero within a band $-P < 0 < P$, while high frequencies are ignored $c(u) = 0 : |u| > |P|$. A particular characteristic has the coefficient $c(u) : u = 0$, which presents the centre position of the shape. By setting $c(0) = 0$ the shape description becomes translation invariant. The next positive frequency component $c(u) : u = 1$ determines the size of the shape. This component can be used to normalise all other coefficients so that the method becomes also scale invariant. The rotation of the shape is only coded into the phase of the Fourier coefficients ϕ_c and thus can be disregarded to obtain rotation invariance. Finally, to compare the shape of two objects, only their filtered and normalised power spectra of the Fourier coefficients $|\hat{c}(u)|$ are used of which the sum of squared difference is calculated. An example in which the complex Fourier descriptor method is used, is shown in figure 3.6.

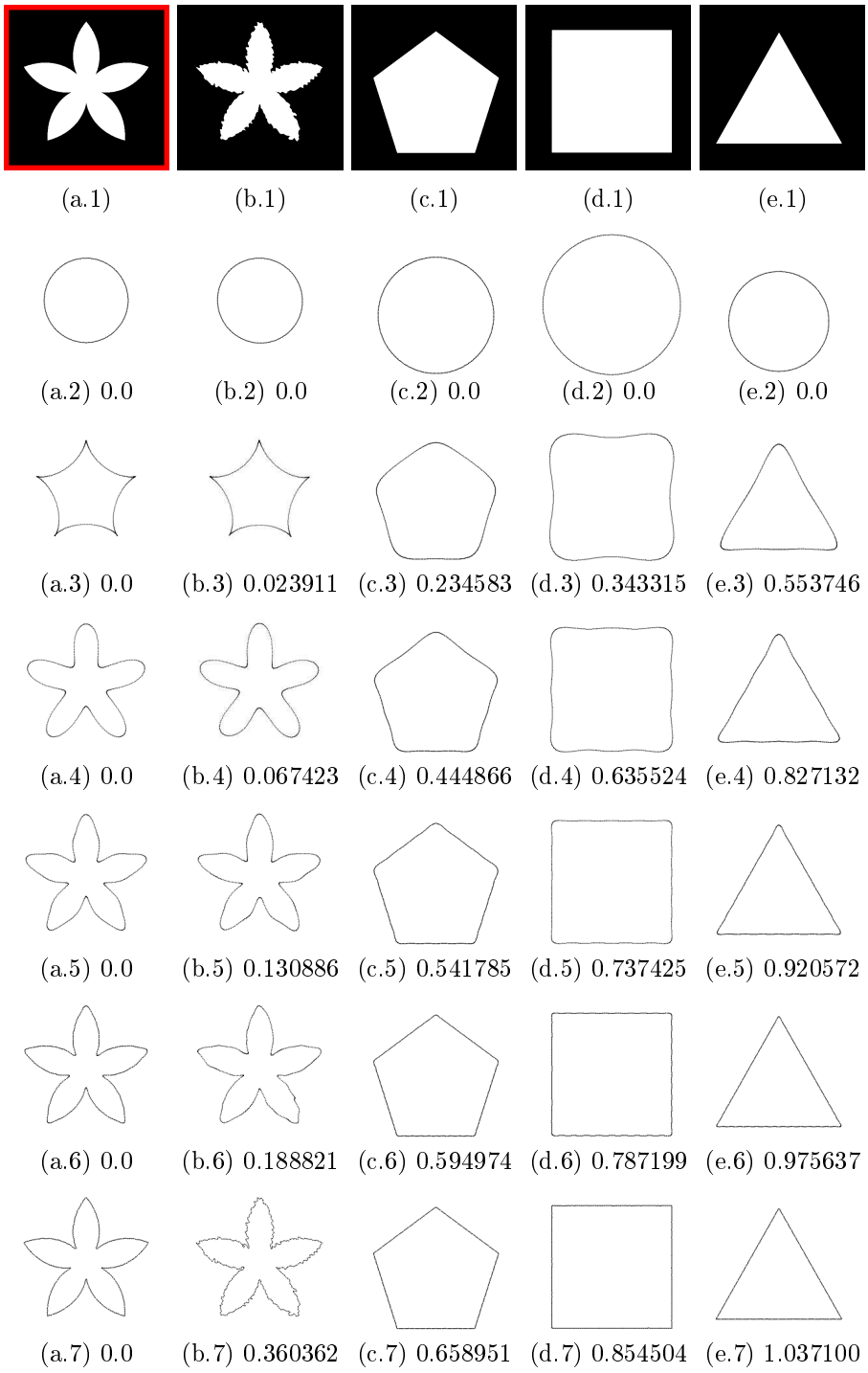

Figure 3.6: Shape comparison using complex Fourier descriptors (512 points), on images of the MPEG-7 dataset [Latecki]. The first shape is used as reference and compared against all others, using the frequency bands: (x.2) P=1, (x.3) P=5, (x.4) P=10, (x.5) P=20, (x.6) P=40, (x.7) P=256.

While making the shape description translation and rotation invariant seems reasonable, it might be arguable whether scale invariance is necessary in the context of this work. Two cross-sections of roots that are located close to each other are likely to be of similar size. Therefore, a change in size might indicate a difference between the two objects. This might be generally true, but an exception to this assumption arises, for instance, at the seed of the plant, where the size of an object can change drastically. In addition, if the power spectrum of the Fourier coefficients is not normalised, then the effect it would have on the dissimilarity measure is relatively large, becoming overly sensitive to changes in size and therefore unreliable for assessing shapes.

3.5 A novel level set method for visual tracking

To provide objective, accurate and automatic extraction of plant roots from μCT images, we propose a novel method based on object tracking. Due to the nature of tracking, the connectivity of the reported root system is guaranteed; target objects (root sections) are followed through the image sequence until they disappear from the scene. Because tracking follows objects from one image to the next based on their state and information available in the current image frame, this approach allows a higher degree of adaptability than previous methods and thus can adjust more easily to local changes than other three-dimensional segmentation techniques. While three-dimensional segmentation considers the task to be the extraction of a single object, a tracking framework operates on a much smaller scale, aiming only to finding a given target in the next image frame. To locate a complete three-dimensional object, it must repeat its task successfully throughout the entire image stack. Since the overall task can be divided into many small steps, each can be adjusted so that the likelihood of successfully locating the target is increased. This is true, not only when tracking a single object, but also when multiple objects are tracked. Each can be treated independently, and each tracker tailored to the target it follows. These are important characteristics required for successful extraction of root systems. How this concept is applied to the proposed extraction technique is described in the rest of this section.

The proposed tacking method is based on the level set method and uses the narrow band strategy for increased efficiency and sweeping method for re-initialisation. The level set function is solved using a first order upwind scheme and is defined as follows

$$\begin{aligned}\Phi(x,y,t+1) =& \Phi(x,y,t) + \Delta t\,[\ (1-\alpha)\,(\kappa) \\ & -(\alpha)\left(max\left(F_{JSD},0\right)\nabla^{+} + min\left(F_{JSD},0\right)\nabla^{-}\right)]\end{aligned} \tag{3.19}$$

where $\alpha \in [0,1]$ is a weighting parameter between the speed coefficient F_{JSD} and the curvature dependency $\kappa = \nabla \cdot \frac{\nabla\Phi}{|\nabla\Phi|}$ of the front. F_{JSD} is based on the Jensen-Shannon divergence, which computes the distance between two given probability density functions. In this context, one probability density function, referred as root model, represents the distribution of greyscale values of previously computed root sections and, as shown later in this section, is updated continuously. The other probability density function, to which the root model is matched, is built from the actual data in the current image, around the interface of the evolving level set function. As already mentioned in section 3.2, other distance measures can be used as alternatives. The Jensen-Shannon divergence was selected, because of its symmetric and bounded properties [Lin, 1991]. The term F_{JSD} is obtained as given below

$$F_{JSD} = \begin{cases} 1 & \text{if } JS \leq \beta \\ -1 & \text{if } JS > \beta \end{cases} \tag{3.20}$$

$\beta \in [0,1]$ is used as a parameter to determine what distance between model and data is considered acceptable.

In order to apply the Jensen-Shannon divergence we first need to transform the different greyscale intensity estimates into a statistical probability density function. A straightforward way to achieve this is to generate and normalise a histogram. However, the histogram is a rather crude statistical density estimator, sensitive to the choice of origin and bin width, and is usually not suitable for small data points. A better alternative is the use of kernel density estimators, which are defined as follows

$$\hat{p}(x) = \frac{1}{nh}\sum_{i=0}^{n} K\left(\frac{x - x\,(i)}{h}\right) \tag{3.21}$$

where n is the number of data points, h the bandwidth and K the smoothing kernel. A commonly used kernel for K, is the Gaussian kernel $K(x) = \frac{1}{\sqrt{2\pi}} e^{-\frac{1}{2}x^2}$.

The level set function is computed within a narrow band of distance $d = 6$ in both directions. If d is indefinitely large then the level set function would be computed over its entire domain and thus no efficiency saving would be obtained. A value of $d = 1$ means that the narrow band has to be repositioned almost every time and thus becomes counterproductive.

The evolution of the level set function is based on the Jensen-Shannon divergence, using an estimate of the probability density function of the root as reference. The easiest way of defining such a model is to select a representative set of voxels corresponding to root material before processing begins and use their greyscale intensity values to create a model that is employed throughout the segmentation. In that case we could easily distance ourselves from the tracking framework and adapt instead a three-dimensional level set method, since the level set approach can be extended to an N-dimensional domain [Sethian, 1999]. In fact, we believe that a level set method based on the Jensen-Shannon divergence in three-dimensional space, would be suitable for extracting data that shares a common distribution of greyscale intensities. Unfortunately, in the context of root system extraction from its soil environment, this approach is not viable as the intensity values can change across the root system architecture (and along individual root branches) as the soil and root moisture content and soil organic mineralogy matrix changes. Figure 3.2, in the introduction of this chapter, shows the intensity distribution of a single root obtained at different soil depths. This highlights why methods based on global information, such as thresholding or voxel classification, cannot extract roots accurately as it is necessary to update the root model while tracking root branches through the X-ray μCT volume. In addition, each object has also to be differentiated among others found within the same image slice. These observations of different and changing intensities within target objects support our decision of using a tracking framework, since it easily accommodates the above mentioned issues. This, however, is based on the assumption that the intensity variations occur along the z-direction of the image stack, which we believe is the orientation of the majority of roots. While we observed horizontally oriented roots in many samples, they are rarely at a straight 90 degrees angle , but show slight changes in orienta-

tions, which divides them into smaller root segments spread across multiple cross-sections. For the few cases in which large root objects are only present in a single cross-section , it does not necessarily imply that there will be a change in intensity values. If present, however, there is a chance of losing the target.

The root model used to drive the evolution of the interface is obtained by considering the greyscale intensity values identified as root materials in the previous image. It is assumed that those values do not change excessively between two consecutive images, but vary smoothly throughout the image stack (figure 3.2).

We deal with multiple root objects on the same image plane by using the classical two-pass connected component algorithm [Rosenfeld, 1970] to assign a label to each object before proceeding with the next image. This is possible, as at this stage in the process the level set method has already identified all the different root objects in the current image slice. The different root objects and their interfaces are therefore distinguishable. Labels are propagated when constructing the narrow band around an interface and thus it is possible to evolve the level set function using different models for each root object. This means that we do not have a single model that represents all the root objects at the same time, but several models that are generated, each representing a single target.

Updating the root model is an inevitable step, yet it conceals potential problems. Noise or small areas of background might be included in the representation of its probability density function. These errors can accumulate and result in a model that is no longer an appropriate representation of a tracked root object. Therefore, an additional test is performed to continue the approach described above. The assumption is made that in normal situations the shape of a root object changes only slightly, if at all, between two consecutive images. At the high resolutions achieved when using μCT, we believe this assumption holds as images are typically separated by < 50 μm. Thus, a model is only updated if the object's shape is considered similar. An exceptional case is, for instance, when a root starts bending from the vertical direction to the horizontal or vice versa. Then, a change in object shape does not necessarily mean that the previously detected object's model is incorrect. Another common scenario is an emerging lateral root, which will cause a change in the shape of the root's measured cross section. Even

though an update of the root model is likely to be rejected, the model still represents a valid root object that is reasonably accurate. However, when a crack shaped pore in the soil is falsely interpreted as a branching root, then updating the model would imply that both the pore space and the root section should be included in the model representation. Should the pore space dominate the overall distribution of the model, then the tracker would lose its target and continue following the cracking pore instead. Therefore in both instances not updating the model is the preferable choice.

Parameter	Value	Description
Seed point radius (pixels)	5	Defines the area around the seed point from which an initial root model distribution is built
JS weighting parameters w_p, w_q (Equation 3.14)	0.5	Balance between the two probability density functions
Fourier shape descriptor points N (Equation 3.17-3.18)	512	N-periodic sequence
Fourier shape descriptor window P	20	Defines the spectrum window for low frequencies
α (Equation 3.19)	variable	Defines the smoothness of the level set front
β (Equation 3.20)	variable	Defines the acceptance rate of the similarity measure
Kernel density estimator bandwidth h (Equation 3.21)	1	Defines the smoothness of the distribution curve
Narrow band width d	6	Defines the width around the front in which the level set function is calculated

Table 3.1: Constant and variable parameters

Based on this, the complex Fourier descriptor technique, which was described in detail in section 3.3, is adopted to determine the amount of change

between two shapes. To transform the interface from the special domain into the frequency domain, we use a Fast Fourier Transform (FFT) algorithm with a length of 512 points. Only when shapes are considered similar, which is the case when the sum of squared differences of their filtered and normalised power spectra is below a given threshold, is the root model updated, otherwise the tracker continues with the current model. This aids in keeping the root model robust against drift due to accumulating errors.

Table 3.1 summarises the constant and variable parameters defined for the proposed root extraction method. All the parameters are determined empirically and can in principle be changed. The ones marked constant have been fixed throughout the thesis, the other two control the response to more detailed properties of the input data and have been varied from sample to sample. Figure 3.7 shows how each described component is integrated into the plant root extraction process; the connected component algorithm [Rosenfeld, 1970] is used for labelling each root object, whose shape information is retrieved using the Fourier shape descriptors [Granlund, 1972; Gonzalez and Woods, 2002], which is further used in the decision of updating the root model required for evolving the level set function [Sethian, 1999] guided by the Jensen-Shannon divergence [Lin, 1991].

3.6 Extraction of plant root systems from X-ray μCT images

Maize Jubilee F1 (*Zea mays L. convar. saccharata var. Rugosa*), winter wheat Cordiale (*Triticumaestivum L.*) and tomato (*Solanumlycopersicum L.*) were grown in a Newport series loamy sand (brown soil) and a Worcester series clay loam soil (argillicpelosol) from the University of Nottingham farm at Bunny, Nottinghamshire, UK (52.52 °N, 1.07 °W). Both were air-dried and sieved to <2mm. For each plant species, eight samples were prepared of which half were grown in loamy sand and the other half in clay loam. From the total of 24 samples, 12 were scanned and used to evaluate the extraction method, two of each plant species in both soil textural types. Figure 3.8 shows cross-sections of samples prepared with loamy sand (left) and clay loam (right). The seeds were germinated in Petri dishes on wet filter papers, covered with an aluminium foil to shield them from sunlight, and planted after two days in plastic columns of 30mm diameter filled with soil. The

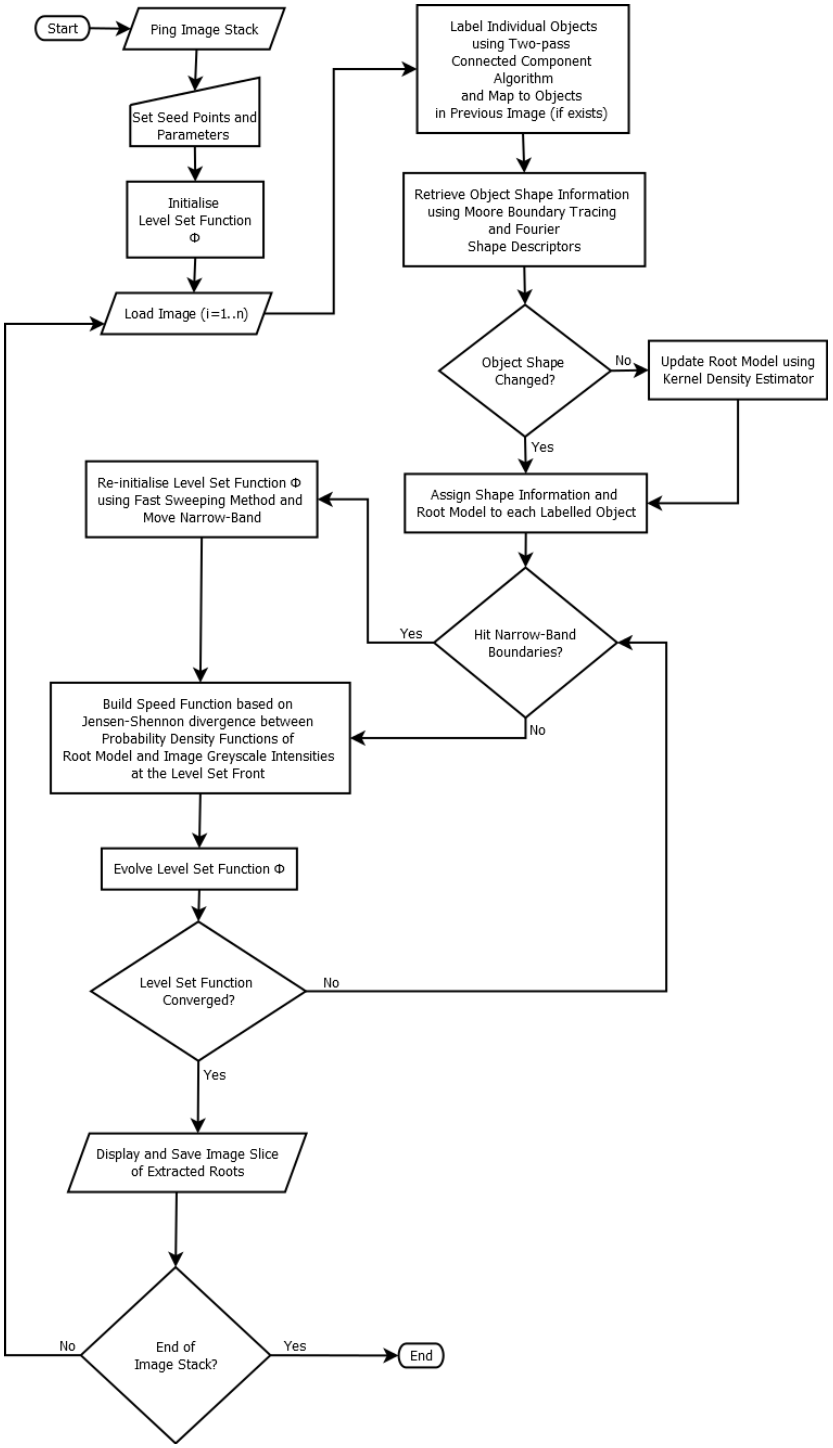

Figure 3.7: Flowchart of the tracking process for plant root extraction

plants grew in environmental controlled growth rooms with 16/8 hours light cycle at a temperature of 23/18 degree Celsius and were scanned ten days after germination. The water status of the samples at the point of imaging was approximately at field capacity. It should be noted that the root systems analysed in this work are from both monocot (maize and wheat) and dicot (tomato) plants.

The imaging device used in this experiment was a Nanotom (Phoenix X-ray / GE Measurement & Control Systems) X-ray μCT scanner. The extraction was initialised by setting suitable parameters for the tracking process as well as one or multiple seed points on the stem of the plant or at the top of the root system to define plant root material as the target object, which we aimed to recover. Table 3.2 lists the size of the data volume acquired from the scans and the parameters used in the process of recovering plant root systems from the soil. All other parameters are kept constant as listed in table 3.1. The values for α and β have been chosen empirically. It should be noted, that in the context of this work, the extraction method has been applied on 8-bit greyscale image data. Figure 3.9-3.11 show the rendered root systems extracted with the proposed tracking method. The rendering has been done using the methods described in chapter 5.

3.7 Summary

In this chapter we presented a method capable of segmenting X-ray μCT images to recover 3D descriptions of plant roots grown in soil. The task is complicated by the high heterogeneity found within the image data, usually arising through the combination of air- and water-filled pore spaces, organic matter in soil and the characteristics of the soil texture, and also by the variability introduced through the imaging process, such as the noise and artefacts as introduced in chapter 2. Such circumstances require a highly adaptive technique to successfully extract sought information, as highlighted in this chapter. A solution able to deal with the high variability in the data is found in adapting a visual tracking framework. This allows the

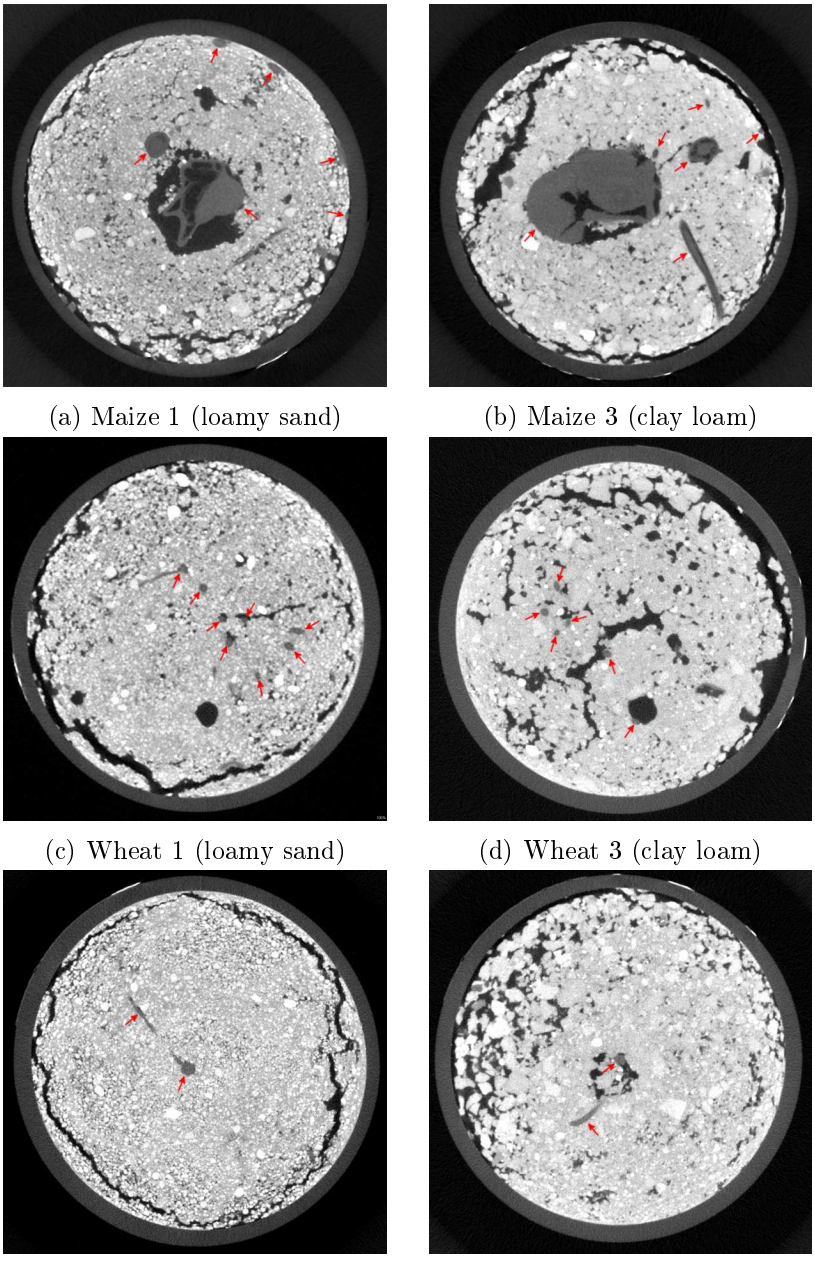

(a) Maize 1 (loamy sand) (b) Maize 3 (clay loam)

(c) Wheat 1 (loamy sand) (d) Wheat 3 (clay loam)

(e) Tomato 1 (loamy sand) (f) Tomato 3 (clay loam)

Figure 3.8: X-ray μCT cross-sectional image slices of (a-b) maize, (c-d) wheat and (e-f) tomato (highlighted) in both loamy sand (left) and clay loam (right)

(a) (b) (c) (d)

Figure 3.9: Extracted root systems of maize 1-4 using the here presented tracking method

(a) (b) (c) (d)

Figure 3.10: Extracted root systems of wheat 1-4 using the here presented tracking method

(a) (b) (c) (d)

Figure 3.11: Extracted root systems of tomato 1-4 using the here presented tracking method

Sample	Soil texture	Volume (voxel)	Voxel (μm)	Curv (α)	J-S (β)
Maize 1	loamy sand	740×740×1,152	48.48	0.806	0.421
Maize 2	loamy sand	740×740×1,152	48.48	0.802	0.398
Maize 3	clay loam	740×740×1,152	48.48	0.786	0.418
Maize 4	clay loam	740×740×1,152	48.48	0.787	0.409
Wheat 1	loamy sand	1,400×1,400×2,200	25.00	0.574	0.416
Wheat 2	loamy sand	1,400×1,400×2,200	25.00	0.588	0.404
Wheat 3	clay loam	1,400×1,400×2,200	25.00	0.606	0.406
Wheat 4	clay loam	1,400×1,400×2,200	25.00	0.588	0.368
Tomato 1	loamy sand	1,400×1,400×1,800	25.00	0.393	0.399
Tomato 2	loamy sand	1,400×1,400×1,800	25.00	0.386	0.383
Tomato 3	clay loam	1,400×1,400×1,800	25.00	0.419	0.397
Tomato 4	clay loam	1,400×1,400×1,800	25.00	0.364	0.388

Table 3.2: Image data properties and parameters used in the extraction process of plant root systems

method to respond to changes between images, but also to treat a target as an individual and therefore to choose object-specific characteristics for identification and segmentation. The proposed technique is based on the level set method, guided by the Jensen-Shannon divergence. The level set method evolves towards object boundaries and, due to its ability to handle complex topological changes in geometry, also able to successfully identify branching root structures. The Jensen-Shannon divergence was found to be a reliable measure for comparing greyscale intensities and can easily be integrated into the evolving level set equation, providing a powerful tool for extracting root systems from their surrounding soil environment in X-ray μCT images.

The proposed tracking method was applied to X-ray μCT image data of different plant species; maize, wheat and tomato. The plants were grown in loamy sand and clay loam, two soil textural types widely found in the United Kingdom. The extracted root systems are from both monocot and dicot plants. This demonstrates that the developed approach is independent of the root system architecture. For better interpretation of results, the

extracted data was rendered in three dimensions, showing the architectural structure of the recovered root system.

Detailed analysis of the ability of the method to recover root system architecture traits is presented in chapter 6. In the following chapter (chapter 4) we discuss a mechanism that allows recovery of plagiotropic roots, for a more complete root system extraction.

Chapter 4

Extraction of plagiotropic root systems

In the previous chapter we provided the ideas and concepts needed to bring forth a technique for separating plant root systems from their growth environment in X-ray μCT image data. While the method presented has the advantage of adapting to local changes in the greyscale intensity values of root objects and so allowing a clear distinction between root and non-root material, it poses additional difficulties that can prevent the extraction of the complete root system. This limitation arises from the way data is processed and is found in particular in samples of plant root systems that show a strong plagiotropic response, developing roots that grow upwards or horizontally. In section 4.1 we explain why the recovery of plagiotropic root systems can be challenging using the tracking based approach of chapter 3. A partial extraction of the root system can conceal important structural characteristics and lead to misleading conclusions being drawn. In this chapter we outline the impact that an incomplete root system has on the measurement accuracy of some global root system traits. An extension to the proposed technique which addresses this problem is then presented in section 4.2 and applied to X-ray μCT image data of plants in section 4.3.

4.1 Plant roots and plagiotropism

Plagiotropism in plant biology refers to the slanted growth of a plant. With regard to the root system this describes the tendency of roots to grow laterally or at any angle away from the vertical [Leitner et al., 2010]. Many root systems contain some roots that grow plagiotropically [Nakamoto and Oyanagi, 1994], mostly driven by external stimuli or in the course of exploring the soil environment for additional resources. Roots that do not follow a straight vertical path are not necessarily difficult to recover using a tracking approach, the technique described in the previous chapter allows root objects identified as targets to move across the image in any direction. Splitting targets are dealt with by the level set method, so root branching does not cause any difficulties either. The problem arises from the method's fixed traversal of the image stack (from top to bottom). Plagiotropic roots with an angle greater than 90 degrees, those which are 'upward' oriented, will be missed due to this limited search of reduced dimension. Examples of two lateral roots, one with a 'downward' and the other one with an 'upward' oriented growth direction, are shown in figure 4.1 and highlight the limitation of the proposed technique. In both cases the image sequence corresponds to the direction of search (from top to bottom) of the image stack. Figure 4.1(a-e) shows a scenario in which an identified target divides into two separate objects, which are both successfully followed by the tracker after branching. Figure 4.1(f-j) describes a scenario in which the method, as presented in chapter 3, fails to recover the lateral root. This is because the object comes into view before it connects to the primary root and therefore is unknown to the tracker at the moment of its appearance. When the tracker arrives at the image in which the branching occurs, the images containing the lateral root have long been processed without including it in the extraction data. The point of issue is once more illustrated in figure 4.4.

This limitation is to be expected. Kaestner et al. [2006], for instance, considered a top to bottom tracking approach to clearing the thresholded image data of unwanted speckles. However, the authors pointed out that this approach would miss upward oriented roots (figure 4.2) and therefore decided to apply a dilation by reconstruction operation [Vincent, 1993] instead, which avoids the problem. This solution, however, is not applicable in our context, where we use tracking to identify objects in an unknown and unprocessed

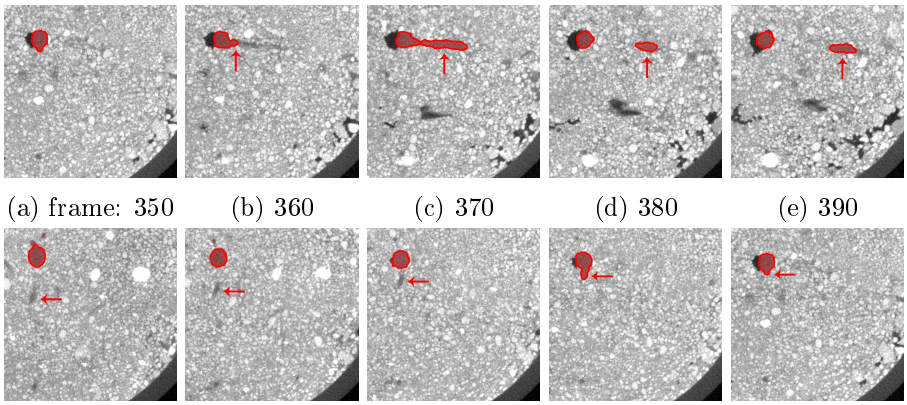

(a) frame: 350 (b) 360 (c) 370 (d) 380 (e) 390

(f) frame: 310 (g) 320 (h) 330 (i) 340 (j) 350

Figure 4.1: Sequence of images showing the emergence of a lateral root and the targets followed by the tracker; (a-e) downward oriented and (f-j) upward oriented lateral root (highlighted by the arrow)

domain. In Kaestner et al.'s method, the extraction was already performed and the morphological operation only used to refine the outcome.

The method developed by Flasque et al. [2001] is based on a three-dimensional tracing approach to the extraction of cerebral vascular networks. In the presented work there was no additional mechanism that focused on recovering vessels that were upward oriented, even though vessel objects were followed in a stepwise manner, similar to a tracking approach. This does not mean that upward oriented vessels were missed or were not present in the image data, but their approach did not suffer from the same limitation. A fundamental difference is the domain in which the search for target objects is performed. While in our approach the search domain is reduced to a two dimensional image plane, following a fixed direction (from top to

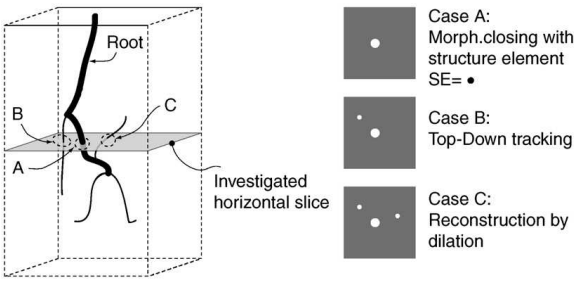

Figure 4.2: Kaestner et al. pointing out that a top-down tracking approach would miss upward oriented roots - image taken from [Kaestner et al., 2006]

bottom), the extraction method of Flasque et al. narrows the space to a three-dimensional parallelepiped which can be oriented at any angle without decreasing the search dimension (figure 4.3). Their method resembles more closely the tracing method used by SmartRoot [Lobet et al., 2011], which was developed for the extraction of roots in two-dimensional images. Since the tracing mechanism is free to move in any direction, it requires continuous access to the entire dataset, which for large samples requires an amount of memory resource that in our context would exceed the capacity of ordinary computers. It is also essential that the direction of growth is determined during the tracking process. Both are elements that the method presented here was not designed for. Besides that, a tracing approach that is free to move in any direction, suffers from other weaknesses, such as a significant risk of the tracker becoming trapped in loops [Collorec and Coatrieux, 1988].

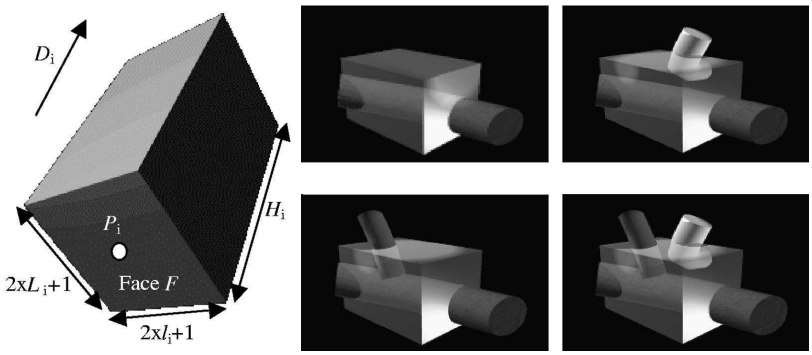

Figure 4.3: Flasque et al. using a parallelepiped to trace vessel segments, which can be oriented at any angle - images taken from [Flasque et al., 2001]

None of these methods offer any concrete solution or strategy that can be adopted to overcome the present limitation. Yet, there are other ways to deal with upward oriented roots.

4.2 Recovering upwards oriented roots

The method presented in chapter 3 provides the means for following identified root objects through subsequent image slices and separates them into individual targets when root branching occurs. The moment of branching can be easily recorded. Connected component analysis allows every object to be labelled with a unique integer. As discussed in chapter 3 this is neces-

sary if objects are to be treated as individuals. When the root model is not updated but inherited, it is also necessary to identify its parent object in the previous image. Note that objects are not guaranteed to get the same label every time and thus the same label number does not imply lineage. The labelling depends on the object's location as well as the number of objects preceding the object in question. Therefore, in order to associate a child object to its parent, the root objects identified in the previous step are used as references; child objects are associated with a parent if the two object regions overlap. While making associations, it is also possible to count how many children a parent object has and, when there is more than one, note that a split has occurred. This is a key component of the process of recovering upward oriented roots.

Processing begins as described in chapter 3, with the stack being traversed from top to bottom. Because the images in a stack are processed one by one, the order in which they are processed can, however, easily be changed. If the stack is analysed in reverse order, upward oriented lateral roots appear no different from downward oriented roots traversed top to bottom and, given two adjacent images, it is possible to detect a split in the target object. The only additional step that needs to be performed to identify upward growing branches is to identify which of the two child objects has already been recovered in the previous, downwards processing step. This can be achieved by referring to the extracted data and asking whether there is a new object not connected to any of the previously recovered roots. The presence of such an object indicates that there might be a root which is upward oriented. In the extended method, after a given image has been processed in the usual, top to bottom direction, a further analysis is performed in the opposite direction; as if moving from that image to its predecessor. Any new objects detected while looking back up the stack signal the beginning of an upward growing branch and so are temporarily stored as markers. Processing then continues downwards until the entire stack has been traversed. The result at this point, following a single completed traversal of the image stack, is as produced by the technique described in chapter 3, but with markers indicating possible backward growing roots. It should be noted that the extension does not only apply to branching roots, but to any root segment that switches between upwards and downwards growth, such as a root segment in an upright position making a 'U-turn'.

To complete the root system extraction, the method then tracks upwards from each marker. Markers are examined in fixed order, from the lowest in the stack to the highest. These tracking operations may generate further markers, identifying possible downward growing roots that are connected to the primary root not directly, but via an upward growing root segment. When all upward growing markers have been processed, the tracker again moves down the stack, tracking from newly reported downward markers. This process is repeated, alternating directions, until all targets are lost and no markers remain (figure 4.4 and 4.5). Note that only the first pass must examine the entire image stack. Subsequent processing focuses on detected markers and each pass only considers images in which a previously undetected plagiotropic root is expected to be visible.

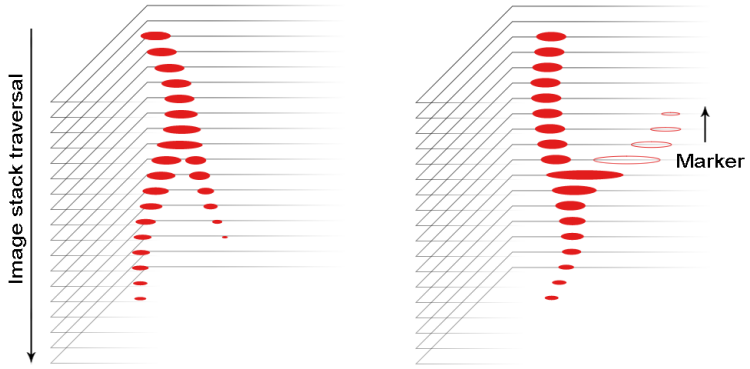

(a) (b)

Figure 4.4: (a) When tracking roots from top to bottom of the image sequence, the presented tracking mechanism allows targets to split, successfully recovering branched architectures. (b) Plagiotropic roots, however, are overlooked. They only appear in the image sequence before they join the primary root and therefore it requires the extension to identify and mark them for later process - image taken from [Mairhofer et al., 2013]

The additional 'backward-looking' step introduced here brings additional computational cost; the time required to process an image stack is doubled at best. This is because every image has to be visited at least twice; during the normal forward traversal and while looking backward (the additional step). The effort of looking for markers, however, has its advantages. Once candidate roots are located, extraction can be continued from each marker

and stop when no objects remain to be tracked. The tracker is not required to go through the entire image stack again in its search for opposite-facing roots. Figure 4.5 shows how an artificially generated root object is stepwise extended by alternating the direction of analysis until the full object is recovered.

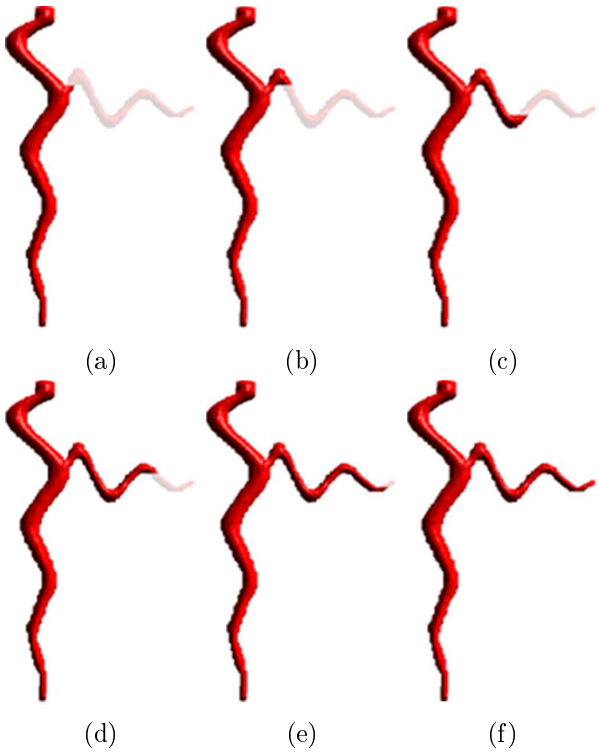

Figure 4.5: Extraction of a simple, artificially generated, plagiotropic root. (a) The primary root is extracted and one upward growing section marked on the first pass through the stack. (b-f) Subsequent processing focuses on the marked branch, extracting a complete description following five further tracking stages - image taken from [Mairhofer et al., 2013]

Figure 4.6 shows the updated flowchart of the plant root extraction process including the extended mechanism introduced in this chapter for recovering plagiotropic roots. After the evolution of the level set function in the regular operation step, a copy of the level set function is made and used on the previous image of the CT data stack. The copy evolves the same way as the level set function in the main routine.

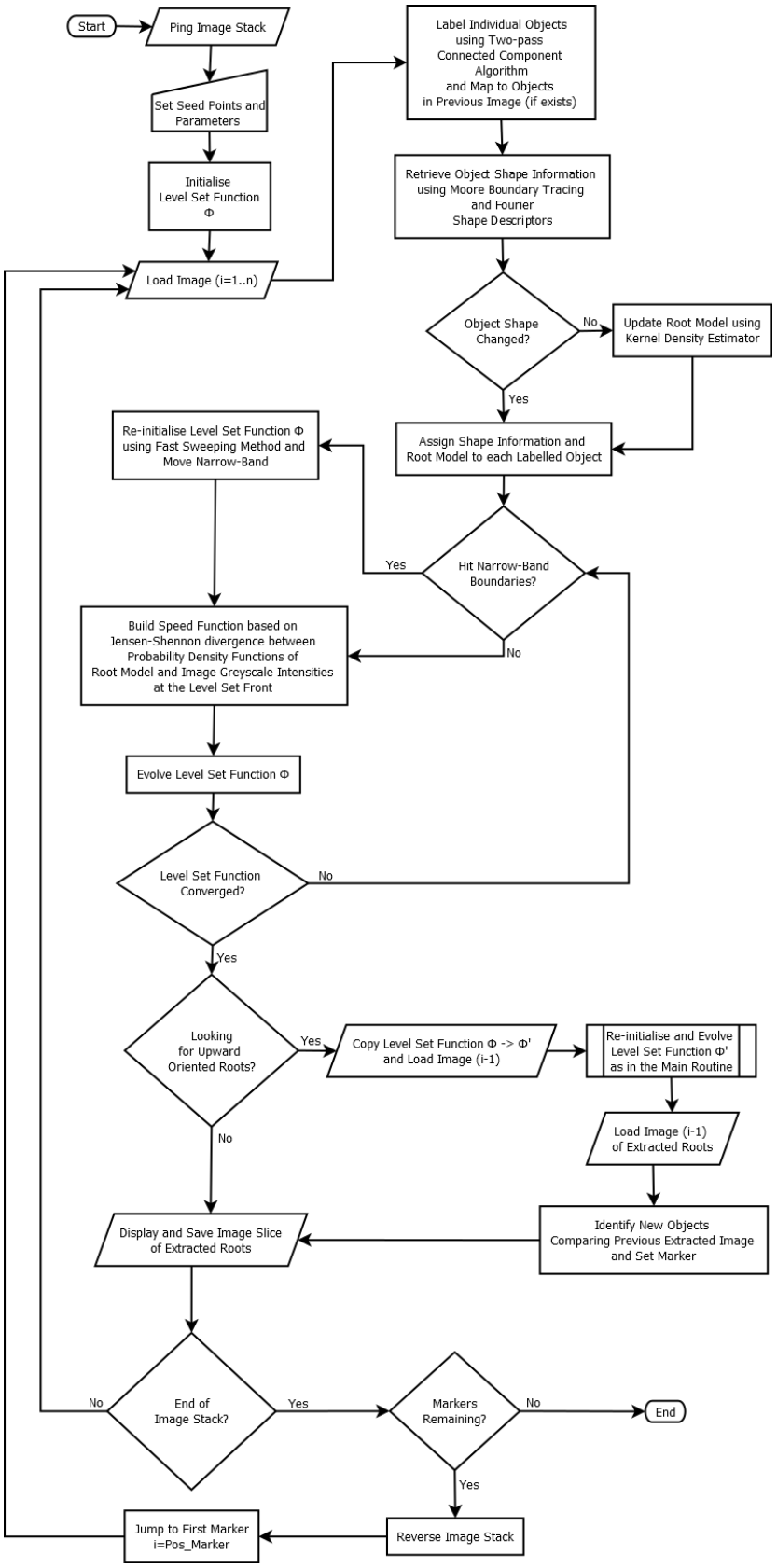

Figure 4.6: Flowchart of the tracking process for plant root extraction including the extended mechanism for plagiotropic roots

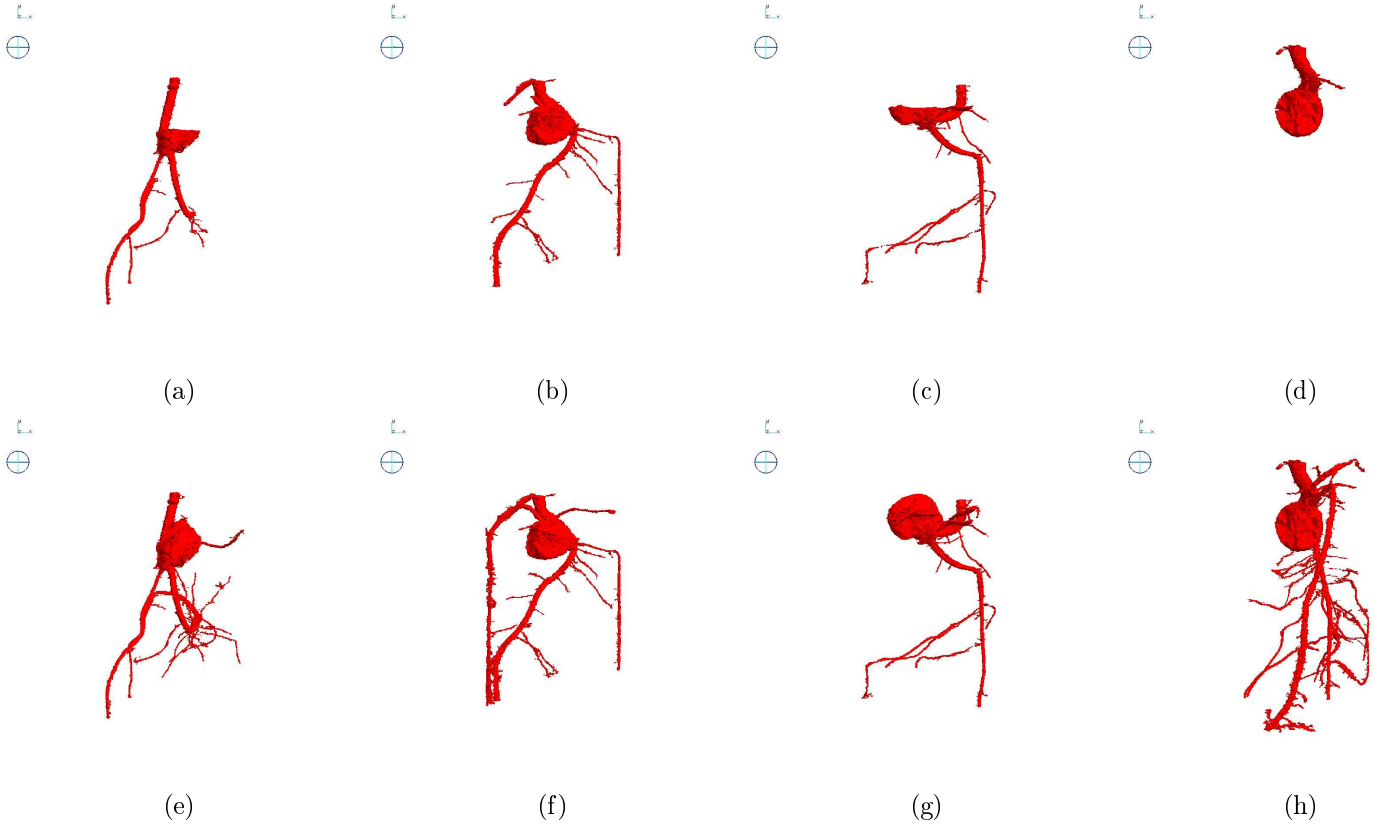

(a) (b) (c) (d)

(e) (f) (g) (h)

Figure 4.7: Extracted root systems of maize 1-4 using (a-d) unidirectional and (e-h) backward enabled tracking method (for the reader's convenience, figures (a-d) are repeated from figure 3.9 in chapter 3)

Figure 4.8: Extracted root systems of wheat 1-4 using (a-d) unidirectional and (e-h) backward enabled tracking method(for the reader's convenience, figures (a-d) are repeated from figure 3.10 in chapter 3)

(a) (b) (c) (d)

(e) (f) (g) (h)

Figure 4.9: Extracted root systems of tomato 1-4 using (a-d) unidirectional and (e-h) backward enabled tracking method (for the reader's convenience, figures (a-d) are repeated from figure 3.11 in chapter 3)

4.3 Extraction of plant root systems with plagiotropic roots

In this experiment we return to the X-ray data acquired in chapter 3 for maize, wheat and tomato grown in both loamy sand and clay loam soil and rerun the extraction process with the same input parameters for the curvature constraint and the Jensen-Shannon divergence, but enabling the new mechanism for recovering plagiotropic roots. Figure 4.7-4.9 show the rendered root systems extracted with the initial method and the extension described above. Table 4.1 highlights the differences in their measured traits. More details on root system traits and how they are measured is described later, in chapter 5.

The number of roots that have an initiation angle greater than 90 degrees account for a substantial part of the overall root system and therefore play a significant role in the quantification of root system traits. The average increase in surface area and volume, using the extended mechanism, is 81.4 percent and 60.5 percent for maize, 27.3 percent and 18.5 percent for wheat and 22.2 percent and 15.4 percent for tomato. The Pearson's product moment correlation coefficient between the unidirectional and the extended mechanism are $r_{area} = -0.1592$ and $r_{volume} = 0.8184$ with a p-value of 0.8407 and 0.1815 for maize, $r_{area} = 0.9351$ and $r_{volume} = 0.9387$ with a p-value of 0.0648 and 0.0612 for wheat, and $r_{area} = 0.9711$ and $r_{volume} = 0.973$ with a p-value of 0.0288 and 0.0269 for tomato. The p-values were calculated based on Fisher's Z transform. A clear difference between the two root representations is visually observable in many of the root systems shown in figure 4.7-4.9. For those samples in which the difference is less apparent, there is still a notable variation in the measured traits. This is especially the case for those traits measured in higher spatial dimensions, such as the volume enclosed by the convex hull. In contrast, one-dimensional characteristics, such as root system depth, only show a difference in a small number of samples. This also indicates the general sensitivity of measured root system traits to the absence of roots missed during the extraction process. Care should therefore be taken when interpreting measured traits, in particular when two or more sample groups are compared with each other during the course of an experiment.

Sample	Area (mm^2)	Volume (mm^3)	CX Hull (mm^3)	Depth (mm)	Width (mm)	Centroid (z) (mm)
unidirectional						
Maize 1	997.8	312.8	10,394.7	49.9	28.8	20.9
Maize 2	1,572.5	457.6	17,585.5	48.5	30.4	17.4
Maize 3	1,180.1	239.3	18,664.0	48.5	30.8	17.0
Maize 4	912.4	470.6	1,323.7	17.2	18.7	10.8
Wheat 1	1,602.5	168.9	22,399.7	48.5	30.9	27.2
Wheat 2	1,420.8	154.7	24,496.8	48.0	31.2	24.1
Wheat 3	900.0	100.5	22,316.0	55.0	31.1	18.5
Wheat 4	766.0	90.5	19,649.9	55.0	31.0	17.3
Tomato 1	181.2	19.9	2,075.7	34.2	24.2	9.9
Tomato 2	213.2	22.2	2,639.0	38.0	24.6	16.9
Tomato 3	130.5	17.3	752.9	17.8	15.4	7.4
Tomato 4	113.3	14.6	714.0	20.8	16.0	7.6
extended mechanism						
Maize 1	1,849.7	464.4	18,472.6	49.9	31.0	21.0
Maize 2	2,087.7	589.8	22,429.2	48.5	30.8	18.0
Maize 3	1,724.4	504.5	20,201.3	48.5	31.0	13.1
Maize 4	2,386.0	725.6	28,888.8	52.4	30.6	15.7
Wheat 1	1,831.2	184.0	23,728.3	48.5	30.9	26.7
Wheat 2	1,827.4	198.9	30,439.7	54.5	31.2	21.3
Wheat 3	1,003.5	106.4	24,145.0	55.0	31.1	18.7
Wheat 4	1,188.3	118.3	29,699.2	55.0	31.2	16.6
Tomato 1	242.3	24.2	4,952.5	34.2	30.4	9.9
Tomato 2	257.4	26.5	3,178.5	39.1	24.6	15.7
Tomato 3	143.0	18.3	933.2	17.8	15.4	7.3
Tomato 4	141.7	16.8	1,576.9	20.8	24.7	7.4

Table 4.1: Measured root system traits from the extraction of the unidirectional technique and its upward oriented extension

Although difficult to see in figure 4.7-4.9, it is worth mentioning that in a few extracted root systems, lateral roots were missed at their emergence, but have been partially recovered by the extension mechanism, after having touched another root further down the image stack.

4.4 Summary

Given that the majority of plant root systems show some degree of plagiotropic response, though the proportion and angle of plagiotropic branches varies widely between different plant species, the presence of upward oriented roots cannot be neglected. These roots account for a substantial portion of the overall root system and have a noticeable impact on quantitative measurements of global root system traits. It is therefore important that they are included in the extracted data, which otherwise might conceal important structural information.

The method introduced in chapter 3 lacks the ability to detect upward oriented root segments. That is, roots that grow at an angle greater than 90 degrees to the vertical axis. The benefit of being more adaptable to local changes in the image data comes with the cost of an additional weakness which as such is not present in conventional three-dimensional segmentation techniques. To compensate this drawback we introduced a mechanism to overcome the limitation, by adding an additional step of 'backward-looking'. This allows us to detect upward oriented roots, which are marked for subsequent processing, and thus to recover more complete root system descriptions that lead to a more accurate computation of architectural traits.

The extraction of plant root systems showed how important it is to search for upward oriented roots and the difference they can make to measured root system traits. A large portion of the root system would have been remained undetected if not for the extended mechanism presented in this chapter. In certain situations it could be observed that lateral roots which were missed at their emergence during the normal downward oriented process, have been partially recovered because they were touching another root segment further down the image stack, from where the extended mechanism picked up the lateral root and followed it back to where it branched.

Further evaluation of the method on the ability of recovering plant root systems from soil is presented in chapter 6. In the following chapter (chapter 5) we discuss the three-dimensional visualisation of extracted root architectures and the measurement of common root system traits.

Chapter 5

Visualisation and characterisation of root system architectures

Separating root material from soil in X-ray μCT images is a key step towards the recovery of descriptions of plant root systems. The segmented image stacks alone, however, do not reveal much information on below-ground processes to any plant or soil scientist working with such instruments. Improved understanding of root systems requires visualisation of the three-dimensional root structure, and meaningful and quantitative data for further analysis. Both elements are briefly introduced in this chapter, giving the user the possibility of obtaining additional information relevant to experimental studies. In section 5.1 we briefly describe how three-dimensional data can be visualised, following with section 5.2 in which we discuss methods to quantify and express root system traits, given the results of the segmentation methods described in chapters 3 and 4.

5.1 Three-dimensional volume rendering

Volume rendering is the mapping of three-dimensional scalar data onto a two-dimensional image plane, and includes a wide range of techniques. These can be divided into two categories; indirect and direct. The difference is that indirect volume rendering requires an intermediate step which generates a model of the volume data, usually a mesh of polygons, that can be efficiently

rendered using a graphics API (such as OpenGL). Visualisation of the volume data is thus limited only to its isosurface, and is therefore often referred to as surface rendering. Indirect volume rendering techniques include, among others, contour tracing [Keppel, 1975], cuberille (opaque cubes) [Herman and Liu, 1979], marching cubes [Lorensen and Cline, 1987] and marching tetrahedra [Shirley and Tuchman, 1990]. The latter two methods have gained particularly wide popularity due to their simplicity. Direct volume rendering methods, on the other hand, visualise three-dimensional data without extracting intermediate geometries; they map volumetric data directly onto the two-dimensional plane. This allows better control of each voxel's contribution to the final colour and opacity of the corresponding image pixel. The development of direct volume rendering techniques has been driven by the areas of medical imaging and scientific visualisation. Unlike surface rendering, direct volume rendering has the ability to render semi-transparent internal structures. Texture slicing [Cabral et al., 1994], shear warp [Cameron and Undrill, 1992; Lacroute and Levoy, 1994], splatting [Westover, 1990] and volume ray-casting [Levoy, 1988] are among the better known direct volume rendering methods. In this section we briefly introduce two of the techniques mentioned above (marching cubes and volume ray-casting), since both have been implemented in the context of this work and are used here to render the extracted volumetric data. For a comprehensive introduction to the most important concepts of volume rendering, the reader may refer to [Drebin et al., 1988; Kajiya, 1986; Elvins, 1992; Hadwiger et al., 2009].

5.1.1 Marching cubes

Marching cubes is an indirect rendering technique and as such aims to extract the isosurface of an object given a volumetric dataset. Since the introduction of the technique by Lorensen and Cline [1987], many variants have been developed [Newman and Yi, 2006]. Marching cubes subdivides the volume into small cubes, each composed of eight vertices, which can either reside inside or outside the object. The cubes are then traversed and tested for intersection with the object's surface, intersection is detected if a cube has vertices both inside and outside the object. The triangles making up the isosurface are generated using a predefined look-up table that stores all possible states. Since each cube has eight vertices, with each vertex having only two possible conditions of either being inside or outside, there are a total of $2^8 = 256$

different states and so triangle combinations. However, by taking reflection and rotation into consideration, this set can be reduced to 15 different states as shown in figure 5.1.

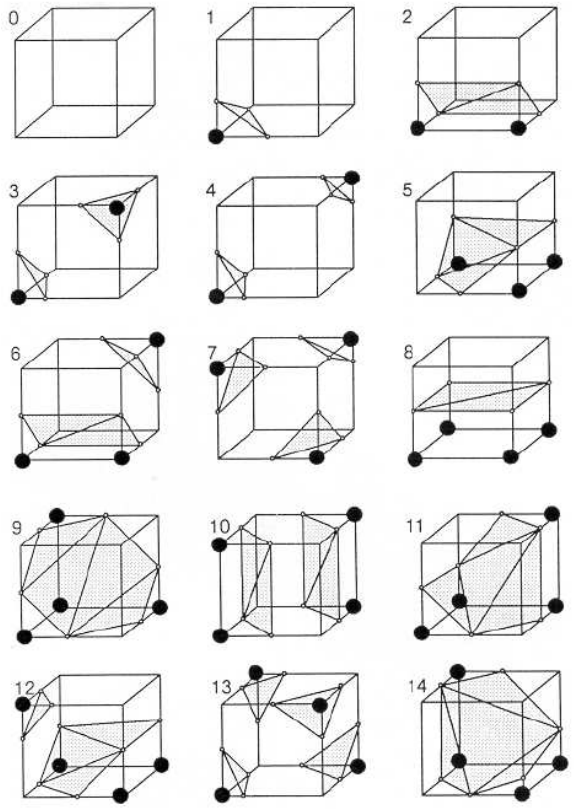

Figure 5.1: Marching cubes table for triangle generation [Lorensen and Cline, 1987]

For continuous data, the intersection point on a cube's edge, and with that the vertices of the generated triangle, are usually calculated using linear interpolation. This results in a smoothed isosurface. For binary data, such as the data obtained from the extraction of the root system, the intersection point is usually chosen at half the distance between the two vertices of the cube. This, however, often gives the object a blocky appearance, which can be reduced by applying either mesh smoothing methods or various shading techniques within the rendering process.

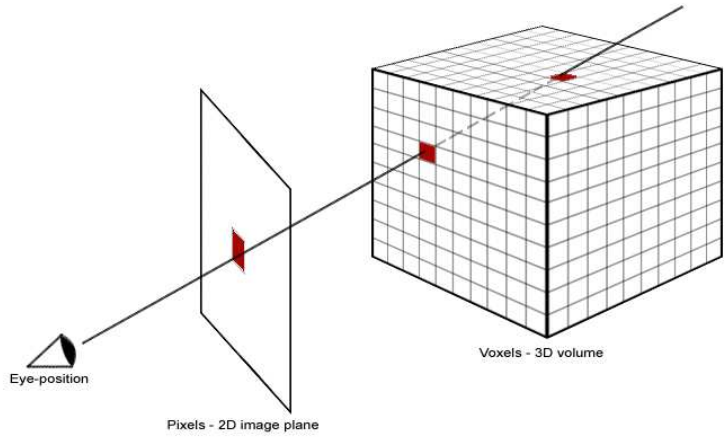

Figure 5.2: Volume ray-casting - ray starting from the eye position going through the pixel into the volume data

5.1.2 Volume ray-casting

Volume ray-casting is a popular method used for three-dimensional visualisation of volumetric data and belongs to the group of direct volume rendering techniques. The idea of volume ray-casting, as the name implies, is to cast a ray from the viewer's eye position through the image pixel into the volume data as illustrated in figure 5.2. The pixel value is determined by accumulating colour and opacity values of each voxel along its viewing ray. An important component of any direct volume rendering technique is an optical model of light emission, absorption and scattering. A simplified model of the light emission-absorption model is described by the volume rendering integral. Here we refer to the notation outlined in [Hadwiger et al., 2009] where $x(t)$ denotes the viewing ray passing through the volume with distance t from the eye, and $s(x(t))$ its scalar value at the corresponding position. The absorption $k(s)$ and emission $c(s)$ coefficients along the ray are defined for simplicity as a function of the distance t

$$k(t) = k(s(x(t))) \tag{5.1}$$

$$c(t) = c(s(x(t))) \tag{5.2}$$

The light emitted at distance t is continuously absorbed along the ray until it reaches the eye. Since the absorption is not constant but depends on the path of the ray, the complete absorption can be obtained by integration.

The emission of light is similar. Since light is not emitted from a single position, but composed of all the light emitted along the path of the ray, the total energy of light is accumulated. By taking these two aspects into consideration, the simple volume rendering integral can be written as follows

$$C = \int_0^D c(d) \cdot e^{\left(-\int_0^d k(t)dt\right)} dd \tag{5.3}$$

Volume ray-casting is a simple approximation to the solution of the volume rendering integral. Data points are re-sampled along the ray at equally spaced intervals as in general the volume is not necessarily aligned with the viewing ray. The pixel value at the two-dimensional plane, corresponding to the received light energy emitted and absorbed along the ray path, can be evaluated either through back-to-front or front-to-back composition. The latter approach can benefit from the so called 'early ray termination', which allows the evaluation of the light energy to stop as soon as the alpha blending has reached full opaqueness [Hadwiger et al., 2009]. The alpha blending (opacity) stands in direct relation to the absorption of light [Max, 1995] and is defined as

$$A = 1 - e^{\left(-\int_0^d k(t)dt\right)} \tag{5.4}$$

Using the Riemann sum to evaluate the integral,

$$C_i = c(i \cdot \Delta t)\Delta t \tag{5.5}$$

$$1 - A_i = e^{(-k(i \cdot \Delta t)\Delta t)} \tag{5.6}$$

equation 5.3 can be approximated as follows

$$C' = \sum_{i=0}^{n} C_i \prod_{j=0}^{i-1} (1 - A_j) \tag{5.7}$$

which can be solved iteratively in front-to-back order

$$C'_i = C'_{i-1} + (1 - A'_{i-1})C_i \tag{5.8}$$

$$A'_i = A'_{i-1} + 1 - A'_{i-1}A_i \tag{5.9}$$

where C_i is the colour of the voxel (or the interpolated colour of its neighbouring voxels) at position i along the ray and A_i its opacity, starting with

$C'_0 = 0$ and $A'_0 = 0$. The calculation of the pixel value is terminated when A'_i reaches a value of 1.

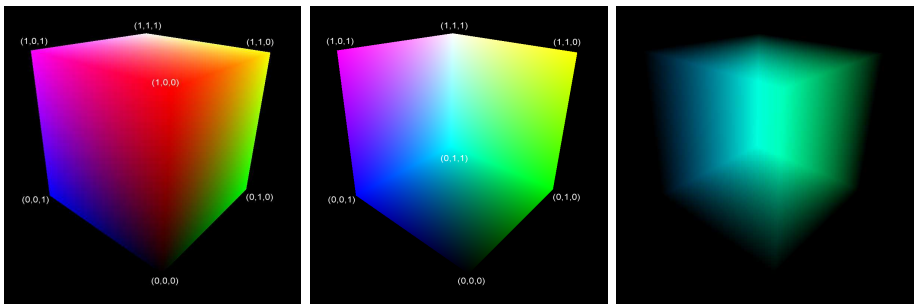

(a) (b) (c)

Figure 5.3: Front-face cube (left), back-face cube (centre) and its subtraction giving the ray direction vector (right)

Volume ray-casting can be efficiently implemented with the aid of a GPU, as presented in [Krüger and Westermann, 2003]. The volumetric data is loaded and passed into the GPU memory as a 3D texture. For each pixel, the fragment shader evaluates colour and opacity from the ray starting at the pixel's location and passing through the volume, using equations 5.8 and 5.9. To determine the direction of the ray passing through the volume, the front and back faces of a unit cube, which define the volume's bounding box, are rendered with colours representing the coordinates along each axis. Subtracting the back faces from the front faces of the cube, gives the ray direction vector and length (figure 5.3). Figure 5.4 shows an example of the rendered volume using both the marching cubes and volume ray-casting techniques as implemented in the presented work.

5.2 Quantification of root system traits

A fundamental requirement in plant root studies is the ability to describe characteristics that distinguish a particular root system from others, or to find similarities that plants of a certain variety have in common. This is particularly relevant when searching for differences in plant root systems that arise as a result of the influences received from their environment. It is not only important to highlight what these traits are, but also to find a way to measure them accurately. In this section we briefly introduce the subject of root system traits and describe the way in which some of the measurements have been implemented in the context of this work.

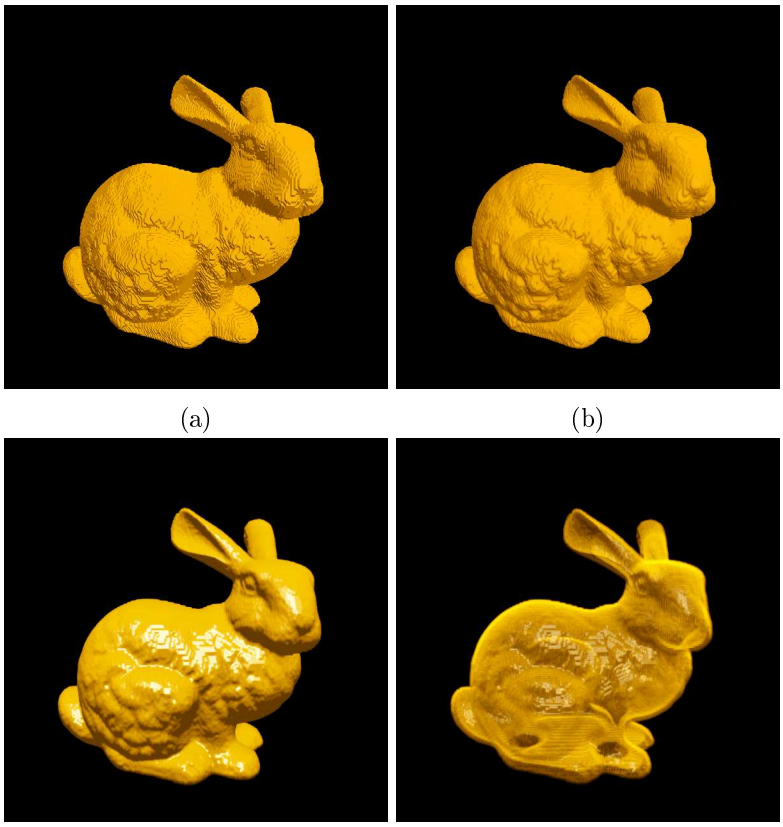

Figure 5.4: Volume rendering of the Stanford bunny dataset [Levoy, 2000] using (a) marching cubes with flat shading, (b) marching cubes with gouraud shading, (c) volume ray-casting with phong shading and (d) volume ray-casting with phong shading and semi-transparency

5.2.1 Traits defining root system characteristics

Root system traits are observable and inheritable physical characteristics that are used for the classification of a plant's root system into phenotypes. With a wide range of plant species and varieties and due to the structural complexity of their root systems, it is difficult to find a single trait that by itself provides sufficient information for a unique classification. However, by defining a number of traits and using them in combination, we can form a meaningful description of the root system and reveal valuable insights about its structural development. Root system volume is a commonly used trait that could be sufficient if, for example, plants of the same variety are compared against each other, since the roots' basic characteristics are expected

to be similar. If, however, plants of different species are being examined, root volume does not necessarily distinguish between a root system with many long and thin roots compared to a root system with short and thick roots. Here, a ratio of volume and total root length would make the classification more meaningful. Numerous measurements have been used in the literature to define plant root characteristics. These can be categorised as either static or dynamic and local or global traits [Clark et al., 2011]. Dynamic traits require the consideration of time, such as the emergence time or growth rate of roots. Static traits are fixed, including, for instance, the number of lateral roots. Local traits are derived from a portion of the root system, and comprise for example the angle formed between a lateral root and its primary root, while global traits, on the other hand, include the entire system as in the case of root system volume and surface area. A fairly comprehensive list of different root phenotypes can be found in [Iyer-Pascuzzi et al., 2010] and [Clark et al., 2011].

Trait	Description
Length (L)	Length along the skeleton of the whole root system
Maximum width (MaxW)	Maximum horizontal width of the whole root system
Minimum width (MinW)	Minimum horizontal width of the whole root system
Maximum depth (MaxD)	Maximum vertical depth of the whole root system
MinW/MaxW ratio	Ratio of minimum width to maximum width
MaxW/MaxD ratio	Ratio of maximum width to maximum depth
Centroid	Vertical position of the center of mass of the entire root system
Exploitation volume	Volume surrounding the root system at a specified radius minus the root system volume
Exploitation index	Ratio of the exploitation volume to root system length

Table continues on following page

Median number of roots (MedR)	Median number of roots from root counts taken from all horizontal cross-sectional slices through the entire root system
Maximum number of roots (MaxR)	Number of roots at the 84th percentile of a sorted list (smallest to largest) of root counts from all horizontal cross-sections through the entire root system
MaxR/MedR ratio (bushiness)	Ratio of the maximum number of roots to the median number of roots
Surface area (SA)	Summed surface area of the whole root system
SA/V ratio	Ratio of surface area to volume
SA/L ratio	Ratio of surface area to length
Volume distribution	Ratio of the volume of the root system contained above one-third depth of the root system to the volume of the root system contained below one-third depth of the root system
Convex hull volume (CHV)	Volume of the convex hull that encompasses the whole root system
V/CHV (solidity)	Ratio of volume to convex hull volume
Emergence time	Average root emergence time for a given root type in relation to the planting date
Initiation angle	Average horizontal root initiation angle for a given root type
Gravitropic response	Difference in the horizontal root angle divided by the length of the root
Circumnutation	Difference in the root turn angle divided by the length of the root
Narrowness index	Average ratio of minimum width to maximum width for each horizontal cross-sectional slice through the whole root system

Table continues on following page

Volume (V)	Volume of the whole root system
Count	Number of roots of a particular type
Tip count	Number of root tips in the whole root system
L/V (specific root length)	Ratio of length to volume of the whole root system

Table 5.1: Summary of various root traits - taken from [Clark et al., 2011]

5.2.2 Measuring root system traits

Because of their relevance to plant root studies, some of the measurements for plant root traits presented in the literature have been implemented in the course of this work. However, since the main focus lies on the extraction of the root system, we have limited them to some of the static and global traits only, which we believe are of significant value. These measurements are listed in table 5.2 and described in detail in the following paragraphs.

Trait	Description
Volume	Number of voxels multiplied by voxel-size cubed
Surface area	Approximation of the isosurface with a mesh of triangles, calculating the sum of all their areas multiplied by voxel-size squared
Maximum Depth	Number of slices between first and last voxel in the image stack multiplied by voxel-height
Maximum width	Diameter of the computed minimum enclosed circle multiplied by voxel-size
Centroid	Mean of x, y and z coordinates over all voxels in relation to voxel-size
Convex hull volume	Estimation of the volume within the convex hull multiplied by voxel-size cubed

Table 5.2: Measurements for the estimation of root system parameters

Probably the most straightforward measurement to perform is root volume, which can be estimated by counting the number of voxels making up the extracted root system. Knowing the dimensions of a voxel, and hence

its volume, the total root system volume can be estimated. From this, assuming a constant density within the root system, it is possible to derive its biomass. Biomass is a useful and popular parameter, partly because it is relevant to many studies but probably also due to the ease with which it can be measured.

Another frequently used measurement is root surface area. Consider an object in two-dimensional space; if we want to calculate the length of its boundary, then a simple approximation would be obtained by counting the number of object pixels of which at least one neighbour is part of the background. This however, leads to a substantial overestimation. A better solution was presented by Freeman [1961], who distinguished between pixels lying either on a straight or diagonal line, multiplying the latter by a factor of $\sqrt{2}$. In three-dimensional space, using voxel counting to estimate the surface area would lead to an even larger error and a simple generalisation of straight and diagonal planes is not applicable. Because of that we use a solution similar to that presented in [Lindblad, 2005], where the isosurface is presented as a mesh of triangles and the surface area estimated by summing their areas. Triangle mesh data is obtained via the marching cubes [Lorensen and Cline, 1987] algorithm. This is also used for surface rendering as described in section 5.1.

A further measurement that is easy to calculate from the extracted data is the root system depth, which is obtained by counting the number of slices along the vertical axis of the image stack that lie between the first and the last appearance of a voxel. Knowing the voxels' height it is easy to determine the root system's total depth.

The maximum width along the horizontal plane is also calculated. This is computed by projecting all voxels onto the two dimensional x-y plane and then using Welzl's [1991] algorithm for the minimum enclosing circle. The diameter of the circle corresponds to the maximum width of the extracted root system.

Interesting in relation to the root system's depth and maximum width, is its centroid, which is the geometric centre of an object and corresponds to its centre of mass, if it is assumed that the mass per unit volume is constant throughout. The centroid is obtained by calculating the mean coordinates of all voxels for each of the three axes x, y and z.

The convex hull of the root system is also calculated. This is obtained using the QuickHull algorithm [Barber et al., 1996]. The convex hull itself is not of great interest, but the volume enclosed by it is. Therefore, using Monte Carlo integration, an estimation of the volume within the convex hull [Rubinstein and Kroese, 2008] is calculated.

Figure 5.5 shows some of the measurable traits mentioned above, along with the extracted and rendered root system of a maize plant.

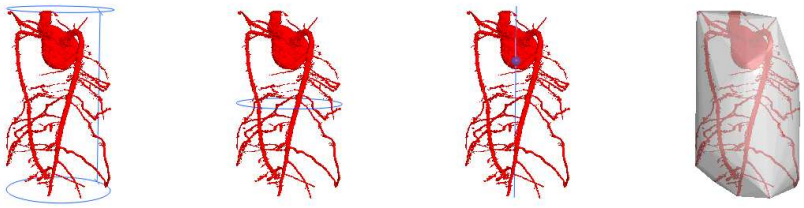

(a) (b) (c) (d)

Figure 5.5: Root system traits (a) depth, (b) maximum width, (c) centroid and (d) convex hull

5.3 Summary

The extraction of root material from X-ray CT data produces a volume data structure in which root material is labelled. If researchers are to draw conclusions from these large, complex, three-dimensional data objects they must be able to render them in a meaningful way, viewing the root system from different angles. Being able to measure quantities of the extracted data is essential for characterising root system traits, making it further possible to compare and distinguish between different plant root systems. For the sake of completeness, we discussed two different techniques, a direct and an indirect volume rendering algorithm, that were implemented to allow researchers to visualise the three-dimensional structure of the extracted root system. In addition, we discussed various root system traits of which some are measured within the context of this work.

The visualisation and measurement of root characteristics has been used extensively throughout this work, for demonstrating and highlighting differences between results obtained. In the following chapter (chapter 6) we perform a detailed analysis of the ability of the presented methods to recover root system architecture traits.

Chapter 6

Evaluation of the root extraction technique

In chapter 3 we introduced a technique that was designed for identifying and tracking root objects in X-ray μCT images, which was extended by an additional mechanism in chapter 4 to allow recovery of the upward oriented root segments found in plagiotropic root systems. Together, both elements allow the extraction of plant root systems grown in soil and imaged with X-ray μCT. So far however, we have not demonstrated how well the method performs, what detail of structural information can be obtained from the extraction process and what the capabilities and limitations of the described technique are. In this chapter we focus on answering these questions.

We divide the experiments into four parts, each reflecting a particular perspective. We adopted this approach for two reasons. First, we aim to cover a wide range of scenarios in order to eliminate bias in the analysis. Second, each experiment gives rise to uncertainty, since ground truth data is either not available or is not entirely representative of real data samples. In section 6.1 we assess the performance and accuracy of the method by extracting an idealised test object from artificially generated data with varying noise and contrast. In section 6.2 we investigate the ability of the proposed techniques to detect root segments, in soil, that are of measured size and located at known positions within the sample. In section 6.3 we run the method on real CT image data showing different plant species and soil textures and compare the results to the actual root systems after removing and

washing them free of soil. The extracted data is further compared in section 6.4 against segmentation data obtained by other techniques previously introduced in the literature.

6.1 Artificially generated data

One way to test the proposed extraction technique is to run it on artificially generated data. The benefit of this approach is that we have full control of the target object and so can test the method against a particular application. When wishing to test a certain scenario, it is difficult to grow a real plant whose root system exhibits the desired behaviour at the required level of detail. A further advantage is that artificially generated objects provide accurate ground truth that can be used to determine the error in the extracted data, since the sampled object is completely known. If the target object is artificially generated, then it is also possible to use the same object under changing conditions. Input parameters can be varied to see how the method performs under different circumstances, exploring its limitations. However, it is important that the test data resembles to a certain degree the characteristics of real image data, otherwise the findings would be less meaningful. Details of the generation of artificial data used in the testing process, are described in section 6.1.1. In section 6.1.2 we specify the details of the experiment and discuss the results in section 6.1.3.

6.1.1 Generating artificial test images

In order to generate artificial image data that reflects characteristics similar to those found in real CT data, it is necessary to quantify its noise and quality. To perform this task we pick up from chapter 2, where we described the process of measuring image noise. As a reference for the analysis we use a cross-section from a column that was filled with an agar solution and imaged with a Nanotom (Phoenix X-ray / GE Measurement & Control Systems) X-ray μCT scanner (figure 6.1). From this the point spread function (PSF), modulation transfer function (MTF) and noise power spectrum (NPS) are determined and shown in figure 6.2. To generate realistic artificial data, we first take the two-dimensional cross-sections from the image stack of our test object and then apply the Radon transform [Kak and Slaney, 1988] to obtain its sinogram. From chapter 2 we know that the X-ray photon noise follows

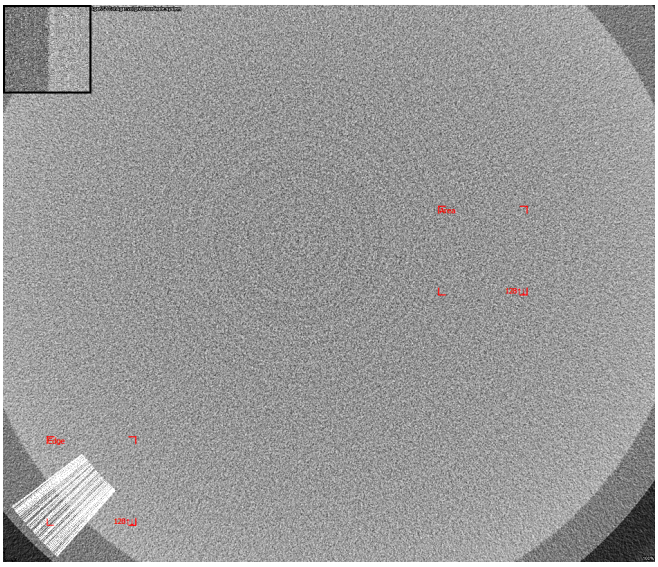

(a)

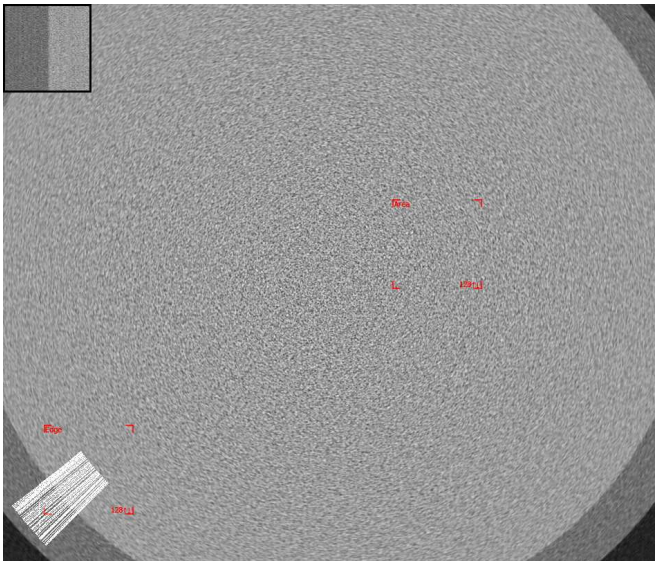

(b)

Figure 6.1: Cross-sectional X-ray μCT image of a column filled with agar solution (top) and an artificially generated image (bottom). Areas selected for the calculation of the NPS and MTF are highlighted by red squares. The extracted and aligned signals used in the calculation of the MFT are shown in the top-left corner of each image. Note that the original image has slight ring artefacts. In this context we do not simulate any CT scanning artefacts in the artificially generated data.

a Poisson distribution and therefore the sinogram is degraded with Poisson noise and blurred with a Gaussian kernel. The Gaussian blur reflects the inaccuracy of the detector panel when measuring the signal (for more details on the physical aspects of X-ray CT see [Herman, 2009]). The sinogram is then reconstructed using filtered back-projection reconstruction as described in chapter 2. The artificially generated image is shown in figure 6.1 and its noise and quality characteristics plotted in figure 6.2 alongside the original data.

The NPS of the image data is calculated using equation 2.17 on a manually selected and approximately uniform area of 128x128 pixels near the centre of the image. To calculate the MTF, it is first necessary to determine the PSF, which is given by the first-derivative of the edge spread function (ESF). Because of image noise, it is difficult to select a signal that allows calculation of the MTF without affecting the outcome of the result too much. Therefore, to reduce noise while preserving edge information, we selected and averaged 128 different signals. These signals, however, have to be aligned along their edges, so that the edge information is not blurred, but keeps its original sharpness. Edges are found by segmenting the data in a selected area into two regions using the k-means++ algorithm [Arthur and Vassilvitskii, 2007]. Signal information, normal to the edge, is extracted by resampling the image using a bi-linear interpolation for a length of 128 pixel points. With the aligned and averaged ESF we can use equation 2.15 to obtain an estimate of the MTF. It should be noted that due to these steps, but also because of the presence of noise, the analytical MTF is likely to be underestimated.

The noise characteristics are similar, yet there are observable differences. This is to a large extent because of the simplicity of the noise simulation model, but also due to the simplification of the reconstruction process. However, compared to ordinary Gaussian noise, which usually has a flat NPS, the noise applied here reflects the properties of X-ray CT data more closely and therefore is more suitable for the generation of artificial test data. It should be noted that both the original and the artificially generated image have the same NPS curve, showing a higher concentration of low frequency noise that decreases as the signal frequency becomes higher. The MTF function shows a similar decrease of contrast at increasing spatial resolution. This,

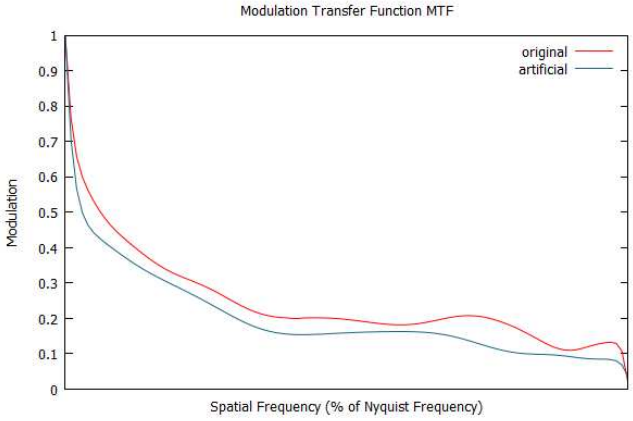

(a)

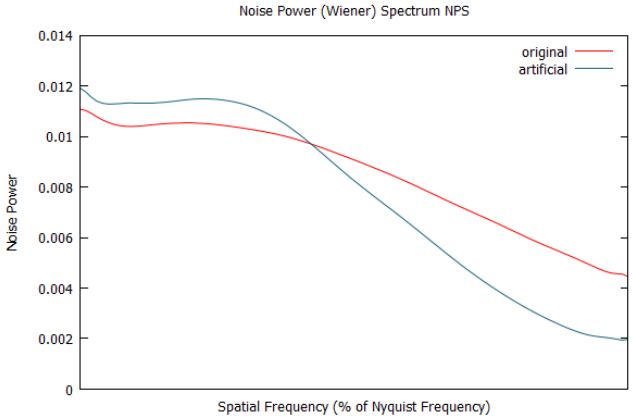

(b)

Figure 6.2: MTF (top) and NPS (bottom) from the original (red) and the artificially generated (blue) image data as shown in figure 6.1

however, can be easily adjusted by varying the blur before reconstructing the sinogram. In the artificial data generated here we do not simulate any CT scanning artefacts, such as ring artefacts, beam hardening or others that are sometimes present in original CT image data.

6.1.2 Extracting artificial root objects

In this experiment we artificially generate a set of image stacks with differing degradation levels and apply the proposed root extraction method with the aim of assessing the efficiency of the extraction compared to the actual test

object. For that purpose we use a simple cone, which viewed from a cross-sectional perspective looks like a circle that gradually shrinks in radius. The object is placed in the centre of the image stack at a straight vertical angle. The image stack is 512x512x512 voxels in size. The radius of the cone is 23 pixels in the first image slice, reducing until it reaches a radius of 1 pixel in the last image .The layout of the test image stack is illustrated in figure 6.3.

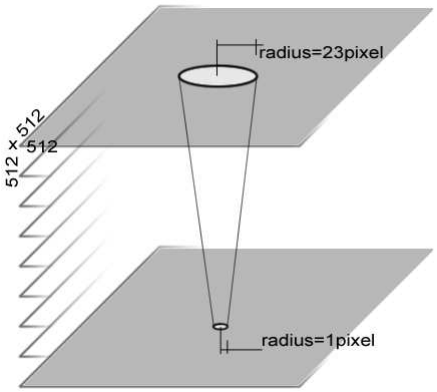

Figure 6.3: Illustration of artificially generated test image stack

Test objects are generated under varying contrast (2, 4, 8, 16, 32, 64) and noise levels (0, 2, 4, 6, 8, 16, 32, 64), resulting in a total of 42 different image stacks. Contrast values represent the difference in greyscale intensities between back- and fore-ground. The noise is modelled by a Poisson distribution with a parameter equal to the signal intensity in the sinogram and multiplied by a factor of noise level intensity. Together all these samples cover a range of scenarios, from low to high contrasts and from no noise at all to very noisy images. The Gaussian blur in all generated samples is kept constant at $\sigma = 1$ for a radius of 3σ. Each image stack under different conditions has been simulated only once. A wide range of different contrast and noise levels were chosen, since it is difficult to generalise these parameters to typical real situations, as image quality varies between CT scanners but also depend on the scan settings and the physical composition of the imaged samples.

We initially planned to keep the two parameters of the extraction method constant, to better show the effect of the evolution of the level set function

under changing image conditions. However, this would be highly unrealistic, since the parameter controlling the Jensen-Shannon divergence, which determines the acceptable distance between root model and image data, is strongly dependant on the contrast between target and background. A parameter suitable for detecting low contrast objects in low noise images cannot deal with objects in a noisy environment even when contrast is high. It is therefore necessary to vary those parameters across the artificial data set.

The parameter controlling the curvature constraint is less restricted by the lack of contrast between target and background but plays an important role in keeping the level set function within the target object at high levels of noise. By smoothing the level set front, it prevents the level set function from spreading through gaps and so beyond the objects' boundaries. While a high value for the curvature parameter has its benefits in noisy environments, it also exerts a resilient force against forward expansion and thus causes small objects to collapse until they vanish. An increased curvature value, therefore, disallows the extraction of very thin objects. By slightly adapting the input parameters to the different testing scenarios, it is possible to adapt to the different circumstances in order to extract meaningful data from the images. This however, does not imply that the parameters chosen for each image stack reflects the optimal choice for the best possible result, but can be considered as a 'good guess' for the extraction process. Table 6.1 shows the input parameters for the curvature constraint and the Jensen-Shannon divergence.

Sample	Curvature (α)	Jensen-Shannon (β)
Contrast 2 / Noise 0-64	0.400	0.028
Contrast 4 / Noise 0-64	0.400	0.068
Contrast 8 / Noise 0-64	0.400	0.128
Contrast 16 / Noise 0-64	0.400	0.208
Contrast 32 / Noise 0-64	0.400	0.288
Contrast 64 / Noise 0-64	0.400	0.368

Table 6.1: Parameters used in the extraction process of artificially generated data

All analyses were initialised with a single seed point placed at the centre of the object ($x = 256, y = 256$). The target is then extracted and followed through the image stack. In the course of the extraction the target can be lost, either because the level set function shrinks until there is no inside area left or because it grows past the object boundary, including both the target and the background. To deal with the latter case we have to define a threshold value which, if exceeded, will be considered to signal loss of the target. In this experiment we set the maximum acceptable area to 125 percent of the actual target object.

6.1.3 Results and discussions

Figures 6.4-6.9 show how far down the image stack the target object was successfully tracked, as well as the number of enclosed pixels extracted for each image slice, together with false positives (type I error - the number of voxels extracted as root material but belonging to the background) and false negatives (type II error - the number of voxels belonging to roots not extracted). To be able to distinguish low contrast objects, it is necessary to choose a sensitive distance value for the Jensen-Shannon divergence parameter. While this allows the detection and tracking of low contrast objects, it can also be observed that the addition of even low level noise soon makes it impossible to extract any data at all (figure 6.4). At high noise levels only high contrast target objects can be successfully extracted (figures 6.4-6.9). This however, is only possible if the input parameters are adjusted as well. An increased level of noise makes the greyscale intensity distribution vary much more than with the absence of noise, and therefore a low parameter value for the Jensen-Shannon divergence would not be able to deal with the large variation, resulting in the target being lost. Even though the curvature constraint was kept constant, it played an important role in the extraction process. Especially when dealing with low contrast and high noise content, the level set function can easily find its way around pixels into the background, shifting the root model slowly away from the target representation to a representation of the background. Figure 6.10 shows the percentage of the object recovered for all changing contrast and noise intensity levels. The plotted curve clearly demonstrates the difficulty of extracting data from low contrast and high noise images. If, however, only one of the two factors is high, the parameters can be adjusted to allow the recovery of the sought ob-

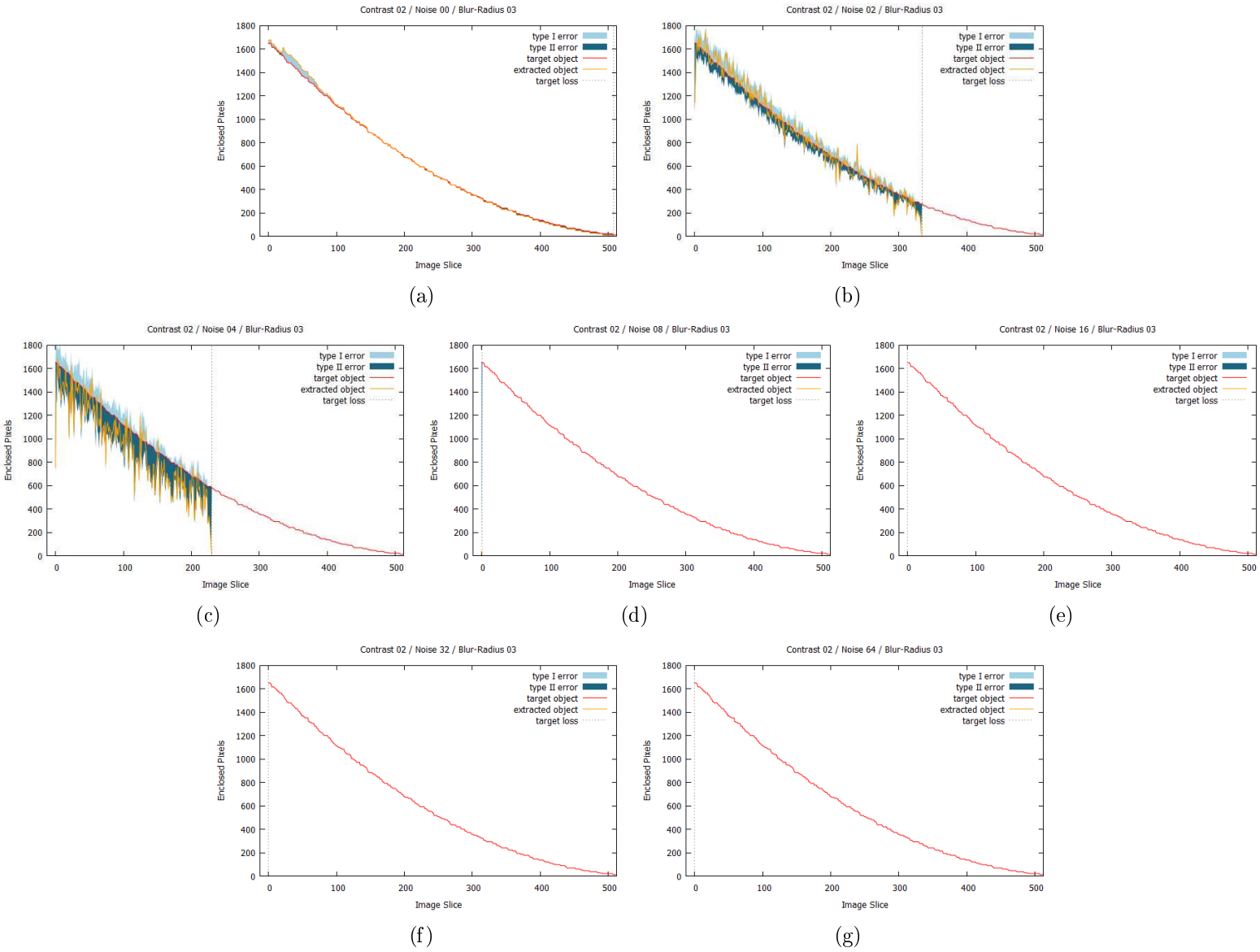

Figure 6.4: Extraction from artificially generated images with contrast = [2] and noise = [0,2,4,8,16,32,64]

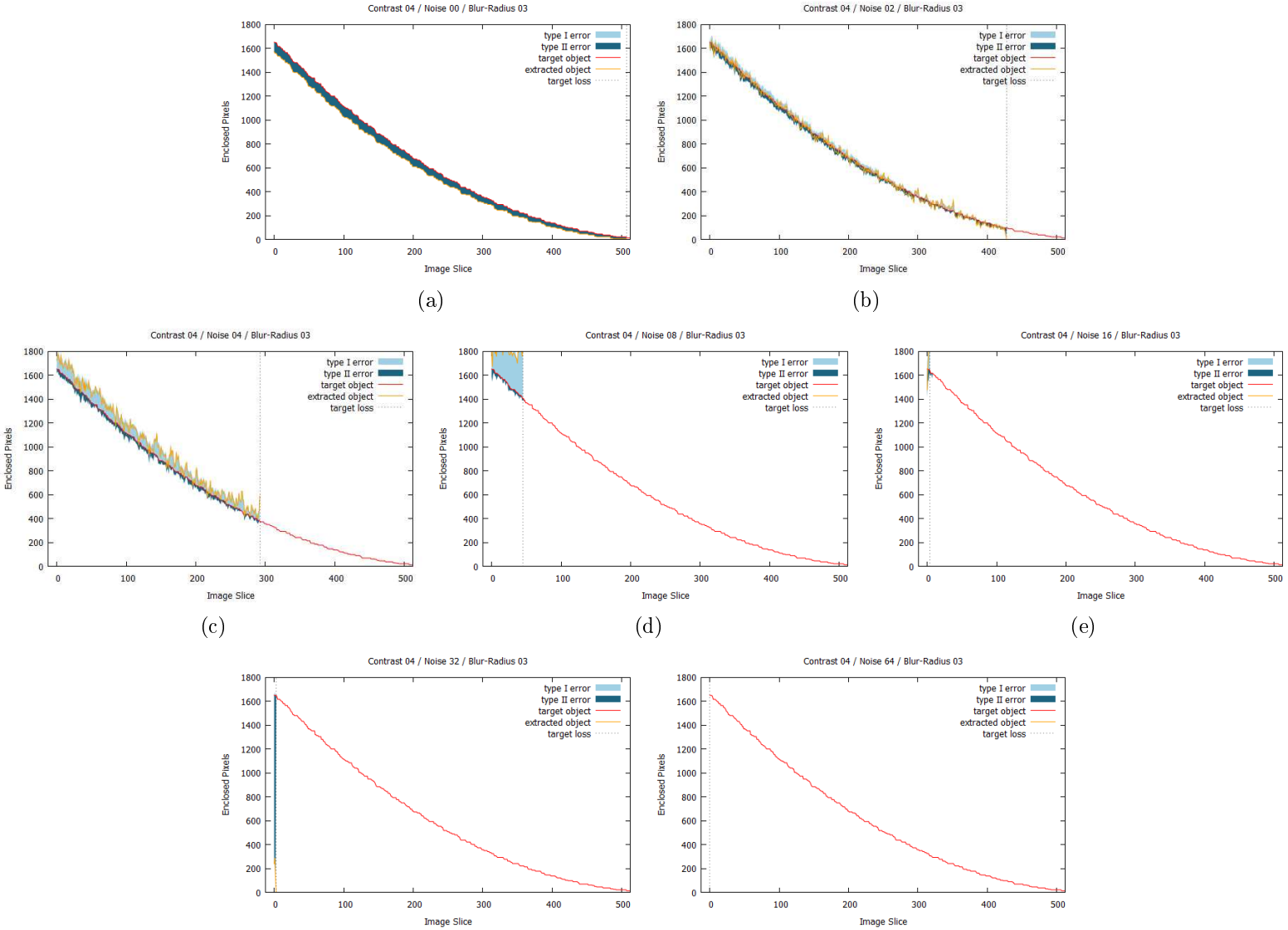

Figure 6.5: Extraction from artificially generated images with contrast = [4] and noise = [0,2,4,8,16,32,64]

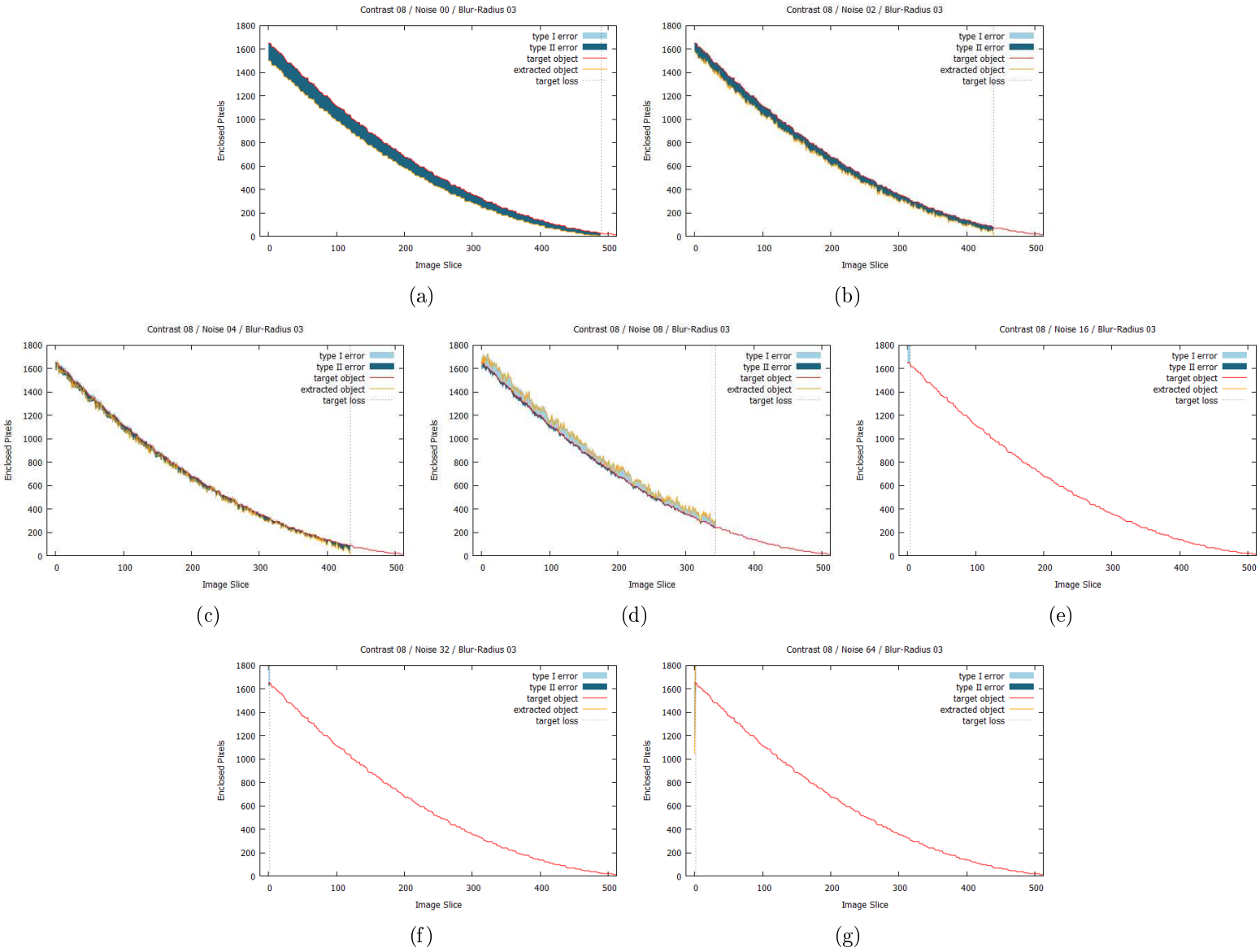

Figure 6.6: Extraction from artificially generated images with contrast = [8] and noise = [0,2,4,8,16,32,64]

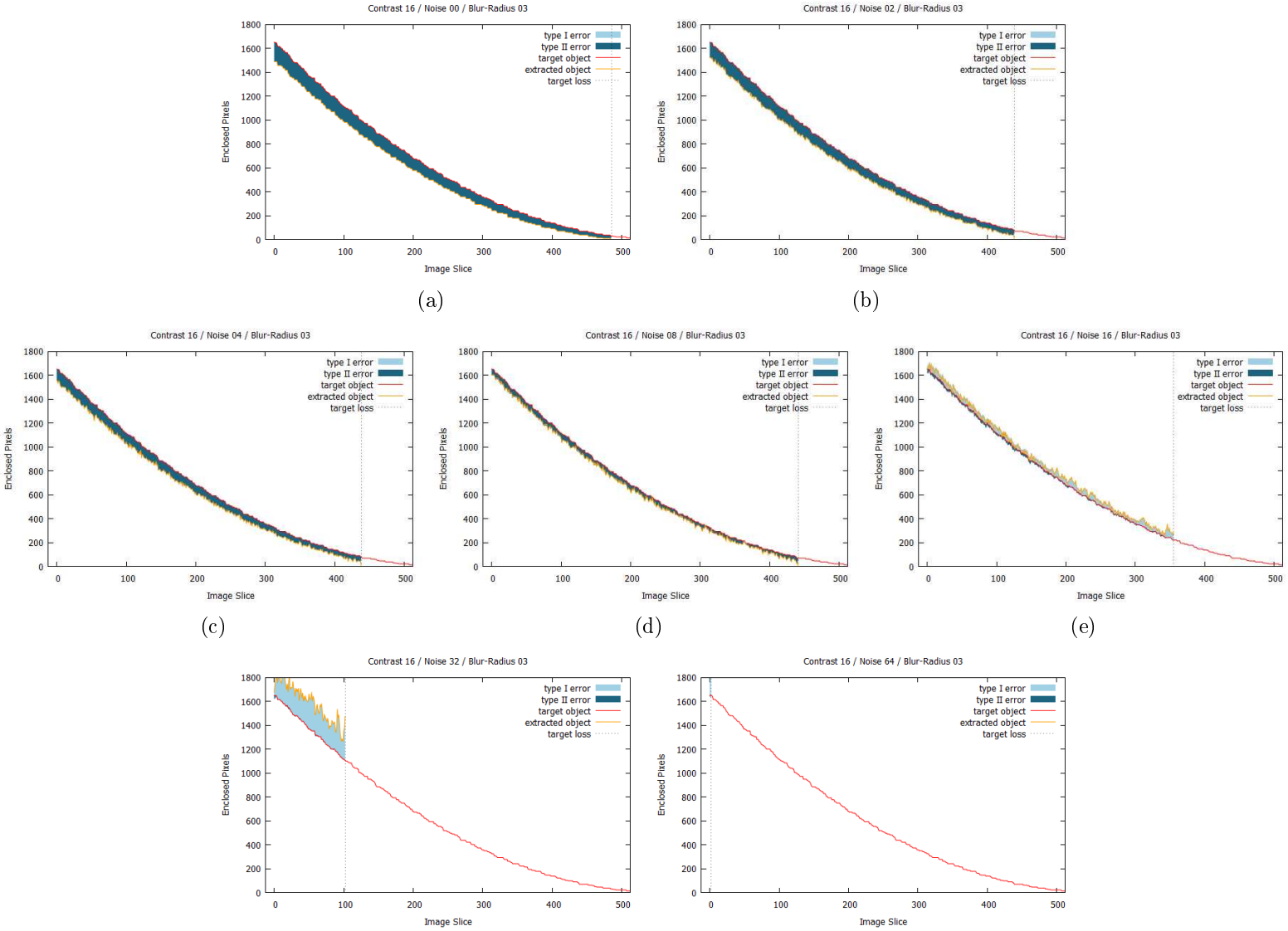

Figure 6.7: Extraction from artificially generated images with contrast = [16] and noise = [0,2,4,8,16,32,64]

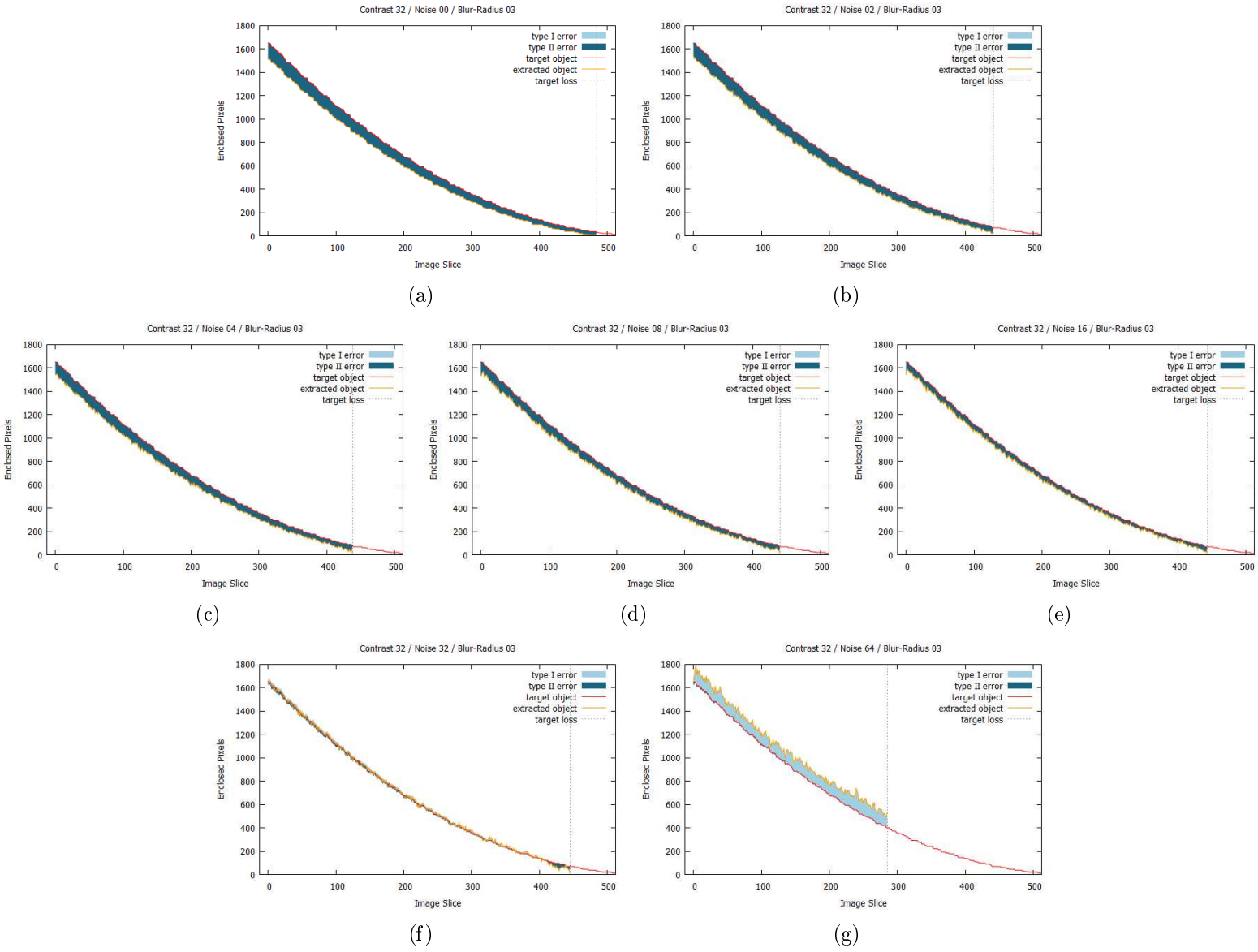

Figure 6.8: Extraction from artificially generated images with contrast = [32] and noise = [0,2,4,8,16,32,64]

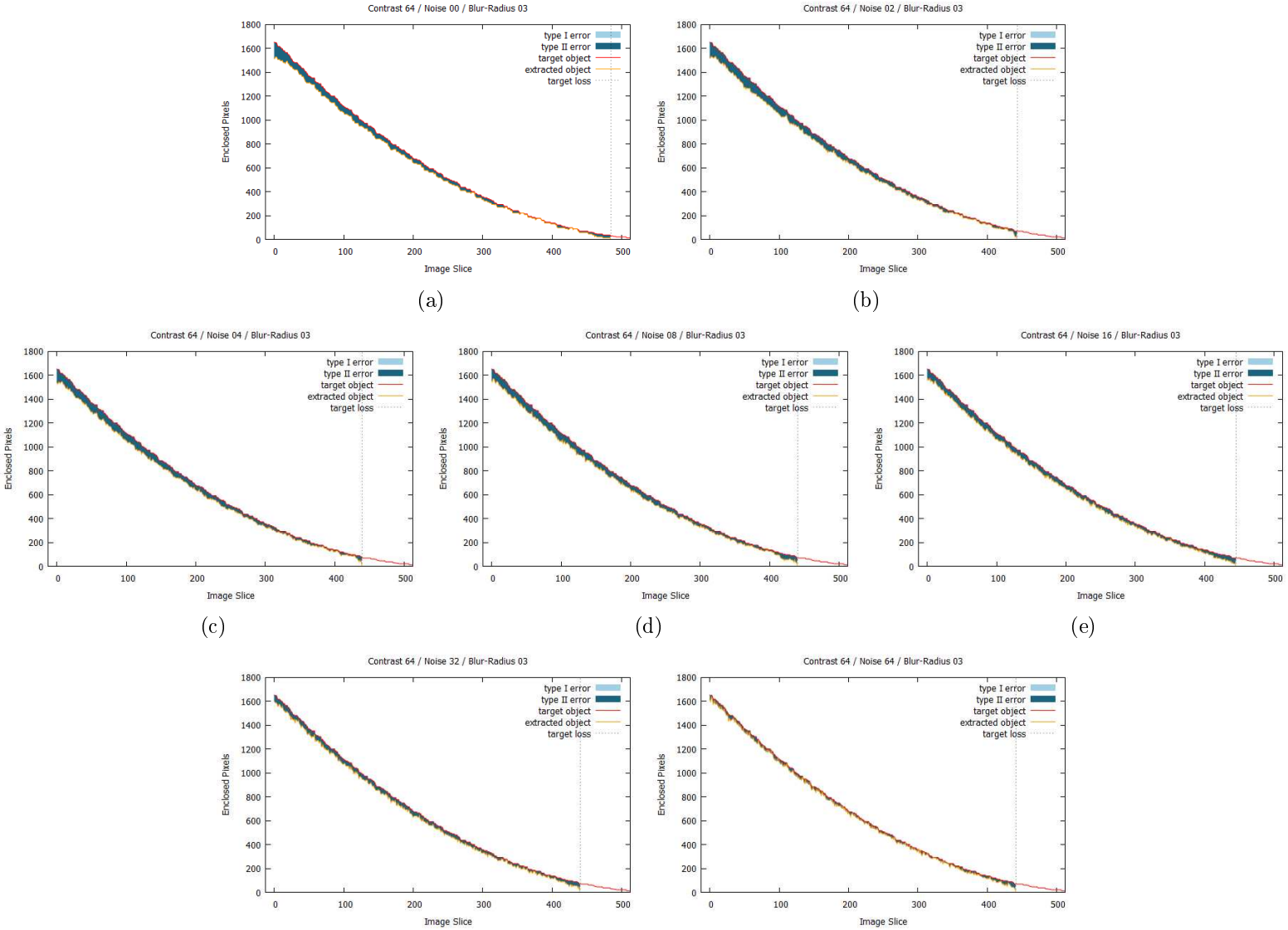

Figure 6.9: Extraction from artificially generated images with contrast = [64] and noise = [0,2,4,8,16,32,64]

ject. Images of high contrast and low noise can be successfully analysed using a wider range of parameters and thus are less restrictive, allowing the user to adjust and compensate for other sources of interference, such as scanning artefacts.

Another observation that can be made from figures 6.4-6.9, is that in the majority of cases, the extraction method tends to slightly underestimate the real object. A reason for that might be the presence of blur, since pixels that have been missed are only located at the object boundary. The interior of the extracted object is completely filled. The blur, as well as the curvature constraint used in the experiment, which causes small areas of the level set function to collapse, explain the loss of the target towards the end of the image stack.

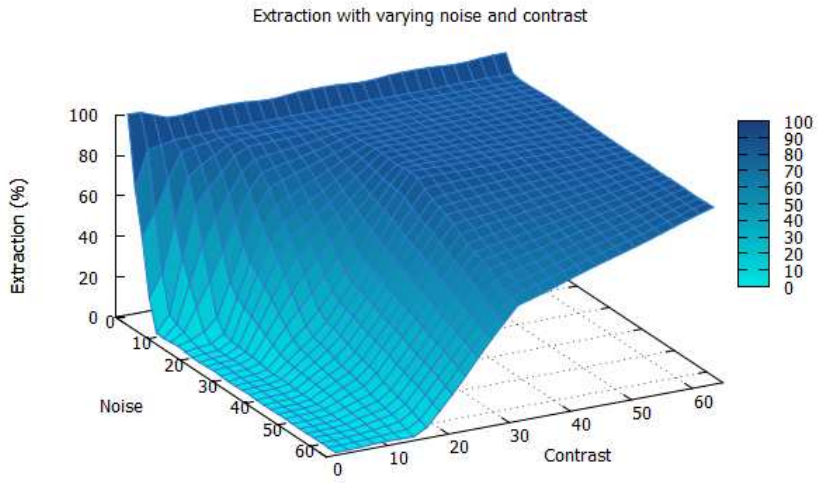

Figure 6.10: Extraction efficiency under varying contrast and noise levels

It should be noted that in the artificially generated data, even though the image characteristics have been designed to resemble real CT data, the object and its background have been highly simplified. They do not reflect the complexity and heterogeneity that is found in real images of plant roots embedded in soil. While in this experiment a cone shaped object was used as a test sample, we would ideally want to move from simple shapes to more

complicated structures that resemble the shape of complete root systems. This could be achieved with root simulation tools, such as SimRoot [Lynch, 2007], but at the time of writing such data was not available. A soil simulation tool could add the complexity to the background and as such making the artificial test data complete and, if made publically available, could serve as reference data to the community for future development of root recovery methods.

6.2 Root segments buried in soil

Artificially generated data allows verifiable interpretation of the extracted outcome, since the exact object is known. However, the data is often generally simplified and does not always reflect the full complexity of real data. To compensate for the simplification, in this experiment we assess the method on segments of the roots of real plants, which are placed in soil before imaging and image analysis. In the following sections we present the details of the experiment (6.2.1) and discuss the results obtained (6.2.2).

Sample	Voltage (keV)	Current (μA)	Projections	Exposure (ms)	Voxel (μm)
Segments 1-6	120	140	1,440	500	16.80
Segments 7-12	120	140	1,440	500	16.80
Plastic wire	120	140	1,440	500	16.80
Sample	Time (min)	Filter (mm)	Signal Average/Skip	Binning Mode	Distance (mm)
Segments 1-6	64	0.1 Cu	4x1	1x1	84.00
Segments 7-12	64	0.1 Cu	4x1	1x1	84.00
Plastic wire	64	0.1 Cu	4x1	1x1	84.00

Table 6.2: Scan parameters used for imaging root segments and plastic wire

6.2.1 Extracting root segments

Winter wheat Cordiale (*Triticumaestivum L.*) was grown in loamy sand for 10 days after germination before the plant was removed from the column.

Segments approximately 10mm long were cut from 12 randomly selected root branches and measured with a digital high-precision calliper that has an accuracy of approximately 10μm. The root segments were viewed under a dissecting microscope and their diameter measured by line counting on a Haemocytometer slide. The root segments were then buried in loamy sand, which had been air-dried and sieved to <2mm. Samples were watered from beneath with tap water, before being scanned under X-ray μCT (Nanotom (Phoenix X-ray / GE Measurement & Control Systems)). After the scan, all root segments were recovered from the soil and analysed again under the dissecting microscope, to check for deformation or breakage. Alongside the 12 root segments used in the experiment, a plastic wire was also buried in loamy sand, providing a non-root reference object. The samples were scanned with parameters listed in table 6.2 and extracted with the input parameters for the curvature constraint and the Jensen-Shannon divergence listed in table 6.3.

Sample	Curvature (α)	Jensen-Shannon (β)
Segments 1-6	0.392	0.368
Segments 7-12	0.392	0.368
Plastic wire	0.392	0.368

Table 6.3: Parameters used in the extraction process of root segments and plastic wire

6.2.2 Results and discussions

The root segments of the wheat plant were measured in length and diameter, from which the surface area and volume were estimated. For this calculation it was assumed that the roots were perfectly cylindrical. This might not always be the case in reality. Root measurement [Iyer-Pascuzzi et al., 2010] or modelling [Lynch et al., 1997] tools, however, often make the assumption that root systems are composed of multiple conical frustums, and hence that their cross-section is always circular with a given radius. For a short segment, that radius can be assumed to be constant, resulting in a cylinder. Table 6.4 shows the measured and calculated parameters of the test objects before and after the scan.

The root segments and plastic wire were extracted from the X-ray μCT images after the scan. The rendered data is shown in figure 6.11. To this

Sample	Radius (mm)	Surface area (mm^2)	Volume (mm^3)
before scanning			
Segment 1	0.3000	19.4150	2.8274
Segment 2	0.3062	19.8315	2.9465
Segment 3	0.3125	20.2485	3.0680
Segment 4	0.3312	21.5025	3.4472
Segment 5	0.3000	19.4150	2.8274
Segment 6	0.3187	20.6660	3.1919
Segment 7	0.3000	19.4150	2.8274
Segment 8	0.2937	18.9990	2.7109
Segment 9	0.2750	17.7539	2.3758
Segment 10	0.3000	19.4150	2.8274
Segment 11	0.2812	18.1685	2.4850
Segment 12	0.2500	16.1007	1.9635
after scanning			
Segment 1	0.3125	20.2485	3.0680
Segment 2	0.3125	20.2485	3.0680
Segment 3	0.3062	19.8315	2.9465
Segment 4	0.3187	20.6660	3.1919
Segment 5	0.3125	20.2485	3.0680
Segment 6	0.3062	19.8315	2.9465
Segment 7	0.2875	18.5835	2.5967
Segment 8	0.3062	19.8315	2.9465
Segment 9	0.2875	18.5835	2.5967
Segment 10	0.2875	18.5835	2.5967
Segment 11	0.2875	18.5835	2.5967
Segment 12	0.2625	16.9263	2.1648
non-root reference object			
Plastic wire	0.6650	44.5618	13.8929

Table 6.4: Measured parameters of root segments before and after the scan

data we applied the measurement tool, presented in chapter 5, to determine their surface area and volume, which are shown in table 6.5.

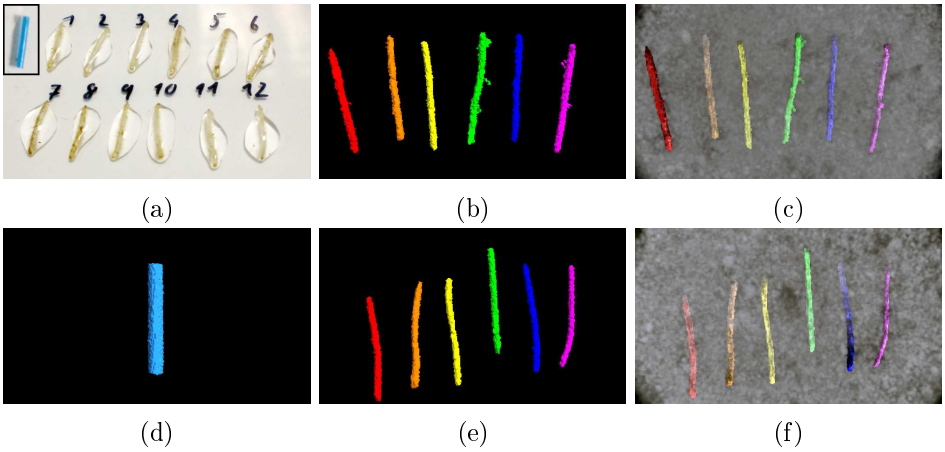

Figure 6.11: (a) Root segments on a Petri dish, (b-c) root segments 1-6, (e-f) root segments 7-12 and (d) plastic wire extracted from the CT data

The measured values obtained with the microscope, before and after the scan, are used to calculate the average surface area and volume for each root segment. Based on these numbers, we obtain a mean error in surface area of 12.9 percent and volume of 10.4 percent. Figure 6.12 shows the measured results in comparison. Because roots are easily deformable they might respond to the pressure that they experience while being buried in soil, whereas no force is applied when they are exposed to the air. Roots are able to store a large amount of water but at the same time dry out very quickly if kept in the air for too long. To prevent the root segments drying out, they were covered with a thin layer of water in the time between being measured under the microscope and buried in the soil (figure 6.11). However, while the root segments were viewed under the microscope, they had to be removed from the water. It would have made the measurement difficult if the roots were kept in water due to the many root hairs becoming visible and blurring the edges of the root in the image. It is not known whether the water content in the root segments remained constant while segments were viewed under the microscope and imaged with X-ray μCT. These circumstances might have caused variations in the physical shape of the root during the experiment and led to errors in measurements. Roots under the microscope were measured only at their ends. The entire root

Sample	Surface area (mm^2)	Volume(mm^3)
Segment 1	22.6147	2.6144
Segment 2	23.5022	2.8229
Segment 3	21.7491	2.7134
Segment 4	30.8885	3.3708
Segment 5	22.3320	2.6858
Segment 6	23.9120	2.6929
Segment 7	20.0776	2.4189
Segment 8	23.2115	2.9229
Segment 9	21.6120	2.6531
Segment 10	21.4292	2.4713
Segment 11	19.7598	2.1212
Segment 12	15.5715	1.4493
Plastic wire	50.8871	13.9404

Table 6.5: Measured parameters of root segments from the extracted data

segment would not fit within the field of view without sacrificing the high magnification which is crucial in determining the root diameter.

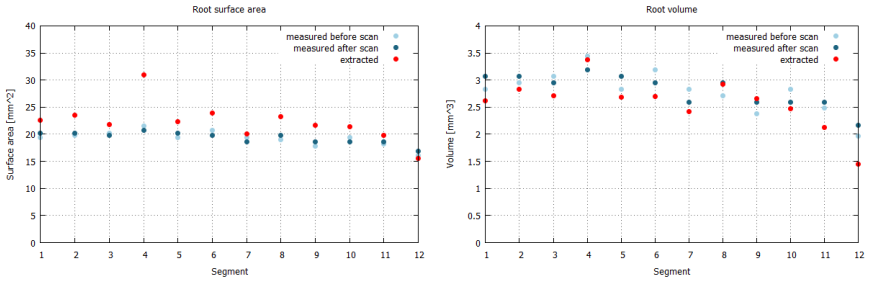

(a) (b)

Figure 6.12: Measured root segments before and after the scan compared to the objects extracted from the image data: (a) Surface area and (b) Volume

The acceptability of the error in measurement under the different circumstances in which the analysis was performed is debateable. However, there is a strong correlation between the two groups, which means that the results obtained under the same conditions are representative of the samples. The Pearson's product moment correlation coefficient between the measured and

extracted data are $r_{area} = 0.8683$ and $r_{volume} = 0.8909$ for the measurements of surface area and volume respectively, with a p-value of 0.0002 and 0.0001 based on Fisher's Z transform. The paired Wilcoxon signed rank test gives a p-value of 0.0009 and 0.0068 for the two datasets.

6.3 Plant root systems washed free from soil

In this section we move from the extraction of root segments to description of complete plant root systems and apply the method to the type of datasets for which it was designed. Root segments, while representing real material within a real environment, have very simplified geometrical and topological structures. There is no branching, change in size or direction present, which makes tracking them through a few cross-sectional image slices a comparatively simple task. Complete root systems are far more complex and in order to assess the ability of the presented method to recover them from X-ray μCT image data, we conducted an experiment in which different plant species grown in two different soil textural types were prepared for analysis. After X-ray CT analysis the plants are root-washed free of soil, imaged on a flatbed scanner and root descriptions extracted from the grey level images using standard commercial software (WinRhizo, version 2002c). The results of this traditional analysis method are used to determine the efficiency of the proposed X-ray segmentation method in extracting plant root systems. In the following sections we describe in detail the condition and steps of the experiment (6.3.1) and discuss the correlation between the root systems extracted from the X-ray μCT image data to the actual plant root systems recovered from the soil cores (6.3.2).

6.3.1 Extracting plant root systems

The image data used in this experiment is the data acquired from the root systems of maize, wheat and tomato as described in chapter 3. The samples were scanned with the parameter settings listed in table 6.6. The image stacks were processed using the proposed tracking method with the extension mechanism for plagiotropic roots enabled using the same parameters for controlling the curvature constraint and the Jensen-Shannon divergence as

in the previous chapters 3 and 4.

Sample	Voltage (keV)	Current (μA)	Projections	Exposure (ms)	Voxel (μm)
Maize 1-4	120	120	1,200	750	48.48
Wheat 1-4	120	250	1,200	750	25.00
Tomato 1-4	120	250	1,200	750	25.00
Sample	Time (min)	Filter (mm)	Signal Average/Skip	Binning Mode	Distance (mm)
Maize 1-4	75	0.1 Cu	4x1	2x2	160
Wheat 1-4	67	0.1 Cu	3x1	1x1	200
Tomato 1-4	67	0.1 Cu	3x1	1x1	200

Table 6.6: Scan parameters used for imaging plant root systems

After the plants were scanned with X-ray μCT, they were removed from the columns and washed free of soil. In doing so, the three-dimensional structure of the root system is lost, but soil removal allows two-dimensional analysis of the root system with other tools such as WinRhizo (version 2002c). WinRhizo is a popular and widely used tool in plant root studies, a de facto standard [Bouma et al., 2000; Himmelbauer et al., 2004], which is why it is used here. The roots were placed on a water tray and scanned with a flatbed scanner at 400dpi. The images were analysed using WinRhizo's automatic thresholding for normal roots, ignoring speckles that had an area less than $2mm^2$.

6.3.2 Results and discussions

The root systems extracted from the X-ray μCT image data are compared to the root-washed images quantified using the WinRhizo tool. Both set of images are shown in figure 6.13-6.15, with the thresholded and skeletonised architecture of the root system highlighted in colour. The measured surface area and volume reported by each method are listed in table 6.7.

Figures 6.16-6.18 show the plotted surface area and volume for each sample. The average error in surface area and volume are 19.6 percent and 39.1

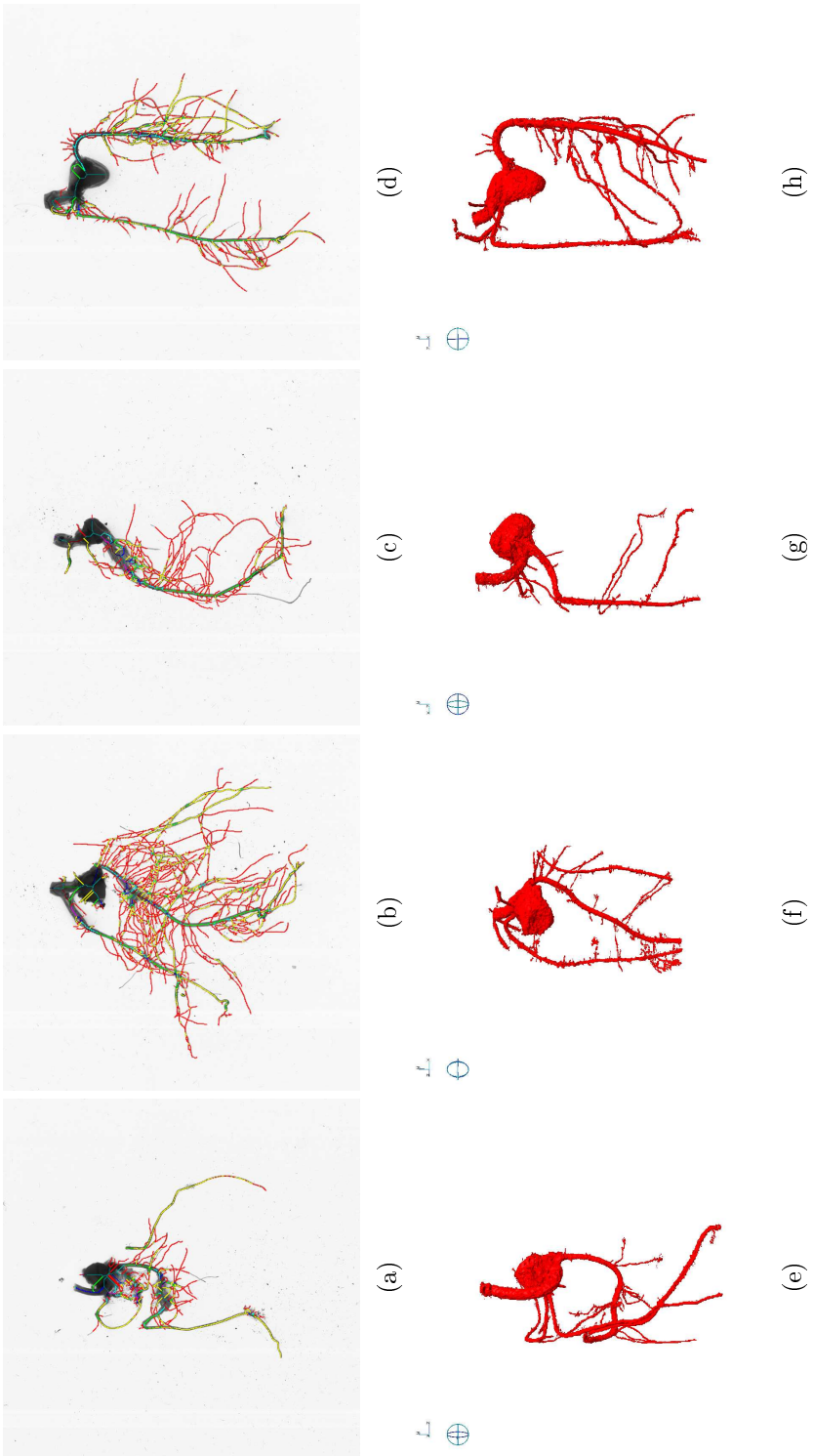

Figure 6.13: Root systems of maize 1-4 (a-d) analysed with WinRhizo and (e-h) extracted from X-ray μCT data

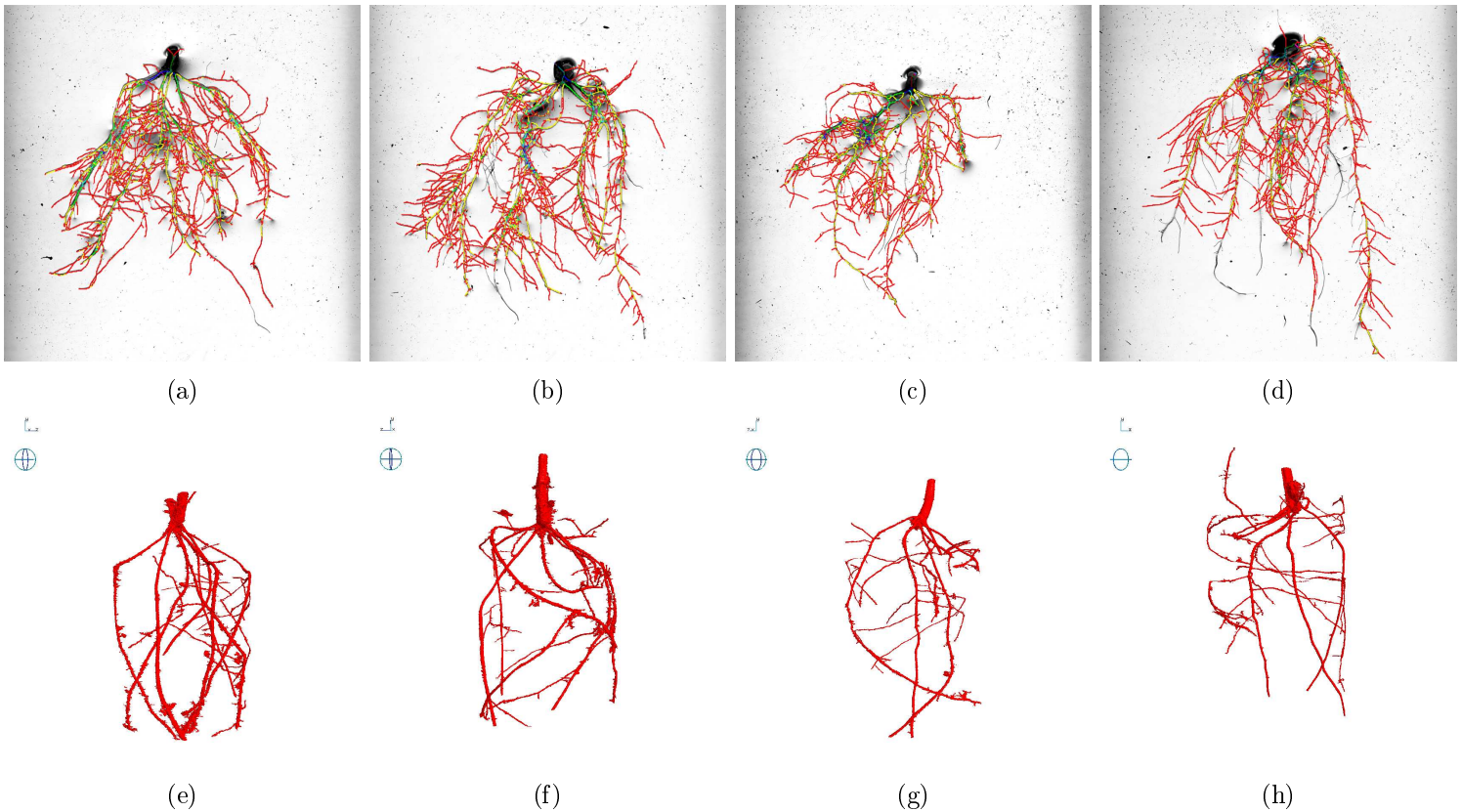

Figure 6.14: Root systems of wheat 1-4 (a-d) analysed with WinRhizo and (e-h) extracted from X-ray μCT data

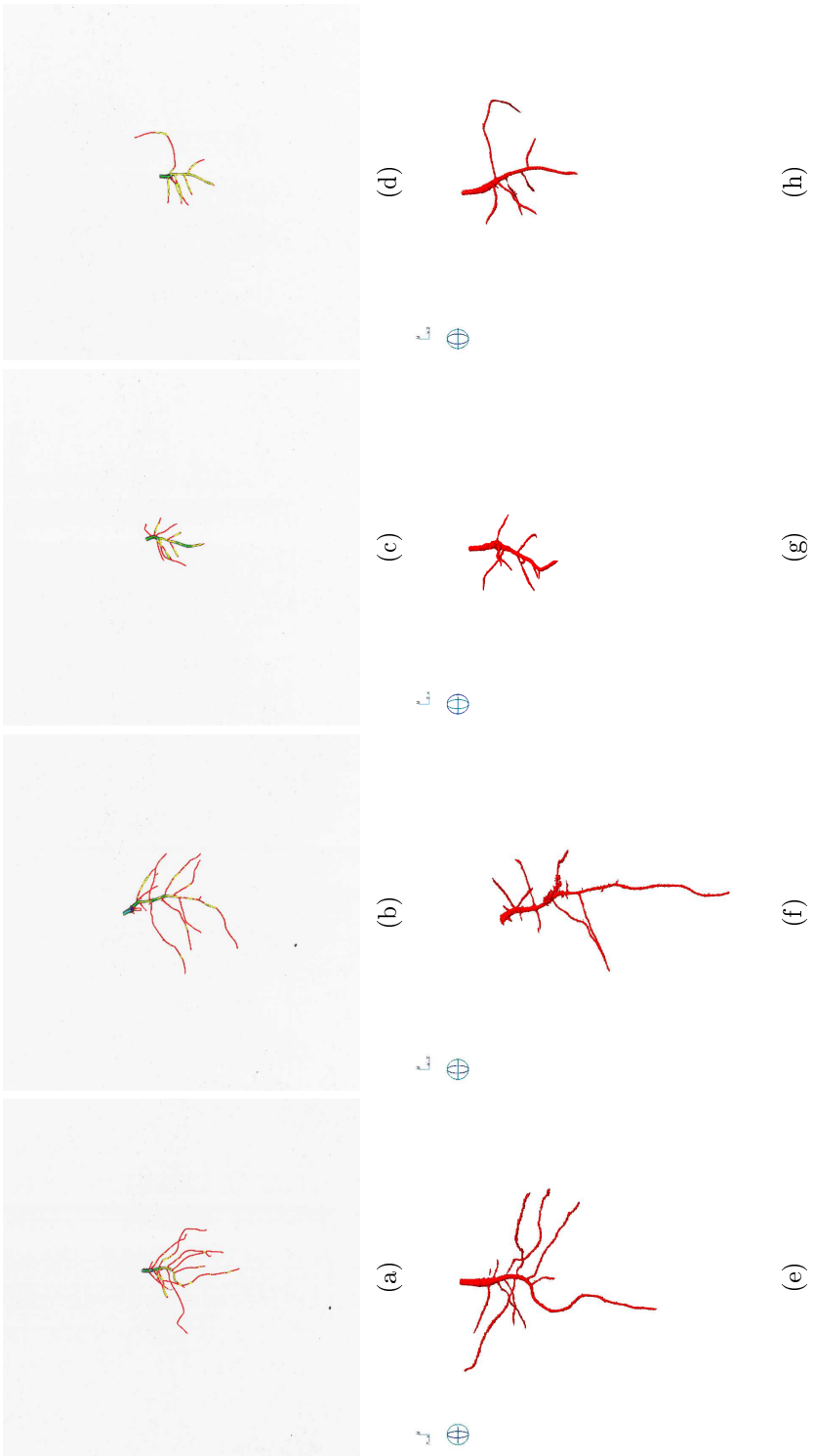

Figure 6.15: Root systems of tomato 1-4 (a-d) analysed with WinRhizo and (e-h) extracted from X-ray μCT data

Sample	WinRhizo		X-ray μCT	
	Area (mm^2)	Volume (mm^3)	Area (mm^2)	Volume (mm^3)
Maize 1	1,528.8	389.0	1,849.7	464.4
Maize 2	3,850.0	558.0	2,087.7	589.8
Maize 3	1,653.3	279.0	1,724.4	504.5
Maize 4	2,575.3	481.0	2,386.0	725.6
Wheat 1	3,524.4	411.0	1,831.2	184.0
Wheat 2	3,726.6	405.0	1,827.4	198.9
Wheat 3	2,459.1	281.0	1,003.5	106.4
Wheat 4	2,865.3	280.0	1,188.3	118.3
Tomato 1	254.7	28.0	242.3	24.2
Tomato 2	284.5	33.0	257.4	26.5
Tomato 3	126.1	18.0	143.0	18.3
Tomato 4	155.0	22.0	141.7	16.8

Table 6.7: Measured root system traits from WinRhizo images and X-ray μCT extracted data

percent for maize, 54.1 percent and 56.5 percent for wheat and 9.0 percent and 14.0 percent for tomato. The Pearson's product moment correlation coefficient between WinRhizo and the data extracted from X-ray μCT images are $r_{area} = 0.5670$ and $r_{volume} = 0.5924$ with a p-value of 0.433 and 0.4076 for maize, $r_{area} = 0.9831$ and $r_{volume} = 0.9802$ with a p-value of 0.0168 and 0.0197 for wheat, and $r_{area} = 0.9847$ and $r_{volume} = 0.9209$ with a p-value of 0.0152 and 0.079 for tomato. The p-values were calculated based on Fisher's Z transform. Care should be taken in drawing conclusions from the significance of the statistical test, due to the small sample size.

The best results were obtained from the tomato samples, which yielded the smallest error and a high correlation. The root system of the tomato is the least complex among all the samples, with only a few lateral roots. Relatively good data was also obtained from the maize samples, although the mean error is slightly increased and the results are not as well correlated as the measured traits from the other samples. Maize 2 showed a large error in surface area, which is very likely due to the high number of fine

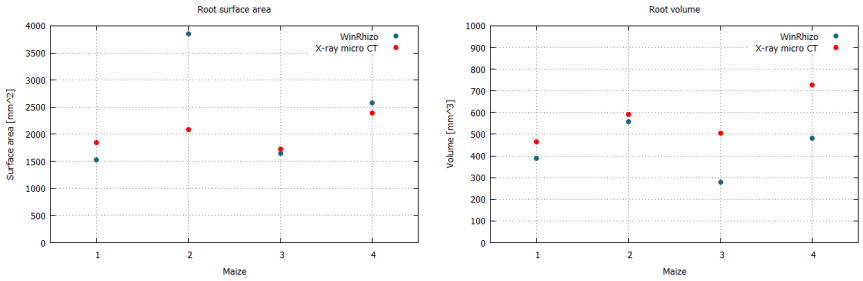

(a) (b)

Figure 6.16: (a) Surface area and (b) Volume of maize 1-4 obtained with WinRhizo and X-ray μCT

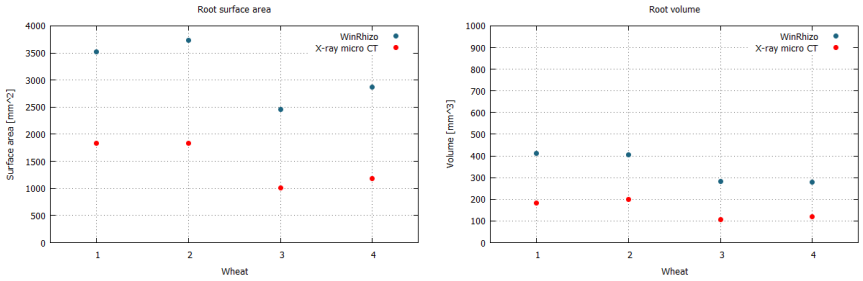

(a) (b)

Figure 6.17: (a) Surface area and (b) Volume of wheat 1-4 obtained with WinRhizo and X-ray μCT

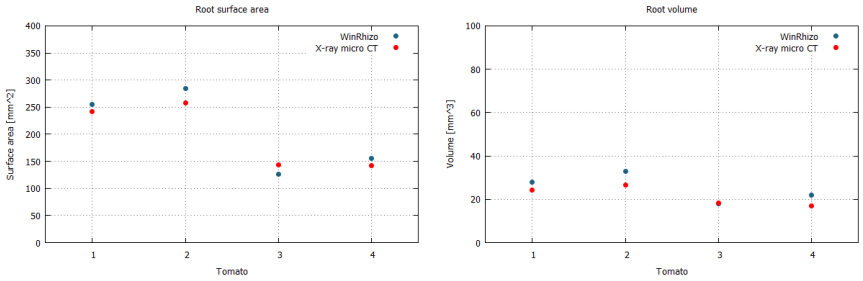

(a) (b)

Figure 6.18: (a) Surface area and (b) Volume of tomato 1-4 obtained with WinRhizo and X-ray μCT

lateral roots that were not present in the other maize plants, and have been missed during the extraction process. It should be noted that the maize plants have been scanned at a lower resolution than the tomato and wheat samples. Roots can only be extracted from the data if they are large enough to be visible in the cross-sectional images that are processed. The main root architecture, however, has been fully recovered as shown in figure 6.13. Surface area and volume measurements recovered from the wheat samples are largely underestimated. The extraction of the many fine later roots proved to be problematic, though the primary roots have been successfully recovered. This is clearly shown in figure 6.14. However, it should be noted that the exact surface area and volume of the root systems are unknown. WinRhizo estimates the parameter from two-dimensional image data and might overestimate traits, especially if roots cross and overlap. From figure 6.14(a-d) it can be observed that some roots, located close to each other, are treated as a single thick root instead of separate roots. Therefore the true value might be somewhere in between. No difference in extraction efficiency was observed between the two soil textural types; loamy sand and clay loam.

6.4 Comparison to other extraction techniques

In the previous section we demonstrated the presented techniques' ability to recover the structure of plant root systems from X-ray μCT data. In this section we revisit the X-ray μCT image data collected from the plant samples in the previous experiment and extract the root system using alternative techniques similar to methods presented in the literature. Because none of the tools are publically available, and published descriptions lack the detail needed for a complete re-implementation, several assumptions had to be made, but the methods were implemented to our best knowledge and ability. The results are used to evaluate how the proposed extraction technique performs in comparison to other extraction strategies and to identify potential weaknesses and strengths. In section 6.4.1 we describe the details of the techniques used for comparison and discuss the outcome in section 6.4.2.

6.4.1 Details of the extraction techniques

The first method used in this experiment is similar to the method described in [Heeraman et al., 1997], which takes a statistical classification approach. The method is initialised by manually selecting 20 points for each group of components. Here we choose three different groups representing air, soil and root material, as in [Heeraman et al., 1997]. These groups are tested for normality using the Kolmogorov-Smirnov Goodness-of-Fit test. For each of the components the mean and standard deviation are calculated and its 95 percent confidence interval determined. The volumetric dataset is then examined. Each voxel is compared to Gaussian distributions formed using each of the groups' calculated mean and standard deviations as parameters. The probability of a given voxel being generated by each Gaussian is determined and the voxel assigned to the component with highest probability. If a voxel does not fall within any of the determined confidence intervals, then the value is ignored and not assigned to any component. In this experiment we are interested in the root material component and hence we use that group for comparison to our presented method.

The second method that we use in this experiment is a region growing based technique similar to that presented by [Perret et al., 2007], who used thresholding along with a 26-neighbour connectivity constraint, starting from the plant seed, to achieve the same goal. Related to this technique is the method in [Lontoc-Roy et al., 2005, 2006], in which manual thresholding is used to extract the large root fragments before an iterative region growing technique, based on a second threshold boundary, is applied to extract finer root fractions. It is not clear whether root regions are hand selected prior to applying the region growing technique or whether any region after the first step is used for further processing. The former approach would lead to a similar result to the techniques developed here, in that the region growing process is started from selected seed points. In this experiment we use 20 seed points that are manually selected throughout the volumetric data, placed within regions that belong to the root system. These seed points define the initial location from which the process starts, but are also used to define the overall threshold boundaries. Seed points are therefore selected to include a range of different values that are taken from bright as well as dark root segments. For the region growing segmentation method a 6-neighbour

connectivity is used, which is different from that in [Perret et al., 2007], where a 26-neighbour connectivity was applied. However, the image data that we use has a much higher resolution and therefore we believe that small roots are still detectable even though a lower connectivity is used. The advantage on the other hand is that less non-root material is included in the extracted data.

6.4.2 Results and discussions

The image stacks obtained from maize, wheat and tomato grown in the two soil textures loamy sand and clay loam, have been used as samples to evaluate alternative strategies. The results are shown in figure 6.19-6.21. Due to the weak performance of the alternative methods, measured surface area and volume are not analysed, since no data were obtained that would allow a meaningful comparison.

Though region growing ensures connectivity, the rendered images shown in figure 6.19-6.21(e-h) appear to contain particles floating in the air, and not connected to the root system. This visual appearance is an artefact of the low resolution of the volume rendering process. In reality, all the marked voxels are connected. From the rendered extractions it can be observed that in general region growing performed better than the voxel classification strategy, for which the best results were obtained from the maize samples. One reason for this might be the lower resolution of the imaging process. It should be noted that in both studies, where similar approaches have been applied [Heeraman et al., 1997; Lontoc-Roy et al., 2006; Perret et al., 2007], the resolution of the scans were much coarser at a voxel size of $0.16\times0.16\times0.20$mm, $0.12\times0.12\times0.1$mm and $0.275\times0.275\times1.0$mm respectively, compared to the maize ($0.04848\times0.4848\times0.04848$mm), and wheat and tomato ($0.025\times0.025\times0.025$mm) used in this study. Apart from root objects, the other objects included in the segmented data were outlines along cracks, as shown in figure 6.22. For image data with lower resolution, this might become a minor issue. When looking at the extraction of the root system, such as in figure 6.19 showing the maize plants, the number of roots recovered is still relatively low compared to the root system extracted with the method proposed here. The reason is the stiffness and static behaviour of these methods, which have difficulties coping with the dynamic change of greyscale intensities in root objects.

Figure 6.19: Root systems of maize 1-4 extracted from X-ray μCT data using (a-d) statistical classification, (e-h) region growing and (i-l) tracking based strategy

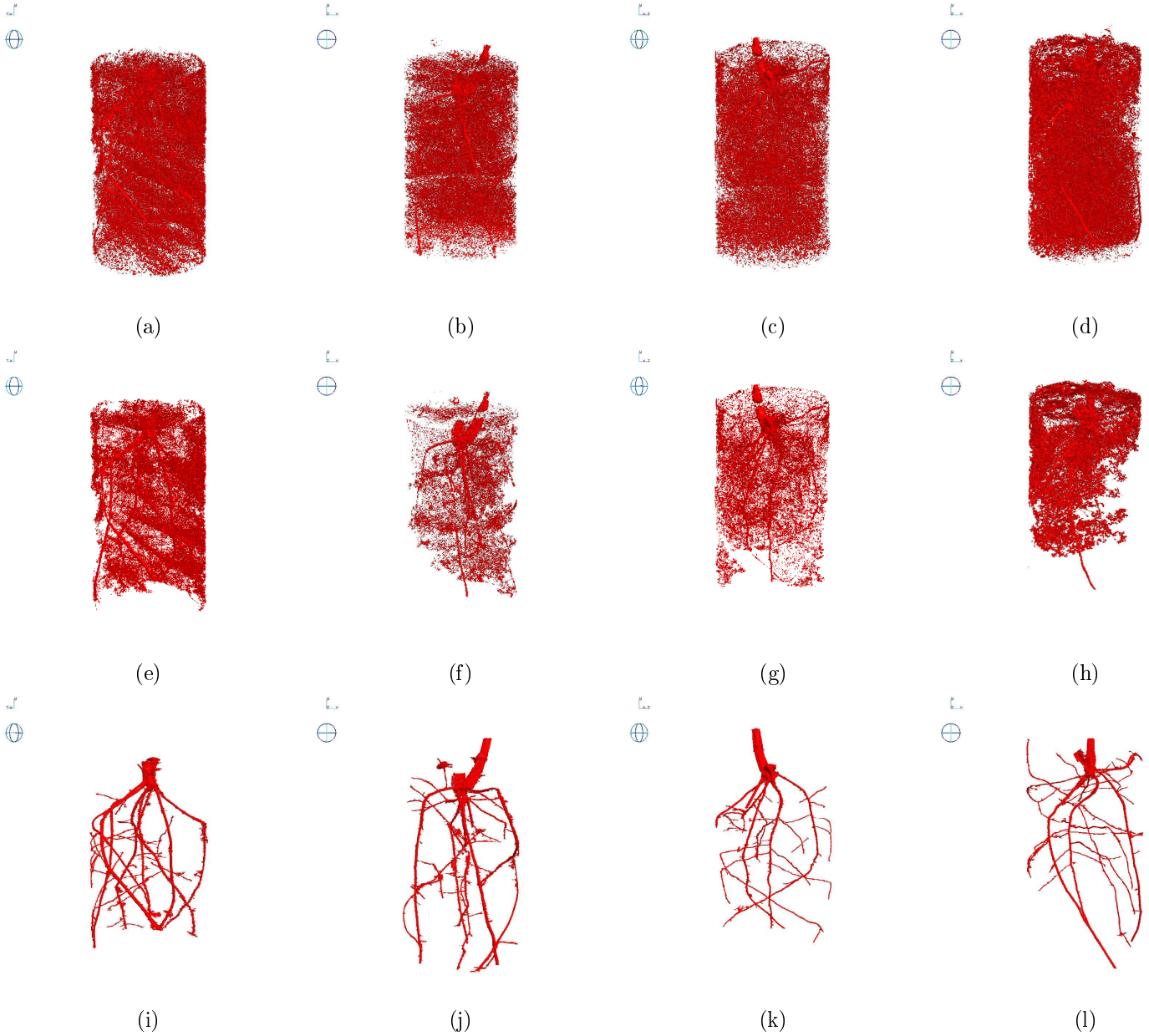

Figure 6.20: Root systems of wheat 1-4 extracted from X-ray μCT data using (a-d) statistical classification, (e-h) region growing and (i-l) tracking based strategy

Figure 6.21: Root systems of tomato 1-4 extracted from X-ray μCT data using (a-d) statistical classification, (e-h) region growing and (i-l) tracking based strategy

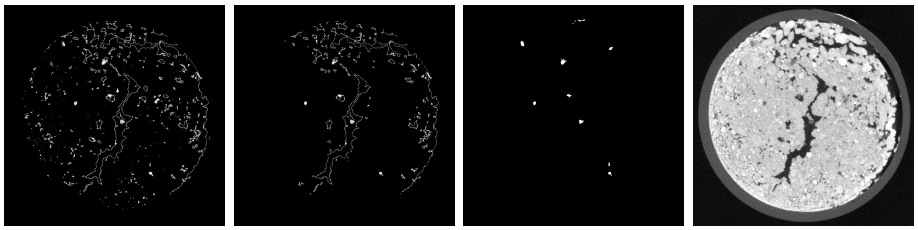

(a) (b) (c) (d)

Figure 6.22: Cross-sectional slice (wheat 3) of extracted data obtained with (a) classification, (b) region growing and (c) tracking method, alongside (d) the X-ray μCT cross-section

While the region growing strategy extracted less non-root material, the voxel classification approach was more successful in recovering root material (figure 6.22). One reason for that was that the voxel classification method is not limited to keeping the root system connected and therefore found more partial root segments. This is useful if only the root system mass is of interest, but at the same time makes it difficult to derive any architectural and structural traits. Both methods require a number of seed points to be selected, which determine the overall process, defining the threshold boundary or finding sample distributions that are used for further classification. Especially for the latter it is difficult to select seed points for each component which form a Gaussian distribution. Non-parametric tests that do not make an assumption about the distribution of sample points, might be more suitable. Also, in this experiment, only three distinguishing components were used, as in [Heeraman et al., 1997]; air, soil and root material. Including additional components, such as water and minerals, might have improved the outcome. However, it is not aim of this study to modify and improve other strategies, but to implement their methods as accurately as possible. Only a few simple and reasonable changes have been made, such as the neighbourhood connectivity, which was changed from 26 used in [Perret et al., 2007] to 6, since both selected neighbourhood values lead to a similar amount of extracted roots, but noticeably less non-root material was included when only a 6-neighbourhood constraint was applied.

The extraction technique proposed in this thesis has not been compared to methods developed outside the field of soil-root studies. It is not clear, for instance, if applications designed for medical images are suitable for the extraction of plant root systems in soil. Even though medical images taken

with X-ray CT might have similar characteristics and artefacts, the scanned object, image resolution, as well as the scanner device, however, differ from those used in plant sciences. We therefore focused on techniques that have been designed specifically for the purpose of extracting roots from soil.

6.5 Summary

The presented method was tested and evaluated in a number of experiments, which range from artificially generated data to root segments buried in soil up to the extraction of complete root systems of real plants. The experiment with artificially generated data showed that small objects can be extracted from qualitatively good images, but becomes more difficult as the image quality decreases. The ability to extract information from the image data depends on the tracker parameters, which dictate the behaviour of the process and can be critical under poor image conditions. Qualitatively good image data allows roots to be successfully extracted using a wider range of initial parameters.

The artificially generated test object, however, was fairly simple and thus easier to extract than real roots embedded in soil, where the image data is much more heterogeneous and complex. That the presented technique can also deal with real plant roots was shown in the experiments that followed. Both root segments and complete root systems were extracted successfully. The method was tested on root system architectures of monocot and dicot plants growing in two different soil textural types that represent a large portion of United Kingdom's soil. This shows that the technique can not only be applied to a specific plant or root architecture, but is able to cope with different situations. Difficulty arises when there are many fine lateral roots, which might remain undetected, especially when imaged at lower resolutions. Increasing the resolution implies also scaling down the size of the sample, which then limits the space available for the root system to explore.

Evaluation of the extraction accuracy is a difficult task, since ground truth data is either not available or is not entirely representative of real data samples. Data can be artificially generated to allow a precise determination of missed or incorrectly classified voxels, but are less representative of real plants grown in soil. Extracted root systems can be compared to excavated plants, by measuring characteristics such as volume or surface area, which

are often estimated from other parameters and fail to completely describe the structural complexity. Application of a number of different evaluation procedures both reduces bias and increases the reliability of the conclusions drawn.

In the following chapter (chapter 7) we discuss the extraction of multiple interacting root systems, extending the method with multiple trackers and a collision detection mechanism to keep track of which root belongs to which plant.

Chapter 7

Extraction of multiple interacting root systems

Plants use their root systems to explore the environment for water and nutrient sources which, in the open field, are shared with other neighbouring plants. Especially situations where these resources are scarce, plants will have to compete for their survival. Researchers have strived for decades to understand the degree of belowground competition among plants [Casper and Jackson, 1997; Rubio et al., 2001; Maina et al., 2002] and to discover if there exists any form of communication between root systems that allows them to grow in harmony and make the best use of limited amount of resources [Mahall and Callaway, 1992; Fang et al., 2013]. This is of particular interest for intercrop cultivation, to find the optimal combination of plants for a certain field environment, which in turn can have a large effect on crop yield [Mead and Willey, 1980; Willey, 1985; Anil et al., 1998].

In the present context, this means that if multiple plants are grown within the same soil column, their roots need to be distinguished from each other while at the same time being separated from the background. While it is straightforward to apply separate tracking processes to individual plant root systems, difficulty arises when two or more tracked root sections collide, which is the case when roots come into contact with each other. That such an event is possible has been demonstrated by the experiment described in chapter 4, where roots from the same plant were seen to touch each other. For a single plant, this is not really an issue, since it does not affect the extraction of the root system as such. However, when multiple root systems

are present it is important to keep track of which root belongs to which plant so that correct conclusions can be drawn from the measured data. The extraction method introduced in the previous chapters looks for root material only, and does not make any distinction among different plants. In this chapter we seek a solution to the extraction of multiple root systems.

The problem of interacting targets is a widespread feature of multiple target tracking and an actively discussed topic in computer vision [Khan et al., 2005]. The task is complicated with targets of identical appearance. Whatever the form of model is, similar targets will always be tracked with the same model. If targets interact, each tracker will tend to lock on the target that best fits the model. This can result in trackers swapping targets or trackers following the same target while losing track of others.

In section 7.1 we briefly describe how a single tracker is expanded to multiple trackers for a number of different targets. As the roots of different plants may have identical density and so grey level distributions, particularly if they are of the same species, our proposed solution relies on measures of the shape of root sections. We therefore describe a method for shape registration in section 7.2. In section 7.3 we address the issue of object collision and present a method which keeps two or more individual targets separated. The proposed solution is applied to a number of plant samples and the results obtained presented and discussed in section 7.4.

7.1 Multiple level sets

Given the approach adopted here, extraction of multiple root systems requires tracking of multiple targets (which may of course split as roots branch). This in turn requires multiple instantiations of the proposed level set technique to be active together. The level set method was initially developed to evolve the interface of a single front, based solely on its velocity along surface normals [Osher and Sethian, 1988; Sethian, 1999]. This has been extended by simulating the flow of two-phase fluids [Sussman et al., 1994, 1999]. Here the interface is affected by the physics on both sides, but the area remained divided into two regions; inside and outside. Other variations of the level set methods have been developed that overcame that limitation, allowing the simulation of the complex interaction of more than two fluids [Merriman et al., 1994; Sethian, 1994; Losasso et al., 2006].

In this work we adapt the solution defined in [Sethian, 1994], where multiple level set functions are evolved simultaneously. This or similar approaches have been established as a popular technique in computer vision, such as the segmentation of greyscale and colour images into multiple distinguishable regions [Vese and Chan, 2002]. The method enjoys the advantages of simplicity and efficiency, but lacks the high precision required in many physics-based application [Losasso et al., 2006].

Let Φ_A^t and Φ_B^t be two level set functions occupying two different regions at time step n. The level set functions are evolved based on a defined speed function, resulting in a temporary state of Φ_A^* and Φ_B^*. Φ_A^* and Φ_B^* are then combined to obtain the level set function Φ_A^{t+1} and Φ_B^{t+1} at time step $t+1$. The combination of the temporary level set functions depends on whether or not the interface of A can penetrate the interface of B, or vice versa. Assuming that A can penetrate B, but B cannot penetrate A, then the new level set function at time step $t+1$ will be updated accordingly

$$\begin{aligned} \Phi_A^{t+1} &= \Phi_A^* \\ \Phi_B^{t+1} &= \max\left(\Phi_B^*, -\Phi_A^*\right) \end{aligned} \tag{7.1}$$

Rules can also be defined such that during an encounter of two level set fronts, neither is allowed to penetrate the other. This will stop them from advancing further and give an exact partition of the two regions at the front of collision. The mechanism of multiple fronts can be easily extended to any number of level set functions using the same principles of combination. In that case, each evolving front in the set must be compared to all other level set function of the same set. Figure 7.1 shows three different scenarios where two level set functions (front A (red) and front B (orange)) are evolved until their fronts interact with each other, at which point different combination rules are applied. This is a key element in the extraction of multiple interacting root systems, but not sufficient enough. While the combination rules of different level set function allows individual trackers to be separated, the true boundary between touching root sections remains unknown. Therefore, although level set functions can penetrate each other's interface, there is no definition given yet, when these are to be applied. For this, shape information is used in estimating the boundary of root objects and thus to find the intersecting front in between.

Figure 7.1: Two level set function A (red) and B (orange) interacting with each other, where (a) front A penetrates front B, (b) front B penetrates front A and (c) neither A or B is penetrated

7.2 Iterative closest point

The iterative closest point (ICP) algorithm is a technique that allows the registration of two point clouds [Besl and McKay, 1992]. Given a set of points, the aim is to find the rotation and translation matrix that aligns the data to a predefined model, which also takes the form of a point cloud. Registration techniques aim at overlaying images often taken at different times or camera perspectives, for the purpose of change detection or time-series analysis, but also for target matching in which the shape of a known target is sought to be matched to an object in an image [Zitová and Flusser, 2003]. Here, we use registration for aligning the shape of a root section to a targeted object within the tracking process, to be precise, in dealing with object collisions. Detailed information is given in the following section (section 7.3). In this section we describe the ICP algorithm, following the notation presented in [Besl and McKay, 1992].

Let $U = \{\vec{u}_i = (x_i \quad y_i \quad z_i \quad 1) | i = 1..N_u\}$ be a set of data points and $V = \{\vec{v}_i = (x_i \quad y_i \quad z_i \quad 1) | i = 1..N_v\}$ be the points of a given model. For simplicity, let N_u be equal to N_v. The rotation matrix $\mathbf{R}$ and the translation matrix $\mathbf{T}$ are sought, to minimise the root mean square distance between model and data

$$\frac{1}{N_u}\sum_{i=1}^{N_u}\|\vec{v}_i - \mathbf{TR}\vec{u}_i\| \tag{7.2}$$

This is achieved using a quaternion-based least square method [Horn, 1987]. First, the centres of mass $\vec{\mu_u}$ and $\vec{\mu_v}$ of the two point clouds are calculated

$$\begin{aligned}\vec{\mu_u} &= \frac{1}{N_u}\sum_{i=1}^{N_u}\vec{u}_i \\ \vec{\mu_v} &= \frac{1}{N_v}\sum_{i=1}^{N_v}\vec{v}_i\end{aligned} \tag{7.3}$$

and used to determine the cross-covariance matrix cov_{uv} for U and V.

$$cov_{uv} = \frac{1}{N_u}\sum_{i=1}^{N_u}[(\vec{u}_i - \vec{\mu_u})(\vec{v}_i - \vec{\mu_v})^\intercal] \tag{7.4}$$

This results in a matrix $\mathbf{A} = cov_{uv} - cov_{uv}^{\intercal}$ from which the cyclic components are taken to form the vector $\vec{a} = (A_{23}, A_{31}, A_{12})$ that is used to generate the matrix

$$\mathbf{Q}_{4\times4} = \begin{pmatrix} tr(cov_{uv}) & \vec{a}^{\intercal} \\ \vec{a} & cov_{uv} + cov_{uv}^{\intercal} - tr(cov_{uv})\mathbf{I}_3 \end{pmatrix} \tag{7.5}$$

The eigenvector $\vec{r} = (q_1 \quad q_2 \quad q_3 \quad q_4)$ of the matrix $\mathbf{Q}$ with the maximum eigenvalue is used to define the rotation matrix $\mathbf{R}$

$$\mathbf{R} = \begin{pmatrix} q_1^2 + q_2^2 - q_3^2 - q_4^2 & 2(q_2q_3 - q_1q_4) & 2(q_2q_4 + q_1q_3) & 0 \\ 2(q_2q_3 + q_1q_4) & q_1^2 + q_3^2 - q_2^2 - q_4^2 & 2(q_3q_4 - q_1q_2) & 0 \\ 2(q_2q_4 - q_1q_3) & 2(q_3q_4 + q_1q_2) & q_1^2 + q_4^2 - q_2^2 - q_3^2 & 0 \\ 0 & 0 & 0 & 1 \end{pmatrix} \tag{7.6}$$

The vector $\vec{t} = (\vec{\mu_v} - \mathbf{R}\vec{\mu_u})$ is used to define the translation matrix $\mathbf{T}$

$$\mathbf{T} = \begin{pmatrix} 1 & 0 & 0 & t_1 \\ 0 & 1 & 0 & t_2 \\ 0 & 0 & 1 & t_3 \\ 0 & 0 & 0 & 1 \end{pmatrix} \tag{7.7}$$

The ICP algorithm for registering two sets of point clouds is an iterative process seeking a good alignment by converging to the nearest local minimum. To find the distance of a point in U to its closest neighbour point in V the following metric $d(\vec{u}, V)$ is used

$$d(\vec{u}, V) = min_{\vec{v}\in V}\|\vec{v} - \vec{u}\| \tag{7.8}$$

The algorithm is initialised by setting the rotation and translation matrices equal to the identity matrix $\mathbf{R} = \mathbf{T} = \mathbf{I}$ and begins by identifying for each point $\vec{u} \in U$ the best match with the shortest distance $d(\vec{u}, V)$. This step can be efficiently performed using a k-d tree [Rusinkiewicz and Levoy, 2001]. With the set of matching pairs as input, the best registration is calculated using the quaternion-based least square method, determining $\mathbf{R}$ and $\mathbf{T}$ which

are then applied to U. The whole process is repeated iteratively, finding new matching points and their transformation, until the change in mean square error falls below a given threshold.

In the context of this work we limit our discussion to the basic principles of the ICP algorithm. For alternative strategies and further information on shape registration, the interested reader is referred to [Brown, 1992; Zitová and Flusser, 2003; van Kaick et al., 2011].

7.3 Collision of target objects

When extracting roots from image data of samples that contain more than one plant, individual level set functions are associated with each root system and evolved according to the principles presented in chapters 3 and 4. Since the computation of the level set function is limited to a band around the interface (narrow band), they are in general not influenced by each other. This, however, is not true when two or more root objects make contact. Assuming all the target objects have similar greyscale characteristics, contact between two roots will cause the image regions representing their sections to combine to form a single, larger region with the same grey level distribution. Each level set, as per definition, would then expand into that region, although certain areas are already occupied by others. This can be easily prevented by setting combination rules as described in section 7.1, to make the inside area of any level set function impenetrable. This, however, has as a consequence; the generation of race conditions. Here, one level set function can block the way for others and as a result take over tracking their target. Such a scenario is illustrated in figure 7.2.

If more reliable extraction of multiple root systems is to be provided, it is necessary to refine the combination rules to take into account the location and current state of the root objects. At this point, the reader is reminded that throughout the tracking process, the shape of a target object is captured and used to decide whether or not the root model distribution is to be updated (chapter 3). This knowledge of the shape of root sections can also help in making decisions when it comes to object collisions. We assume that the shape of a root cross-section is approximately constant during the period of contact. This assumption may not always hold, but we believe it will be true in the majority of cases, since the number of cross-sections at which a

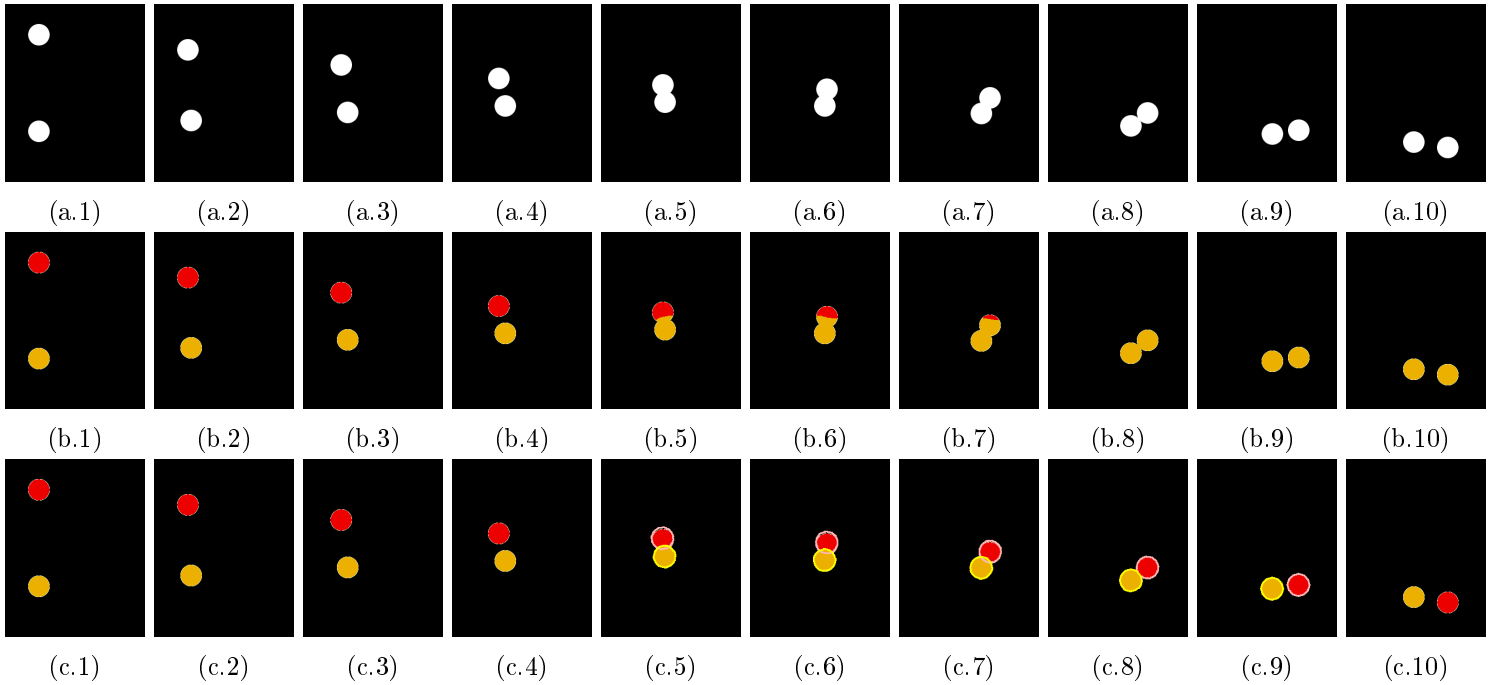

Figure 7.2: Two colliding target objects; (a) raw data, (b) extracted using the conventional level set tracking approach and (c) combined with the ICP algorithm during the period of contact (5-9)

root bends is low in comparison to the number of slices through which the root follows a steady direction. When a bend occurs, it is also likely that the root will lose contact with any neighbouring roots, and hence leave the critical collision area of the corresponding image.

The occurrence of a collision between two or more root objects can be easily identified by checking which of the level set functions Φ_N^* have a negative value. This can be determined while testing for the condition given in equation 7.1. When no collision is detected, so the boundary of the root sections can be assumed to be clearly visible, their shape is recorded. These stored shape descriptions are then used to guide the evolution of the level set functions during interactions; when a collision is detected. The ICP algorithm, as described in section 7.2, is used to find the best alignment of the prestored shape to the moving interface. This leaves the level set function in one of two possible states: the interface is either outside or inside of its aligned region. If the interface is located outside, then the level set function is not protected from penetration and at the same time cannot penetrate others. If the interface is inside its aligned area, then it is protected from any other level set function and therefore cannot be penetrated, but at the same time can penetrate others. The different states and their combination rules are illustrated in figure 7.3. The effect of applying this mechanism is illustrated in figure 7.2.

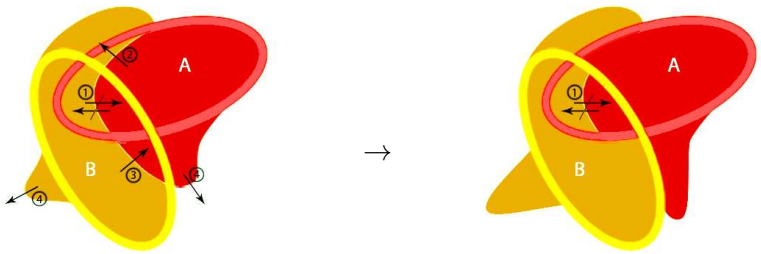

(a) (b)

Figure 7.3: Combination rules of overlapping level set functions A and B (a) before and (b) after evolution. (1) A and B are both protected from penetration, (2) A penetrates B, (3) B penetrates A, (4) A and B cannot penetrate other interfaces, but continue evolving in unoccupied areas

More formally, let $L = \{\Phi_1..\Phi_n\}$ be the set of level set functions and $L^* = \{\Phi_1^*..\Phi_n^*\}$ the set of their temporary states. The shape of each object tracked with the level set function, is stored and associated with its root

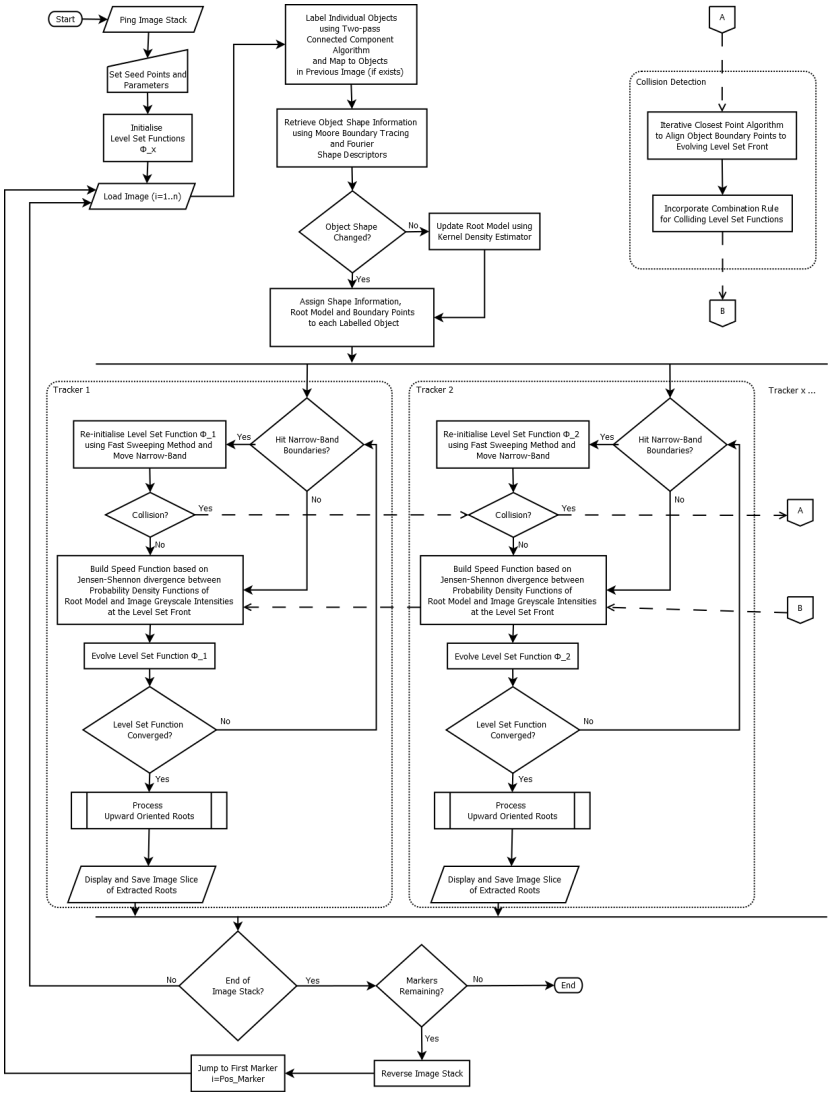

Figure 7.4: Flowchart of the tracking process for the extraction of multiple and interacting plant root systems

object. On the detection of a collision between objects belonging to different level set functions, the stored object shape is aligned to the points along the evolving interface using the ICP algorithm and its enclosed area denoted as set $S = \{S_1..S_n\}$. The final value of the level set function Φ_i at time step $t+1$ and position p is then calculated as follows

$$\Phi_i^{t+1} = \begin{cases} \Phi_i^* & \text{if } (p \in S_i) \wedge (p \notin \{S \backslash S_i\}) \\ \max\left(\Phi_i^*, -\{L_j | p \in S_j\}\right) & \text{if } (p \in S_i) \wedge (p \cap \{S \backslash S_i\} \neq \emptyset) \\ \max\left(\Phi_i^*, -L^*\right) & \text{if } (p \cap S = \emptyset) \end{cases} \tag{7.9}$$

A particular benefit of this solution is that, although it constrains the movement of the front, the selected root object is not required to maintain the registered shape. This allows the detection of lateral roots, since a level set function can still evolve beyond the aligned region. At the same time it prevents the path of a level set function being blocked by faster evolving level sets and allows their interface to be penetrated so that control over its target is maintained.

Figure 7.4 shows the updated flowchart of the process for the extraction of multiple and interacting root systems introduced in this chapter. Multiple level set functions are evolved in parallel and the ICP algorithm applied when triggered by a collision of different level set fronts.

7.4 Extracting data with colliding objects

The technique proposed here has been applied to a number of image stacks, both artificially generated and acquired via X-ray μCT. The extraction is performed twice for each dataset, with the collision mechanism enabled and disabled, to determine the differences that the additional integrated method brings. In the following subsections we will describe in detail both experiments and discuss the results obtained. Artificial data is used here as access to real X-ray data on interacting root systems is currently limited. The Nanotom (Phoenix X-ray / GE Measurement & Control Systems) X-ray μCT scanner used throughout this project has a restricted sample size which reduces the number of different plant configurations that can be considered. Although, there is the chance of root sections from different plants to interact, this behaviour cannot be controlled. Artificially generated data allows

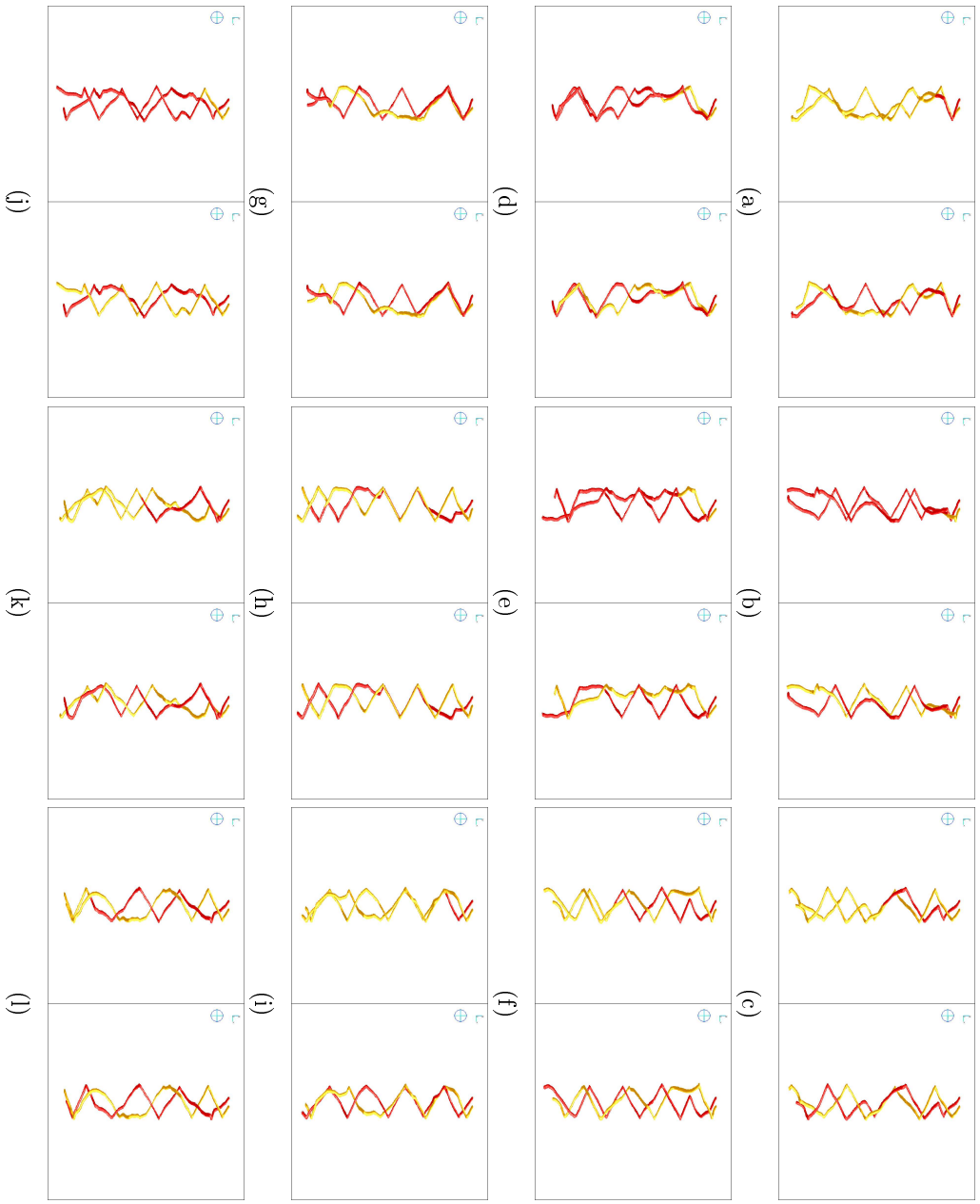

Figure 7.5: Extraction of artificially generated data with collision mechanism disabled (left) and enabled (right)

simulating the interaction of root objects and therefore facilitates the testing of the presented method. Artificial data is commonly used in the broader computer vision community and brings a number of advantages, as discussed in chapter 6.

7.4.1 Artificially generated data

Artificial image data was generated by moving two white circles across a black background at a speed of 6 pixels per time step, changing direction through a randomly selected angle $\angle = [-16°, 16°]$ to obtain a random path. The circles bounce off the image boundaries to keep them within the scene and ensure they are trackable throughout the entire image stack. The circle radius is set to a constant value of 20 pixels, moving within a field of 320×320 pixels for a total of 500 images. 12 different image stacks were generated and used to test the extraction of colliding objects. The obtained results are rendered in figure 7.5.

The focus of this trial lies in observing the behaviour of the extraction technique when the different target objects interact with each other. The initial formulation of the method did not consider the possibility of different root objects interacting and therefore nothing prevented the targets being confused with each other. Although the aim of separating target from background was successfully achieved, it can be observed how easily targets were passed between trackers, making it impossible to tell whether the final target really belongs to the object its tracker was initialised to. With the collision mechanism activated, the method performed much better in keeping track of the correct target and as such increases confidence in its ability to distinguish objects with similar appearance.

7.4.2 X-ray μCT acquired data of plants

To assess the benefit of the proposed approach in practice, the collision mechanism was applied to multiple plants grown within the same soil environment. That environment was restricted in size, increasing the likelihood of interactions between root systems. Five samples were prepared, using columns 30mm in diameter. In each column two winter wheat Cordiale (*Triticum aestivum L.*) were grown, 10 to 15mm apart, for 10 days after germination in a Newport series loamy sand (brown soil). They were then scanned using

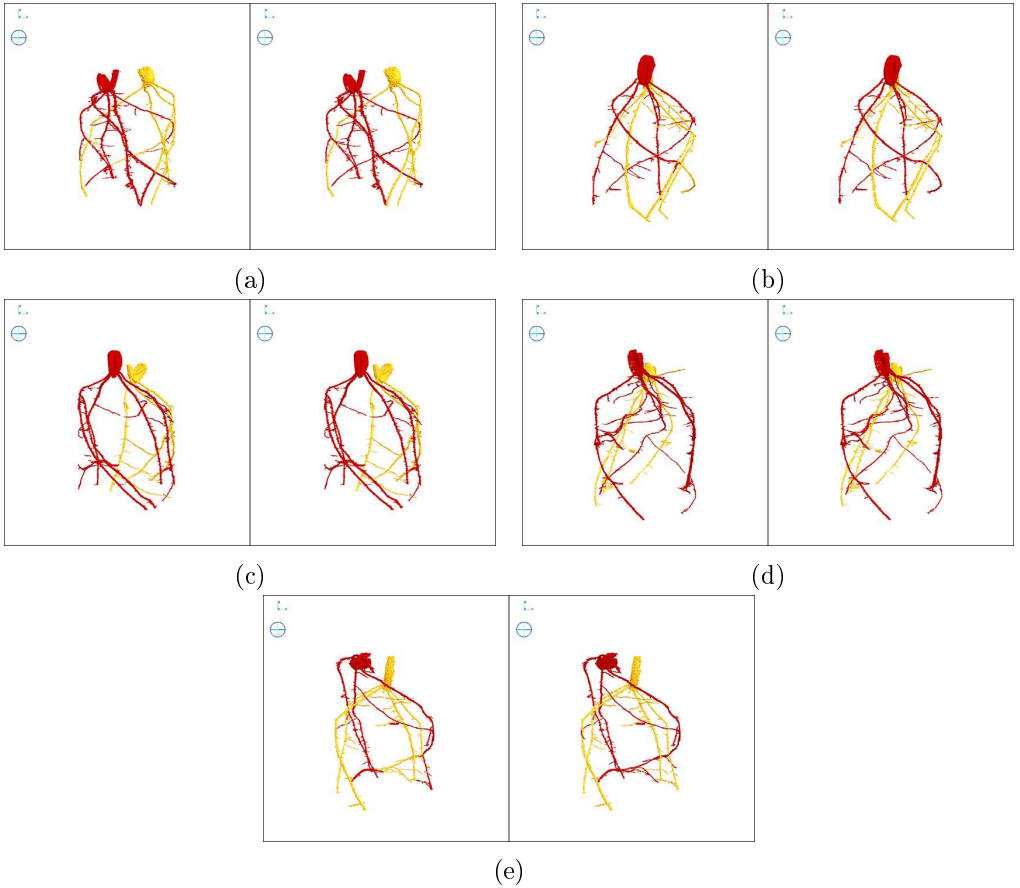

Figure 7.6: Extraction of X-ray μCT acquired data with collision mechanism disabled (left) and enabled (right)

a Nanotom (Phoenix X-ray / GE Measurement & Control Systems) X-ray μCT scanner. The plants were kept in an environmentally controlled growth room with a 16/8 hours light cycle at a temperature of 23/18 degree Celsius. The scan was performed at 120 keV and 110 μA, taking 1440 projections at an exposure time of 750ms, using a signal averaging of 3 and 1 skipping per projection. The samples were placed 134mm away from the X-ray gun, resulting in a volume with resolution of 22.33μm voxel size. The X-rays were filtered through a 0.1mm copper plate. Note that using a single plant species means that all the root material present in the experiment will generate intensity values drawn from the same distribution.

Figure 7.6 shows the reported root system architectures of the two interacting plants, extracted with the collision mechanism both disabled and enabled. Figure 7.7 shows a close-up of selected regions, to better illustrate the difference and the benefit the proposed collision detection mechanism brings. Although the additional mechanism clearly increases the method's ability to keep different root systems apart, from figure 7.7e, for instance, it is apparent that it does not guarantee perfect separation of interacting root systems. In the section shown in the figure, both trackers picked up the same root fragment at different locations in the image data. The collision occurred after the root has already been targeted by the trackers and followed across a number of image slices, until they eventually met.

7.5 Summary

The proposed mechanism was tested in an experiment involving two interacting wheat plants grown in the same soil environment. The results clearly show an improvement in the extraction of multiple root systems in comparison to the extraction process in which no collision detection was applied. While no guarantee can be given that root objects are associated to the correct plant, the additional operation adds a higher degree of certainty. Only by explicit reasoning about the structure of particular species' root system architectures would it be possible to increase confidence in assigning root objects to the right plant. This however, is a very challenging task, as root system architectures vary considerably with species and environment. Nonetheless, we believe that the extracted data allows obtaining a good indication of the overall interaction between multiple root systems and provides meaningful information for the study of interacting and competing plant root systems.

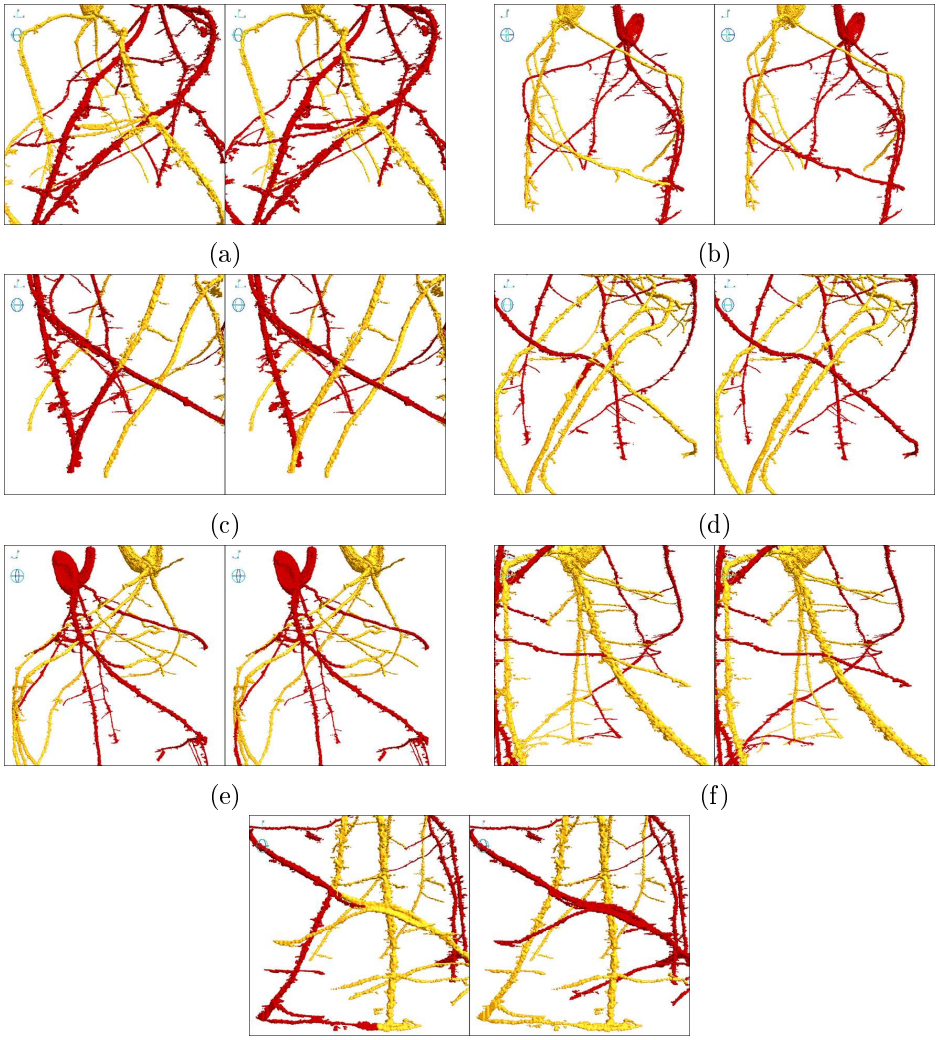

Figure 7.7: Extraction of X-ray μCT acquired data with collision mechanism disabled (left) and enabled (right)

Chapter 8

Conclusions and future work

Understanding of the development of plant roots and their interaction with the soil environment is fundamental if global yield production is to be increased and food security ensured. X-ray micro computed tomography (μCT) provides a valuable tool when studying the complex soil-root relationship, by allowing non-destructive visualisation of the 'hidden half' of plants. By measuring the attenuation of ionising radiation passing through the scanned plant sample and taking multiple projections at different angles, it is possible to reconstruct a volumetric density representation of the sample's interior. To make sense of the acquired X-ray CT data, root system information must be recovered from the raw images. The aim of this work was the development of a technique to facilitate plant root system extraction.

In the course of this research we contributed by presenting a novel technique for the extraction of plant root systems from X-ray μCT images. Unlike previous methods applied to CT data of plant roots, which segment the data first into regions that are then used for identifying and building the structure of the root system (bottom-up fashion), we start from a distribution model that we believe represents root material and match it to the image data to find objects that belong to the root system (top-down fashion). This was realised by adapting a visual tracking framework, which is applied to a sequence of images obtained by traversing the stack of cross-sectional slices. The detection of root objects is accomplished by introducing a modified formulation of the level set method, using a function for the evolving front that is driven by the greyscale intensity values of the image data via the Jensen-Shannon divergence. Root representation models are used as indicators for

target objects and updated along the way. This allows the tracker to adapt and so cope with variations inside target root objects. Instability in root models, caused by drifting away from actual root material, was countered by representing the targets' object shapes, which are used when deciding whether or not to update the model. The proposed extraction technique was extended by two mechanisms; a method sensitive to plagiotropic responses in root systems, and a strategy that allows the extraction of multiple root systems sharing the same space and growth environment while interacting with each other.

8.1 Summary

In **chapter 2** we provided an overview of different root study methodologies and reviewed extraction methods of plant roots in two- and three-dimensional image data as well as methods developed in the field of medical imaging. Background information was provided on the physical principles of X-ray CT imaging, to promote better understanding of the characteristic nature of the image data it produces.

In **chapter 3** we presented a novel technique for the extraction of three-dimensional root systems from X-ray μCT image data realised through a visual tracking based strategy using a modified, Jensen-Shannon divergence-based, level set formulation. The proposed method was applied to root systems of monocot and dicot plants grown in different soil textural types, commonly found in the United Kingdom.

In **chapter 4** we introduced a mechanism for the extraction of plagiotropic roots that allows more complete recovery of plant root systems by considering roots that are upward oriented, and thus missed by the initial technique. The extended method was applied to the same raw image data used in the experiment of chapter 3. Results obtained from the initial and extended method were compared.

In **chapter 5** we provided the means to visualise extracted data and to perform measurements of global root system traits. This was undertaken to promote better understanding of the complexity of plant root systems grown in natural environment. Measuring root system traits is essential for the evaluation of the presented extraction method.

In **chapter 6** the proposed extraction technique was thoroughly tested and compared to results obtained through alternative procedures, both by artificially generating data as well as using other tools developed for similar purposes. The evaluation of the presented method was divided into separate steps, each addressing particular aspects.

In **chapter 7** we extended the proposed extraction method by adding the ability to recover multiple root systems grown in the same soil environment. The different plants are distinguished during the segmentation process by a novel collision detection and handling process. The method for multiple root system extraction was tested on a number of samples with collision detection mechanism both enabled and disabled.

The proposed methods form the basis of an open source software tool, RooTrak, which allows the extraction of root systems from X-ray μCT image data, as well as their visualisation and trait recovery. At time of writing, RooTrak has been downloaded approximately 260 times by September 23rd 2013.

8.2 Alternative applications

Although the methods presented here were developed for the purpose of extracting the root systems of plants grown in soil from X-ray μCT images, the design of the various techniques was kept general. No explicit models of root system architectures are involved. This raises the possibility of extracting any kind of root architecture without being limited to specific plant species, and of applying the proposed methods to data of a different nature. During the course of this work, we had the chance to apply our method to data sets of different origin. Thanks are due to Dr. Randy T. Clark, the lead developer of RootReader2D and RootReader3D [Clark et al., 2011, 2013], who generously shared a data set of a rice root system acquired with their gellan gum system and silhouette-based back-projection algorithm, to be used as test data for our extraction method. His PhD research was conducted in the Robert W. Holley Center for Agriculture and Health, USDA-ARS, Cornell University, lead by the director and research leader Prof. Leon V. Kochian. Figure 8.1 shows the root system published in [Clark et al., 2011] in comparison to results obtained by applying the methods described here to the

same data.

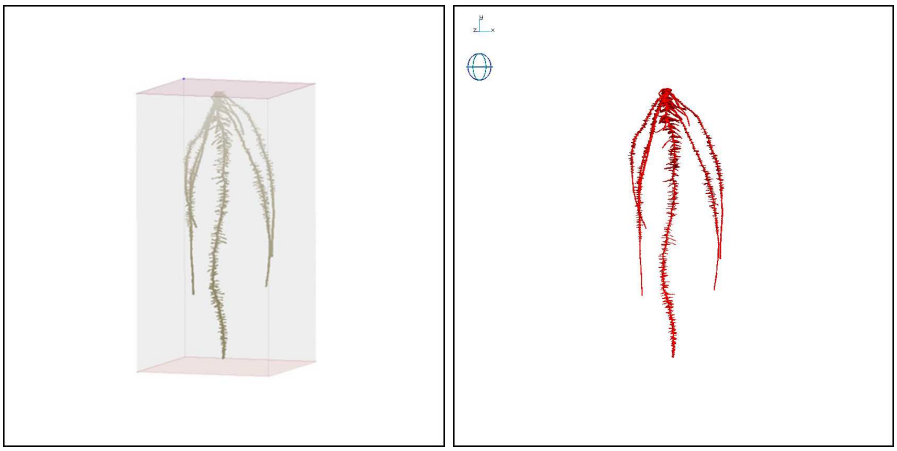

(a) (b)

Figure 8.1: Root system of rice showing the image presented in [Clark et al., 2011] (left) and extracted data using the proposed method (right) - raw data is courtesy of Dr. Randy T. Clark

A very different area of application, but one requiring a tracking algorithm with similar properties, is the tracking of cell nuclei and the chronological detection of mitosis. A slight modification of an earlier version of our method, incorporating elements presented in chapter 4 for the detection of splitting objects, and using additional concepts for preventing already separated nuclei to merge, was applied to a sequence of images. Selected image frames showing the lineage of cells and the detection of mitosis is shown in figure 8.2. The image data was provided by a research team lead by Prof. Pierre Hilson, to whom we express our gratitude for providing the image data.

The proposed methods may find application in medical image analysis. Another set of image data, acquired using a medical X-ray CT scanner and showing a human body, was segmented to extract bladder, prostate and the seminal vesicles, using the technique presented for extracting multiple objects. The result is shown in figure 8.3. Our deep appreciation goes to Dr. Keith Langmack from the Clinical Radiotherapy Physics centre at the Nottingham University Hospitals NHS Trust, who provided the medical image data.

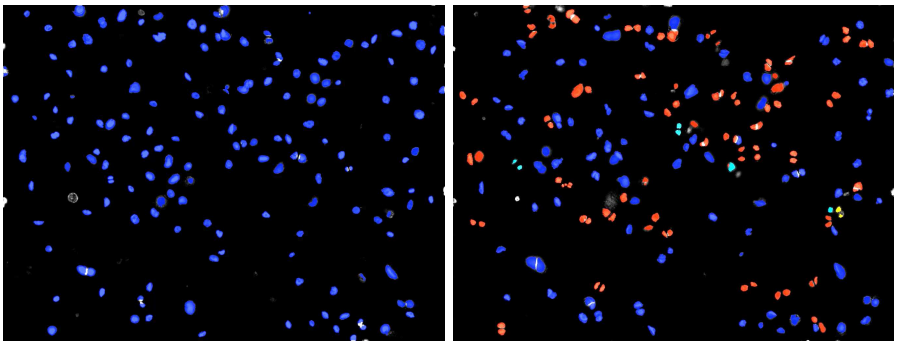

(a) (b)

Figure 8.2: Nuclei extraction and chronological detection of mitosis showing their linage (dark blue, red, light blue, yellow, ...) in image 12 (left) and 162 (right) - raw data is courtesy of Prof. Pierre Hilson

8.3 Future work and perspectives

X-ray μCT allows the non-destructive observation of plant root systems embedded in soil. The addition of image analysis techniques for the extraction of root architecture information provides plant biologists with a valuable tool that will assist them in bringing forth new scientific findings about the complex development of roots and their interaction with the soil environment. We predict that in the following years, the number of experiments and breakthrough discoveries made using X-ray CT imaging, will greatly increase, as the technology rapidly improves while at the same time becoming lower in cost and so more accessible. While scanners of very high resolution will remain of importance, since they allow the study of very fine details, it seems likely that the number of mid-resolution scanners in use will increase as they take centre stage. The resolution dictates and often limits the maximum possible sample size. The higher the resolution, the finer the details that are observable, but the smaller the sample size needs to be. Small samples allow only the growth of very young plants, due to the limited space. Some of the plants used in the experiments described here reached the boundary wall less than ten days after germination, which alters the natural growth. Many aspects of plant root studies require plants to be analysed in a mature stage, which in turn implies the use of larger samples. By lowering the resolution, root object will appear smaller and therefore be more difficult to identify and hence extract. This brings new challenges to computational

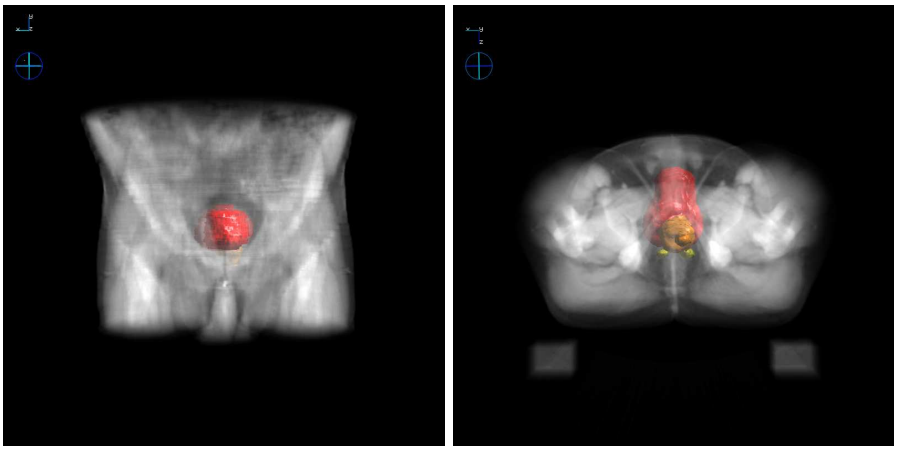

(a) (b)

Figure 8.3: Extraction of bladder (red), prostate (orange) and seminal vesicles (yellow) visualised from the front (left) and below (right) - raw data is courtesy of Dr. Keith Langmack

methods for recovering root systems. Root objects between two consecutive images might not overlap anymore, and thus a motion model for tracking might become necessary.

Living roots that are part of the root system, although are physically connected, might appear invisible for a number of image slices, due to blending into the background or because of the presence of scanning artefacts. The proposed methods expect to find the target in every image, and if its target is lost assume it has reached the end of the root. Even though we mentioned that proper occlusion can never occur in the volumetric image data, this situation can be considered a similar issue. Introducing a mechanism that guesses the location of the root object through a number of images with the hope of picking up lost targets, might be a significant improvement to the extraction method, since it would allow more complete recovery of the plant root system.

Interesting in root development studies is not only the architectural structure of the root system at a particular point in time, but also the observable variation of growth over a longer period. Non-destructive imaging is key to acquire time series data. Four-dimensional data needs to be aligned and registered in order to obtain information about root systems' growth rate. To increase throughput of time series analysis, we anticipate that initial scans can be performed quicker at the cost of lower image quality, finishing

with a single high quality scan that allows a detailed extraction of the root system's architecture. The result obtained can be used in the analysis of previous scans, using the final root system structure in the decision making process of identifying root material in less qualitative image data.

Plant root systems, especially if analysed at a mature stage, can become highly complex in structure, which might prove to be a high challenging task. Mathematical models of developing root systems can be used to predict and estimate the formation of lateral roots. Great care needs to be taken not to include root sections that are to be expected but in reality are not existent; a danger for many knowledge-based extraction techniques. However, we believe that if applied to a moderate extent, root system models can contribute to extraction accuracy and form an interesting mechanism.

With increased sample size, while not sacrificing too much resolution, the size of the image data will drastically increase. Dealing with large data decreases computational performance, which can be compensated by using targeted devices such as the graphics processing unit (GPU). Although the nature of tracking is a sequential process, the evolution of the level set function and thus the extraction of object boundaries, can be parallelised, which for a large number of root objects might save tremendous computation time and thus increase throughput.

Important is the testing of developed methods. Evaluating the accuracy of root recovery methods is a difficult task and requires further attention. While we tried to test the presented extraction methods in a wide range of different test scenarios, a detailed sensitivity test is still missing, but is essential to improve reliability.

Appendices

Appendix A

Root Segments

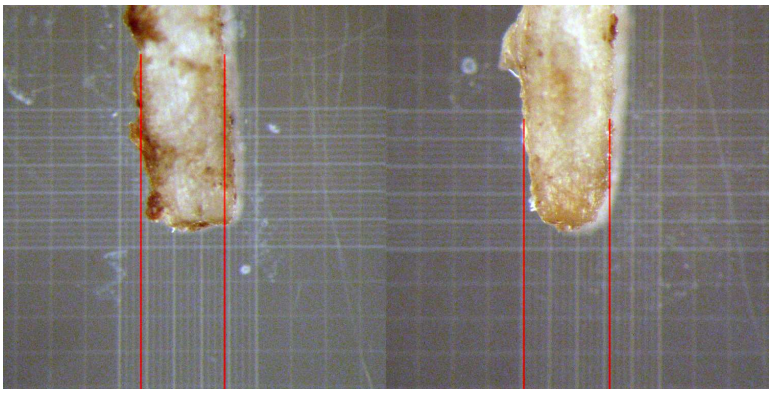

(a) Root segment 1

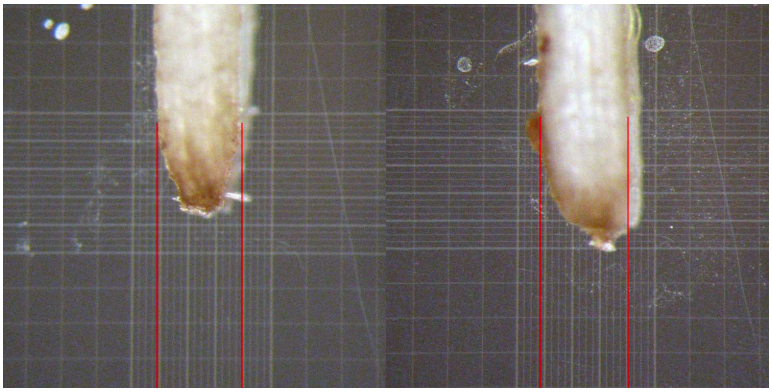

(b) Root segment 2

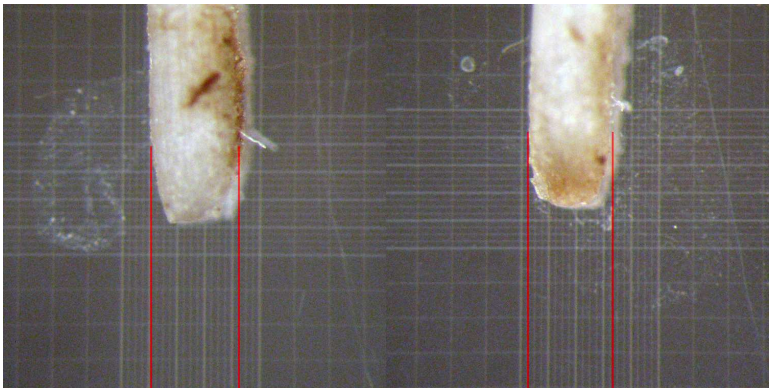

(c) Root segment 3

Figure A.1: Root segments used in the experiment of chapter 6 viewed under the microscope (left) before and (right) after scanned using X-ray μCT

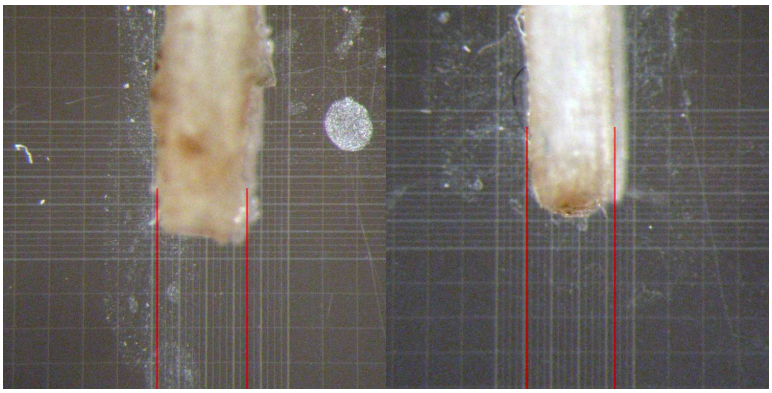

(d) Root segment 4

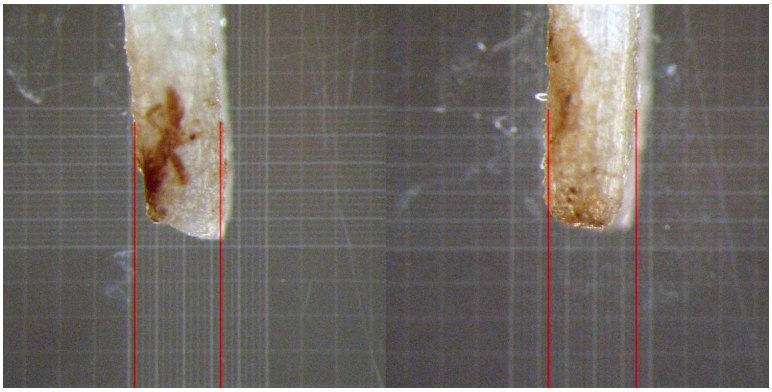

(e) Root segment 5

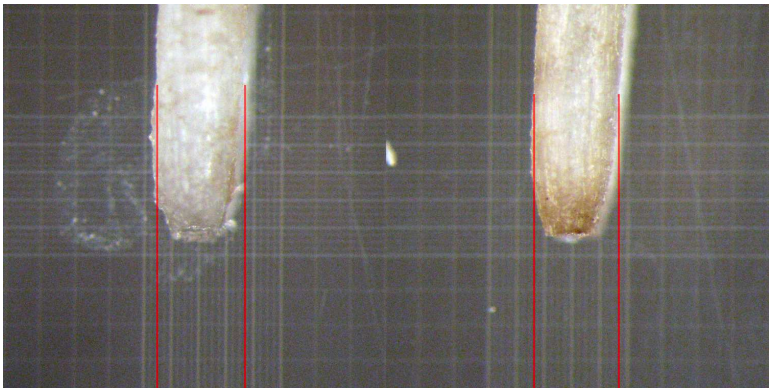

(f) Root segment 6

Figure A.1: Root segments used in the experiment of chapter 6 viewed under the microscope (left) before and (right) after scanned using X-ray μCT

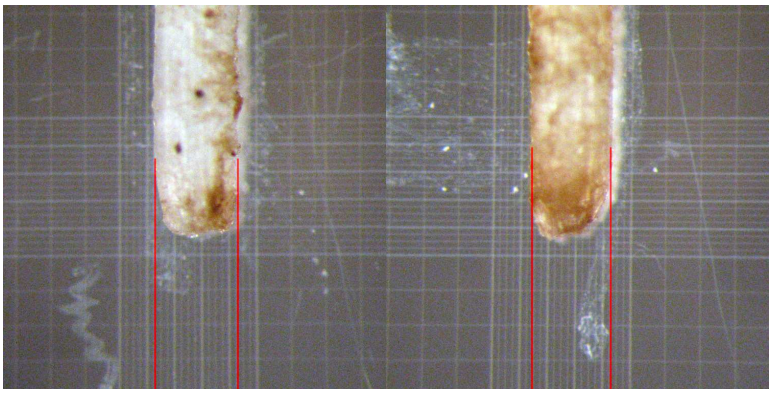

(g) Root segment 7

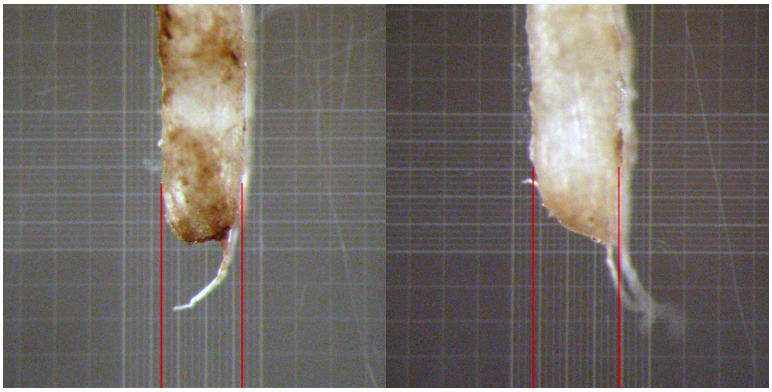

(h) Root segment 8

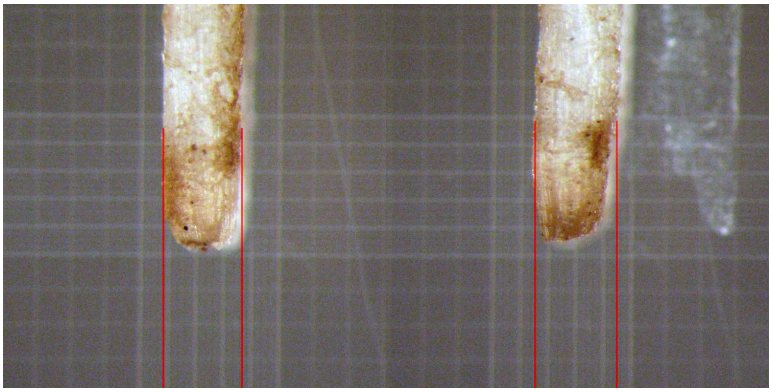

(i) Root segment 9

Figure A.1: Root segments used in the experiment of chapter 6 viewed under the microscope (left) before and (right) after scanned using X-ray μCT

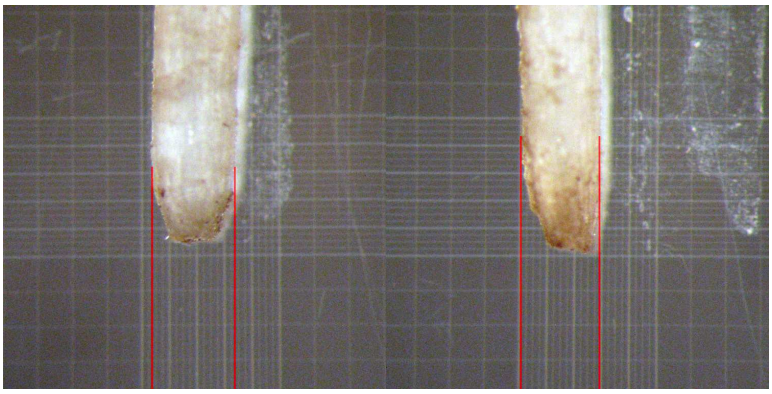

(j) Root segment 10

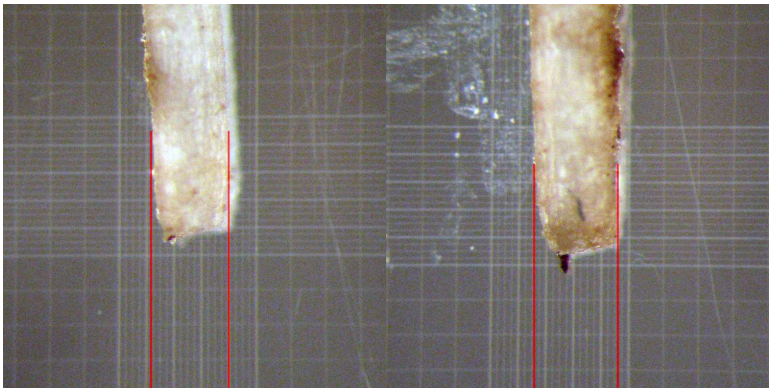

(k) Root segment 11

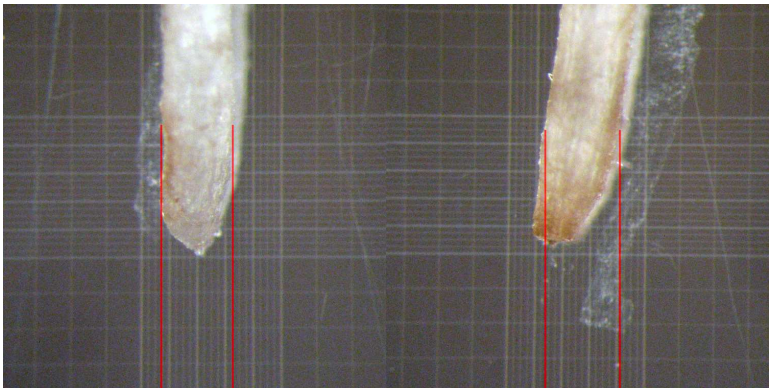

(l) Root segment 12

Figure A.1: Root segments used in the experiment of chapter 6 viewed under the microscope (left) before and (right) after scanned using X-ray μCT

Appendix B

Plant Root Systems

No.	*01*
Plant:	*Maize - Zea mays convar. saccharata var. rugosa*
	Sweet Corn Jubilee F1
Soil:	*Loamy sand*
Germinated:	*20.08.2011*
Planted:	*22.08.2011*
Scanned:	*31.08.2011*
Sample size:	*⌀= 30mm, height = 65mm*
Weight (start):	*58.66g soil-dry*
Weight (end):	*85.11g (9.83g tube, 0.99g plant, 74.29g soil-wet)*
Growth envir.:	*Growthroom, 16/8 photoperiod, 23/18°C*
Scan settings:	*80 keV, 150µA, 0.1mm Cu filter, 1200 projections,*
	750ms exposure time, 2x2 binning, 4x1 avg/skip,
	48.48 µm voxel size, 75min scan time,
	160mm (source-sample), 330mm(source-detector)
Notes:	*1.2767 g/cm³ soil compaction*
	θ_x = 26.64% soil moisture

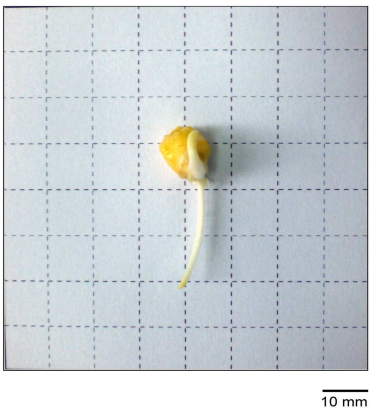

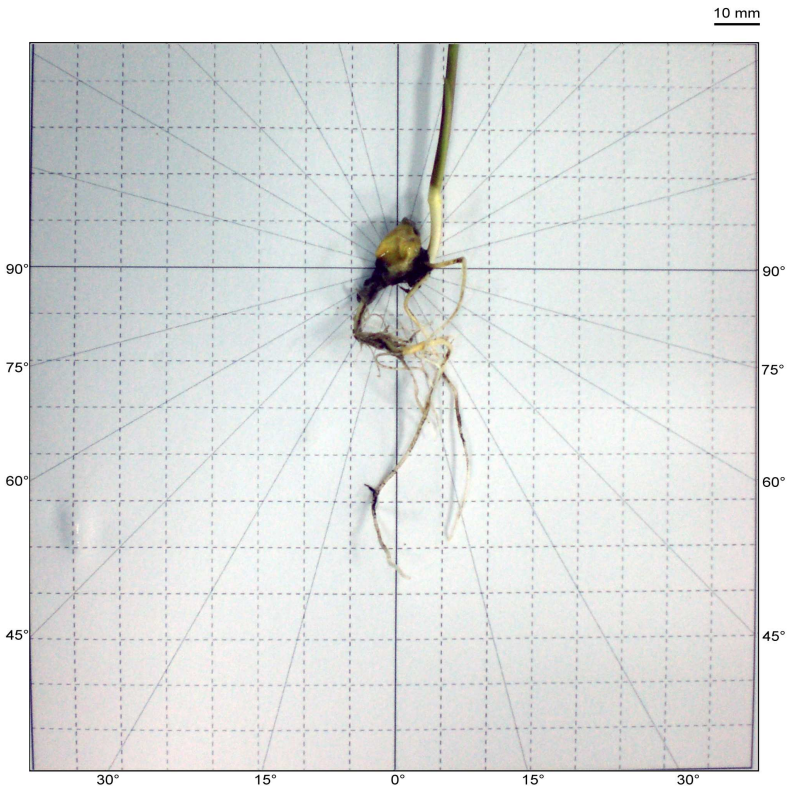

Figure B.1: Maize 1 datasheet

No.	02
Plant:	Maize - Zea mays convar. saccharata var. rugosa
	Sweet Corn Jubilee F1
Soil:	Loamy sand
Germinated:	20.08.2011
Planted:	22.08.2011
Scanned:	31.08.2011
Sample size:	⌀= 30mm, height = 65mm
Weight (start):	57.88g soil-dry
Weight (end):	83.17g (9.42g tube, 1.94g plant, 71.81g soil-wet)
Growth envir.:	Growthroom, 16/8 photoperiod, 23/18°C
Scan settings:	80 keV, 150µA, 0.1mm Cu filter, 1200 projections,
	750ms exposure time, 2x2 binning, 4x1 avg/skip,
	48.48 µm voxel size, 75min scan time,
	160mm (source-sample), 330mm(source-detector)
Notes:	1.2597 g/cm³ soil compaction
	θ_s = 24.06% soil moisture

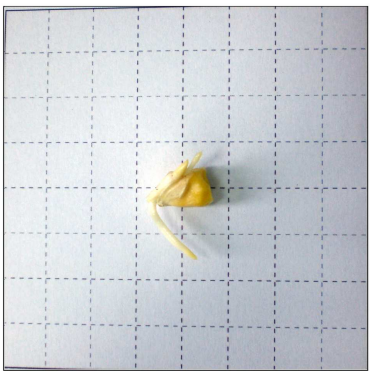

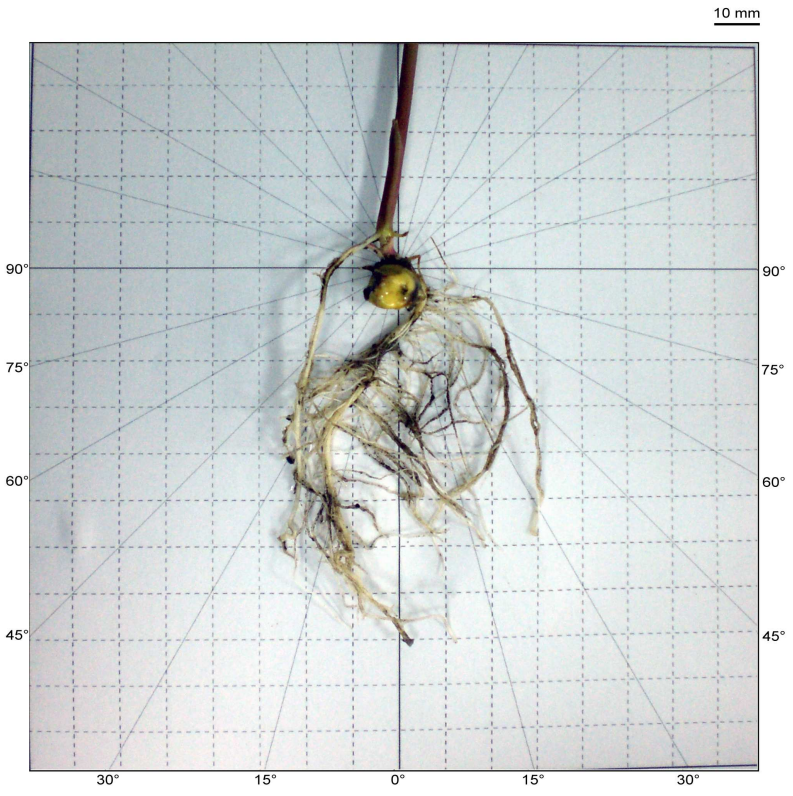

Figure B.2: Maize 2 datasheet

No.	*03*
Plant:	*Maize - Zea mays convar. saccharata var. rugosa*
	Sweet Corn Jubilee F1
Soil:	*Clay loam*
Germinated:	*20.08.2011*
Planted:	*22.08.2011*
Scanned:	*31.08.2011*
Sample size:	*⌀= 30mm, height = 65mm*
Weight (start):	*57.44g soil-dry*
Weight (end):	*86.00g (9.38g tube, 1.20g plant, 75.42g soil-wet)*
Growth envir.:	*Growthroom, 16/8 photoperiod, 23/18°C*
Scan settings:	*80 keV, 150µA, 0.1mm Cu filter, 1200 projections,*
	750ms exposure time, 2x2 binning, 4x1 avg/skip,
	48.48 µm voxel size, 75min scan time,
	160mm (source-sample), 330mm(source-detector)
Notes:	*1.2501 g/cm³ soil compaction*
	θ_x = 31.30% soil moisture

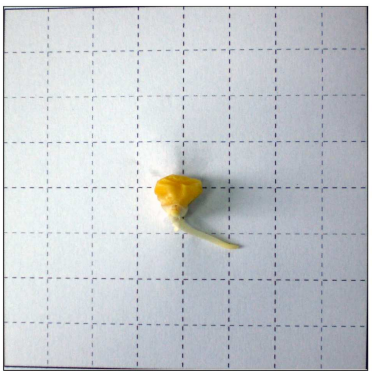

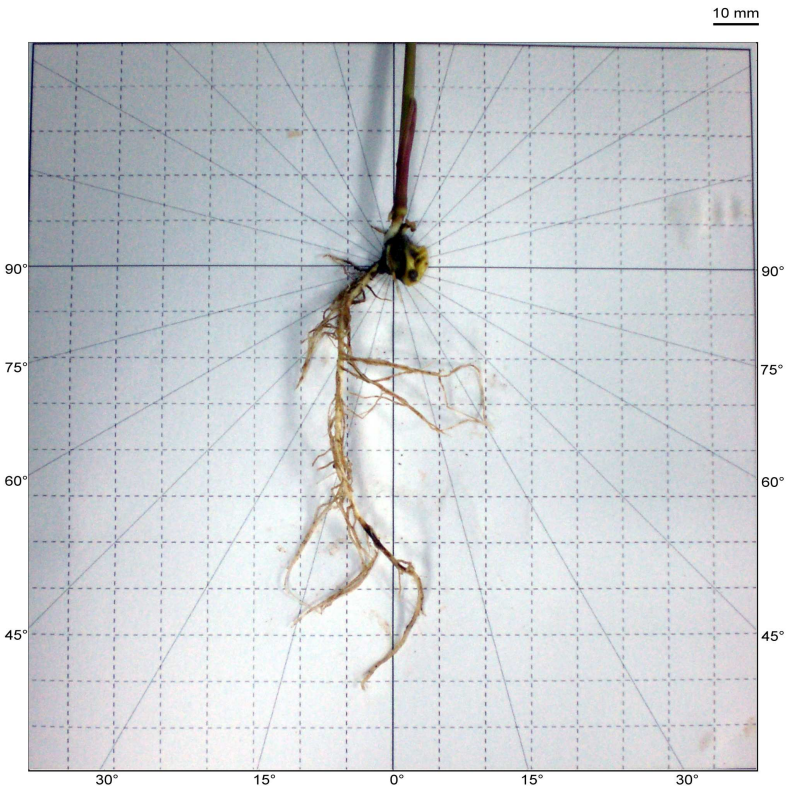

Figure B.3: Maize 3 datasheet

No.	04
Plant:	Maize - Zea mays convar. saccharata var. rugosa
	Sweet Corn Jubilee F1
Soil:	Clay loam
Germinated:	20.08.2011
Planted:	22.08.2011
Scanned:	31.08.2011
Sample size:	⌀= 30mm, height = 65mm
Weight (start):	56.26g soil-dry
Weight (end):	84.06g (9.76g tube, 1.85g plant, 72.45g soil-wet)
Growth envir.:	Growthroom, 16/8 photoperiod, 23/18°C
Scan settings:	80 keV, 150µA, 0.1mm Cu filter, 1200 projections,
	750ms exposure time, 2x2 binning, 4x1 avg/skip,
	48.48 µm voxel size, 75min scan time,
	160mm (source-sample), 330mm(source-detector)
Notes:	1.2244 g/cm³ soil compaction
	θ_x = 28.77% soil moisture

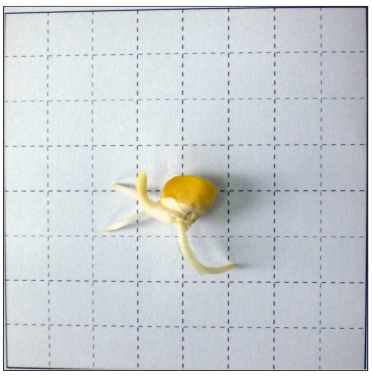

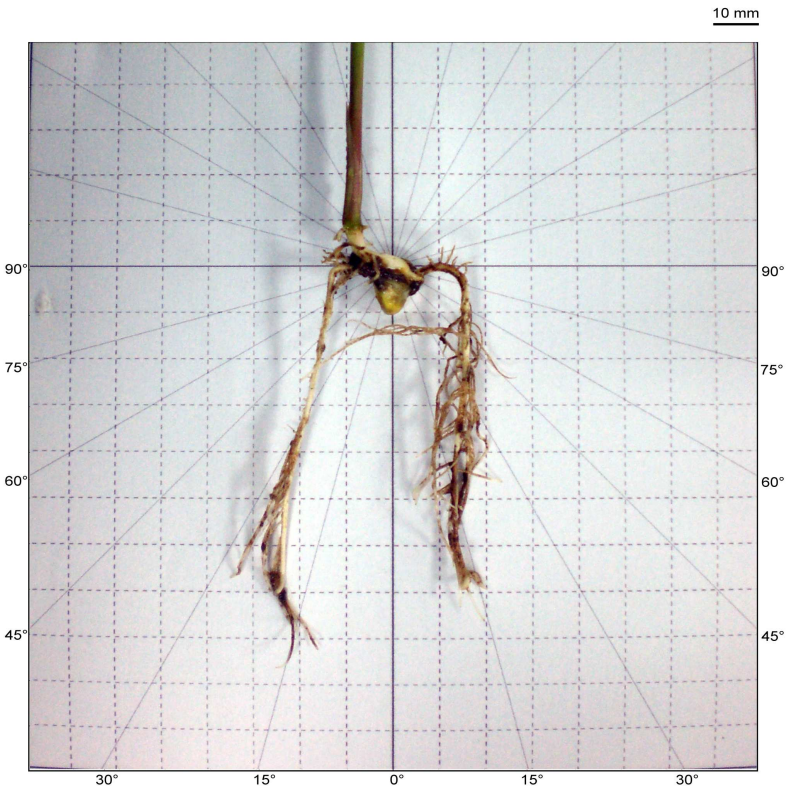

Figure B.4: Maize 4 datasheet

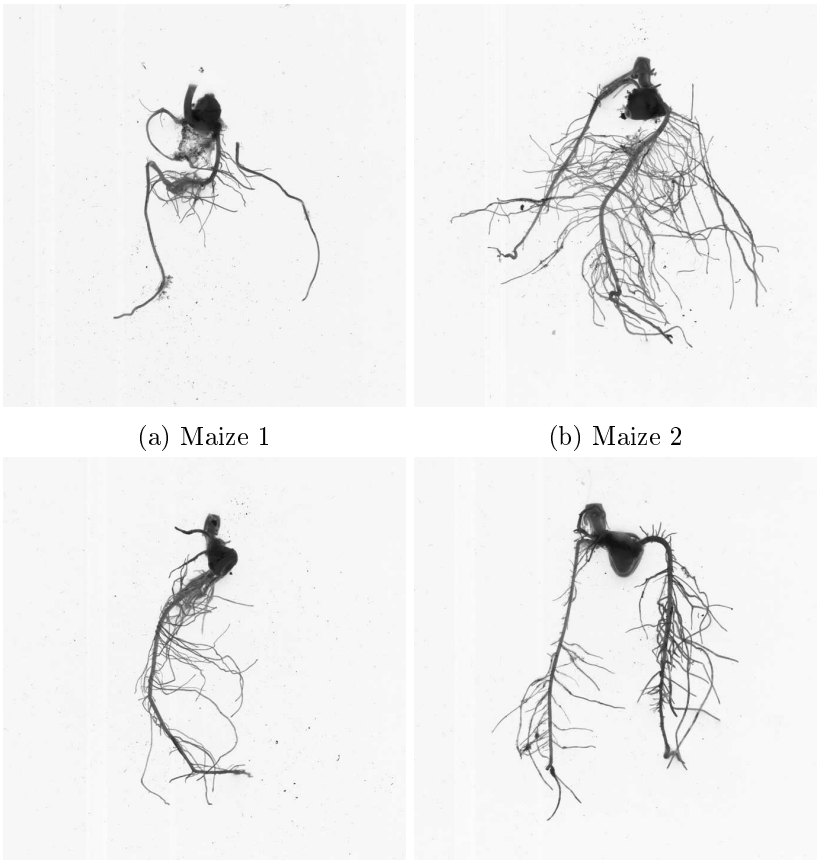

(a) Maize 1 (b) Maize 2

(c) Maize 3 (d) Maize 4

Figure B.5: Root-washed images of maize used for two-dimensional analysis

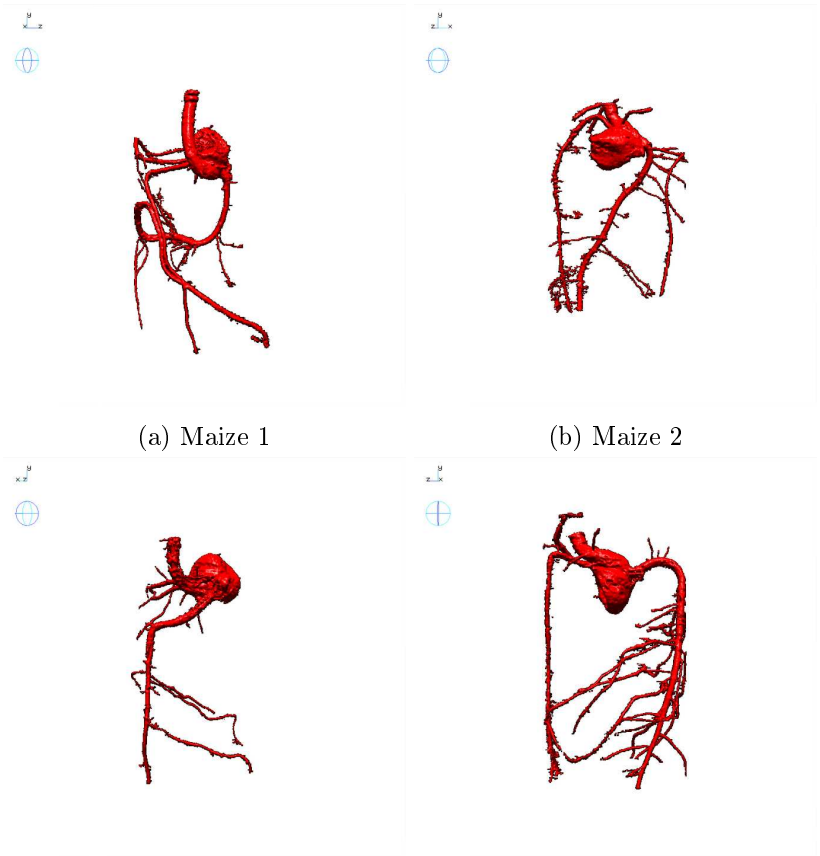

(a) Maize 1 (b) Maize 2

(c) Maize 3 (d) Maize 4

Figure B.6: Maize root systems rendered with volume ray-casting

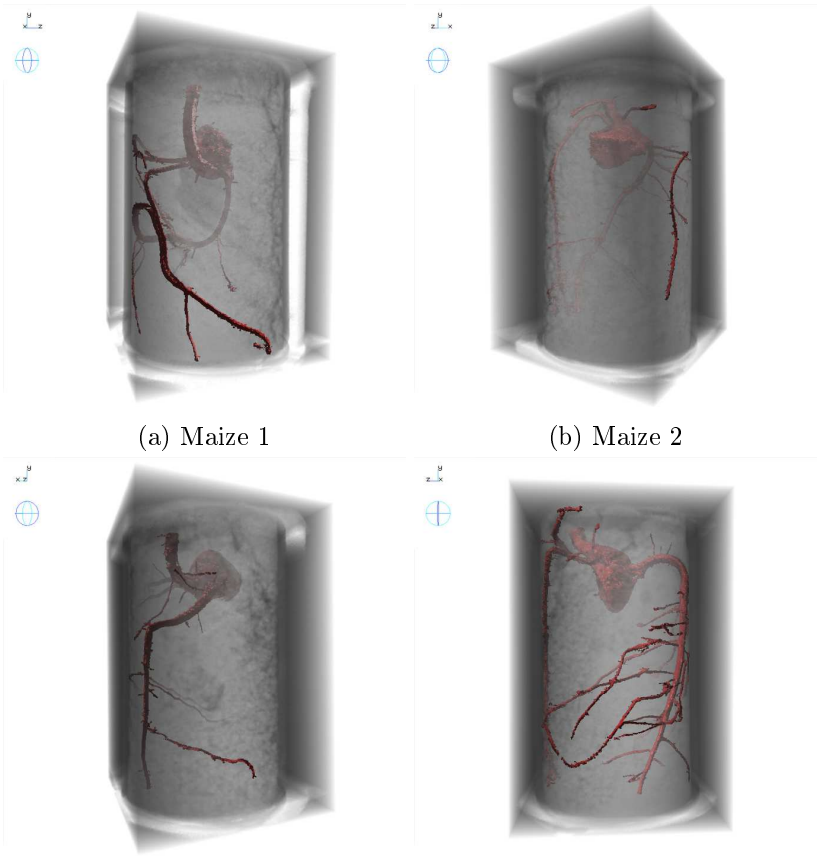

(a) Maize 1 (b) Maize 2

(c) Maize 3 (d) Maize 4

Figure B.7: Maize root systems in soil rendered with volume ray-casting

No.	05
Plant:	Winter Wheat - Triticum aestivum
	Cordiale
Soil:	Loamy sand
Germinated:	12.11.2011
Planted:	14.11.2011
Scanned:	23.11.2011
Sample size:	⌀= 30mm, height = 65mm
Weight (start):	60.01g soil-dry
Weight (end):	90.67g (9.96g tube, 1.04g plant, 79.67g soil-wet)
Growth envir.:	Growthroom, 16/8 photoperiod, 23/18°C
Scan settings:	120 keV, 250µA, 0.1mm Cu filter, 1200 projections,
	750ms exposure time, 1x1 binning, 3x1 avg/skip,
	25.00 µm voxel size, 67min scan time,
	200mm (source-sample), 400mm(source-detector)
Notes:	1.3061 g/cm³ soil compaction
	θ_x = 32.76% soil moisture

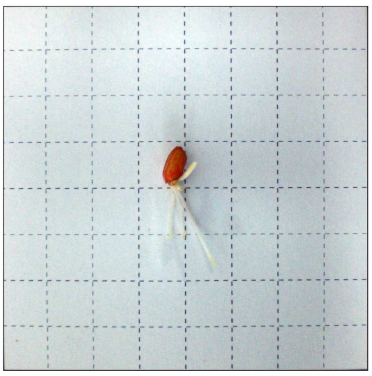

Figure B.8: Wheat 1 datasheet

No.	*06*
Plant:	*Winter Wheat - Triticum aestivum*
	Cordiale
Soil:	*Loamy sand*
Germinated:	*12.11.2011*
Planted:	*14.11.2011*
Scanned:	*23.11.2011*
Sample size:	*⌀= 30mm, height = 65mm*
Weight (start):	*57.59g soil-dry*
Weight (end):	*88.46g (10.01g tube, 0.91g plant, 77.54g soil-wet)*
Growth envir.:	*Growthroom, 16/8 photoperiod, 23/18°C*
Scan settings:	*120 keV, 250µA, 0.1mm Cu filter, 1200 projections,*
	750ms exposure time, 1x1 binning, 3x1 avg/skip,
	25.00 µm voxel size, 67min scan time,
	200mm (source-sample), 400mm(source-detector)
Notes:	*1.2534 g/cm³ soil compaction*
	θ_x = 34.64% soil moisture

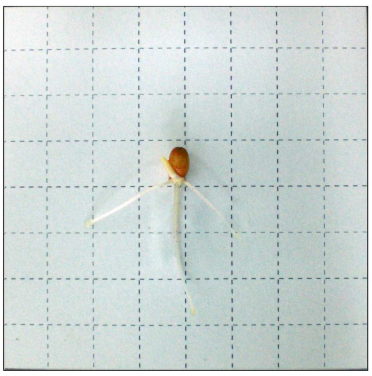

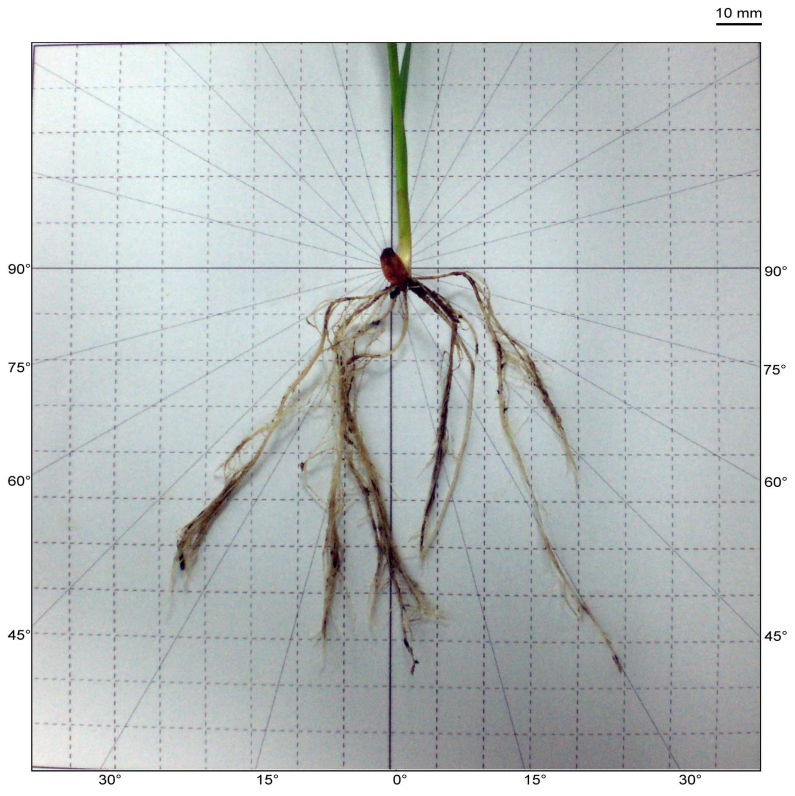

Figure B.9: Wheat 2 datasheet

No.	07
Plant:	Winter Wheat - Triticum aestivum Cordiale
Soil:	Clay loam
Germinated:	12.11.2011
Planted:	14.11.2011
Scanned:	23.11.2011
Sample size:	⌀= 30mm, height = 65mm
Weight (start):	57.84g soil-dry
Weight (end):	90.40g (10.16g tube, 0.54g plant, 79.70g soil-wet)
Growth envir.:	Growthroom, 16/8 photoperiod, 23/18°C
Scan settings:	120 keV, 250µA, 0.1mm Cu filter, 1200 projections, 750ms exposure time, 1x1 binning, 3x1 avg/skip, 25.00 µm voxel size, 67min scan time, 200mm (source-sample), 400mm(source-detector)
Notes:	1.2588 g/cm³ soil compaction θ_x = 37.79% soil moisture

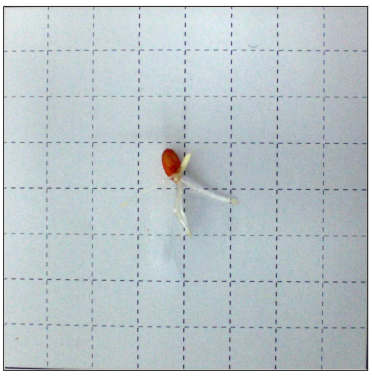

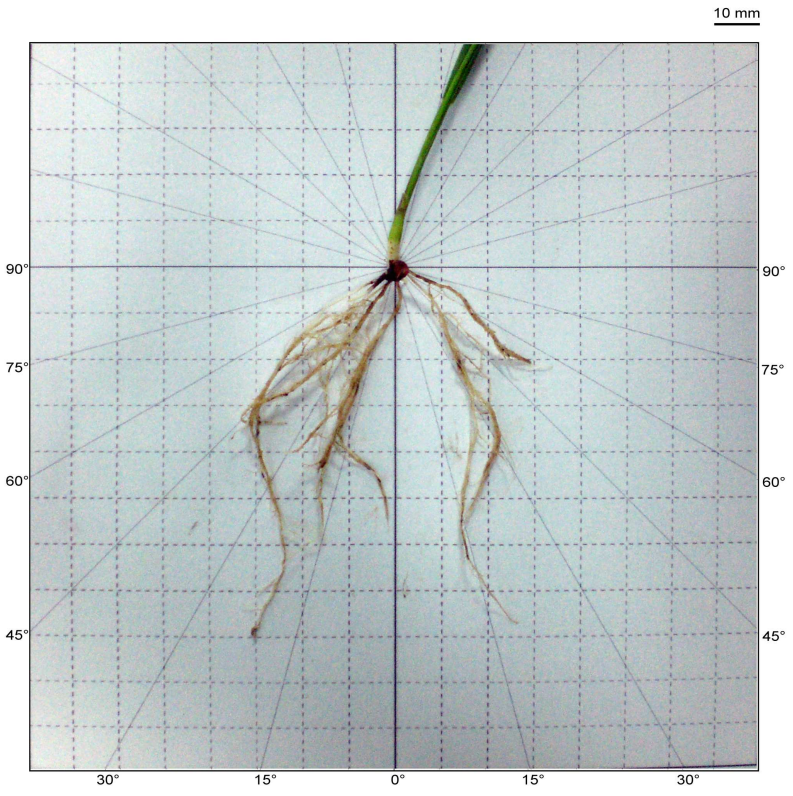

Figure B.10: Wheat 3 datasheet

No.	*08*
Plant:	*Winter Wheat - Triticum aestivum*
	Cordiale
Soil:	*Clay loam*
Germinated:	*12.11.2011*
Planted:	*14.11.2011*
Scanned:	*23.11.2011*
Sample size:	*⌀= 30mm, height = 65mm*
Weight (start):	*59.80g soil-dry*
Weight (end):	*92.68g (10.15g tube, 0.63g plant, 81.90g soil-wet)*
Growth envir.:	*Growthroom, 16/8 photoperiod, 23/18°C*
Scan settings:	*120 keV, 250µA, 0.1mm Cu filter, 1200 projections,*
	750ms exposure time, 1x1 binning, 3x1 avg/skip,
	25.00 µm voxel size, 67min scan time,
	200mm (source-sample), 400mm(source-detector)
Notes:	*1.3015 g/cm³ soil compaction*
	θ_x = 36.95% soil moisture

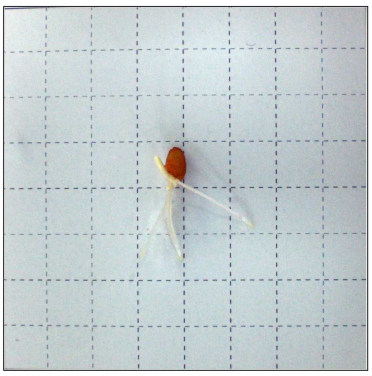

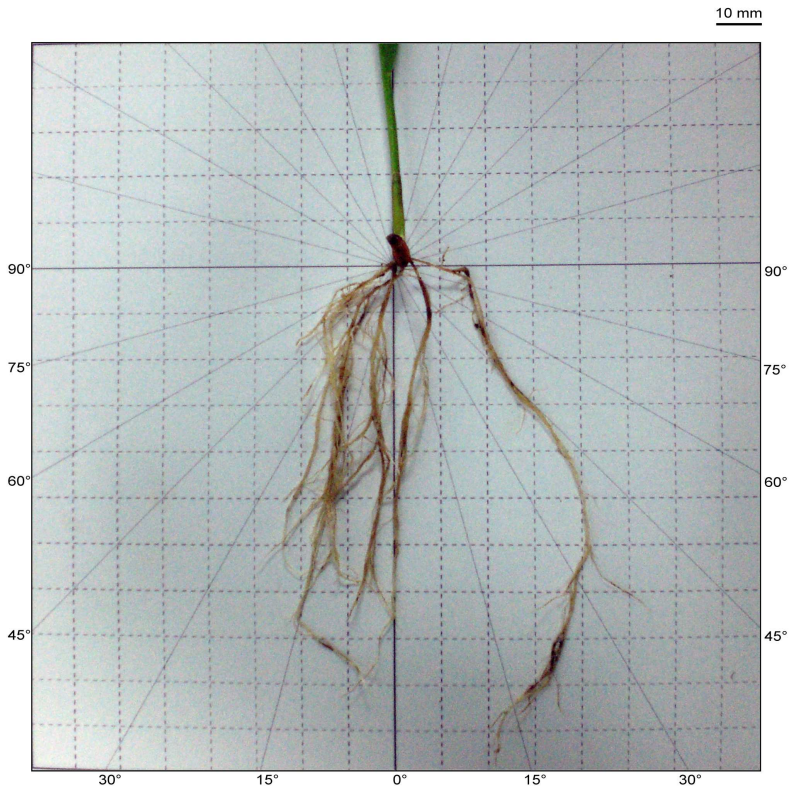

Figure B.11: Wheat 4 datasheet

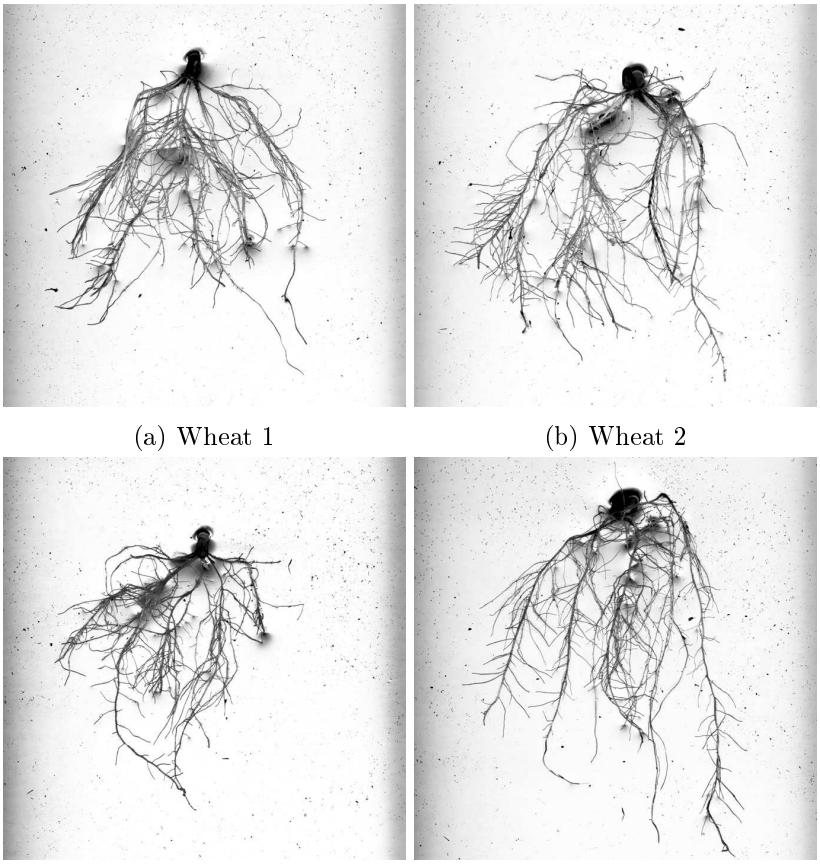

(a) Wheat 1 (b) Wheat 2

(c) Wheat 3 (d) Wheat 4

Figure B.12: Root-washed images of wheat used for two-dimensional analysis

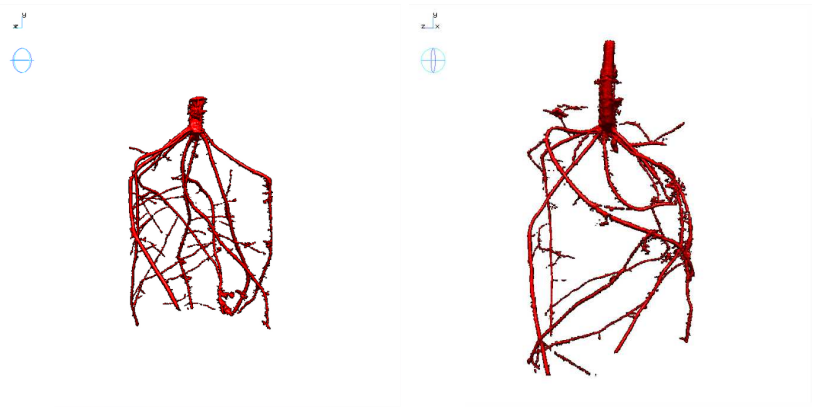

(a) Wheat 1 (b) Wheat 2

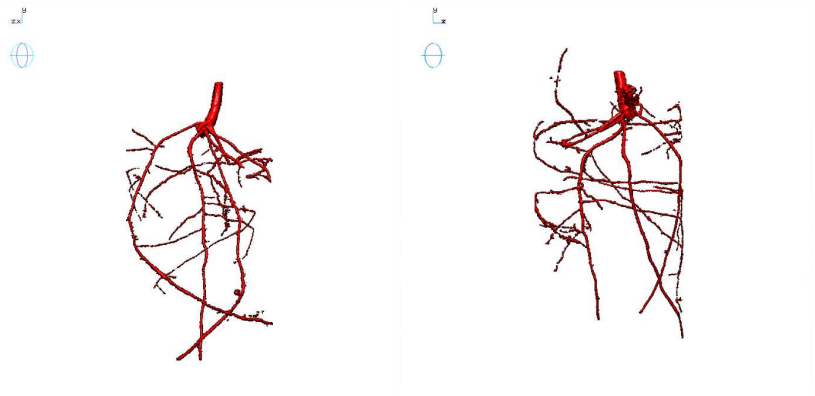

(c) Wheat 3 (d) Wheat 4

Figure B.13: Wheat root systems rendered with volume ray-casting

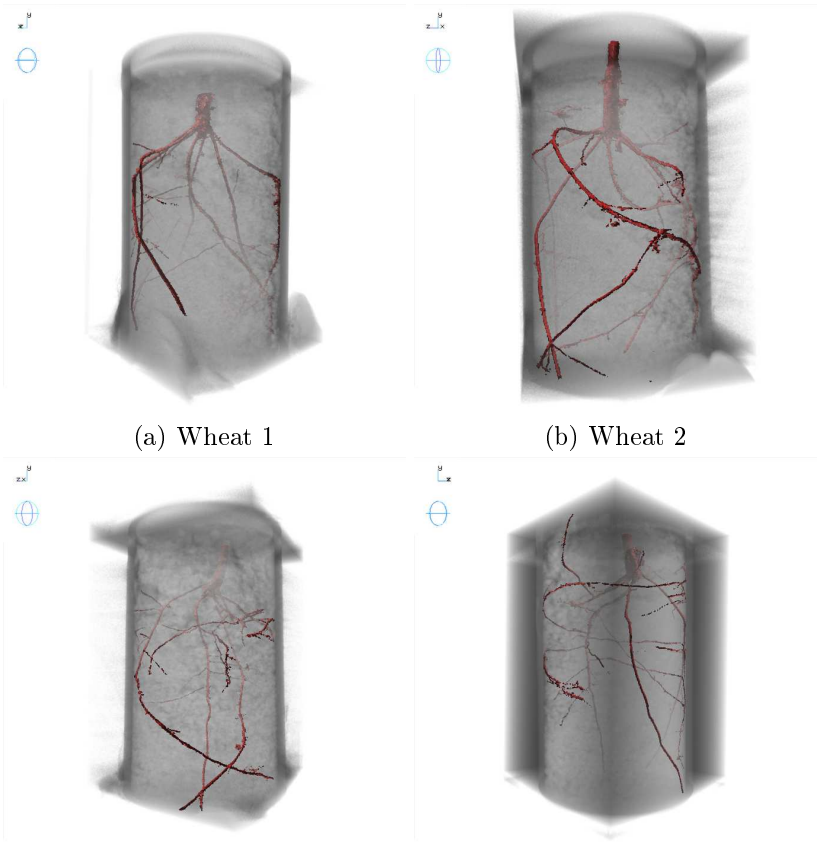

(a) Wheat 1 (b) Wheat 2

(c) Wheat 3 (d) Wheat 4

Figure B.14: Wheat root systems in soil rendered with volume ray-casting

No.	09
Plant:	Tomato - Solanum lycopersicum
Soil:	Loamy sand
Germinated:	03.02.2012
Planted:	05.02.2012
Scanned:	14.02.2012
Sample size:	⌀ = 30mm, height = 65mm
Weight (start):	55.18g soil-dry
Weight (end):	84.96g (10.22g tube, 0.13g plant, 74.61g soil-wet)
Growth envir.:	Growthroom, 16/8 photoperiod, 23/18°C
Scan settings:	120 keV, 250μA, 0.1mm Cu filter, 1200 projections, 750ms exposure time, 1x1 binning, 3x1 avg/skip, 25.00 μm voxel size, 67min scan time, 200mm (source-sample), 400mm(source-detector)
Notes:	1.2009 g/cm³ soil compaction θ_d = 35.21% soil moisture

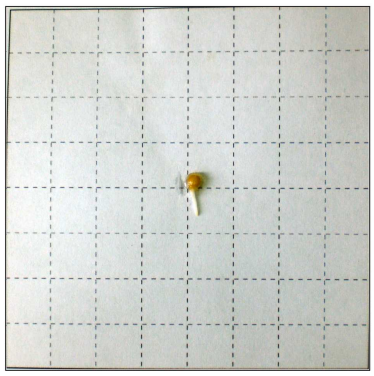

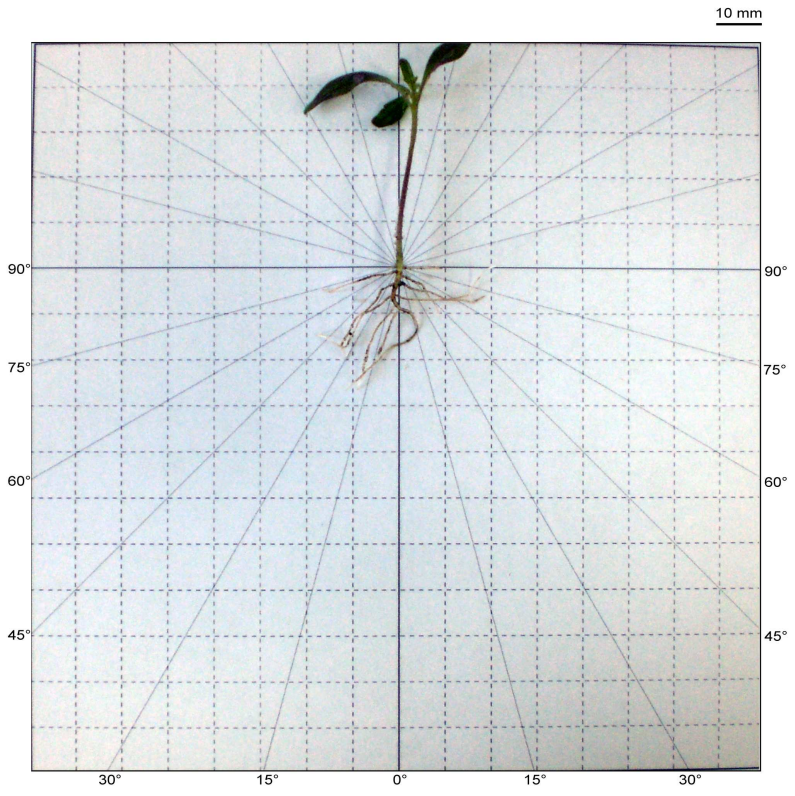

Figure B.15: Tomato 1 datasheet

No.	10
Plant:	Tomato - Solanum lycopersicum
Soil:	Loamy sand
Germinated:	03.02.2012
Planted:	05.02.2012
Scanned:	14.02.2012
Sample size:	⌀ = 30mm, height = 65mm
Weight (start):	56.23g soil-dry
Weight (end):	86.98g (9.66g tube, 0.09g plant, 77.23g soil-wet)
Growth envir.:	Growthroom, 16/8 photoperiod, 23/18°C
Scan settings:	120 keV, 250µA, 0.1mm Cu filter, 1200 projections, 750ms exposure time, 1x1 binning, 3x1 avg/skip, 25.00 µm voxel size, 67min scan time, 200mm (source-sample), 400mm(source-detector)
Notes:	1.2238 g/cm³ soil compaction θ_d = 37.34% soil moisture

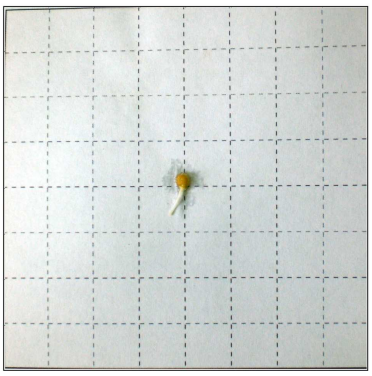

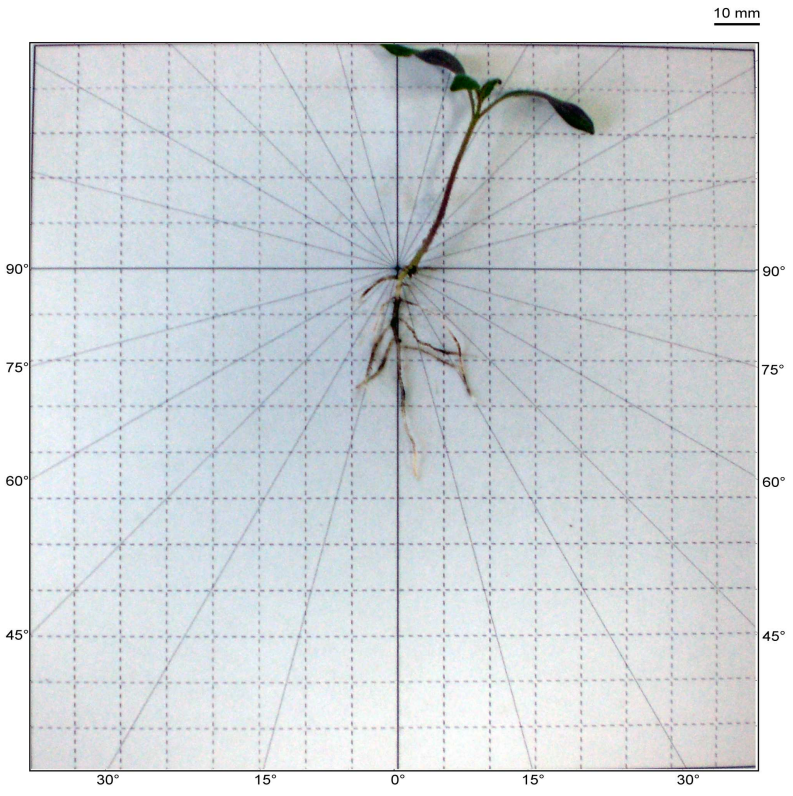

Figure B.16: Tomato 2 datasheet

No.	*11*
Plant:	*Tomato - Solanum lycopersicum*
Soil:	*Clay loam*
Germinated:	*03.02.2012*
Planted:	*05.02.2012*
Scanned:	*14.02.2012*
Sample size:	*⌀ = 30mm, height = 65mm*
Weight (start):	*53.88g soil-dry*
Weight (end):	*85.06g (10.13g tube, 0.09g plant, 74.84g soil-wet)*
Growth envir.:	*Growthroom, 16/8 photoperiod, 23/18°C*
Scan settings:	*120 keV, 250µA, 0.1mm Cu filter, 1200 projections,*
	750ms exposure time, 1x1 binning, 3x1 avg/skip,
	25.00 µm voxel size, 67min scan time,
	200mm (source-sample), 400mm(source-detector)
Notes:	*1.1726 g/cm³ soil compaction*
	θ_d = 38.90% soil moisture

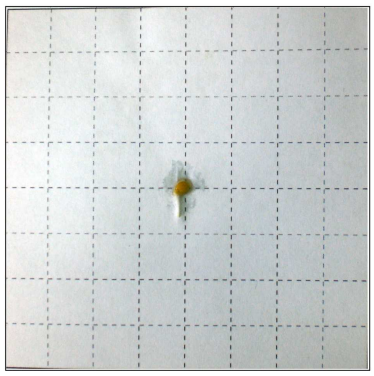

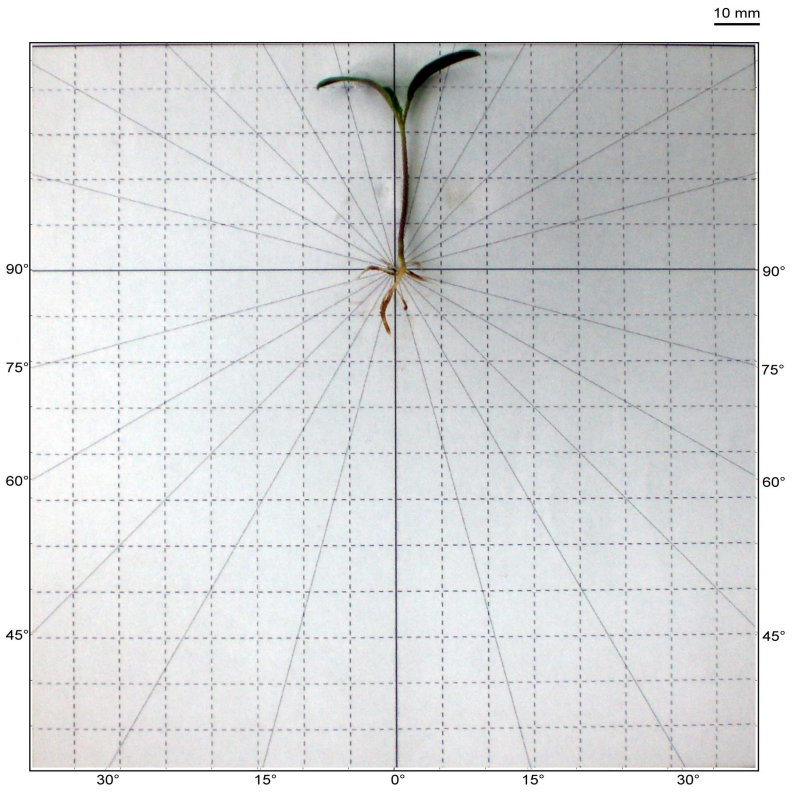

Figure B.17: Tomato 3 datasheet

No.	12
Plant:	Tomato - Solanum lycopersicum
Soil:	Clay loam
Germinated:	03.02.2012
Planted:	05.02.2012
Scanned:	14.02.2012
Sample size:	⌀ = 30mm, height = 65mm
Weight (start):	55.60g soil-dry
Weight (end):	86.10g (9.96g tube, 0.08g plant, 76.06g soil-wet)
Growth envir.:	Growthroom, 16/8 photoperiod, 23/18°C
Scan settings:	120 keV, 250µA, 0.1mm Cu filter, 1200 projections, 750ms exposure time, 1x1 binning, 3x1 avg/skip, 25.00 µm voxel size, 67min scan time, 200mm (source-sample), 400mm(source-detector)
Notes:	1.2112 g/cm³ soil compaction θ_d = 36.79% soil moisture

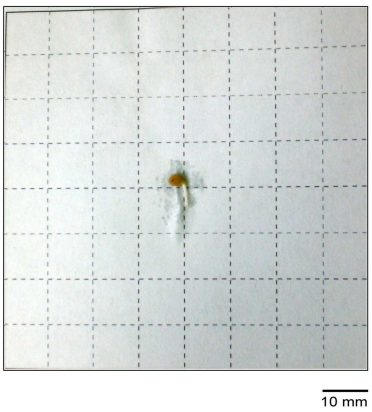

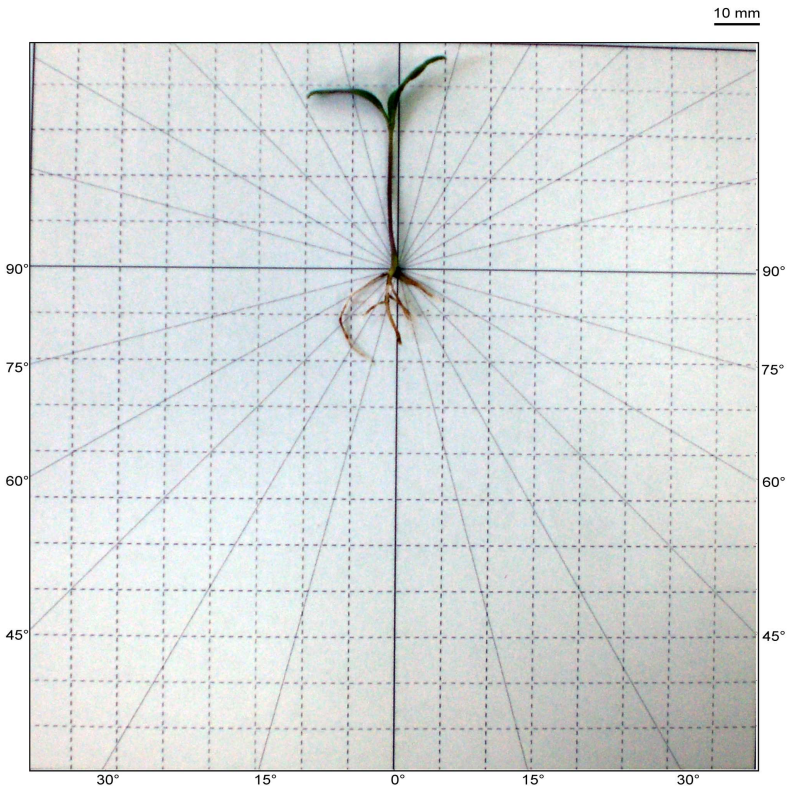

Figure B.18: Tomato 4 datasheet

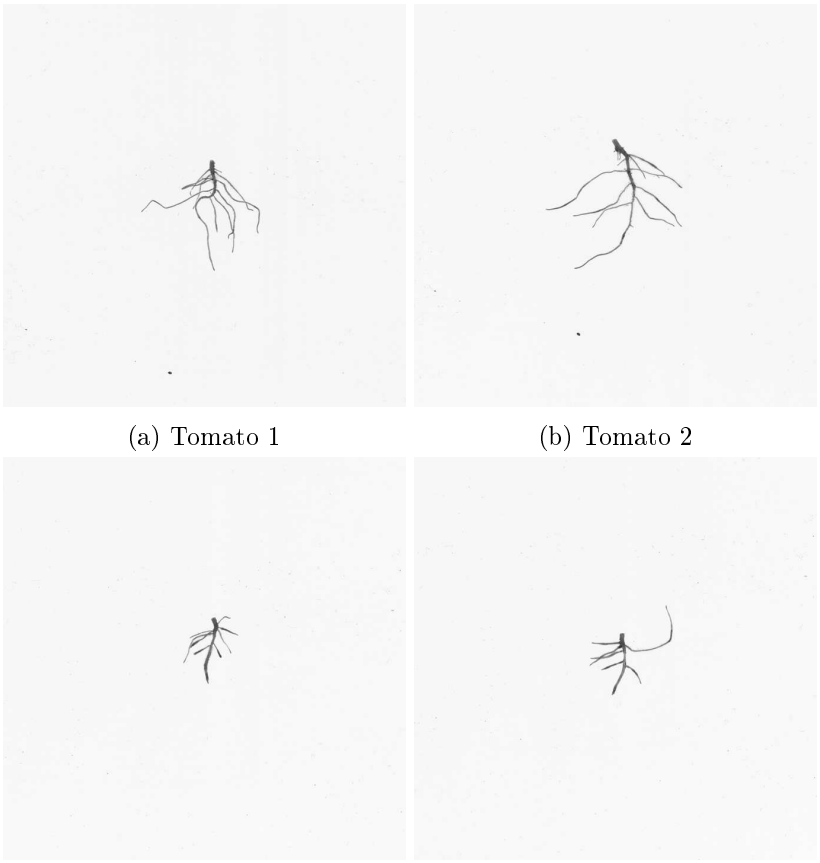

(a) Tomato 1 (b) Tomato 2

(c) Tomato 3 (d) Tomato 4

Figure B.19: Root-washed images of tomato used for two-dimensional analysis

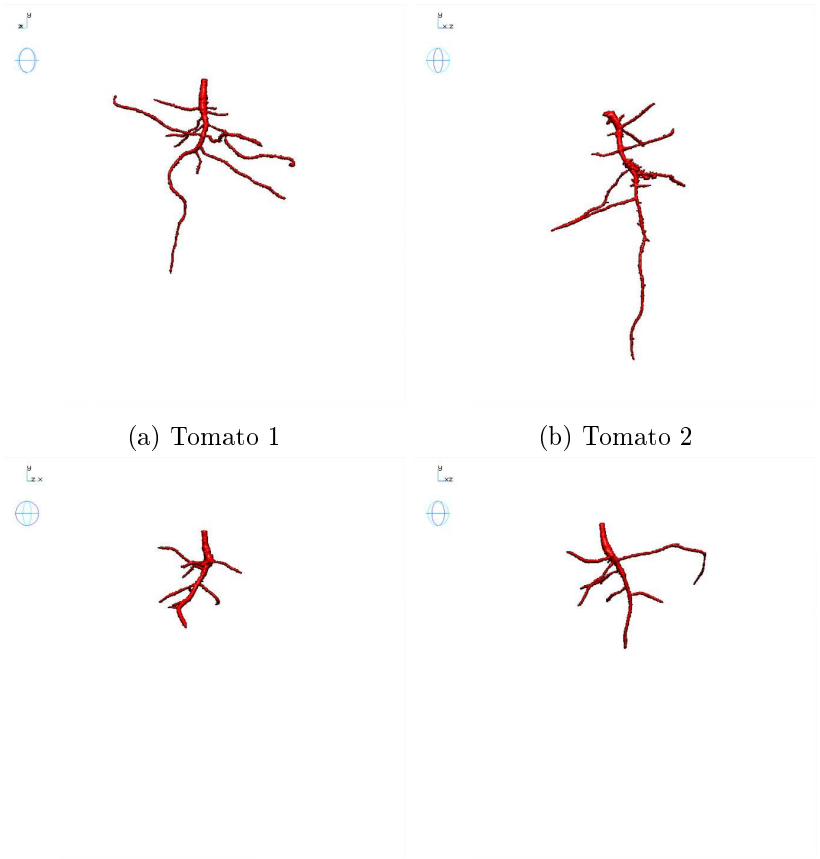

(a) Tomato 1

(b) Tomato 2

(c) Tomato 3

(d) Tomato 4

Figure B.20: Tomato root systems rendered with volume ray-casting

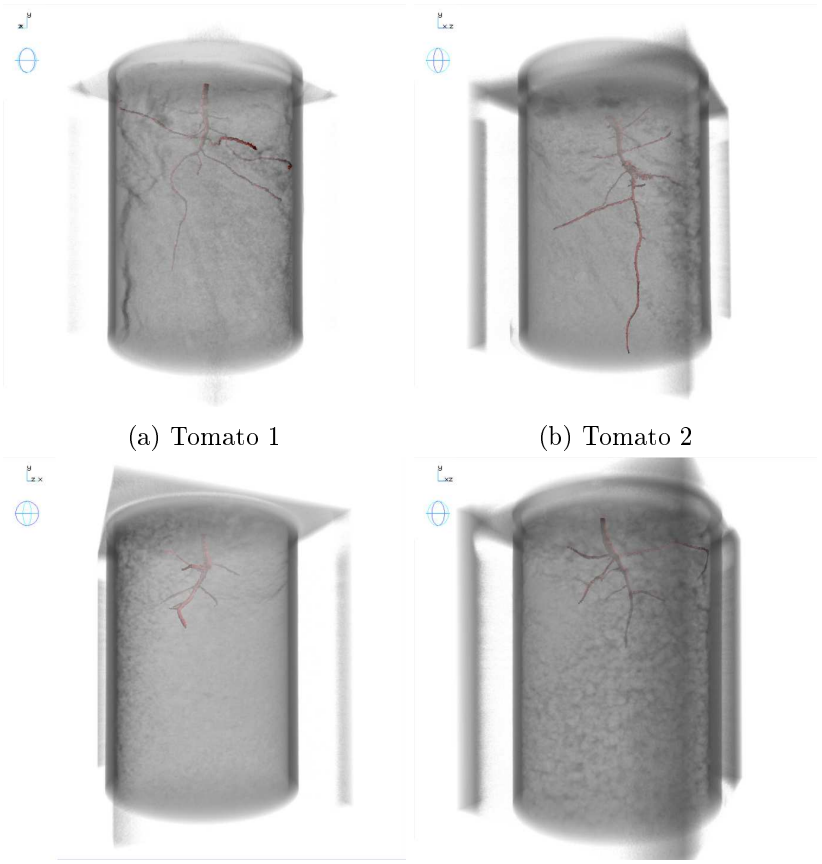

(a) Tomato 1 (b) Tomato 2

(c) Tomato 3 (d) Tomato 4

Figure B.21: Tomato root systems in soil rendered with volume ray-casting

Bibliography

Ikram E. Abdou and Nicolas J. Dusaussoy. Survey of image quality measurements. In *Proceedings of 1986 ACM Fall joint computer conference*, ACM '86, pages 71–78, Los Alamitos, CA, USA, 1986. IEEE Computer Society Press. ISBN 0-8186-4743-4.

James Ambrose. Computerized transverse axial scanning (tomography): Part 2. clinical application. *British Journal of Radiology*, 46(552):1023–1047, 1973. doi: 10.1259/0007-1285-46-552-1023.

Olof Andrèn, Kàlmàn Rajkai, and Thomas Kätterer. A non-destructive technique for studies of root distribution in relation to soil moisture. *Agriculture, Ecosystems & Environment*, 34(1-4):269–278, 1991. ISSN 0167-8809. doi: 10.1016/0167-8809(91)90114-D.

Olof Andrèn, Helena Elmquist, and Ann-Charlotte Hansson. Recording, processing and analysis of grass root images from a rhizotron. *Plant and Soil*, 185:259–264, 1996. ISSN 0032-079X. doi: 10.1007/BF02257531.

Anil, Park, Phipps, and Miller. Temperate intercropping of cereals for forage: a review of the potential for growth and utilization with particular reference to the uk. *Grass and Forage Science*, 53(4):301–317, 1998. ISSN 1365-2494. doi: 10.1046/j.1365-2494.1998.00144.x.

Frank Antonsen, Anders Johnsson, Cecilia Futsaether, and Jostein Krane. Nuclear magnetic resonance imaging in studies of gravitropism in soil mixtures. *New Phytologist*, 142(1):59–66, 1999. ISSN 1469-8137. doi: 10.1046/j.1469-8137.1999.00369.x.

João Lobo Antunes. Egas moniz and cerebral angiography. *Journal of Neurosurgery*, 40(4):247–432, 1974.

Patrick Armengaud, Kevin Zambaux, Adrian Hills, Ronan Sulpice, Richard J. Pattison, Michael R. Blatt, and Anna Amtmann. Ez-rhizo: integrated software for the fast and accurate measurement of root system architecture. *The Plant Journal*, 57(5):945–956, 2009. ISSN 1365-313X. doi: 10.1111/j.1365-313X.2008.03739.x.

David Arthur and Sergei Vassilvitskii. k-means++: the advantages of careful seeding. In *Proceedings of the eighteenth annual ACM-SIAM symposium on Discrete algorithms*, SODA '07, pages 1027–1035, Philadelphia, PA, USA, 2007. Society for Industrial and Applied Mathematics. ISBN 978-0-898716-24-5.

Jean-Francois Aujol, Gilles Aubert, and Laure Blanc-Feraud. Wavelet-based level set evolution for classification of textured images. *Image Processing, IEEE Transactions on*, 12(12):1634–1641, 2003. ISSN 1057-7149. doi: 10.1109/TIP.2003.819309.

Bradford C. Barber, David P. Dobkin, and Hannu Huhdanpaa. The quickhull algorithm for convex hulls. *ACM Transactions on Mathematical Software (TOMS)*, 22(4):469–483, 1996. ISSN 0098-3500. doi: 10.1145/235815.235821.

Julia F. Barrett and Nicholas Keat. Artifacts in ct: Recognition and avoidance. *Radiographics*, 24(6):1679–1691, 2004. doi: 10.1148/rg.246045065.

Suzie Bash, Pablo J. Villablanca, Reza Jahan, Gary Duckwiler, Monica Tillis, Chelsea Kidwell, Jeffrey Saver, and James Sayre. Intracranial vascular stenosis and occlusive disease: Evaluation with ct angiography, mr angiography, and digital subtraction angiography. *American Journal of Neuroradiology*, 26(5):1012–1021, 2005.

Malcolm J. Bennett, Alan Marchant, Haydn G. Green, Sean T. May, Sally P. Ward, Paul A. Millner, Amanda R. Walker, Burkhard Schulz, and Kenneth A. Feldmann. Arabidopsis aux1 gene: A permease-like regulator of root gravitropism. *Science*, 273(5277):948–950, 1996. doi: 10.1126/science.273.5277.948.

Paul J. Besl and Neil D. McKay. A method for registration of 3-d shapes. *Pattern Analysis and Machine Intelligence, IEEE Transactions on*, 14(2):239–256, 1992. ISSN 0162-8828. doi: 10.1109/34.121791.

Anil Bhattacharyya. On a measure of divergence between two statistical populations defined by their probability distributions. *Bulletin of the Calcutta Mathematical Society*, 35(99-109):4, 1943.

Eric J. Biddinger, Chunming Liu, Robert J. Joly, and K. G. Raghothama. Physiological and molecular responses of aeroponically grown tomato plants to phosphorus deficiency. *Journal of the American Society for Horticultural Science*, 123(2):330–333, 1998.

Norman Ernest Borlaug. *The green revolution, peace and humanity*. Centro Internacional de Mejoramiento de Maíz y Trigo Mexico City, 1970.

Paul A. Bottomley, Hugo H. Rogers, and Thomas H. Foster. Nmr imaging shows water distribution and transport in plant root systems in situ. *Proceedings of the National Academy of Sciences*, 83(1):87–89, 1986.

Tjeerd J. Bouma, Kai L. Nielsen, and Bas Koutstaal. Sample preparation and scanning protocol for computerised analysis of root length and diameter. *Plant and Soil*, 218(1-2):185–196, 2000. ISSN 0032-079X. doi: 10.1023/A:1014905104017.

Lisa Gottesfeld Brown. A survey of image registration techniques. *ACM Computing Surveys*, 24(4):325–376, 1992. ISSN 0360-0300. doi: 10.1145/146370.146374.

Thorsten M. Buzug. *Computed Tomography - From Photon Statistics to Modern Cone-Beam CT*. Springer, 1st edition, 2008. ISBN 9783642072574, 9783540394075.

Brian Cabral, Nancy Cam, and Jim Foran. Accelerated volume rendering and tomographic reconstruction using texture mapping hardware. In *Proceedings of the 1994 symposium on Volume visualization*, VVS '94, pages 91–98, New York, NY, USA, 1994. ACM. ISBN 0-89791-741-3. doi: 10.1145/197938.197972.

George G. Cameron and Peter E. Undrill. Rendering volumetric medical image data on a simd-architecture computer. In *Proceedings of the Third Eurographics Workshop on Rendering*, pages 135–145, 1992.

Kevin Cannons. A review of visual tracking. Technical report, Department of Computer Science and Engineering, York University, Toronto, Canada, Technical Report CSE-2008-07, 2008.

Andrea Carminati, Ahmad B. Moradi, Doris Vetterlein, Peter Vontobel, Eberhard Lehmann, Ulrich Weller, Hans-Jörg Vogel, and Sascha E. Oswald. Dynamics of soil water content in the rhizosphere. *Plant and Soil*, 332:163–176, 2010. ISSN 0032-079X. doi: 10.1007/s11104-010-0283-8.

Brenda B. Casper and Robert B. Jackson. Plant competition underground. *Annual Review of Ecology and Systematics*, 28:545–570, 1997. ISSN 00664162.

Sung-Hyuk Cha. Comprehensive survey on distance/similarity measures between probability density functions. *International Journal of Mathematical Models and Methods in Applied Sciences*, 1(4):300–307, 2007.

Tony Chan and Wei Zhu. Level set based shape prior segmentation. In *Computer Vision and Pattern Recognition, 2005. CVPR 2005. IEEE Computer Society Conference on*, volume 2, pages 1164–1170, 2005. doi: 10.1109/CVPR.2005.212.

Tony F. Chan and Luminita A. Vese. Active contours without edges. *Image Processing, IEEE Transactions on*, 10(2):266–277, 2001a. ISSN 1057-7149. doi: 10.1109/83.902291.

Tony F. Chan and Luminita A. Vese. A level set algorithm for minimizing the mumford-shah functional in image processing. In *Variational and Level Set Methods in Computer Vision, 2001. Proceedings. IEEE Workshop on*, pages 161–168, 2001b. doi: 10.1109/VLSM.2001.938895.

Subhasis Chaudhuri, Shankar Chatterjee, Norman Katz, Mark Nelson, and Michael Goldbaum. Detection of blood vessels in retinal images using two-dimensional matched filters. *Medical Imaging, IEEE Transactions on*, 8 (3):263–269, 1989. ISSN 0278-0062. doi: 10.1109/42.34715.

U. N. Chaudhuri, R. B. Burnett, M. B. Kirkham, and E. T. Kanemasu. Effect of carbon dioxide on sorghum yield, root growth, and water use. *Agricultural and Forest Meteorology*, 37(2):109–122, 1986. ISSN 0168-1923. doi: 10.1016/0168-1923(86)90002-X.

David L. Chopp. Computing minimal surfaces via level set curvature flow. *Journal of Computational Physics*, 106(1):77–91, 1993.

Albert C. S. Chung and Alison J. Noble. Statistical 3d vessel segmentation using a rician distribution. In Chris Taylor and Alain Colchester, editors, *Medical Image Computing and Computer-Assisted Intervention - MICCAI'99*, volume 1679 of *Lecture Notes in Computer Science*, pages 82–89. Springer Berlin Heidelberg, 1999. ISBN 978-3-540-66503-8. doi: 10.1007/10704282_9.

L. J. Clark, W. R. Whalley, R. A. Leigh, A. R. Dexter, and P. B. Barraclough. Evaluation of agar and agarose gels for studying mechanical impedance in rice roots. *Plant and Soil*, 207(1):37–43, 1999. ISSN 0032-079X. doi: 10.1023/A:1004489501678.

Randy T. Clark, Robert B. MacCurdy, Janelle K. Jung, Jon E. Shaff, Susan R. McCouch, Daniel J. Aneshansley, and Leon V. Kochian. Three-dimensional root phenotyping with a novel imaging and software platform. *Plant Physiology*, 156(2):455–465, 2011. doi: 10.1104/pp.110.169102.

Randy T. Clark, Adam N. Famoso, Keyan Zhao, Jon E. Shaff, Eric J. Craft, Carlos D. Bustamante, Susan R. McCouch, Daniel J. Aneshansley, and Leon V. Kochian. High-throughput two-dimensional root system phenotyping platform facilitates genetic analysis of root growth and development. *Plant, Cell & Environment*, 36(2):454–466, 2013. ISSN 1365-3040. doi: 10.1111/j.1365-3040.2012.02587.x.

Benjamin Coifman, David Beymer, Philip McLauchlan, and Jitendra Malik. A real-time computer vision system for vehicle tracking and traffic surveillance. *Transportation Research Part C: Emerging Technologies*, 6(4):271–288, 1998. ISSN 0968-090X. doi: http://dx.doi.org/10.1016/S0968-090X(98)00019-9.

Renè Collorec and Jean Louis Coatrieux. Vectorial tracking and directed contour finder for vascular network in digital subtraction angiography. *Pattern Recognition Letters*, 8(5):353–358, 1988. ISSN 0167-8655. doi: 10.1016/0167-8655(88)90086-4.

Dorin Comaniciu, Visvanathan Ramesh, and Peter Meer. Real-time tracking of non-rigid objects using mean shift. In *Computer Vision and Pattern*

Recognition, 2000. Proceedings. IEEE Conference on, volume 2, pages 142–149, 2000. doi: 10.1109/CVPR.2000.854761.

Patrick L. Combettes and Jian Luo. An adaptive level set method for non-differentiable constrained image recovery. *Image Processing, IEEE Transactions on*, 11(11):1295–1304, 2002. ISSN 1057-7149. doi: 10.1109/TIP.2002.804527.

Allan M. Cormack. Representation of a function by its line integrals, with some radiological applications. *Journal of Applied Physics*, 34(9):2722–2727, 1963. ISSN 0021-8979. doi: 10.1063/1.1729798.

James M. Cortese and Brian P. Dyre. Perceptual similarity of shapes generated from fourier descriptors. *Journal of Experimental Psychology: Human Perception and Performance*, 22(1):133–143, 1996.

Daniel Cremers and Stefano Soatto. A pseudo-distance for shape priors in level set segmentation. In *2nd IEEE workshop on variational, geometric and level set methods in computer vision*, pages 169–176, 2003.

Daniel Cremers, Mikael Rousson, and Rachid Deriche. A review of statistical approaches to level set segmentation: Integrating color, texture, motion and shape. *International Journal of Computer Vision*, 72(2):195–215, 2007. ISSN 0920-5691. doi: 10.1007/s11263-006-8711-1.

Bernard Dennis Cullity. *Element of X-ray Diffraction*. Addison-Wesley Publishing Company, Inc., 2nd edition, 1978.

Ian A. Cunningham and Rodney Shaw. Signal-to-noise optimization of medical imaging systems. *Journal of the Optical Society of America - A*, 16 (3):621–632, 1999. doi: 10.1364/JOSAA.16.000621.

Per-Erik Danielsson. Euclidean distance mapping. *Computer Graphics and Image Processing*, 14(3):227–248, 1980. ISSN 0146-664X. doi: 10.1016/0146-664X(80)90054-4.

Bruno De Man and Samit Basu. A study of noise and spatial resolution for 2d and 3d filtered backprojection reconstruction. In *Nuclear Science Symposium Conference Record, 2004 IEEE*, volume 6, pages 3937–3939, 2004. doi: 10.1109/NSSMIC.2004.1466739.

Edsger W. Dijkstra. A note on two problems in connexion with graphs. *Numerische Mathematik*, 1:269–271, 1959. ISSN 0029-599X. doi: 10.1007/BF01386390.

Ming Ding, Anders Odgaard, and Ivan Hvid. Accuracy of cancellous bone volume fraction measured by micro-ct scanning. *Journal of Biomechanics*, 32(3):323–326, 1999. ISSN 0021-9290. doi: 10.1016/S0021-9290(98)00176-6.

Robert A. Drebin, Loren Carpenter, and Pat Hanrahan. Volume rendering. *SIGGRAPH Computer Graphics*, 22(4):65–74, 1988. ISSN 0097-8930. doi: 10.1145/378456.378484.

Marc Droske and Wolfgang Ring. A mumfordshah levelset approach for geometric image registration. *SIAM Journal on Applied Mathematics*, 66 (6):2127–2148, 2006. doi: 10.1137/050630209.

Shigeru Eiho and Ying Qian. Detection of coronary artery tree using morphological operator. In *Computers in Cardiology 1997*, pages 525–528, 1997. doi: 10.1109/CIC.1997.647950.

Todd T. Elvins. A survey of algorithms for volume visualization. *SIGGRAPH Computer Graphics*, 26(3):194–201, 1992. ISSN 0097-8930. doi: 10.1145/142413.142427.

Dominik M. Endres and Johannes E. Schindelin. A new metric for probability distributions. *Information Theory, IEEE Transactions on*, 49(7):1858–1860, 2003. ISSN 0018-9448. doi: 10.1109/TIT.2003.813506.

Robert Robert Eugene Evenson and Douglas Gollin. *Crop variety improvement and its effect on productivity. The impact of international agricultural research*. Cabi, 2003.

Suqin Fang, Randy T. Clark, Ying Zheng, Anjali S. Iyer-Pascuzzi, Joshua S. Weitz, Leon V. Kochian, Herbert Edelsbrunner, Hong Liao, and Philip N. Benfey. Genotypic recognition and spatial responses by rice roots. *Proceedings of the National Academy of Sciences*, 110(7):2670–2675, 2013. doi: 10.1073/pnas.1222821110.

FAO. The state of food and agriculture 2013. food systems for better nutrition, 2013a. URL http://www.fao.org/publications/sofa/en/.

FAO. Fao statistical yearbook 2013 world food and agriculture, 2013b. URL http://www.fao.org/docrep/018/i3107e/i3107e00.htm.

FAO, WFP, and IFAD. The state of food insecurity in the world 2012. economic growth is necessary but not sufficient to accelerate reduction of hunger and malnutrition, 2012. URL http://www.fao.org/publications/sofi/en/.

K. Faulkner and B. M. Moores. Analysis of x-ray computed tomography images using the noise power spectrum and autocorrelation function. *Physics in Medicine and Biology*, 29(11):1343–1352, 1984. doi: 10.1088/0031-9155/29/11/003.

Màrio. A. T. Figueiredo and Josè M. N. Leitão. A nonsmoothing approach to the estimation of vessel contours in angiograms. *Medical Imaging, IEEE Transactions on*, 14(1):162–172, 1995. ISSN 0278-0062. doi: 10.1109/42.370413.

Nicolas Flasque, Michel Desvignes, Jean-Marc Constans, and Marinette Revenu. Acquisition, segmentation and tracking of the cerebral vascular tree on 3d magnetic resonance angiography images. *Medical Image Analysis*, 5(3):173–183, 2001. ISSN 1361-8415. doi: 10.1016/S1361-8415(01)00038-X.

Richard J. Flavel, Christopher N. Guppy, Matthew Tighe, Michelle Watt, Ann McNeill, and Iain M. Young. Non-destructive quantification of cereal roots in soil using high-resolution x-ray tomography. *Journal of Experimental Botany*, 63(7):2503–2511, 2012. doi: 10.1093/jxb/err421.

Helga Förster, James E. Adaskaveg, Do H. Kim, and Michael E. Stanghellini. Effect of phosphite on tomato and pepper plants and on susceptibility of pepper to phytophthora root and crown rot in hydroponic culture. *Plant Disease*, 82(10):1165–1170, 1998. doi: 10.1094/PDIS.1998.82.10.1165.

Alejandro F. Frangi, Wiro J. Niessen, Koen L. Vincken, and Max A. Viergever. Multiscale vessel enhancement filtering. In William M. Wells, Alan Colchester, and Scott Delp, editors, *Medical Image Computing and Computer-Assisted Interventation - MICCAI'98*, volume 1496 of *Lecture Notes in Computer Science*, pages 130–137. Springer Berlin Heidelberg, 1998. ISBN 978-3-540-65136-9. doi: 10.1007/BFb0056195.

Herbert Freeman. On the encoding of arbitrary geometric configurations. *Electronic Computers, IRE Transactions on*, 10(2):260–268, 1961. ISSN 0367-9950. doi: 10.1109/TEC.1961.5219197.

Andrew French, Susana Ubeda-Tomàs, Tara J. Holman, Malcolm J. Bennett, and Tony P. Pridmore. High-throughput quantification of root growth using a novel image-analysis tool. *Plant Physiology*, 150(4):1784–1795, 2009. doi: 10.1104/pp.109.140558.

Hironori Fujita and Kunihiko Syōno. Pis1, a negative regulator of the action of auxin transport inhibitors in arabidopsis thaliana. *The Plant Journal*, 12(3):583–595, 1997. ISSN 1365-313X. doi: 10.1111/j.0960-7412.1997.00583.x.

Cecilia M. Futsaether and Unni Oxaal. A growth chamber for idealized studies of seedling root growth dynamics and structure. *Plant and Soil*, 246:221–230, 2002. ISSN 0032-079X. doi: 10.1023/A:1020609224525.

Luomin Gao, David G. Heath, Brian S. Kuszyk, and Elliot K. Fishman. Automatic liver segmentation technique for three-dimensional visualization of ct data. *Radiology*, 201(2):359–364, 1996.

Donald Geman, Stuart Geman, Christine Graffigne, and Ping Dong. Boundary detection by constrained optimization. *Pattern Analysis and Machine Intelligence, IEEE Transactions on*, 12(7):609–628, 1990. ISSN 0162-8828. doi: 10.1109/34.56204.

Andrew L. Goertzen, Vivek Nagarkar, Robert A. Street, Michael J. Paulus, John M. Boone, and Simon R. Cherry. A comparison of x-ray detectors for mouse ct imaging. *Physics in Medicine and Biology*, 49(23):5251–5265, 2004. doi: 10.1088/0031-9155/49/23/004.

Lee W. Goldman. Principles of ct and ct technology. *Journal of Nuclear Medicine Technology*, 35(3):115–128, 2007. doi: 10.2967/jnmt.107.042978.

JuanFrancisco Gómez-Lopera, José Martínez-Aroza, AurelianoM. Robles-Pérez, and Ramón Román-Roldán. An analysis of edge detection by using the jensen-shannon divergence. *Journal of Mathematical Imaging and Vision*, 13:35–56, 2000. ISSN 0924-9907. doi: 10.1023/A:1008325607354.

Rafael C. Gonzalez and Richard E. Woods. *Digital image processing*. Prentice Hall Press, 2nd edition, 2002. ISBN 0201180758.

Gösta H. Granlund. Fourier preprocessing for hand print character recognition. *Computers, IEEE Transactions on*, C-21(2):195–201, 1972. ISSN 0018-9340. doi: 10.1109/TC.1972.5008926.

Peter J. Gregory. A periscope method for observing root growth and distribution in field soil. *Journal of Experimental Botany*, 30(1):205–214, 1979. doi: 10.1093/jxb/30.1.205.

Peter J. Gregory. Roots, rhizosphere and soil: the route to a better understanding of soil science? *European Journal of Soil Science*, 57(1):2–12, 2006a. ISSN 1365-2389. doi: 10.1111/j.1365-2389.2005.00778.x.

Peter J. Gregory. *Plant Roots: Growth, Activity and Interactions with the Soil*. Wiley-Blackwell, 2006b. ISBN 978-1-4051-1906-1.

Peter J. Gregory and Philippe Hinsinger. New approaches to studying chemical and physical changes in the rhizosphere: an overview. *Plant and Soil*, 211:1–9, 1999. ISSN 0032-079X. doi: 10.1023/A:1004547401951.

Peter J. Gregory, D. J. Hutchison, Derek B. Read, Paul M. Jenneson, Walter B. Gilboy, and Edward J. Morton. Non-invasive imaging of roots with high resolution x-ray micro-tomography. *Plant and Soil*, 255:351–359, 2003. ISSN 0032-079X. doi: 10.1023/A:1026179919689.

Pierre A. Gremaud and Christopher M. Kuster. Computational study of fast methods for the eikonal equation. *SIAM journal on scientific computing*, 27(6):1803–1816, 2006.

Markús Gudmundsson, Essam A. El-Kwae, and Mansur R. Kabuka. Edge detection in medical images using a genetic algorithm. *Medical Imaging, IEEE Transactions on*, 17(3):469–474, 1998. ISSN 0278-0062. doi: 10.1109/42.712136.

Julian Guerrero, Septimiu E. Salcudean, James A. McEwen, Bassam A. Masri, and Savvakis Nicolaou. Real-time vessel segmentation and tracking for ultrasound imaging applications. *Medical Imaging, IEEE Transactions on*, 26(8):1079–1090, 2007. ISSN 0278-0062. doi: 10.1109/TMI.2007.899180.

Markus Hadwiger, Patric Ljung, Christof Rezk Salama, and Timo Ropinski. Advanced illumination techniques for gpu-based volume raycasting. In *ACM SIGGRAPH 2009 Courses*, SIGGRAPH '09, pages 1–166, New York, NY, USA, 2009. ACM. doi: 10.1145/1667239.1667241.

Ben A. Hamza and Hamid Krim. Geodesic object representation and recognition. In Ingela Nyström, Gabriella Sanniti di Baja, and Stina Svensson, editors, *Discrete Geometry for Computer Imagery*, volume 2886 of *Lecture Notes in Computer Science*, pages 378–387. Springer Berlin Heidelberg, 2003. ISBN 978-3-540-20499-2. doi: 10.1007/978-3-540-39966-7_36.

Kenneth M. Hanson. Noise and contrast discrimination in computed tomography. *Radiology of the Skull and Brain: Technical Aspects of Computed Tomography*, 5:3941–3955, 1981.

Caroline Hargreaves, Peter Gregory, and Glyn A. Bengough. Measuring root traits in barley (hordeum vulgaressp. vulgare and ssp. spontaneum) seedlings using gel chambers, soil sacs and x-ray microtomography. *Plant and Soil*, 316:285–297, 2009. ISSN 0032-079X. doi: 10.1007/s11104-008-9780-4.

Arthur G. Haus and Martin J. Yaffe. Screen-film and digital mammography: Image quality and radiation dose considerations. *Radiologic Clinics of North America*, 38(4):871–898, 2000. ISSN 0033-8389. doi: 10.1016/S0033-8389(05)70207-4.

Peter B. R. Hazell and C. Ramasamy. *The green revolution reconsidered.* International Food Policy Research Institute, 1991.

Deo A. Heeraman, Peter H. Crown, and Noorallah G. Juma. A color composite technique for detecting root dynamics of barley (hordeum vulgare l.) from minirhizotron images. *Plant and Soil*, 157:275–287, 1993. ISSN 0032-079X. doi: 10.1007/BF00011056.

Deo A. Heeraman, Jan W. Hopmans, and Volker Clausnitzer. Three dimensional imaging of plant roots in situ with x-ray computed tomography. *Plant and Soil*, 189:167–179, 1997. ISSN 0032-079X. doi: 10.1023/B:PLSO.0000009694.64377.6f.

William R. Hendee and E. Russell Ritenour. *Medical Imaging Physics.* Wiley-Liss, New York, NY, 4th edition, 2002. ISBN 0471382264, 9780471382263.

Gabor T. Herman. *Fundamentals of Computerized Tomography: Image Reconstruction from Projections*. Springer Publishing Company, Incorporated, 2nd edition, 2009. ISBN 185233617X, 9781852336172.

Gabor T. Herman and Hsun Kao Liu. Three-dimensional display of human organs from computed tomograms. *Computer Graphics and Image Processing*, 9(1):1–21, 1979. ISSN 0146-664X. doi: 10.1016/0146-664X(79)90079-0.

R. J. Hilton, D. S. Bhar, and G. F. Mason. A rhizotron for in situ root growth studies. *Canadian Journal of Plant Science*, 49(1):101–104, 1969. doi: 10.4141/cjps69-018.

Margarita L. Himmelbauer, Willibald Loiskandl, and Ferdinand Kastanek. Estimating length, average diameter and surface area of roots using two different image analyses systems. *Plant and Soil*, 260(1-2):111–120, 2004. ISSN 0032-079X. doi: 10.1023/B:PLSO.0000030171.28821.55.

Philippe Hinsinger, George R. Gobran, Peter J. Gregory, and Walter W. Wenzel. Rhizosphere geometry and heterogeneity arising from root-mediated physical and chemical processes. *New Phytologist*, 168(2):293–303, 2005. ISSN 1469-8137. doi: 10.1111/j.1469-8137.2005.01512.x.

Angela Hodge, David Robinson, Bryan S. Griffiths, and Alastair H. Fitter. Nitrogen capture by plants grown in n-rich organic patches of contrasting size and strength. *Journal of Experimental Botany*, 50(336):1243–1252, 1999. doi: 10.1093/jxb/50.336.1243.

Berthold K. P. Horn. Closed-form solution of absolute orientation using unit quaternions. *Journal of the Optical Society of America A*, 4(4):629–642, 1987. doi: 10.1364/JOSAA.4.000629.

Eva Hörster, Rainer Lienhart, and Malcolm Slaney. Image retrieval on large-scale image databases. In *Proceedings of the 6th ACM international conference on Image and video retrieval*, CIVR '07, pages 17–24, New York, NY, USA, 2007. ACM. ISBN 978-1-59593-733-9. doi: 10.1145/1282280.1282283.

Godfrey N. Hounsfield. Computerized transverse axial scanning (tomography): Part 1. description of system. *British Journal of Radiology*, 46(552):1016–1022, 1973. doi: 10.1259/0007-1285-46-552-1016.

Shiying Hu, Eric A. Hoffman, and Joseph M. Reinhardt. Automatic lung segmentation for accurate quantitation of volumetric x-ray ct images. *Medical Imaging, IEEE Transactions on*, 20(6):490–498, 2001. ISSN 0278-0062. doi: 10.1109/42.929615.

Weiming Hu, Tieniu Tan, Liang Wang, and Steve Maybank. A survey on visual surveillance of object motion and behaviors. *Systems, Man, and Cybernetics, Part C: Applications and Reviews, IEEE Transactions on*, 34 (3):334–352, 2004. ISSN 1094-6977. doi: 10.1109/TSMCC.2004.829274.

Keith T. Ingram and Gary A. Leers. Software for measuring root characters from digital images. *Agronomy Journal*, 93:918–922, 2001. doi: 10.2134/agronj2001.934918x.

Michael Isard and Andrew Blake. Condensation - conditional density propagation for visual tracking. *International Journal of Computer Vision*, 29 (1):5–28, 1998. ISSN 0920-5691. doi: 10.1023/A:1008078328650.

Anjali S. Iyer-Pascuzzi, Olga Symonova, Yuriy Mileyko, Yueling Hao, Heather Belcher, John Harer, Joshua S. Weitz, and Philip N. Benfey. Imaging and analysis platform for automatic phenotyping and trait ranking of plant root systems. *Plant Physiology*, 152(3):1148–1157, 2010. doi: 10.1104/pp.109.150748.

Siegfried Jahnke, Marion I. Menzel, Dagmar Van Dusschoten, Gerhard W. Roeb, Jonas Bühler, Senay Minwuyelet, Peter Blümler, Vicky M. Temperton, Thomas Hombach, Matthias Streun, Simone Beer, Maryam Khodaverdi, Karl Ziemons, Heinz H. Coenen, and Ulrich Schurr. Combined mriâĂŞpet dissects dynamic changes in plant structures and functions. *The Plant Journal*, 59(4):634–644, 2009. ISSN 1365-313X. doi: 10.1111/j.1365-313X.2009.03888.x.

Paul M. Jenneson, Walter B. Gilboy, Edward J. Morton, and Peter J. Gregory. An x-ray micro-tomography system optimised for the low-dose study of living organisms. *Applied Radiation and Isotopes*, 58(2):177–181, 2003. ISSN 0969-8043. doi: 10.1016/S0969-8043(02)00310-X.

Mark G. Johnson, David T. Tingey, Donald L. Phillips, and Marjorie J. Storm. Advancing fine root research with minirhizotrons. *Environmental*

and Experimental Botany, 45(3):263–289, 2001. ISSN 0098-8472. doi: 10.1016/S0098-8472(01)00077-6.

Sarang Joshi, Stephen Pizer, P. Thomas Fletcher, Paul Yushkevich, Andrew Thall, and J. S. Marron. Multiscale deformable model segmentation and statistical shape analysis using medial descriptions. *Medical Imaging, IEEE Transactions on*, 21(5):538–550, 2002. ISSN 0278-0062. doi: 10.1109/TMI.2002.1009389.

Anders Kaestner, Martin Schneebeli, and Frank Graf. Visualizing three-dimensional root networks using computed tomography. *Geoderma*, 136(1-2):459–469, 2006. ISSN 0016-7061. doi: 10.1016/j.geoderma.2006.04.009.

James T. Kajiya. The rendering equation. *SIGGRAPH Computer Graphics*, 20(4):143–150, 1986. ISSN 0097-8930. doi: 10.1145/15886.15902.

Avinash C. Kak and Malcolm Slaney. *Principles of Computerized Tomographic Imaging*. IEEE Press, 1988.

Willi A. Kalender. X-ray computed tomography. *Physics in Medicine and Biology*, 51(13):R29–43, 2006. doi: 10.1088/0031-9155/51/13/R03.

Rudolph E. Kalman and Richard S. Bucy. New results in linear filtering and prediction theory. *Journal of Basic Engineering*, 83(3):95–108, 1961. doi: 10.1115/1.3658902.

Michael Kass, Andrew Witkin, and Demetri Terzopoulos. Snakes: Active contour models. *International Journal of Computer Vision*, 1(4):321–331, 1988. ISSN 0920-5691. doi: 10.1007/BF00133570.

Eric Keppel. Approximating complex surfaces by triangulation of contour lines. *IBM Journal of Research and Development*, 19(1):2–11, 1975. ISSN 0018-8646. doi: 10.1147/rd.191.0002.

Richard A. Ketcham and William D. Carlson. Acquisition, optimization and interpretation of x-ray computed tomographic imagery: applications to the geosciences. *Computers & Geosciences*, 27(4):381–400, 2001. ISSN 0098-3004. doi: 10.1016/S0098-3004(00)00116-3.

Zia Khan, Tucker Balch, and Frank Dellaert. Mcmc-based particle filtering for tracking a variable number of interacting targets. *Pattern Analysis*

and Machine Intelligence, IEEE Transactions on, 27(11):1805–1819, 2005. ISSN 0162-8828. doi: 10.1109/TPAMI.2005.223.

Marie F. Kijewski and Philip F. Judy. The noise power spectrum of ct images. *Physics in Medicine and Biology*, 32(5):565–575, 1987. doi: 10.1088/0031-9155/32/5/003.

Thomas Andrew Knight. On the direction of the radicle and germen during the vegetation of seeds. *Philosophical Transactions of the Royal Society of London*, 96:99–108, 1806. ISSN 02610523.

Thomas Andrew Knight. On the origin and formation of roots. *Philosophical Transactions of the Royal Society of London*, 99:169–176, 1809. ISSN 02610523.

Thomas Andrew Knight. On the causes which influence the direction of the growth of roots. *Philosophical Transactions of the Royal Society of London*, 101:209–219, 1811. ISSN 02610523.

E. G. Kokko, K. M. Volkmar, B. E. Gowen, and T. Entz. Determination of total root surface area in soil core samples by image analysis. *Soil and Tillage Research*, 26(1):33–43, 1993. ISSN 0167-1987. doi: 10.1016/0167-1987(93)90084-3.

John E. Koss, F. D. Newman, T. K. Johnson, and D. L. Kirch. Abdominal organ segmentation using texture transforms and a hopfield neural network. *Medical Imaging, IEEE Transactions on*, 18(7):640–648, 1999. ISSN 0278-0062. doi: 10.1109/42.790463.

Dane P. Kottke and Ying Sun. Segmentation of coronary arteriograms by iterative ternary classification. *Biomedical Engineering, IEEE Transactions on*, 37(8):778–785, 1990. ISSN 0018-9294. doi: 10.1109/10.102793.

Jens Krüger and Rüdiger Westermann. Acceleration techniques for gpu-based volume rendering. In *Proceedings of the 14th IEEE Visualization 2003 (VIS'03)*, VIS '03, pages 287–292, Washington, DC, USA, 2003. IEEE Computer Society. ISBN 0-7695-2030-8. doi: 10.1109/VIS.2003.10001.

Rolf O. Kuchenbuch and Keith T. Ingram. Image analysis for non-destructive and non-invasive quantification of root growth and soil water content

in rhizotrons. *Journal of Plant Nutrition and Soil Science*, 165(5):573–581, 2002. ISSN 1522-2624. doi: 10.1002/1522-2624(200210)165:5<573::AID-JPLN573>3.0.CO;2-W.

Jan-Martin Kuhnigk, Horst Hahn, Milo Hindennach, Volker Dicken, Stefan Krass, and Heinz-Otto Peitgen. Lung lobe segmentation by anatomy-guided 3d watershed transform. *Medical Imaging 2003: Image Processing*, 5032:1482–1490, 2003. doi: 10.1117/12.480321.

Solomon Kullback and Richard A. Leibler. On information and sufficiency. *The Annals of Mathematical Statistics*, 22(1):79–86, 1951. ISSN 00034851.

Philippe Lacroute and Marc Levoy. Fast volume rendering using a shear-warp factorization of the viewing transformation. In *Proceedings of the 21st annual conference on Computer graphics and interactive techniques*, SIGGRAPH '94, pages 451–458, New York, NY, USA, 1994. ACM. ISBN 0-89791-667-0. doi: 10.1145/192161.192283.

Longin Jan Latecki. Mpeg-7 core experiment ce-shape-1 test set. URL http://www.dabi.temple.edu/~shape/MPEG7/dataset.html.

Jacques Le Bot, Valèrie Serra, Josè Fabre, Xavier Draye, Stèphane Adamowicz, and Loïc Pagès. Dart: a software to analyse root system architecture and development from captured images. *Plant and Soil*, 326:261–273, 2010. ISSN 0032-079X. doi: 10.1007/s11104-009-0005-2.

Joseph K. Leader, Bin Zheng, Robert M. Rogers, Frank C. Sciurba, Andrew Perez, Brian E. Chapman, Sanjay Patel, Carl R. Fuhrman, and David Gur. Automated lung segmentation in x-ray computed tomography: development and evaluation of a heuristic threshold-based scheme. *Academic Radiology*, 10(11):1224–1236, 2003. ISSN 1076-6332. doi: 10.1016/S1076-6332(03)00380-5.

R. J. Lebowitz. Digital image analysis measurement of root length and diameter. *Environmental and Experimental Botany*, 28(3):267–273, 1988. ISSN 0098-8472. doi: 10.1016/0098-8472(88)90037-8.

Daniel Leitner, Sabine Klepsch, Astrid Knieß, and Andrea Schnepf. The algorithmic beauty of plant roots - an l-system model for dynamic root

growth simulation. *Mathematical and Computer Modelling of Dynamical Systems*, 16(6):575–587, 2010. doi: 10.1080/13873954.2010.491360.

Clifford Levi, Joel E. Gray, Edwin C. McCullough, and Robert R. Hattery. The unreliability of ct numbers as absolute values. *American Journal of Roentgenology*, 139(3):443–447, 1982.

Marc Levoy. Display of surfaces from volume data. *Computer Graphics and Applications, IEEE*, 8(3):29–37, 1988. ISSN 0272-1716. doi: 10.1109/38.511.

Marc Levoy. Ct scan of the stanford terra-cotta bunny, 2000. URL http://graphics.stanford.edu/data/voldata/.

Chunming Li, Chenyang Xu, Changfeng Gui, and Martin D. Fox. Level set evolution without re-initialization: a new variational formulation. In *Computer Vision and Pattern Recognition, 2005. CVPR 2005. IEEE Computer Society Conference on*, volume 1, pages 430–436, 2005. doi: 10.1109/CVPR.2005.213.

Yuan Li, Haizhou Ai, T. Yamashita, Shihong Lao, and M. Kawade. Tracking in low frame rate video: A cascade particle filter with discriminative observers of different life spans. *Pattern Analysis and Machine Intelligence, IEEE Transactions on*, 30(10):1728–1740, 2008. ISSN 0162-8828. doi: 10.1109/TPAMI.2008.73.

Jianhua Lin. Divergence measures based on the shannon entropy. *Information Theory, IEEE Transactions on*, 37(1):145–151, 1991. ISSN 0018-9448. doi: 10.1109/18.61115.

Joakim Lindblad. Surface area estimation of digitized 3d objects using weighted local configurations. *Image and Vision Computing*, 23(2):111–122, 2005. ISSN 0262-8856. doi: 10.1016/j.imavis.2004.06.012.

Guillaume Lobet, Loïc Pagès, and Xavier Draye. A novel image-analysis toolbox enabling quantitative analysis of root system architecture. *Plant Physiology*, 157(1):29–39, 2011. doi: 10.1104/pp.111.179895.

Sven Loncaric. A survey of shape analysis techniques. *Pattern Recognition*, 31(8):983–1001, 1998. ISSN 0031-3203. doi: 10.1016/S0031-2023(97)00122-2.

Sven Loncaric, Atam P. Dhawan, Joseph Broderick, and Thomas Brott. 3-d image analysis of intra-cerebral brain hemorrhage from digitized ct films. *Computer Methods and Programs in Biomedicine*, 46(3):207–216, 1995. ISSN 0169-2607. doi: 10.1016/0169-2607(95)01620-9.

Melinda Lontoc-Roy, Pierre Dutilleul, Shiv O. Prasher, Liwen Han, and Donald L. Smith. Computed tomography scanning for three-dimensional imaging and complexity analysis of developing root systems. *Canadian Journal of Botany*, 83(11):1434–1442, 2005. doi: 10.1139/b05-118.

Melinda Lontoc-Roy, Pierre Dutilleul, Shiv O. Prasher, Liwen Han, Thomas Brouillet, and Donald L. Smith. Advances in the acquisition and analysis of ct scan data to isolate a crop root system from the soil medium and quantify root system complexity in 3-d space. *Geoderma*, 137(1-2):231–241, 2006. ISSN 0016-7061. doi: 10.1016/j.geoderma.2006.08.025.

William E. Lorensen and Harvey E. Cline. Marching cubes: A high resolution 3d surface construction algorithm. *SIGGRAPH Computer Graphics*, 21(4): 163–169, 1987. ISSN 0097-8930. doi: 10.1145/37402.37422.

Frank Losasso, Tamar Shinar, Andrew Selle, and Ronald Fedkiw. Multiple interacting liquids. *ACM Transactions on Graphics*, 25(3):812–819, 2006. ISSN 0730-0301. doi: 10.1145/1141911.1141960.

Mikaël Lucas, Ranjan Swarup, Ivan A. Paponov, Kamal Swarup, Ilda Casimiro, David Lake, Benjamin Peret, Susan Zappala, Stefan Mairhofer, Morag Whitworth, Jiehua Wang, Karin Ljung, Alan Marchant, Goran Sandberg, Michael J. Holdsworth, Klaus Palme, Tony Pridmore, Sacha Mooney, and Malcolm J. Bennett. Short-root regulates primary, lateral, and adventitious root development in arabidopsis. *Plant Physiology*, 155 (1):384–398, 2011. doi: 10.1104/pp.110.165126.

Jonathan P. Lynch. Root architecture and plant productivity. *Plant Physiology*, 109(1):7–13, 1995. doi: 10.1104/pp.109.1.7.

Jonathan P. Lynch. Roots of the second green revolution. *Australian Journal of Botany*, 55(5):493–512, 2007.

Jonathan P. Lynch, Kai L. Nielsen, Robert D. Davis, and Andrei G. Jablokow. Simroot: Modelling and visualization of root systems. *Plant*

and Soil, 188(1):139–151, 1997. ISSN 0032-079X. doi: 10.1023/A:1004276724310.

Janet S. MacFall, G. Allan Johnson, and Paul J. Kramer. Comparative water uptake by roots of different ages in seedlings of loblolly pine (pinus taeda l.). *New Phytologist*, 119(4):551–560, 1991. ISSN 1469-8137. doi: 10.1111/j.1469-8137.1991.tb01047.x.

Bruce E. Mahall and Ragan M. Callaway. Root communication mechanisms and intracommunity distributions of two mojave desert shrubs. *Ecology*, 73(6):pp. 2145–2151, 1992. ISSN 00129658.

Godfrey G. Maina, Joel S. Brown, and Mordechai Gersani. Intra-plant versus inter-plant root competition in beans: avoidance, resource matching or tragedy of the commons. *Plant Ecology*, 160(2):235–247, 2002. ISSN 1385-0237. doi: 10.1023/A:1015822003011.

Stefan Mairhofer, Susan Zappala, Saoirse R. Tracy, Craig Sturrock, Malcolm J. Bennett, Sacha J. Mooney, and Tony P. Pridmore. Rootrak: Automated recovery of three-dimensional plant root architecture in soil from x-ray microcomputed tomography images using visual tracking. *Plant Physiology*, 158(2):561–569, 2012. doi: 10.1104/pp.111.186221.

Stefan Mairhofer, Susan Zappala, Saoirse R. Tracy, Craig Sturrock, Malcolm J. Bennett, Sacha J. Mooney, and Tony P. Pridmore. Recovering complete plant root system architectures from soil via x-ray mucomputed tomography. *Plant Methods*, 9(1):1–8, 2013. ISSN 1746-4811. doi: 10.1186/1746-4811-9-8.

Ravi Malladi and James A. Sethian. Image processing via level set curvature flow. *Proceedings of the National Academy of Sciences*, 92(15):7046–7050, 1995.

Ravi Malladi, James A. Sethian, and Baba C. Vemuri. Topology-independent shape modeling scheme. In *SPIE's 1993 International Symposium on Optics, Imaging, and Instrumentation*, pages 246–258. International Society for Optics and Photonics, 1993.

Ravi Malladi, James A. Sethian, and Baba C. Vemuri. Shape modeling with front propagation: a level set approach. *Pattern Analysis and Machine*

Intelligence, IEEE Transactions on, 17(2):158–175, 1995. ISSN 0162-8828. doi: 10.1109/34.368173.

Daniele Marin, Rendon C. Nelson, Sebastian T. Schindera, Samuel Richard, Richard S. Youngblood, Terry T. Yoshizumi, and Ehsan Samei. Low-tube-voltage, high-tube-current multidetector abdominal ct: Improved image quality and decreased radiation dose with adaptive statistical iterative reconstruction algorithm-initial clinical experience. *Radiology*, 254(1):145–153, 2010. doi: 10.1148/radiol.09090094.

Antonio Marquina and Stanley Osher. Explicit algorithms for a new time dependent model based on level set motion for nonlinear deblurring and noise removal. *SIAM Journal on Scientific Computing*, 22(2):387–405, 2000. doi: 10.1137/S1064827599351751.

Francesco Masulli and Andrea Schenone. A fuzzy clustering based segmentation system as support to diagnosis in medical imaging. *Artificial Intelligence in Medicine*, 16(2):129–147, 1999. ISSN 0933-3657. doi: 10.1016/S0933-3657(98)00069-4.

Iain Matthews, Takahiro Ishikawa, and Simon Baker. The template update problem. *Pattern Analysis and Machine Intelligence, IEEE Transactions on*, 26(6):810–815, 2004. ISSN 0162-8828. doi: 10.1109/TPAMI.2004.16.

Nelson Max. Optical models for direct volume rendering. *Visualization and Computer Graphics, IEEE Transactions on*, 1(2):99–108, 1995. ISSN 1077-2626. doi: 10.1109/2945.468400.

Stephen J. McKenna, Sumer Jabri, Zoran Duric, Azriel Rosenfeld, and Harry Wechsler. Tracking groups of people. *Computer Vision and Image Understanding*, 80(1):42–56, 2000. ISSN 1077-3142. doi: http://dx.doi.org/10.1006/cviu.2000.0870.

R. Mead and R. W. Willey. The concept of a 'land equivalent ratio' and advantages in yields from intercropping. *Experimental Agriculture*, 16: 217–228, 1980. ISSN 1469-4441. doi: 10.1017/S0014479700010978.

Babu M. Mehtre, Mohan S. Kankanhalli, and Wing Foon Lee. Shape measures for content based image retrieval: A comparison. *Information*

Processing & Management, 33(3):319–337, 1997. ISSN 0306-4573. doi: 10.1016/S0306-4573(96)00069-6.

Erik Meijering. Neuron tracing in perspective. *Cytometry Part A*, 77A(7): 693–704, 2010. ISSN 1552-4930. doi: 10.1002/cyto.a.20895.

Manoj Menon, Brett Robinson, Sascha E. Oswald, Anders Kaestner, Karim C. Abbaspour, Eberhard Lehmann, and Rainer Schulin. Visualization of root growth in heterogeneously contaminated soil using neutron radiography. *European Journal of Soil Science*, 58(3):802–810, 2007. ISSN 1365-2389. doi: 10.1111/j.1365-2389.2006.00870.x.

Barry Merriman, James K. Bence, and Stanley J. Osher. Motion of multiple junctions: A level set approach. *Journal of Computational Physics*, 112 (2):334–363, 1994. ISSN 0021-9991. doi: http://dx.doi.org/10.1006/jcph.1994.1105.

F. Meyer. Contrast features extraction. *SPIE Milestone Series*, 127:139–145, 1996.

Chohong Min. On reinitializing level set functions. *Journal of Computational Physics*, 229(8):2764–2772, 2010. ISSN 0021-9991. doi: http://dx.doi.org/10.1016/j.jcp.2009.12.032.

Egas Moniz. L'encèphalographie artèrielle, son importance dans la localisation des tumeurs cèrèbrales. *Revue Neurologique*, 2:72–90, 1927.

Sacha J. Mooney, Tony P. Pridmore, Jonathan Helliwell, and Malcolm J. Bennett. Developing x-ray computed tomography to non-invasively image 3-d root systems architecture in soil. *Plant and Soil*, 352:1–22, 2012. ISSN 0032-079X. doi: 10.1007/s11104-011-1039-9.

Ahmad B. Moradi, Héctor M. Conesa, Brett Robinson, Eberhard Lehmann, Guido Kuehne, Anders Kaestner, Sascha Oswald, and Rainer Schulin. Neutron radiography as a tool for revealing root development in soil: capabilities and limitations. *Plant and Soil*, 318:243–255, 2009. ISSN 0032-079X. doi: 10.1007/s11104-008-9834-7.

Christopher J. Moran, Alain Pierret, and A. Stevenson. X-ray absorption and phase contrast imaging to study the interplay between plant roots and

soil structure. *Plant and Soil*, 223:101–117, 2000. ISSN 0032-079X. doi: 10.1023/A:1004835813094.

David Mumford and Jayant Shah. Optimal approximations by piecewise smooth functions and associated variational problems. *Communications on Pure and Applied Mathematics*, 42(5):577–685, 1989. ISSN 1097-0312. doi: 10.1002/cpa.3160420503.

Kerstin A. Nagel, Bernd Kastenholz, Siegfried Jahnke, Dagmar van Dusschoten, Til Aach, Matthias Mühlich, Daniel Truhn, Hanno Scharr, Stefan Terjung, Achim Walter, and Ulrich Schurr. Temperature responses of roots: impact on growth, root system architecture and implications for phenotyping. *Functional Plant Biology*, 36:947–959, 2009. doi: 10.1071/FP09184.

Tomomi Nakamoto and Atsushi Oyanagi. The direction of growth of seminal roots of triticum aestivum l. and experimental modification thereof. *Annals of Botany*, 73(4):363–367, 1994. doi: 10.1006/anbo.1994.1045.

Edward A. Nater, Keith D. Nater, and John M. Baker. Application of artificial neural system algorithms to image analysis of roots in soil, i. initial results. *Geoderma*, 53(3-4):237–253, 1992. ISSN 0016-7061. doi: 10.1016/0016-7061(92)90057-E.

E. I. Newman. Relationship between root growth of flax (linum usitatissimum) and soil water potential. *New Phytologist*, 65(3):273–283, 1966. ISSN 1469-8137. doi: 10.1111/j.1469-8137.1966.tb06362.x.

Timothy S. Newman and Hong Yi. A survey of the marching cubes algorithm. *Computers & Graphics*, 30(5):854–879, 2006. ISSN 0097-8493. doi: 10.1016/j.cag.2006.07.021.

OECD and FOA. Oecd-fao agricultural outlook 2013, 2013. URL http://www.oecd-ilibrary.org/agriculture-and-food/oecd-fao-agricultural-outlook-2013_agr_outlook-2013-en.

Stanley Osher and James A. Sethian. Fronts propagating with curvature-dependent speed: Algorithms based on hamilton-jacobi formulations. *Journal of Computational Physics*, 79(1):12–49, 1988. ISSN 0021-9991. doi: 10.1016/0021-9991(88)90002-2.

Ferdinand Österreicher and Igor Vajda. A new class of metric divergences on probability spaces and its applicability in statistics. *Annals of the Institute of Statistical Mathematics*, 55:639–653, 2003. ISSN 0020-3157. doi: 10.1007/BF02517812.

Mehmed Özkan, Benoit M. Dawant, and Robert J. Maciunas. Neural-network-based segmentation of multi-modal medical images: a comparative and prospective study. *Medical Imaging, IEEE Transactions on*, 12 (3):534–544, 1993. ISSN 0278-0062. doi: 10.1109/42.241881.

David Page, Andreas Koschan, Mongi Abidi, Ron Michaels, and Dan McDonald. Novel x-ray imaging and segmentation of root structures. *Sensor Review*, 28:46–51, 2008. ISSN 0260-2288. doi: 10.1108/02602280810850026.

Nikos Paragios and Rachid Deriche. Geodesic active regions and level set methods for supervised texture segmentation. *International Journal of Computer Vision*, 46(3):223–247, 2002. ISSN 0920-5691. doi: 10.1023/A:1014080923068.

Vladimir I. Pavlovic, Rajeev Sharma, and Thomas S. Huang. Visual interpretation of hand gestures for human-computer interaction: a review. *Pattern Analysis and Machine Intelligence, IEEE Transactions on*, 19(7):677–695, 1997. ISSN 0162-8828. doi: 10.1109/34.598226.

J. S. Perret, M. E. Al-Belushi, and M. Deadman. Non-destructive visualization and quantification of roots using computed tomography. *Soil Biology and Biochemistry*, 39(2):391–399, 2007. ISSN 0038-0717. doi: 10.1016/j.soilbio.2006.07.018.

B. J. Perry and C. Bridges. Computerized transverse axial scanning (tomography): Part 3. radiation dose considerations. *British Journal of Radiology*, 46(552):1048–1051, 1973. doi: 10.1259/0007-1285-46-552-1048.

Eric Persoon and King-sun Fu. Shape discrimination using fourier descriptors. *Pattern Analysis and Machine Intelligence, IEEE Transactions on*, PAMI-8(3):388–397, 1986. ISSN 0162-8828. doi: 10.1109/TPAMI.1986.4767799.

Wilhelm Pfeffer. Geotropic sensitiveness of the root-tip. *Annals of Botany*, 8(3):317–320, 1894.

Alain Pierret, Yvan Capowiez, Christopher J. Moran, and Andrè Kretzschmar. X-ray computed tomography to quantify tree rooting spatial distributions. *Geoderma*, 90(3-4):307–326, 1999. ISSN 0016-7061. doi: 10.1016/S0016-7061(98)00136-0.

Alain Pierret, Mac Kirby, and Chris Moran. Simultaneous x-ray imaging of plant root growth and water uptake in thin-slab systems. *Plant and Soil*, 255:361–373, 2003. ISSN 0032-079X. doi: 10.1023/A:1026130532683.

Michel Piotin, Philippe Gailloud, Luc M. Bidaut, Shinya Mandai, Michel Muster, Jacques Moret, and Daniel A. Rüfenacht. Ct angiography, mr angiography and rotational digital subtraction angiography for volumetric assessment of intracranial aneurysms. an experimental study. *Neuroradiology*, 45:404–409, 2003. ISSN 0028-3940. doi: 10.1007/s00234-002-0922-8.

Benjamin N. Potkin, Antonio L. Bartorelli, James M. Gessert, Richard F. Neville, Yaron Almagor, William C. Roberts, and Martin B. Leon. Coronary artery imaging with intravascular high-frequency ultrasound. *Circulation*, 81(5):1575–85, 1990. doi: 10.1161/01.CIR.81.5.1575.

Michael P. Pound, Andrew P. French, Jonathan A. Atkinson, Darren M. Wells, Malcolm J. Bennett, and Tony P. Pridmore. Rootnav: Navigating images of complex root architectures. *Plant Physiology*, 162(4):1802–1814, 2013. doi: 10.1104/pp.113.221531.

Adam H. Price, A. D. Tomos, and D. S. Virk. Genetic dissection of root growth in rice (oryza sativa l.) i: a hydrophonic screen. *TAG Theoretical and Applied Genetics*, 95:132–142, 1997. ISSN 0040-5752. doi: 10.1007/s001220050541.

Adam H. Price, Jill E. Cairns, Peter Horton, Hamlyn G. Jones, and Howard Griffiths. Linking drought-resistance mechanisms to drought avoidance in upland rice using a qtl approach: progress and new opportunities to integrate stomatal and mesophyll responses. *Journal of Experimental Botany*, 53(371):989–1004, 2002a. doi: 10.1093/jexbot/53.371.989.

Adam H. Price, K. A. Steele, J. Gorham, J. M. Bridges, B. J. Moore, J. L. Evans, P. Richardson, and R. G. W. Jones. Upland rice grown in soil-filled chambers and exposed to contrasting water-deficit regimes: I. root

distribution, water use and plant water status. *Field Crops Research*, 76 (1):11–24, 2002b. ISSN 0378-4290. doi: 10.1016/S0378-4290(02)00012-6.

Jan Puzicha, Thomas Hofmann, and Joachim M. Buhmann. Non-parametric similarity measures for unsupervised texture segmentation and image retrieval. In *Computer Vision and Pattern Recognition, 1997. Proceedings., 1997 IEEE Computer Society Conference on*, pages 267–272, 1997. doi: 10.1109/CVPR.1997.609331.

Johann Radon. Über die Bestimmung von Funktionen durch ihre Integralwerte längs gewisser Mannigfaltigkeiten. *Berichte über die Verhandlungen der Königlich-Sächsischen Akademie der Wissenschaften zu Leipzig, Mathematisch-Physische Klasse*, 69:262–277, 1917.

Johann Radon. On the determination of functions from their integral values along certain manifolds, translated by parks, p. c. *Medical Imaging, IEEE Transactions on*, 5(4):170–176, 1986. ISSN 0278-0062. doi: 10.1109/TMI.1986.4307775.

J. Mason Robertson, Richard P. Pharis, Yan Y. Huang, David M. Reid, and Edward C. Yeung. Drought-induced increases in abscisic acid levels in the root apex of sunflower. *Plant Physiology*, 79(4):1086–1089, 1985. doi: 10.1104/pp.79.4.1086.

J. Mason Robertson, Kerry T. Hubick, Edward C. Yeung, and David M. Reid. Developmental responses to drought and abscisic acid in sunflower roots: I. root growth, apical anatomy, osmotic adjustment. *Journal of Experimental Botany*, 41(3):325–327, 1990. doi: 10.1093/jxb/41.3.325.

William Conrad Röntgen. Wilhelm conrad röntgen on a new kind of rays: translation of a paper read before the würzburg physical and medical society, 1895, translated by stanton, a. *Nature*, 53(1896):274–276, 1896.

William Conrad Röntgen. Über eine neue art von strahlen. *Sitzungsberichte der Würzburger Physikalisch-Medizinischen Gesellschaft*, n/a:2–16, 1898.

Azriel Rosenfeld. Connectivity in digital pictures. *Journal of the ACM*, 17 (1):146–160, 1970. ISSN 0004-5411. doi: 10.1145/321556.321570.

Paul L. Rosin. Unimodal thresholding. *Pattern Recognition*, 34(11): 2083–2096, 2001. ISSN 0031-3203. doi: http://dx.doi.org/10.1016/S0031-3203(00)00136-9.

Mikael Rousson and Nikos Paragios. Shape priors for level set representations. In Anders Heyden, Gunnar Sparr, Mads Nielsen, and Peter Johansen, editors, *Computer Vision - ECCV 2002*, volume 2351 of *Lecture Notes in Computer Science*, pages 78–92. Springer Berlin Heidelberg, 2002. ISBN 978-3-540-43744-4. doi: 10.1007/3-540-47967-8_6.

Elisabeth Rouy and Agnès Tourin. A viscosity solutions approach to shape-from-shading. *SIAM Journal on Numerical Analysis*, 29(3):867–884, 1992. doi: 10.1137/0729053.

Reuven Y. Rubinstein and Dirk P. Kroese. *Simulation and the Monte Carlo Method*. Wiley Series in Probability and Statistics. Wiley, 2nd edition, 2008. ISBN 9780470230374.

Gerardo Rubio, Tom Walk, Zhenyang Ge, Xiaolong Yan, Hong Liao, and Jonathan P. Lynch. Root gravitropism and below-ground competition among neighbouring plants: A modelling approach. *Annals of Botany*, 88 (5):929–940, 2001. doi: 10.1006/anbo.2001.1530.

Yossi Rubner, Carlo Tomasi, and Leonidas J. Guibas. The earth mover's distance as a metric for image retrieval. *International Journal of Computer Vision*, 40:99–121, 2000. ISSN 0920-5691. doi: 10.1023/A:1026543900054.

Yossi Rubner, Jan Puzicha, Carlo Tomasi, and Joachim M. Buhmann. Empirical evaluation of dissimilarity measures for color and texture. *Computer Vision and Image Understanding*, 84(1):25–43, 2001. ISSN 1077-3142. doi: 10.1006/cviu.2001.0934.

Yong Rui, Thomas S. Huang, and Shih-Fu Chang. Image retrieval: Current techniques, promising directions, and open issues. *Journal of Visual Communication and Image Representation*, 10(1):39–62, 1999. ISSN 1047-3203. doi: 10.1006/jvci.1999.0413.

Szymon Rusinkiewicz and Marc Levoy. Efficient variants of the icp algorithm. In *3-D Digital Imaging and Modeling, 2001. Proceedings. Third International Conference on*, pages 145–152, 2001. doi: 10.1109/IM.2001.924423.

Berta Sandberg, Tony Chan, and Luminita Vese. A level-set and gabor-based active contour algorithm for segmenting textured images. In *UCLA Department of Mathematics CAM report*, 2002.

Yoshinobu Sato, Shin Nakajima, Nobuyuki Shiraga, Hideki Atsumi, Shigeyuki Yoshida, Thomas Koller, Guido Gerig, and Ron Kikinis. Three-dimensional multi-scale line filter for segmentation and visualization of curvilinear structures in medical images. *Medical image analysis*, 2(2): 143–168, 1998.

John W. Schiefelbein and Chris Somerville. Genetic control of root hair development in arabidopsis thaliana. *The Plant Cell Online*, 2(3):235–243, 1990. doi: 10.1105/tpc.2.3.235.

Sonja Schmidt, A. Glyn Bengough, Peter J. Gregory, Dmitri V. Grinev, and Wilfred Otten. Estimating rootâĂŞsoil contact from 3d x-ray microtomographs. *European Journal of Soil Science*, 63(6):776–786, 2012. ISSN 1365-2389. doi: 10.1111/j.1365-2389.2012.01487.x.

Hannes Schulz, Johannes A. Postma, Dagmar van Dusschoten, Hanno Scharr, and Sven Behnke. 3d reconstruction of plant roots from mri images. In *VISAPP 2012: Proceedings of the International Conference on Computer Vision Theory and Applications*, volume 2, pages 24–33, 2012.

J. Anthony Seibert. Tradeoffs between image quality and dose. *Pediatric Radiology*, 34:183–195, 2004. ISSN 0301-0449. doi: 10.1007/s00247-004-1268-7.

James A. Sethian. Curvature and the evolution of fronts. *Communications in Mathematical Physics*, 101(4):487–499, 1985. ISSN 0010-3616. doi: 10.1007/BF01210742.

James A. Sethian. Level set techniques for tracking interfaces: Fast algorithms, multiple regions, grid generation and shape/character recognition. In *In Proceedings of the International Conference on Curvature Flows and Related Topics, Trento, Italy*, pages 215–231, 1994.

James A. Sethian. A fast marching level set method for monotonically advancing fronts. *Proceedings of the National Academy of Sciences*, 93(4): 1591–1595, 1996.

James A. Sethian. *Level Set Methods and Fast Marching Methods: Evolving Interfaces in Computational Geometry, Fluid Mechanics, Computer Vision, and Materials Science ... on Applied and Computational Mathematics*. Cambridge University Press, 2nd edition, 1999. ISBN 0521645573.

James A. Sethian. Evolution, implementation, and application of level set and fast marching methods for advancing fronts. *Journal of Computational Physics*, 169(2):503–555, 2001. ISSN 0021-9991. doi: 10.1006/jcph.2000.6657.

Robert E. Sharp and Mary E. LeNoble. Aba, ethylene and the control of shoot and root growth under water stress. *Journal of Experimental Botany*, 53(366):33–37, 2002. doi: 10.1093/jexbot/53.366.33.

Robert E. Sharp, Wendy Kuhn Silk, and Theodore C. Hsiao. Growth of the maize primary root at low water potentials: I. spatial distribution of expansive growth. *Plant Physiology*, 87(1):50–57, 1988. doi: 10.1104/pp.87.1.50.

Robert E. Sharp, Valeriy Poroyko, Lindsey G. Hejlek, William G. Spollen, Gordon K. Springer, Hans J. Bohnert, and Henry T. Nguyen. Root growth maintenance during water deficits: physiology to functional genomics. *Journal of Experimental Botany*, 55(407):2343–2351, 2004. doi: 10.1093/jxb/erh276.

Lawrence A. Shepp and Benjamin F. Logan. The fourier reconstruction of a head section. *IEEE Transactions on Nuclear Science*, 21(3):21–43, 1974.

Peter Shirley and Allan Tuchman. A polygonal approximation to direct scalar volume rendering. *SIGGRAPH Computer Graphics*, 24(5):63–70, 1990. ISSN 0097-8930. doi: 10.1145/99308.99322.

Jeffrey H. Siewerdsen and David A. Jaffray. Cone-beam ct with a flat-panel imager: noise considerations for fully 3d computed tomography. In *Medical Imaging 2000: Physics of Medical Imaging*, pages 408–416. International Society for Optics and Photonics, 2000. doi: 10.1117/12.384515.

Albert L. Smit, A. Glyn Bengough, C. Engels, Meine van Noordwijk, S. Pellerin, and S. C. van de Geijn, editors. *Root methods: a handbook*. Springer-Verlag, Berlin, 2000.

Steven W. Smith. *Digital signal processing: a practical guide for engineers and scientists*. Newnes, 2003.

Milan Sonka, Xiangmin Zhang, Maria Siebes, Mark S. Bissing, Steven C. DeJong, Steve M. Collins, and Charles R. McKay. Segmentation of intravascular ultrasound images: a knowledge-based approach. *Medical Imaging, IEEE Transactions on*, 14(4):719–732, 1995. ISSN 0278-0062. doi: 10.1109/42.476113.

Milan Sonka, Wonkyu Park, and Eric A. Hoffman. Rule-based detection of intrathoracic airway trees. *Medical Imaging, IEEE Transactions on*, 15 (3):314–326, 1996. ISSN 0278-0062. doi: 10.1109/42.500140.

Thorvald Sørensen. A method of establishing groups of equal amplitude in plant sociology based on similarity of species and its application to analyses of the vegetation on danish commons. *Biologiske Skrifter*, 5:1–34, 1948.

Sharon A. Stansfield. Angy: A rule-based expert system for automatic segmentation of coronary vessels from digital subtracted angiograms. *Pattern Analysis and Machine Intelligence, IEEE Transactions on*, PAMI-8 (2):188–199, 1986. ISSN 0162-8828. doi: 10.1109/TPAMI.1986.4767772.

Laura Stingaciu, Hannes Schulz, Andreas Pohlmeier, Sven Behnke, Hedwig Zilken, Mathieu Javaux, and Harry Vereecken. In situ root system architecture extraction from magnetic resonance imaging for water uptake modeling. *Vadose Zone Journal*, 12(1):1–9, 2013.

Stuart R. Stock. *MicroComputed Tomography: Methodology and Applications*. CRC Press, 1st edition, 2008. ISBN 1420058762.

Mark Sussman, Peter Smereka, and Stanley Osher. A level set approach for computing solutions to incompressible two-phase flow. *Journal of Computational Physics*, 114(1):146–159, 1994. ISSN 0021-9991. doi: http://dx.doi.org/10.1006/jcph.1994.1155.

Mark Sussman, Ann S. Almgren, John B. Bell, Phillip Colella, Louis H. Howell, and Michael L. Welcome. An adaptive level set approach for incompressible two-phase flows. *Journal of Computational Physics*, 148

(1):81–124, 1999. ISSN 0021-9991. doi: http://dx.doi.org/10.1006/jcph.1998.6106.

J. Michael Swain and H. Dana Ballard. Color indexing. *International Journal of Computer Vision*, 7:11–32, 1991. ISSN 0920-5691. doi: 10.1007/BF00130487.

Ranjan Swarup, Eric M. Kramer, Paula Perry, Kirsten Knox, H. M. Ottoline Leyser, Jim Haseloff, Gerrit T. S. Beemster, Rishikesh Bhalerao, and Malcolm J. Bennett. Root gravitropism requires lateral root cap and epidermal cells for transport and response to a mobile auxin signal. *Nat Cell Biol*, 7:1057–1065, 2005. ISSN 1465-7392. doi: 10.1038/ncb1316.

Jean-Baptiste Thibault, Ken D. Sauer, Charles A. Bouman, and Jiang Hsieh. A three-dimensional statistical approach to improved image quality for multislice helical ct. *Medical Physics*, 34:4526–4544, 2007. doi: 10.1118/1.2789499.

Peter Toft. *The Radon Transform - Theory and Implementation*. PhD thesis, Department of Mathematical Modelling, Technical University of Denmark, 1996.

E. W. Tollner. X-ray computed tomography applications in soil ecology studies. *Agriculture, Ecosystems & Environment*, 34(1-4):251–260, 1991. ISSN 0167-8809. doi: 10.1016/0167-8809(91)90112-B.

Samuel Trachsel, Shawn Kaeppler, Kathleen Brown, and Jonathan Lynch. Shovelomics: high throughput phenotyping of maize (zea mays l.) root architecture in the field. *Plant and Soil*, 341:75–87, 2011. ISSN 0032-079X. doi: 10.1007/s11104-010-0623-8.

Saoirse R. Tracy, Jeremy A. Roberts, Colin R. Black, Ann McNeill, Rob Davidson, and Sacha J. Mooney. The x-factor: visualizing undisturbed root architecture in soils using x-ray computed tomography. *Journal of Experimental Botany*, 61(2):311–313, 2010. doi: 10.1093/jxb/erp386.

Saoirse R. Tracy, Colin R. Black, Jeremy A. Roberts, Craig Sturrock, Stefan Mairhofer, Jim Craigon, and Sacha J. Mooney. Quantifying the impact of soil compaction on root system architecture in tomato (solanum lycopersicum) by x-ray micro-computed tomography. *Annals of Botany*, 110(2):511–519, 2012. doi: 10.1093/aob/mcs031.

Richard Tsai and Stanley Osher. Level set methods and their applications in image science. *Communications in Mathematical Sciences*, 1(4):623–656, 2003. ISSN 1539-6746.

Yen-Hsi Richard Tsai, Li-Tien Cheng, Stanley Osher, and Hong-Kai Zhao. Fast sweeping algorithms for a class of hamilton-jacobi equations. *SIAM journal on numerical analysis*, 41(2):673–694, 2003.

Roberto Tuberosa, Maria Corinna Sanguineti, Pierangelo Landi, Marcella Michela Giuliani, Silvio Salvi, and Sergio Conti. Identification of qtls for root characteristics in maize grown in hydroponics and analysis of their overlap with qtls for grain yield in the field at two water regimes. *Plant Molecular Biology*, 48:697–712, 2002. ISSN 0167-4412. doi: 10.1023/A:1014897607670.

Soumik Ukil and Joseph M. Reinhardt. Anatomy-guided lung lobe segmentation in x-ray ct images. *Medical Imaging, IEEE Transactions on*, 28(2):202–214, 2009. ISSN 0278-0062. doi: 10.1109/TMI.2008.929101.

United Nations UN. The millenium development goals report 2013, 2013. URL http://www.un.org/millenniumgoals/reports.shtml.

Teofilo Vamerali, A. Ganis, S. Bona, and Giuliano Mosca. An approach to minirhizotron root image analysis. *Plant and Soil*, 217:183–193, 1999. ISSN 0032-079X. doi: 10.1023/A:1004616217070.

Corine M. Van der Weele, William G. Spollen, Robert E. Sharp, and Tobias I. Baskin. Growth of arabidopsis thaliana seedlings under water deficit studied by control of water potential in nutrient-agar media. *Journal of Experimental Botany*, 51(350):1555–1562, 2000. doi: 10.1093/jexbot/51.350.1555.

Oliver van Kaick, Hao Zhang, Ghassan Hamarneh, and Daniel Cohen-Or. A survey on shape correspondence. *Computer Graphics Forum*, 30(6):1681–1707, 2011. ISSN 1467-8659. doi: 10.1111/j.1467-8659.2011.01884.x.

G. T. Varney and M. J. Canny. Rates of water uptake into the mature root system of maize plants. *New Phytologist*, 123(4):775–786, 1993. ISSN 1469-8137. doi: 10.1111/j.1469-8137.1993.tb03789.x.

Remco C. Veltkamp. Shape matching: similarity measures and algorithms. In *Shape Modeling and Applications, SMI 2001 International Conference on.*, pages 188–197, 2001. doi: 10.1109/SMA.2001.923389.

Baba C. Vemuri, J. Ye, Yunmei Chen, and Christiana M. Leonard. A level-set based approach to image registration. In *Mathematical Methods in Biomedical Image Analysis, 2000. Proceedings. IEEE Workshop on*, pages 86–93, 2000. doi: 10.1109/MMBIA.2000.852364.

Baba C. Vemuri, J. Ye, Yunmei Chen, and Christiana M. Leonard. Image registration via level-set motion: Applications to atlas-based segmentation. *Medical Image Analysis*, 7(1):1–20, 2003. ISSN 1361-8415. doi: http://dx.doi.org/10.1016/S1361-8415(02)00063-4.

Luminita A. Vese and Tony F. Chan. A multiphase level set framework for image segmentation using the mumford and shah model. *International Journal of Computer Vision*, 50(3):271–293, 2002. ISSN 0920-5691. doi: 10.1023/A:1020874308076.

Luc Vincent. Morphological grayscale reconstruction in image analysis: applications and efficient algorithms. *Image Processing, IEEE Transactions on*, 2(2):176–201, 1993. ISSN 1057-7149. doi: 10.1109/83.217222.

Yoav Waisel, Amram Eshel, and Uzi Kafkafi. *Plant Roots: The Hidden Half.* CRC Press, New York, 3rd edition, 2002.

John Ernest Weaver. *Root Development of Field Crops.* McGraw-Hill Book Company New York and London, 1926.

Jürgen Weese, Michael Kaus, Christian Lorenz, Steven Lobregt, Roel Truyen, and Vladimir Pekar. Shape constrained deformable models for 3d medical image segmentation. In Michael F. Insana and Richard M. Leahy, editors, *Information Processing in Medical Imaging*, volume 2082 of *Lecture Notes in Computer Science*, pages 380–387. Springer Berlin Heidelberg, 2001. ISBN 978-3-540-42245-7. doi: 10.1007/3-540-45729-1_38.

Emo Welzl. Smallest enclosing disks (balls and ellipsoids). In Hermann Maurer, editor, *New Results and New Trends in Computer Science*, volume 555 of *Lecture Notes in Computer Science*, pages 359–370. Springer Berlin Heidelberg, 1991. ISBN 978-3-540-54869-0. doi: 10.1007/BFb0038202.

Lee Westover. Footprint evaluation for volume rendering. *SIGGRAPH Computer Graphics*, 24(4):367–376, 1990. ISSN 0097-8930. doi: 10.1145/97880.97919.

Ross T. Whitaker and Xinwei Xue. Variable-conductance, level-set curvature for image denoising. In *Image Processing, 2001. Proceedings. 2001 International Conference on*, volume 3, pages 142–145, 2001. doi: 10.1109/ICIP.2001.958071.

Michael H. F. Wilkinson, Tsiipke Wijbenga, Gijs de Vries, and Michel A. Westenberg. Blood vessel segmentation using moving-window robust automatic threshold selection. In *Image Processing, 2003. ICIP 2003. Proceedings. 2003 International Conference on*, volume 2, pages II–1093–1096, 2003. doi: 10.1109/ICIP.2003.1246876.

S. T. Willatt, R. G. Struss, and H. M. Taylor. In situ root studies using neutron radiography. *Agronomy Journal*, 70:581–586, 1978. doi: 10.2134/agronj1978.00021962007000040016x.

R. W. Willey. Evaluation and presentation of intercropping advantages. *Experimental Agriculture*, 21:119–133, 1985. ISSN 1469-4441. doi: 10.1017/S0014479700012400.

Dale L. Wilson and J. Alison Noble. Segmentation of cerebral vessels and aneurysms from mr angiography data. In James Duncan and Gene Gindi, editors, *Information Processing in Medical Imaging*, volume 1230 of *Lecture Notes in Computer Science*, pages 423–428. Springer Berlin Heidelberg, 1997. ISBN 978-3-540-63046-3. doi: 10.1007/3-540-63046-5_37.

Dale L. Wilson and J. Alison Noble. An adaptive segmentation algorithm for time-of-flight mra data. *Medical Imaging, IEEE Transactions on*, 18 (10):938–945, 1999. ISSN 0278-0062. doi: 10.1109/42.811277.

Carel W. Windt, Frank J. Vergeldt, P. Adrie De Jager, and Henk van As. Mri of long-distance water transport: a comparison of the phloem and xylem flow characteristics and dynamics in poplar, castor bean, tomato and tobacco. *Plant, Cell & Environment*, 29(9):1715–1729, 2006. ISSN 1365-3040. doi: 10.1111/j.1365-3040.2006.01544.x.

Martin J. Yaffe and John A. Rowlands. X-ray detectors for digital radiography. *Physics in Medicine and Biology*, 42(1):1–39, 1997. doi: 10.1088/0031-9155/42/1/001.

Mineo Yamaguchi and Robert E. Sharp. Complexity and coordination of root growth at low water potentials: recent advances from transcriptomic and proteomic analyses. *Plant, Cell & Environment*, 33(4):590–603, 2010. ISSN 1365-3040. doi: 10.1111/j.1365-3040.2009.02064.x.

Hanxuan Yang, Ling Shao, Feng Zheng, Liang Wang, and Zhan Song. Recent advances and trends in visual tracking: A review. *Neurocomputing*, 74 (18):3823–3831, 2011. ISSN 0925-2312. doi: http://dx.doi.org/10.1016/j.neucom.2011.07.024.

Yan Yang, Allen Tannenbaum, and Don Giddens. Knowledge-based 3d segmentation and reconstruction of coronary arteries using ct images. In *Engineering in Medicine and Biology Society, 2004. IEMBS '04. 26th Annual International Conference of the IEEE*, volume 1, pages 1664–1666, 2004. doi: 10.1109/IEMBS.2004.1403502.

Alper Yilmaz, Omar Javed, and Mubarak Shah. Object tracking: A survey. *ACM Computing Surveys*, 38(4):1–45, 2006. ISSN 0360-0300. doi: 10.1145/1177352.1177355.

Charles T. Zahn and Ralph Z. Roskies. Fourier descriptors for plane closed curves. *Computers, IEEE Transactions on*, C-21(3):269–281, 1972. ISSN 0018-9340. doi: 10.1109/TC.1972.5008949.

Frédéric Zana and Jean-Claude Klein. Segmentation of vessel-like patterns using mathematical morphology and curvature evaluation. *Image Processing, IEEE Transactions on*, 10(7):1010–1019, 2001. ISSN 1057-7149. doi: 10.1109/83.931095.

Guang Zeng, Stanley Birchfield, and Christina Wells. Detecting and measuring fine roots in minirhizotron images using matched filtering and local entropy thresholding. *Machine Vision and Applications*, 17:265–278, 2006. ISSN 0932-8092. doi: 10.1007/s00138-006-0024-4.

Dengsheng Zhang and Guojun Lu. A comparative study on shape retrieval using fourier descriptors with different shape signatures. In *In Proc. of*

international conference on intelligent multimedia and distance education (ICIMADE01), pages 1–9, 2001.

Dengsheng Zhang and Guojun Lu. Review of shape representation and description techniques. *Pattern Recognition*, 37(1):1–19, 2004. ISSN 0031-3203. doi: 10.1016/j.patcog.2003.07.008.

Hongkai Zhao. A fast sweeping method for eikonal equations. *Mathematics of computation*, 74(250):603–628, 2005. ISSN 0025-5718.

Jinming Zhu, Paul A. Ingram, Philip N. Benfey, and Tedd Elich. From lab to field, new approaches to phenotyping root system architecture. *Current Opinion in Plant Biology*, 14(3):310–317, 2011. ISSN 1369-5266. doi: 10.1016/j.pbi.2011.03.020.

Barbara Zitová and Jan Flusser. Image registration methods: a survey. *Image and Vision Computing*, 21(11):977–1000, 2003. ISSN 0262-8856. doi: http://dx.doi.org/10.1016/S0262-8856(03)00137-9.

Richard W. Zobel, Peter Del Tredici, and John G. Torrey. Method for growing plants aeroponically. *Plant Physiology*, 57(3):344–346, 1976. doi: 10.1104/pp.57.3.344.